A Systematic Search for the Global Minimum Structures of Cs, Sn and Au Clusters and Corresponding Electronic Properties

A thesis submitted in partial fulfillment of the requirements of the degree
of
Doctor of Philosophy
at
Massey University, Albany
New Zealand.

Behnam Assadollahzadeh

December 5, 2007

Abstract

Clusters of atoms or molecules form the building blocks of nanoscience and are regarded as a new type of material, as they constitute a bridge between microscopic and macroscopic forms of matter. The experimental and quantum theoretical study of structures, chemical and physical properties and reactivities of nanoclusters represents an innovative and very active field of research, which has resulted in a wide range of applications.

Independent of the model used to describe the bonding in these clusters, one of the prime objectives is to find the geometrical arrangement of the atoms or molecules, for a given cluster size, which corresponds to the lowest energy on the potential energy hypersurface, the global minimum. In order to find such an arrangement, a density functional theory based genetic algorithm code, which is rooted in the Darwinian evolution concept of the survival of the fittest, is developed and utilized to systematically search for the global minimum isomers of homo-nuclear clusters consisting of up to twenty atoms of cesium, tin, gold and of nine atoms of copper. The performance of this algorithm is excellent as numerous energetically lower-lying cluster isomers (compared to those reported in the literature) are found. Extensive valence basis sets together with energy-consistent scalar-relativistic pseudopotentials are employed to optimize the geometry of these clusters and to calculate their electronic properties accurately at the density functional level of theory. Moreover, in collaboration with the Technische Universität Darmstadt, the mean static polarizability of tin clusters are measured by a beam deflection method. The qualitative agreement between measured and calculated dipole moments and static electric dipole polarizabilities of tin clusters up to twenty atoms is satisfactory, thus confirming the accuracy of the theoretical models used in this work. Furthermore, the performance of density functional theory in the field of metallophilicity is investigated for dimeric and trimeric [X-M-PH_3] compounds (X = Cl, Br, I; M = Cu, Ag, Au) and it is found that the metallophilicity decreases down the group 11 elements of the periodic table of elements.

Acknowledgements

I wish to thank *Professor Peter Schwerdtfeger* for his distinguished support as a supervisor and am grateful for his generosity throughout the last four years.

I wish to thank *Dr. Robert Krawczyk* and *Dipl. Ing. Sascha Schäfer* for help in the implementation of BELPHEGOR and *Sascha* also for letting me use his beam deflection apparatus and providing experimental data on tin clusters. *Dipl. Phys. Christian Thierfelder* I thank for enlightening discussions on various topics and the 4-component calculations. I like to also thank the former group members *Dr. Ivan Lim* and *Dr. Nicola Gaston*, and current group members *Susan, Elke, Brian, Detlev, Andreas, Joachim, Patrick* and *Matthias* for brightening up my days at uni and/or general support. The financial support from the Marsden Fund, The Royal Society of New Zealand, the New Zealand Postgraduate Study Abroad Award and of Massey University is greatly acknowledged. Thanks goes also to my Kiwi brother in crime *Dr. hon. Sean Story* for his generosity and apparently never-ending story-telling qualities.

My deepest gratitude goes to my parents **Ali Akbar** and **Mahin** for their love, sacrifice and selfless support throughout every stage of my life, and to my brothers **Bahram** and **Behzad**.

Contents

1 Introduction **10**

1.1 Motivation 10

1.2 Theoretical Methods 13

1.2.1 Schrödinger Equation 13

1.2.2 Basis Sets 16

1.2.3 Hartree-Fock 16

1.2.4 Density Functional Theory 22

1.2.5 Relativistic Effects in Chemistry 25

1.2.6 Pseudopotentials 26

1.3 Static Electric Dipole Polarizability 29

1.3.1 Calculation of Polarizabilities 30

1.3.2 Measurement of Polarizabilities 33

2 Clusters **37**

2.1 Definition and Types 37

2.2 Size Effects and Experimental Synthesis 37

3 Global Optimization **40**

3.1 Genetic Algorithm 40

4 Cesium Clusters **46**

4.1 Motivation 46

4.2 Methods 48

4.3 Results and Discussion 49

4.3.1 Structural Data 49

4.3.2 Polarizabilities and other Electronic Properties 61

4.4 Conclusions 75
4.5 Further Work 77

5 Tin Clusters **78**
5.1 Motivation 78
5.2 Methods 82
5.3 Results and Discussion 83
5.3.1 Structural Data 83
5.3.2 Polarizabilities and other Electronic Properties 92
5.4 Conclusions 108
5.5 Further Work 109

6 Gold Clusters **110**
6.1 Motivation 110
6.2 Methods 114
6.3 Results and Discussion 116
6.3.1 Structural Data 116
6.3.2 Polarizabilities and other Electronic Properties 124
6.4 Conclusions 137
6.5 Further Work 139

7 Copper Nonamer Clusters **140**
7.1 Motivation 140
7.2 Methods 142
7.3 Results and Discussion 143
7.3.1 Structural Data 143
7.3.2 Polarizabilities and other Electronic Properties 146
7.4 Conclusions 149
7.5 Further Work 149

8 Metallophilicity, the Performance of DFT **150**
8.1 Motivation 150
8.2 Methods 152
8.3 Results and Discussion 154
8.4 Conclusions 163

8.5 Further Work 164

9 Summary and Conclusions **165**

10 Appendix **167**

10.1 Basis Sets 167

List of Figures

1.1 Radial Distribution Functions of 5s-Pseudo- and 5s-All Electrons Orbitals . 28
1.2 Experimental Setup of the Beam Deflection Apparatus 34
1.3 Overview of the Beam Deflection 35

3.1 Flow Chart of BELPHEGOR 42
3.2 Pictorial Representation of the Cut and Splice Method 43

4.1 Dipole Polarizability of Atomic Cesium 50
4.2 Predicted Global Minima and Lowest-Energy Isomers of Cs_{2-8} 53
4.3 Predicted Global Minima and Lowest-Energy Isomers of Cs_{9-12} 54
4.4 Predicted Global Minima and Lowest-Energy Isomers of Cs_{13-14} 55
4.5 Predicted Global Minima and Lowest-Energy Isomers of Cs_{15-16} 56
4.6 Predicted Global Minima and Lowest-Energy Isomers of Cs_{17-19} 57
4.7 Predicted Global Minimum and Lowest-Energy Isomers of Cs_{20} 58
4.8 Dipole Polarizabilities of Cesium Clusters 63
4.9 Anisotropies in Cesium Clusters 65
4.10 IP and EA of Atomic Cesium 66
4.11 VIPs of Cesium Clusters 67
4.12 VEAs of Cesium Clusters 68
4.13 VEAs and VIPs of Cesium Clusters 69
4.14 $\Delta_2 E_n$ of Cesium Clusters 70
4.15 $\Delta\epsilon$ of Cesium Clusters 71
4.16 Nearest-Neighbor Distances in Cesium Clusters 73
4.17 E_{coh} of Cesium Clusters I 74
4.18 E_{coh} of Cesium Clusters II 75
4.19 ZPVE of Cesium Clusters 76

5.1 Dipole Polarizabilities of Atomic Tin I 85
5.2 Predicted Global Minima and Lowest-Energy Isomers of Sn_{2-8} 87
5.3 Predicted Global Minima and Lowest-Energy Isomers of Sn_{9-12} 88
5.4 Predicted Global Minima and Lowest-Energy Isomers of Sn_{13-15} 89
5.5 Predicted Global Minima and Lowest-Energy Isomers of Sn_{16-17} 90
5.6 Predicted Global Minima and Lowest-Energy Isomers of Sn_{18-20} 91
5.7 Dipole Polarizability of Atomic Tin II 94
5.8 Dipole Polarizabilities of Tin Clusters 95
5.9 Dipole Moments of Tin Clusters 98
5.10 Experimental and Calculated Polarizabilities of Tin Clusters 99
5.11 Anisotropies of Tin Clusters 101
5.12 IP and EA of Atomic Tin 102
5.13 VEAs and VIPs of Tin Clusters 103
5.14 $\Delta_2 E_n$ of Tin Clusters 104
5.15 $\Delta\epsilon$ of Tin Clusters 105
5.16 Nearest-Neighbor Distances of Tin Clusters 106
5.17 E_{coh} of Tin Clusters 107
5.18 ZPVE of Tin Clusters 108

6.1 Publications on Gold Compounds 111
6.2 Dipole Polarizability of Atomic Gold 116
6.3 Predicted Global Minima and Lowest-Energy Isomers of Au_{2-10} 118
6.4 Predicted Global Minima and Lowest-Energy Isomers of Au_{11-13} 119
6.5 Predicted Global Minima and Lowest-Energy Isomers of Au_{14-15} 120
6.6 Predicted Global Minima and Lowest-Energy Isomers of Au_{16-17} 121
6.7 Predicted Global Minima and Lowest-Energy Isomers of Au_{18-20} 122
6.8 Dipole Polarizabilities of Gold Clusters I 126
6.9 Dipole Polarizabilities of Gold Clusters II 128
6.10 Anisotropies of Gold Clusters 131
6.11 IP and EA of Atomic Gold 132
6.12 VEAs and VIPs of Gold Clusters 133
6.13 $\Delta_2 E_n$ of Gold Clusters 134
6.14 $\Delta\epsilon$ of Gold Clusters 135
6.15 Nearest-Neighbor Distances of Gold Clusters 136

6.16 E_{coh} of Gold Clusters 137
6.17 ZPVE of Gold Clusters 138

7.1 Dipole Polarizabilities of Atomic Copper 144
7.2 Global Minimum and Lowest-Energy Isomers of Cu_9 145

8.1 Optimized Structures of $(Cl\text{-}Au\text{-}PH_3)_{n=1-3}$ 154
8.2 Comparison Between the r_{M-X} Bond Lengths in Optimized Structures of $(X\text{-}M\text{-}PH_3)_{n=1-3}$ 158
8.3 Comparison Between the r_{M-P} Bond Lengths in Optimized Structures of $(X\text{-}M\text{-}PH_3)_{n=1-3}$ 159
8.4 Comparison Between the r_{M-M} Bond Lengths in Optimized Structures of $(X\text{-}M\text{-}PH_3)_{n=2-3}$ 160
8.5 Counterpoise Corrected Interaction Energies of $(X\text{-}M\text{-}PH_3)_{n=2,3}$ 161

List of Tables

4.1 Properties of Cesium Clusters I 51
4.2 Properties of Cesium Clusters II 62

5.1 Properties of Tin Clusters I 84
5.2 Properties of Tin Clusters II 93

6.1 Properties of Gold Clusters I 117
6.2 Properties of Gold Clusters II 125

7.1 Properties of Cu_9 I 146
7.2 Properties of Cu_9 II 147
7.3 Properties of Cu_9 III 148

8.1 Comparison of Geometric Data of (X-M-PH_3) (M=Cu, Ag, Au; X= Cl , Br, I) 155
8.2 Optimized Geometric Data for (X-M-PH_3)$_n$ (M=Cu, Ag, Au and X=Cl, Br, I) 157
8.3 r_{M-M}, $E_{Int(CPC)}$ and Non-Counterpoise Corrected Interaction Energies for (X-M-PH_3)$_n$ Dimers and Trimers 162

10.1 Basis Set Used for Cesium 167
10.2 Basis Set Used for Tin (Basis A) 168
10.3 Basis Set Used for Tin (Basis B) 169
10.4 Basis Set Used for Tin (Basis C) 170
10.5 Basis Set Used for Gold Clusters 171
10.6 Basis Set Used for Copper Nonamer Clusters 172

Chapter 1

Introduction

1.1 Motivation

The investigation of new forms of materials presents a formidable challenge and a huge potential for novel discoveries. The reactivity and physical properties of bulk materials change dramatically as their dimensions are reduced to the nano-scale. Among nanoparticles, nanoclusters play a very important role, as they are the building blocks of nanoscience. The field of nano-science extends through physics, chemistry and engineering and deals with a vast number of important issues, ranging from fundamental science to a variety of technological applications.

Nanoclusters are regarded as a new type of material, since they constitute as a bridge between microscopic and macroscopic forms of matter [1]. An aggregate of a countable number of particles (i.e. atoms or molecules) lacking translational symmetry is considered a cluster. In contrast to molecules, nanoclusters do not have a fixed size or a fixed composition. Clusters may contain any number of constituent particles and, for a specific size, present a vast variety of morphologies.

Due to their fascinating and peculiar properties and unique reactivities, the probing of their geometrical and electronic structures and both chemical and physical properties is of great fundamental interest. These exceptional features are highly size-dependent, giving the ability to tailor cluster properties for specific applications by manipulation of the number of atoms.

Due to their small size, nanoclusters have an immense surface to volume ratio and are well suited for many applications. Traditionally, the interest lies in the area of catalysis [2],

but developments towards biological uses and material sciences are ever increasing. Of interest are however also historical applications such as the use of nanoclusters in the decoration of majolicas with luster [3,4].

Besides technological prospects, a driving force for cluster research has been the fundamental question: How does matter develop from the atom to systems of increasing size, and how do properties change in the course of this growing process? This innovative field of research has already resulted in a wide range of applications. Gold clusters, for instance, are known for their superb catalytic properties and are used for partial hydrogenation of acetylene or low-temperature oxidation of CO on an industrial scale. Moreover, they are predicted to play a major role in the design of nano-scale optical and electronic devices (see chapter (6)). In order to develop cluster applications, however, it is imperative to characterize their minimum geometrical structures and to be able to predict their fundamental physical properties as a function of size.

Independent of the model used to describe the bonding in clusters, one of the prime objectives is to find the geometrical arrangement of atoms, for a given cluster size, which corresponds to the lowest potential energy on the potential energy hypersurface. This arrangement is called the *global minimum* (GM) [5]. The number of local minima rises, however, exponentially with increasing cluster size, making it a formidable task to find the global minimum.

One of the above mentioned properties is the static electric dipole polarizability (α), which is important in three broad areas of physics and chemistry [6]:

- Electromagnetic field-matter interactions, where polarizabilities determine the response of neutral particles to applied fields.
- Collision phenomena, where polarizabilities determine the behavior of neutral particles as partners in interactions with other neutral and/or charged particles.
- As an indication of physical size, structure and shape.

The static electric dipole polarizability, which is described thoroughly in section (1.3), is an observable for understanding the electronic properties and structures of small clusters. It is very sensitive to electron correlation, basis sets, electron density of valence electrons and to their delocalization [7]. The theoretical and experimental accurate determination of dipole polarizabilities is a very active and challenging field of research.

For at least three millennia gold has been known as "King of Metals", or the most "noble" of the metals referring to its resistance towards corrosive forces and its pretty color [8]. Maybe unsurprising, the physics and chemistry of gold have a unique position in the periodic table of elements:

- Bulk gold has a yellow color.
- Its electrochemical potential is the lowest of all metals.
- Gold is the most electronegative of all metals.
- Gold vapor consists of diatomic molecules whose dissociation energy is higher than many other non-metal element, such as iodine [9].
- Gold compounds show a strange interatomic attractive force (aurophilicity, (see chapter (8)).

These examples of astonishing properties are strongly influenced by relativistic effects. Indeed, gold has the largest relativistic effects among any other element with Z<100, thus establishing unusual structures, properties and applications for homo-nuclear gold-clusters.

The objective of this study was to find the global minimum structures of homo-nuclear clusters consisting of up to 20 cesium, tin and gold atoms utilizing a *density functional theory* (DFT) based genetic algorithm approach and to calculate their properties from density based methods. Although there have been many publications regarding clusters[1], most of them do not claim to have systematically searched for the global minimum structures. Those who have, utilized in general global optimizations procedures, such as the basin-hopping method for instance, in combination with empirical methods and usually did not study the dipole polarizabilities as a function of cluster size. To my best knowledge, this thesis represents the first systematic search for the most stable homo-nuclear isomers of cesium, tin and gold clusters employing a DFT based genetic algorithm approach. In collaboration with the Technische Universität Darmstadt, cluster synthesis and polarizability measurements of small tin clusters were undertaken in order to obtain hands on experience on the experimental side of this field of research,

[1] In chapter (6) the number of publications on gold compounds using computational methods is depicted for the time scale 1975 to 2005.

to validate the theoretical models used in this work and to aid the experimentalists to gain insight into parts of their experiments that cannot be understood without the use of theoretical approaches. Since experimental measurements of the dipole polarizability on Cs, Sn and Au clusters have not been reported, a thorough theoretical approach to α is of great interest.

To further test the efficiency of the genetic algorithm approach and to discuss the large discrepancy between observed and calculated polarizabilities of copper clusters, the dipole moments and polarizabilities of the most stable copper nonamer isomers were studied utilizing a large basis set.

Finally, the trend in metallophilicity, the attractive interaction between closed-shell species of group 11, in [X-M-PH_3] (X = Cl, Br, I; M = Cu, Ag, Au) dimers and trimers obtained at the DFT level of theory is studied and the performance of DFT in the field of metallophilicity is addressed.

1.2 Theoretical Methods

In the following a brief description of different theoretical methods of theoretical chemistry is given. For detailed information about these methods, the reader is referred to the textbooks of theoretical and computational chemistry [10–12].

1.2.1 Schrödinger Equation

As a result of the postulates of quantum mechanics, a system is assigned a wavefunction Ψ and all properties of the system can be derived from it. Ψ is a function of time (t), the coordinates[2] $\tau = \tau(\tau_1, \tau_2, ..., \tau_N)$ of all the N particles in the system and is in the non-relativistic case a solution to the time-dependent Schrödinger equation[3]:

$$H(\tau)\Psi(\tau, t) = i\frac{\partial\Psi(\tau, t)}{\partial t} \tag{1.1}$$

For a time-independent (stationary) Hamilton operator, the wavefunction can be separated into

$$\Psi(\tau, t) = \Psi(\tau) \cdot \Theta(t) \tag{1.2}$$

[2]Spatial- and spin coordinates.

[3]All equations are given in atomic units.

and the time-independent Schrödinger equation can be derived

$$H\Psi = E\Psi, \tag{1.3}$$

where $E = \langle\Psi|H|\Psi\rangle$ can be identified as the energy of the system for normalized Ψ. The wavefunction is not an observable, however, according to the Copenhagen interpretation (Heisenberg & Born), the square of the wavefunction can be regarded as a probability density. The total Hamilton operator of an atomic or molecular system is the sum of individual operators of the potential V and kinetic T energy of the nuclei (n) and electrons (e):

$$H = T_e + T_n + V_{ee} + V_{nn} + V_{ne} \tag{1.4}$$

For interacting particles, the time-independent Schrödinger equation is only analytically solvable for one particle systems. Hence, for most chemical relevant problems, approximations have to be applied. The Born-Oppenheimer approximation is based upon the large difference of masses of electrons and nuclei, a factor of 10^3 to 10^5. Assuming an instantaneous reaction of the electrons to the movement of the nuclei, it is justified to solve the electronic Schrödinger equation for a given arrangement of the nuclei:

$$H_e\Psi_e = E_e\Psi_e \tag{1.5}$$

where

$$H_e = T_e + V_{ee} + V_{ne}. \tag{1.6}$$

The total energy in the electronic Schrödinger equation (1.5) depends thus only parametrically on the coordinates of the nuclei, hence in this picture the nuclei move on a potential energy surface (PES), which is the solution of the electronic Schrödinger equation. The total energy of a system is the sum of the electronic energy and the energy of the nucleus-nucleus interaction (V_{nn}). The latter can be calculated as a constant for a given geometrical arrangement of the nuclei. Usually, the electronic Hamilton operator is further separated into one- and two-particle terms $h(i)$ and $g(i,j)$

$$H_e = \sum_i^n h(i) + \sum_{i<j}^n g(i,j) + V_{nn}, \tag{1.7}$$

where $h(i)$ is given by

$$h(i) = \frac{1}{2}\nabla^2 + \sum_\lambda^N \left(-\frac{Z_{i\lambda}}{r_{i\lambda}}\right), \tag{1.8}$$

and represents the kinetic energy of an electron i and its potential energy in the potential caused by the nuclei. The two-particle term $g(i,j)$ specifies the instantaneous potential energy between two moving electrons:

$$g(i,j) = \frac{1}{r_{ij}} \tag{1.9}$$

Since equation (1.5) cannot be solved exactly for systems containing more than one particle, approximate wavefunctions Φ are generated from functions containing single electron wavefunctions ϕ_i (orbitals):

$$\Phi = \sum_{j=1} a_j f_j(\phi_1 \cdots \phi_n) \tag{1.10}$$

These trial wavefunctions Φ_i are then improved to resemble the exact wavefunction as close as possible using the variational principle [12]. It states that, as long as H is bound from below, the energy of the trial wavefunction is higher or equal to the energy of the exact wavefunction:

$$E' = \frac{\langle \Phi | H | \Phi \rangle}{\langle \Phi | \Phi \rangle} \geq E = \frac{\langle \Psi | H | \Psi \rangle}{\langle \Psi | \Psi \rangle} \tag{1.11}$$

In practise E' is never equal to E because the expansion in equation (1.10) is finite. The most simple representation of such a function, which must obey the Pauli exclusion principle [12][4], is the *Slater determinant* (SD):

$$f(\phi_1 \cdots \phi_N) = N!^{-1/2} \begin{vmatrix} \phi_1(1) & \phi_2(1) & \dots & \phi_n(1) \\ \phi_1(2) & \phi_2(2) & \dots & \phi_n(2) \\ \vdots & \vdots & \ddots & \vdots \\ \phi_1(N) & \phi_2(N) & \dots & \phi_n(N) \end{vmatrix} \tag{1.12}$$

The columns in a Slater determinant are single-electron wavefunctions multiplied by the electron spin (spin orbital), while the electron coordinates are all along the rows. The SD has N electrons occupying N spin-orbitals $(\phi_1, \phi_2, \cdots, \phi_N)$ without specifying which electron is in which orbital.

[4]Two identical fermions may not occupy the same quantum state simultaneously.

1.2.2 Basis Sets

In order to calculate the trial wavefunction Φ, the orbitals ϕ_k are expanded into a linear combination of basis functions ξ_j:

$$\phi_k = \sum_{j=1}^{M} c_{jk}\xi_j \tag{1.13}$$

In general, the orbitals can be expanded into any arbitrary basis. For molecular systems, however, usually the *Ansatz* of *linear combination of atomic orbitals* (LCAO) is used to generate the basis. Here, the orbitals are expanded into a linear combination of atomic orbitals centered at each atom. From the solution of the Schrödinger equation for the hydrogen atom it can be derived that each single-electron wavefunction is always of the form

$$\xi_{nlm}(r,\theta,\varphi) = NR_{nl}(r)Y_{lm}(\theta,\varphi) \tag{1.14}$$

where N is a normalization constant, $R_{nl}(r)$ the radial function, $Y_{lm}(\theta,\varphi)$ are the spherical harmonics that describe the angular dependence of the orbital and n, l, m the quantum numbers. The calculation of two-electron integrals, arising from equation (1.9), is simplified by approximating the basis functions $\{\xi_j\}$ into classes of exponential functions that resemble the hydrogenic orbitals. The most convenient functions are the *Gauss type orbitals* (GTO) of the form

$$\xi^{GTO}_{ijk\alpha}(x,y,z) = Nx^i y^j z^k e^{-\alpha r^2}. \tag{1.15}$$

N is a normalization constant, the sum of $i+j+k$ yields the angular momentum quantum number l and α is the orbital exponent. A second type, the *Slater type orbitals* (STO), are defined by

$$\xi^{STO}_{nlm}(r,\theta,\varphi) = Nr^{-n}e^{-\alpha r}Y_{ml}(\theta,\varphi). \tag{1.16}$$

In this work GTOs are solely used and contracted with fixed coefficients C_{ap} to further reduce computational requirements

$$\xi^{CGTO}_{p} = \sum_{a} C_{ap}\cdot\xi^{GTO}_{a}. \tag{1.17}$$

1.2.3 Hartree-Fock

The Hartree-Fock approximation (HF) is the first step in quantum mechanical calculations and is also referred to as the mean field approximation because electron correlation is

accounted for in an average fashion. The wavefunction Ψ is represented by a single orbital configuration Φ, which is expressed as a Slater determinant (equation (1.12)), where the orbitals are expanded into a set of basis functions ξ_j (equation (1.13)). The energy E of the system is evaluated as the expectation value $E = \langle\Psi|H|\Psi\rangle / \langle\Psi|\Psi\rangle$ and variational optimization of this energy yields the Hartree-Fock equations:

$$f(i)\phi_k(i) = \epsilon_k\phi_k(i), \tag{1.18}$$

In this *Eigenvalue* equation, $f(i)$ denotes the Fock operator, $\phi_k(i)$ its eigenfunctions and ϵ_k the eigenvalues. The Fock operator is given for the electron i by,

$$f(i) = h(i) + \sum_{l}^{n/2}(2J_l(i) - K_l(i)) \tag{1.19}$$

where $J_l(i)$ denotes the Coulomb operator

$$J_l(i)\phi_k(i) = \left\langle \phi_l(j) \left| \frac{1}{r_{ij}} \right| \phi_l(j) \right\rangle |\phi_k(i)> \tag{1.20}$$

and $K_l(i)$ the exchange operator

$$K_l(i)\phi_k(i) = \left\langle \phi_l(j) \left| \frac{1}{r_{ij}} \right| \phi_k(j) \right\rangle |\phi_l(i)> \tag{1.21}$$

The sums of Coulomb and exchange operators represent in HF theory the electron-electron interaction. Minimization of the energy E with respect to the orbitals ϕ_k (better the orbital coefficients c_{jk}) yields the HF wavefunction of the system. Since the orbitals depend on the Fock operator and the Fock operator on the orbitals, the HF equations must be solved iteratively; i.e. the HF equations are solved until self consistency is achieved. The aforementioned equations describe the *closed shell*-HF method (*restricted* HF, RHF), where the orbitals ϕ_i are either fully occupied or fully unoccupied; i.e. the same set of orbitals is optimized for α- and β-electrons. High spin, i.e. all unpaired electrons possess the same spin, systems can be calculated using *restricted open shell*-HF. For generic *open shell* systems, *unrestricted*-HF (UHF) is used. While restricted Hartree-Fock theory employs a single orbital twice, once multiplied by the α spin function and once multiplied by the β spin function in the SD, unrestricted Hartree-Fock theory uses different orbitals for the α and β electrons. Therefore, this approach is also called the *different orbitals for different spins* (DODS) method.

Electron Correlation

The electron correlation energy is, within the basis set limit, defined as the difference between the non-relativistic Hartree-Fock energy and the lowest possible energy.

$$E_{Corr} = E_{exact} - E_{HF} \tag{1.22}$$

Since the Hartree-Fock method yields the best one-determinantal trial wavefunction, within the given basis set, it seems sensible to use this wavefunction as a starting point and to implement it with further determinants.

$$\Psi = a_0\Phi_{HF} + \sum_i a_i\Phi_i \tag{1.23}$$

Configuration Interaction

In the *multiconfiguration*-SCF (MCSCF) method, the wavefunction is not determined by only one Slater determinant, as opposed to the HF method, but by a sum of Slater determinants. In general, MCSCF methods are employed for calculations of excited states or whenever a realistic treatment of a system by a single Slater determinant is not sufficient. The MCSCF method was not used in this work and the reader is referred to the before mentioned textbooks on theoretical chemistry.

For N electrons and M basis functions, the HF method yields $N/2$ occupied *molecular orbitals* (MOs) and $M - N/2$ unoccupied (virtual) MOs[5]. The additional determinants Φ_i (equation (1.23)) are generated by replacing MOs that are occupied in the HF determinant by MOs that are unoccupied. Depending on the number of electrons that have been excited into virtual MOs, the Slater determinants are denoted singly, doubly, triply, etc. excited relative to the HF determinant.

The determinant Φ_{nm}^{rs} has been generated by excitation of the occupied MOs ϕ_n and ϕ_m into the virtual MOs ϕ_r and ϕ_s. In a *configuration interaction* (CI) calculation the coefficients of the series expansion of the form

$$\Psi_{CI} = a_0\Phi_0 + \sum_{n,r} a_{nr}\Phi_n^r + \sum_{n<m,r<s} a_{nmrs}\Phi_{nm}^{rs} + \cdots \tag{1.24}$$

are variationally optimized. In the *multireference*-CI (MRCI) approach, the reference function Φ_0 denotes a MCSCF-wavefunction. The wavefunction of a *full CI* (FCI) calculation, i.e. taking into account all possible determinants for the respective system in the

[5]Except for the case of a minimal basis.

above equation, is for an indefinite basis identical to the exact wavefunction. It recovers 100 % of the electron correlation.

However, the expansion series has to be truncated as a FCI calculation is infeasible for all but the smallest systems. The number of determinants grows factorialy with the size of the basis set. Typically truncated series containing double excitations (CID = CI doubles) or single and double excitations (CISD = singles & doubles) are considered. Truncated CI calculations have the drawback of being size inconsistent and hence recover less and less electron correlation as the system grows larger and also cannot be used for dissociation reactions if the CI-space is small [10].

Many-body Perturbation Theory

A widespread method to add corrections to solutions in quantum mechanics, is many-body perturbation theory. If the correction terms are small compared to the already solved problem, the total Hamilton operator H can be expressed as the sum of a reference Hamilton operator H_0 and a perturbation operator H'.

$$H = H_0 + \lambda H' \tag{1.25}$$

H' denotes a small perturbation[6] (i.e. correlation, electric field etc.) and the variable λ the magnitude of the perturbation. For $\lambda \neq 0$, the new wavefunction and energy can be expanded into a Taylor series in powers of the perturbation parameter λ.

$$\begin{aligned} \Psi &= \Psi^0 + \lambda\Psi^1 + \lambda^2\Psi^2 + \lambda^3\Psi^3 + \cdots \\ E &= E^0 + \lambda E^1 + \lambda^2 E^2 + \lambda^3 E^3 + \cdots \end{aligned} \tag{1.26}$$

In the *Møller-Plesset Perturbation Theory* (MP) [13], the sum of Fock operators is used as the reference Hamilton operator.

$$H_0 = \sum f_i \tag{1.27}$$

The Møller-Plesset expansion series has to be carried out to second order (MP2) at least, because MP1 only yields the Hartree-Fock energy. The expense of the calculation scales as N^{n+3} for an MPn calculation[7]. Therefore, calculations are not usually carried out to higher than the fourth order. The coupled cluster method is preferred if higher accuracy

[6] In this case time-independent.

[7] N denotes the number of basis functions.

is required. MP perturbation theory is size consistent[8], but not variational. The latter is not necessarily a problem as the interest is usually in energy differences and not in the total energy itself.

MP calculations are less computer-time demanding than CI and are therefore the preferred method for including electron correlation. However, the main drawback of perturbation theory is the assumption of a sufficiently small perturbation operator. In other words, the poorer the HF wavefunction describes the system, the larger the correlation terms and the more terms have to be included into the MP series. Moreover, if the reference state is poorly described, the convergence can be very slow or unpredictable so that perturbation methods cannot be used. This method is for example not applicable for metallic systems.

Coupled Cluster Methods

In the *coupled cluster theory* (CC) [14, 15], the exact wavefunction Ψ is written as an exponential Ansatz, which is expanded into a Taylor series

$$\Psi = e^T \Phi_0 \tag{1.28}$$

$$e^T = 1 + T + \frac{1}{2!}T^2 + \frac{1}{3!}T^3 + \cdots = \sum_{k=0}^{\infty} \frac{T^k}{k!} \tag{1.29}$$

$$T = T_1 + T_2 + T_3 + \cdots + T_n. \tag{1.30}$$

Φ_0 is the HF ground-state determinant and the excitation from the ground-state into various excited Slater determinants is described by the excitation operator T_i

$$\begin{aligned} T_1\Phi_0 &= \sum_{n}^{occ}\sum_{r}^{vir} t_n^r \Phi_n^r \\ T_2\Phi_0 &= \sum_{n<m}^{occ}\sum_{r<s}^{vir} t_{nm}^{rs} \Phi_{nm}^{rs}. \end{aligned} \tag{1.31}$$

where the *amplitudes* (the expansion coefficients t) are equivalent to the coefficients a in equation (1.24). From equations (1.29 and 1.30) the exponential operator may be written

[8] In contrast to truncated CI.

as

$$e^T = 1 + T_1 + \left(T_2 + \frac{1}{2}T_1^2\right) + \left(T_3 + T_2T_1 + \frac{1}{6}T_1^3\right) + \left(T_4 + T_3T_1 + \frac{1}{2}T_2^2 + \frac{1}{2}T_2T_1^2 + \frac{1}{24}T_1^4\right) + \cdots . \tag{1.32}$$

The first term generates the reference HF and the second the first excited determinants. The terms in the first parenthesis, which are labelled connected (T_2) and disconnected (T_1^2), generate all doubly excited states. In analogy the terms in the second parenthesis generate all possible triply excited states.

Operating on the HF wavefunction with T_i generates all possible excited determinants and is hence equivalent to full CI. Moreover, it has the same computational expense. The advantage in CC theory, however, lies in the consequences associated with truncation of T. Considering for instance only double excitations, i.e. $T = T_2$, the exponential function in equation (1.28) remains indefinite and gives

$$\begin{aligned}\Psi_{CCD} &= e^T \Phi_{HF} \\ &= \left(1 + T_2 + \frac{1}{2!}T_2^2 + \frac{1}{3!}T_2^3 + \cdots\right)\Phi_{HF},\end{aligned} \tag{1.33}$$

where *CCD* denotes *coupled cluster doubles*. In other words, if the highest excitation level in T is n

$$T = 1 + T_1 + ... + T_n, \tag{1.34}$$

then Slater determinants excited more than n times may (and usually do) still contribute to the wavefunction Ψ because of the exponential Ansatz. Therefore, coupled cluster terminated at T_n recovers more correlation energy than configuration interaction with n excitations. This is the reason why truncated CC is size-consistent as opposed to truncated CI.

CCSDT, which allows for excitation operators of the first, second and third order, in general recovers 99% of the correlation energy. However, CCSDT scales as N^8 and can only be used for small systems.[9] The most common approach to include triples contributions is to evaluate them by perturbation theory and to add them to the CCSD result. This approach is known as CCSD(T).

The CCSD(T) method is very accurate, fails only for systems containing multi reference character and has emerged as the reference method for quantum mechanical calcu-

[9]Where N denotes the number of basis functions.

lations. However, for the scope of clusters investigated in this work, the application of CCSD(T) is computationally not feasible.

1.2.4 Density Functional Theory

Density functional theory (DFT) is an approach to the same problem as that outlined so far, but from a different perspective. Unlike the wavefunction, the total density is an observable and for a N-particle system it depends only on three coordinates. Hence, while the complexity of a wavefunction increases rapidly with the number of electrons, the electron density has the same number of variables.

The basis for DFT is the proof by Hohenberg and Kohn that the ground-state electronic energy is determined completely by the ground-state electron density ρ [16]. In other words, the ground-state electronic energy of a system can be described as a functional of the electron density $E[\rho]$. This is significantly different from the wave mechanics approach, where the energy is described as a functional of the wavefunction. For two external potentials $v_1(r)$ and $v_2(r)$ resulting from the same density $\rho(r)$, the ground-state energies can be written as

$$E_1^0 = \langle \Psi_1 | H_1 | \Psi_1 \rangle \quad \text{and} \quad E_2^0 = \langle \Psi_2 | H_2 | \Psi_2 \rangle \,. \tag{1.35}$$

As a consequence of the variational principle,

$$\begin{aligned} E_1^0 &= \langle \Psi_1 | H_1 | \Psi_1 \rangle < \langle \Psi_2 | H_1 | \Psi_2 \rangle \\ \langle \Psi_2 | H_1 | \Psi_2 \rangle &= \langle \Psi_2 | H_2 | \Psi_2 \rangle + \langle \Psi_2 | H_1 - H_2 | \Psi_2 \rangle \\ &= E_2^0 + \int \rho(r)[v_1(r) - v_2(r)]dr \end{aligned} \tag{1.36}$$

The latter can only be true if $v_1(r) = v_2(r)$ and shows that two external potentials can only be the result of two different electron densities. Hence the external potential is uniquely determined by $\rho(r)$ and the energy may be written as

$$E[\rho] = T[\rho] + V_{ne}[\rho] + V_{ee}[\rho] = \int \rho(r) v(r) dr + T[\rho] + V_{ee}[\rho] \tag{1.37}$$

where $V_{ne}[\rho]$ describes the interaction between the nuclei and the electrons, $T[\rho]$ the kinetic energy and $V_{ee}[\rho]$ the electron- electron interaction. In analogy to the variation theorem for wavefunctions, the true energy is always a strict lower bound to the energy of an approximate density $E[\tilde{\rho}]$.

$$E_0 \leq E[\tilde{\rho}] = T[\tilde{\rho}] + V_{ne}[\tilde{\rho}] + V_{ee}[\tilde{\rho}] \tag{1.38}$$

For a model system of N-non-interacting electrons in N orbitals ϕ_i, the kinetic energy T_s and the energy can be written as[10]:

$$T_s[\rho] = \sum_i^N \left\langle \phi_i \left| -\frac{1}{2}\nabla^2 \right| \phi_i \right\rangle \tag{1.39}$$

$$E[\rho] = T_s[\rho] + \int v_s(r)\rho(r)dr. \tag{1.40}$$

By including the electron electron interaction V_{ee}, expressed in terms of a Coulomb $J[\rho]$ and an exchange part $E_{xc}[\rho]$, the energy becomes

$$\begin{aligned} E[\rho] &= \int v(r)\rho(r)dr + T[\rho] + V_{ee}[\rho] \\ &= \int v(r)\rho(r)dr + T_s[\rho] + J[\rho] + (T[\rho] - T_s[\rho]) + (V_{ee}[\rho] - J[\rho]) \\ &= \int v(r)\rho(r)dr + T_s[\rho] + J[\rho] + E_{xc}[\rho]. \end{aligned} \tag{1.41}$$

Where the Coulomb interaction is given as

$$J[\rho] = \frac{1}{2}\int\int \frac{\rho(r)\rho(r')}{|r-r'|}drdr'. \tag{1.42}$$

Thus, E_{xc} accounts for the difference between the classical and quantum mechanical electron electron interaction and includes the difference in kinetic energy between the non-interacting system and the real system. The minimization of $E[\rho]$ by variation of ρ leads to an equation of a system of non-interacting electrons in an effective, external potential $v_{eff}(r)$

$$\begin{aligned} \mu = \frac{\partial E[\rho]}{\partial \rho(r)} &= \frac{\partial T_s[\rho]}{\partial \rho(r)} + v_{ne}(r) + v_J(r) + v_{xc}(r) \\ &= \frac{\partial T_s[\rho]}{\partial \rho(r)} + v_{eff}(r). \end{aligned} \tag{1.43}$$

This system of non-interacting electrons can be solved exactly, if the exact exchange-correlation functional could be determined, by N one-particle Schrödinger equations

$$\left[-\frac{1}{2}\nabla^2 + v_{eff}(r_i)\right]\phi_i = \epsilon_i\phi_i. \tag{1.44}$$

Solving the so-called Kohn-Sham equations (Eq. (1.44)) yields the electron density, which is obtained from the wavefunctions ϕ_i (*Kohn-Sham orbitals*),

$$\rho(r) = \sum_i^N |\phi_i(r)|^2. \tag{1.45}$$

[10]The subscript s specifies the non-interacting system of electrons.

The minimization occurs now from the variation of the Kohn-Sham orbitals in the orbital space, where the restriction of orthonormality has to be taken into account for. The Kohn-Sham orbitals are expanded into a set of basis functions and the respective equations are solved iteratively until self-consistency is reached. Furthermore, as the correlation between electrons of parallel spins is different from that between electrons of opposite spins, in open-shell systems coupled Kohn-Sham equations are considered in order to obtain the α- and β-Kohn-Sham orbitals. The coupling is included into the effective potentials which are usually expressed as functions of the spin polarization ξ [10]

$$\xi = \frac{\rho^{\alpha} - \rho^{\beta}}{\rho^{\alpha} + \rho^{\beta}}. \tag{1.46}$$

If $E_{xc}[\rho]$ was known, DFT would provide the exact total energy, including $T[\rho]$, $V_{ne}[\rho]$ and $V_{ee}[\rho]$. However, since the exact form is unknown[11], the difference between DFT methods is the choice of the functional form of the exchange-correlation energy.

In the *local density approximation* (LDA) it is assumed that the electron density can be treated locally as a uniform electron gas and the exchange-correlation energy E_{xc} is written as a sum of exchange energy E_x and correlation energy E_c. While this is a good approach to model the behavior of simple metals in the bulk, it is clear that the shift from a continuous system of spatially uniform density to the finite regime of molecules and clusters with their sharply varying density requires more sophistication. An obvious starting point, is not to make the correlation and exchange energies only dependent on the local value of the density, but also to consider the extent to which the density is locally changing. Such methods are known as *generalized gradient corrected approximation* (GGA) methods.

As discussed in section (1.2.3), HF-theory can determine the exchange energy "exactly". Since this energy can only be accounted for approximatively in DFT-theory, a strategy has been developed to combine the "exact" HF exchange part with the DFT correlation part. Here, only an adjustable part of the exchange energy is calculated via DFT (i.e. GGA) and the rest via the the Kohn-Sham functions according to the Hartree-Fock method. These hybrid functionals are usually more accurate for evaluating molecular geometries than "pure" GGA functionals, but require more computational time.

The limitations and problems of DFT are hence associated with the exchange-correlation potentials. Different GGA-potentials, for instance, yield bonding energies that

[11] And maybe does not exist at all.

can deviate from each other and from experiments significantly. Moreover, DFT fails to account for long-range correlation of the charge density (i.e. *van der Waals* interactions). LDA and GGA underestimate in general the HOMO-LUMO energy gap[12]. For larger systems and even for the small-sized clusters investigated in this work, however, DFT is the method of choice as it makes the best compromise between a realistic treatment of the electronic structure and the computational cost.

1.2.5 Relativistic Effects in Chemistry

Although the theory of relativistic quantum physics had been developed in 1928, its relevance in chemistry was only recognized in the late seventies [17, 18]. For valence shells, these effects increase roughly like Z^2 but have to be considered already for small systems such as H_2^+ or H_2, if very precise calculations are required [19]. Relativistic effects can be defined as anything arising from the finite speed of light (i.e. $c \approx 137.036$ a.u.) as compared to $c = \infty$, and can be evaluated for a given property as the difference between the results obtained in a non-relativistic and relativistic calculation.

The qualitative effects of relativity in chemistry can be ascribed to the high kinetic energy of tightly bound core electrons in heavy atoms. Due to the relativistic mass increase

$$m = \frac{m_0}{\sqrt{1 - v^2/c^2}}, \tag{1.47}$$

where m_0 denotes the rest mass and v the speed of the electron, the effective Bohr radius

$$a_0 = \frac{4\pi\epsilon_0\hbar^2}{me^2}, \tag{1.48}$$

with ϵ_0 denoting the vacuum permittivity, $\hbar$ the Planck constant ($h/2\pi$) and e the elementary charge, decreases for core electrons with large average speeds. The average speed of a 1s-electron is Z a.u., which means that for Au a rough estimation gives a radius of only $\sqrt{1 - 79^2/137^2} \approx 0.82$ times what it would be non-relativistically. The contraction (i.e. energetic stabilization) of s-orbitals with a great density near the nucleus denote *direct* relativistic effects. Due to orthogonality constraints, the energy of the valence s-orbitals must also be stabilized. The contraction of these orbitals improves the shielding of the nucleus and results in the expansion (i.e. energetic destabilization) of the d- and f-orbitals. This is called an *indirect* relativistic effect.

[12]HOMO is the highest occupied molecular orbital and LUMO the lowest unoccupied molecular orbital.

Hence, even though relativistic effects are greatest near the nucleus, the indirect effects on the valence electrons affect the valence orbitals and thus play an important role in bonding. It is well established that gold shows unusually large relativistic effects compared to other elements in the Periodic Table of Elements. The whole chemistry of gold is dominated by relativistic effects and is discussed in the refs. [8, 20–23].

1.2.6 Pseudopotentials

One of the most fundamental assumptions in chemistry is that low lying core electrons are inert and are not perturbed by a molecular environment. In line with this assumption, significant computational savings in a quantum mechanical investigation can be achieved by restricting the actual calculation to the valence electron system and include the influence of the core electrons by means of a (core) potential, i.e. the core orbitals are no longer variationally determined. This approximation is called the *frozen core approximation* (FCA). Even greater computational savings can be obtained, once in addition to the FCA the interaction of the core electrons among each other and the interaction of the core electrons with the valence electrons are replaced by a scalar *pseudopotential* (PP). In other words, the objective of the PP approximation is to construct a Hamiltonian which is only dependent upon the coordinates of the valence electrons, but takes into account the influence of the inert core electrons. This approach goes back to the pioneering work of Hellmann and Gombás [24,25] in the mid thirties. To fully exploit computational simplifications, it turned out to be necessary to introduce a pseudo-orbital transformation, which eliminates radial nodes of valence orbitals yielding pseudo-valence orbitals [26].

A suitably parameterized PP offers two central advantages over an all-electron (AE) calculation. Firstly, the PP approximation is the key step in making calculations of molecules containing heavier atoms feasible[13], since the number of basis functions to describe the oscillating behavior of the valence orbitals in the core region is drastically reduced by the pseudo-orbital transformation. Secondly, it allows in an efficient and elegant way to implicitly introduce direct and indirect relativistic effects into (formally) non-relativistic calculations. Furthermore, the *basis set superposition error* (BSSE) is reduced, since the core orbitals are described by an effective potential rather than basis functions.

[13]PP are already adopted for molecules containing elements of the third period of the Periodic Table of Elements.

Pseudopotentials are distinguished according to the adjustment of their parameters. Shape-consistent PP are parameterized usually from a single atomic (ground) state whereas energy-consistent PP are derived from a multitude of atomic states. Since the general idea of a PP is to develop it once for an atom and then also to use it for different states of the atom as well as in molecules, energy-consistent PP ensure better transferability and accuracy. In both cases, the core-valence division in constructing the PP is performed in a way that the core remains inert, i.e. its polarizability should be small and it should not contain electrons that could overlap with the valence electrons of another atom or molecule.

PPs are generated in the framework of the independent-particle model, as electrons are indistinguishable and a n-particle Hamiltonian cannot be separated into a core and a valence part. Parameterization from Hartree-Fock calculations yields non-relativistic pseudopotentials, whereas adjusting the parameters to Wood-Boring calculations (Dirac-Fock calculations) yields scalar-relativistic (relativistic) ones. Scalar-relativistic PPs account only for direct and indirect relativistic effects, whereas relativistic PPs also consider spin-orbit coupling.

In this work energy consistent pseudopotentials generated by the STUTTGART group [27] are solely used. These are, unless otherwise stated, derived from Dirac-Fock calculations. However, since spin-orbit coupling has not been considered in the investigation of the clusters mentioned in this work[14], the utilized pseudopotentials only account for scalar-relativistic effects.

Pseudo-orbitals need to fulfill two conditions. They have to be consistent in shape with the all electron orbitals in the valence region and smooth (nodeless) in the core region. The former condition ensures comparability with all electron calculations, while the latter gives rise to drastic reductions in computational costs. Figure (1.1) depicts these two requirements by means of the radial distribution functions of fictitious 5s-orbitals.

Approximating the cores as spherical symmetric entities carrying charges $Q_\lambda = Z_\lambda - n_{c,\lambda}$ (where Z is the nuclear charge and n_c the number of core electrons), the non-relativistic valence Hamiltonian can be written as [28]

$$H_{val} = -\frac{1}{2}\sum_{i}^{n_v}\Delta_i + \sum_{i}^{n_v}\sum_{\lambda}^{n_c}\left[-\frac{Q_\lambda}{r_{i\lambda}} + V_\lambda^{PP}(r_{i\lambda})\right] + \sum_{i<j}^{n_v}\frac{1}{r_{ij}} + \sum_{\lambda<\mu}^{n_c}\frac{Q_\lambda Q_\mu}{r_{\lambda\mu}}. \qquad (1.49)$$

Here n_v denotes the number of the valence electrons, i, j are valence-electron indices,

[14] Except for the tin atom.

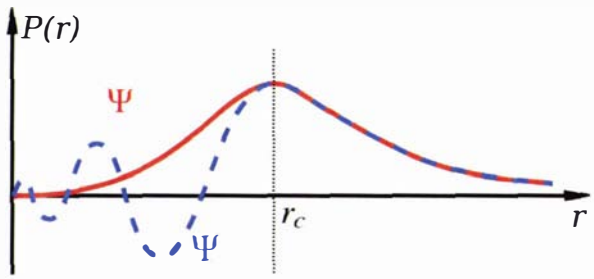

Figure 1.1: Radial distribution functions of fictitious 5s-pseudo- (red) and 5s-all electrons orbitals (blue, dashed)

λ, μ are core-electron indices and V_λ^{PP} denotes the short-range part of the core-valence potential. V_λ^{PP} is the main focus in pseudopotential theory. In the semi-local *Ansatz*, V_λ^{PP} is dependent on the orbital angular momentum of the valence electrons (i.e. V_l^{PP}; $l = s, p, d, f, ...$) and is given for the above mentioned Hamiltonian as

$$V_\lambda^{PP}(r_{i\lambda}) = V_L^{PP}(r_{i\lambda}) + \sum_{l=0}^{L-1}(V_l^{PP}(r_{i\lambda}) - V_L^{PP}(r_{i\lambda}))\mathcal{P}_l. \tag{1.50}$$

Here $L-1$ is the greatest total orbital angular momentum upon which a semi-local pseudopotential term V_l^{PP} can act on and $\mathcal{P}_l$ is a projection operator acting on the spherical harmonics at the nucleus λ:

$$\mathcal{P}_l = \sum_{m_l=-l}^{l} |lm_l><lm_l| \tag{1.51}$$

All local potentials V_L^{PP} can in principle be expressed by semi-local terms. Moreover, since the semi-local terms decrease with increasing orbital angular momentum quantum number l, the local terms can be discarded if L is taken high enough.

$$V_\lambda^{PP}(r_{i\lambda}) = \sum_{l=0}^{L-1} V_l^{PP}(r_{i\lambda})\mathcal{P}_l \tag{1.52}$$

Finally, the semi-local terms of the pseudopotential can be conveniently written as an expansion in terms of Gauss functions multiplied by r_i:

$$V_l^{PP}(r_{i\lambda}) = \sum_k r_{i\lambda}^{n_{lk}} B_{lk} e^{-\beta_{lk} r_{i\lambda}^2} \tag{1.53}$$

where λ and i represent the nuclei and electrons this potential is applied to and k labels the Gauss functions that have exponents β_{lk}^λ and coefficients B_{lk}^λ. Since the exponents n_{lk} are usually set to zero in STUTTGART pseudopotentials, only the exponents and coefficients of the Gauss functions need to be adjusted.

1.3 Static Electric Dipole Polarizability

Arguably, the geometrical structure of a cluster is its most fundamental property. The experimental evidence on the structures of small clusters is however scarce, constituting one of the major difficulties in the understanding of these fascinating materials. In order to gain insight into the geometrical structures of clusters in experiments, theoreticians must guess or predict cluster geometries and find the most stable isomer. Since metal clusters often have several isomers with similar energies, the accuracy of the calculations may not be sufficient to determine which one is the most stable isomer. Hence, it is advisable to also calculate properties that are sensitive to the geometry and compare these with measurements.

As discussed in section (1.1), the static electric dipole polarizability of small clusters is a very interesting property, not only because it probes the response to a simple field perturbation, but also because it is sensitive to the morphology of small clusters. In the experimental studies of polarizabilities, there are in general large variations observed in the per atom polarizability of the cluster on going from one size to the next. These variations are associated with a variation on the clusters' geometric structures. A comparison of experimental polarizabilities with theoretical values predicted for different isomers can thus give clear insight into the structure of the observed cluster.

Indeed, the measurement of the static electric dipole polarizability of sodium clusters [29] and its interpretation in terms of the jellium model [30] can be regarded as one of the triggers for the research activities that today form the field of modern metal cluster physics.

A collection of important physical quantities that depend on the scalar polarizability are listed in [6]. When an external static electric field ($\mathbf{F}$) is applied to a molecule, its charge distribution will interact with the electric field and its dipole moment will change according to equation (1.62). α is defined as the magnitude of that change per unit of electric field strength and denotes a second-rank tensor[15]. That is, the polarization of the molecule is proportional to the external field, but the direction of the induced dipole moment may not be the same as the direction of the applied field.

[15] In other words, α is a measure of the molecule's ability to respond to an electric field and acquire an electric dipole moment.

$$\begin{pmatrix} \mu_x \\ \mu_y \\ \mu_z \end{pmatrix} = \begin{pmatrix} \alpha_{xx} & \alpha_{xy} & \alpha_{xz} \\ \alpha_{yx} & \alpha_{yy} & \alpha_{yz} \\ \alpha_{zx} & \alpha_{zy} & \alpha_{zz} \end{pmatrix} \begin{pmatrix} F_x \\ F_y \\ F_z \end{pmatrix} \tag{1.54}$$

The scalar polarizability is defined to be

$$\alpha = \frac{1}{3}\mathbf{Tr}(\alpha) = \frac{1}{3}\sum_i \alpha_{ii} \tag{1.55}$$

and the anisotropy for the diagonal form of the polarizability tensor is given by

$$\begin{aligned} \alpha_{aniso} &= \left[\frac{1}{2}[3\mathbf{Tr}(\alpha^2) - (\mathbf{Tr}\alpha)^2]\right]^{\frac{1}{2}} \\ &= \left[\frac{1}{2}[(\alpha_{xx} - \alpha_{yy})^2 + (\alpha_{xx} - \alpha_{zz})^2 + (\alpha_{yy} - \alpha_{zz})^2]\right]^{\frac{1}{2}}. \end{aligned} \tag{1.56}$$

For a spherically symmetric system α is a scalar quantity (i.e. $\alpha_{xx} = \alpha_{yy} = \alpha_{zz}$).

1.3.1 Calculation of Polarizabilities

The calculation of static electric dipole polarizabilities can be realized by the *finite field method*, a numerical method first employed by Cohen and Roothaan [31], and analytically following perturbation theory[16]. In the former framework, the perturbation of a small but finite uniform external electric field is applied to a system, where its interaction with the system is described by a perturbing Hamiltonian

$$H^{(1)} = -\boldsymbol{\mu} \cdot \mathbf{F} = -\sum_i q_i \mathbf{r}_i \cdot \mathbf{F}, \tag{1.57}$$

where q_i is the charge of the particle i at the location $\mathbf{r}_i$. The polarizability is then evaluated from numerical differentiation of the change in energy or the induced dipole moment via

$$\alpha_{ij} = -\frac{\partial^2 E}{\partial F_i \partial F_j}\bigg|_{\mathbf{F}=0} = -\frac{\partial \mu_i}{\partial F_j}\bigg|_{\mathbf{F}=0} = -\frac{\partial \mu_j}{\partial F_i}\bigg|_{\mathbf{F}=0} (i, j = \{x, y, z\}). \tag{1.58}$$

This expression origins from the Hellmann-Feynman theorem

$$\frac{dE}{dP} = \left\langle \frac{\partial H}{\partial P} \right\rangle, \tag{1.59}$$

[16] The polarizability is always calculated at $T = 0$ K, unless stated otherwise.

where here the total Hamiltonian is a sum of the unperturbed H^0 and the perturbed H^1 operator and the derivation is with respect to the electric field strength F_i. Since H^0 is independent of F_i it follows from equations (1.57) and (1.59):

$$\frac{\partial E}{\partial F_i} = \left\langle \frac{\partial H}{\partial F_i} \right\rangle = \left\langle \frac{\partial H^{(1)}}{\partial F_i} \right\rangle = -\langle \mu_i \rangle \tag{1.60}$$

The energy E of a molecule in the presence of an external electric field can be developed in terms of a Taylor expansion relative to its energy $E(0)$ in the absence of the field $\mathbf{F}$[17]:

$$\begin{aligned} E = E(0) &+ \left.\frac{\partial E}{\partial F_i}\right|_{\mathbf{F}=0} F_i + \frac{1}{2}\left.\frac{\partial^2 E}{\partial F_i \partial F_j}\right|_{\mathbf{F}=0} F_i F_j \\ &+ \frac{1}{6}\left.\frac{\partial^3 E}{\partial F_i \partial F_j \partial F_k}\right|_{\mathbf{F}=0} F_i F_j F_k + \cdots (i,j,k = \{x,y,z\}) \end{aligned} \tag{1.61}$$

It then follows from equation (1.60) that

$$\begin{aligned} \langle \mu_i \rangle = \underbrace{-\frac{\partial E}{\partial F_i}} &= \underbrace{-\left.\frac{\partial E}{\partial F_i}\right|_{\mathbf{F}=0}} \underbrace{-\left.\frac{\partial^2 E}{\partial F_i \partial F_j}\right|_{\mathbf{F}=0} F_j} \underbrace{-\frac{1}{2}\left.\frac{\partial^3 E}{\partial F_i \partial F_j \partial F_k}\right|_{\mathbf{F}=0} F_j F_k} - \cdots \\ \langle \mu_i \rangle = &\quad \boldsymbol{\mu_0} \qquad + \alpha_{ij} F_j \qquad + \frac{1}{2}\beta_{ijk} F_j F_k \qquad + \cdots , \end{aligned} \tag{1.62}$$

where $\boldsymbol{\mu_0}$ denotes the permanent dipole moment, α_{ij} the polarizability and β_{ijk} the first hyperpolarizability.

For the ground state $|0\rangle$, the perturbation expression for the energy E is given as

$$E_0 = E_0^{(0)} + \langle 0|H^{(1)}|0\rangle + \sum_{n\neq 0} \frac{\langle 0|H^{(1)}|n\rangle \langle n|H^{(1)}|0\rangle}{E_0 - E_n} + \cdots , \tag{1.63}$$

where the summation includes all electronic states. For a homogeneous electric field perturbation along the z-axis with $H^{(1)} = -\mu_z F_z$, it follows

$$E_0 = E_0^{(0)} - \langle 0|\mu_z|0\rangle F_z + \sum_{n\neq 0} \frac{\langle 0|\mu_z|n\rangle \langle n|\mu_z|0\rangle}{E_0 - E_n} F_z^2 + \cdots . \tag{1.64}$$

The first derivative with respect to the external field at $F_z = 0$ states that the permanent electric dipole moment of the molecule is the expectation value of the dipole moment operator in the unperturbed state of the system.

$$\mu_{0z} = -\left.\frac{dE_0}{dF_z}\right|_{F_z=0} = \langle 0|\mu_z|0\rangle \tag{1.65}$$

[17] When an index variable appears twice in a single term, a summation over all its possible values is implied.

As derived above, the dipole polarizability is defined as the second derivative of the energy with respect to the external field, which gives after setting $F_z = 0$ the so-called sum-over-state expression:

$$\alpha_{zz} = -2 \sum_{n \neq 0} \frac{\langle 0|\mu_z|n\rangle \langle n|\mu_z|0\rangle}{E_0 - E_n} \tag{1.66}$$

Using $\Delta E_{n0} = E_n - E_0$ and writing the matrix elements $\langle 0|\mu_z|n\rangle$ as $\mu_{z,0n}$ simplifies the above expression to:

$$\alpha_{zz} = 2 \sum_{n \neq 0} \frac{\mu_{z,0n}\mu_{z,n0}}{\Delta E_{n0}} \tag{1.67}$$

For applied fields along the x- and y-direction, analogous expressions are found and the mean polarizability, the property observed when a molecule is rotating in a fluid and it presents all orientations to the applied field, yields[18]:

$$\begin{aligned} \alpha &= \frac{2}{3} \sum_{n \neq 0} \frac{\mu_{x,0n}\mu_{x,n0} + \mu_{y,0n}\mu_{y,n0} + \mu_{z,0n}\mu_{z,n0}}{\Delta E_{n0}} \\ &= \frac{2}{3} \sum_{n \neq 0} \frac{|\mu_{n0}|^2}{\Delta E_{n0}} = \frac{1}{3} \sum_{i}^{3} \alpha_{ii} \end{aligned} \tag{1.68}$$

In general, the unit of polarizability is given in cubic meters. This is realized after introducing the polarizability volume, α', which is defined as

$$\alpha' = \frac{\alpha}{4\pi\epsilon_0}, \tag{1.69}$$

where ϵ_0 is the vacuum permittivity.

The intensities of spectroscopic transitions also depend on the square of the transition dipole moments and their frequencies. A measure of absorption intensity is the oscillator strength f, which for the transition $n \leftarrow 0$ is

$$f_{n0} = \left(\frac{4\pi m_e}{3e^2\hbar} \right) \nu_{n0} |\mu_{n0}|^2. \tag{1.70}$$

Hence, the polarizability can be expressed in terms of oscillator strengths and so provides a link between spectroscopy and predictions of polarizabilities (oscillator strength formula)[19]. It follows that

$$\alpha = \frac{\hbar^2 e^2}{m_e} \sum_{n \neq 0} \frac{f_{n0}}{\Delta E_{n0}^2}, \tag{1.71}$$

[18]The appearance of the expression is simplified by writing the numerator as a scalar product of two vectors, $\boldsymbol{\mu}_{0n} \cdot \boldsymbol{\mu}_{n0} = \mu_{x,0n}\mu_{x,n0} + \mu_{y,0n}\mu_{y,n0} + \mu_{z,0n}\mu_{z,n0}$ and acknowledging that $\boldsymbol{\mu}$ is hermitian, $\boldsymbol{\mu}_{0n} = \boldsymbol{\mu}_{n0}^*$.

[19]Strong absorptions at low energies give rise to large polarizabilities.

where the summation includes all electronic states, both discrete and continuum. The oscillator strengths of the dominant transitions may be taken from experiment, from a calculation of the excitation spectrum or from estimates based on general sum rules. Their respective energies can be taken from their locations on the frequency scale. Even if it is not feasible to obtain all f_{n0}, equation (1.71) is still extremely useful in establishing the bounds of the dipole polarizability. This results from the fact that oscillator strengths satisfy the Thomas-Reiche-Kuhn (TRK) sum rule [32]

$$\sum_{n\neq 0} f_{n0} = N_e, \tag{1.72}$$

where N_e is the total number of electrons. Hence, for a subset n' of transitions with known oscillator strengths, a lower bound on α is given by

$$\alpha \geq \alpha_{min} = \frac{\hbar^2 e^2}{m_e} \sum_{n'\neq 0} \frac{f_{n'0}}{\Delta E_{n0}^2}. \tag{1.73}$$

Consequently, the upper bound is found by assigning the remaining oscillator strength, $N_e - \sum_{n'\neq 0} f_{n'0}$ to the smallest possible energy difference E_{min}. The exact expression in equation (1.71) can be developed by approximating that all excitation energies are equal

$$\alpha \approx \frac{\hbar^2 e^2}{m_e \Delta E^2} \sum_{n\neq 0} f_{n0} \tag{1.74}$$

and gives according to the TRK sum rule:

$$\alpha \approx \frac{\hbar^2 e^2 N_e}{m_e \Delta E^2} \tag{1.75}$$

Thus, the polarizability increases as the number of total (valence) electrons increases and as the mean excitation energy decreases. The two effects reinforce one another, so molecules composed of heavy atoms are expected to be strongly polarizable.

1.3.2 Measurement of Polarizabilities

There is a variety of experimental methods for determining the polarizability [6]. Since it is linked to the dielectric constant and the refractive index, in traditional methods the polarizability is evaluated after measuring these properties. For small metal clusters, however, beam deflection techniques, as depicted in figure (1.2), have been established as the method of choice. In the following, a brief summary of the theory behind this

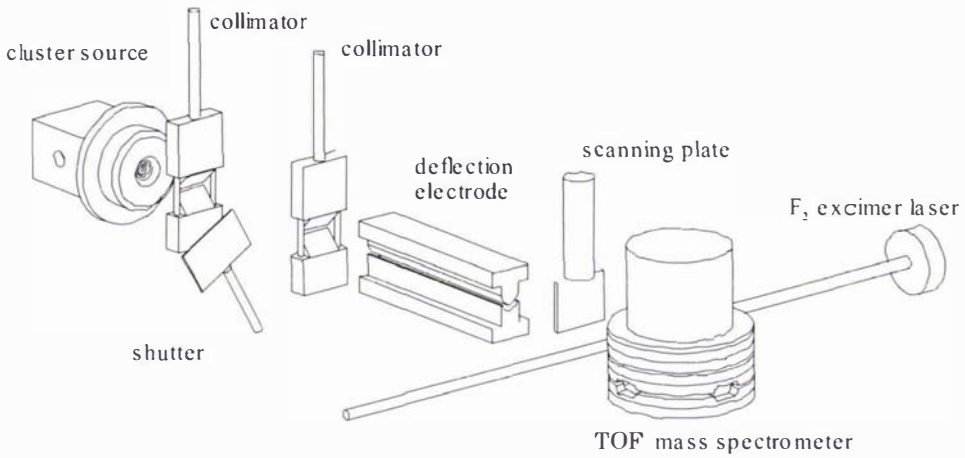

Figure 1.2: Sketch of the experimental setup used to measure the static electric dipole polarizability by deflection of a molecular beam.

method, which was used to measure polarizabilities of small tin clusters, and its technical implementation is given.

Here, the polarizability is determined by observing the deflection of a collimated cluster beam which is passed through a static, inhomogeneous electric field $\mathbf{F}$. The external field induces a dipole moment in a neutral cluster according to equation (1.62). In order to simplify the following expressions, it is assumed that the permanent dipole moment $\boldsymbol{\mu}_0$ and also the hyperpolarizability β can be neglected. Furthermore, the polarizability is regarded as a scalar. Due to the induced dipole moment in the external field $\mathbf{F}$, a force $\mathcal{F} = \nabla\mathbf{F} \cdot \boldsymbol{\mu}$, acts upon the cluster and accelerates it towards higher field strengths. In general, the field is constructed in such a way, that only the z-component of the field gradient in z-direction is significantly different from zero, thus giving:

$$\mathcal{F}_z = \alpha F_z \frac{\partial F_z}{\partial z} \tag{1.76}$$

For a cluster with velocity v and mass m that passes such a field of length L_1 in y-direction, the deflection is given as

$$\Delta d_1 = \frac{L_1^2}{2} \frac{\alpha}{mv^2} F_z \frac{\partial F_z}{\partial z}, \tag{1.77}$$

where L_1 denotes the length of the electrodes as depicted in figure (1.3). This deflection results in a change of the z-component of the velocity

$$v_z = L_1 \frac{\alpha}{mv} F_z \frac{\partial F_z}{\partial z}, \tag{1.78}$$

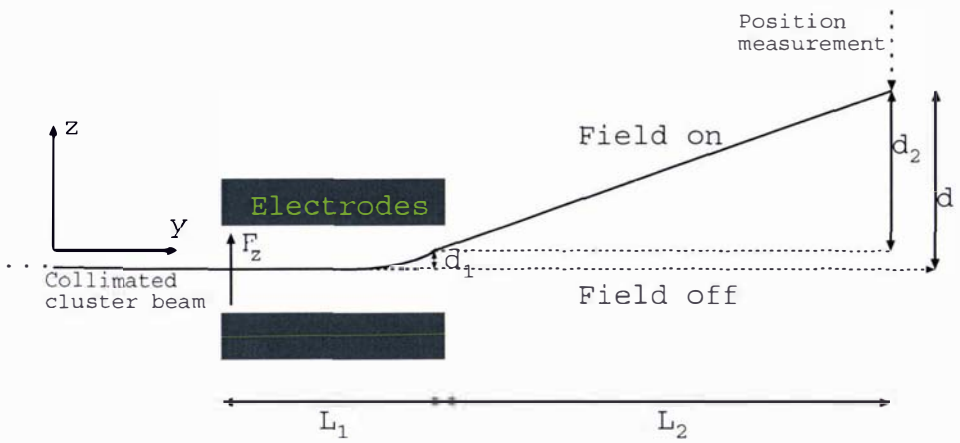

Figure 1.3: Overview of the cluster beam deflection in an inhomogeneous, electric field. The distance between the steel electrodes is 1.4 mm, their length 160 mm, their thicknesses 3.77 mm and 4.00 mm, respectively, and the field strength adjustable up to 30 kV/mm.

and yields, after a second flight route L_2 outside of the electrical field, an additional deflection $\Delta d_2 = \Delta v_z \frac{L_2}{v}$. The total deflection $\Delta d = \Delta d_1 + \Delta d_2$ is thus expressed as

$$\Delta d = \left(\frac{L_1^2}{2} + L_1 L_2 \right) \frac{\alpha}{mv^2} F_z \frac{\partial F_z}{\partial z}. \tag{1.79}$$

According to the above mentioned approximations, the deflection is thus proportional to the polarizability and the product of field strength and field strength gradient. Moreover, the velocity of the cluster needs to be determined experimentally.

A thorough description of the technical implementation of the beam deflection apparatus is given in ref. [33]. Its cluster source consists of a Nd:YAG laser (10 Hz, 6 ns; 50 mJ @ 1064 nm), focused on a rotating metal rod and is connected through a fast nozzle to the helium carrier gas. The so generated plasma cools off in a He atmosphere (1 - 0.1 mbar), recombines and condenses to charged and neutral clusters. These clusters are then expanded through a nozzle, which is connected to a helium cryostat (50 - 300 K), supersonicly into a high vacuum chamber (ca. $5 \cdot 10^{-7}$mbar). A collection of skimmers, pinholes and collimators are used to narrow the cluster beam to approx 0.5 mm in height and 10 mm in width. According to equation (1.79), the product of field strength and field strength gradient need to be constant throughout the whole geometry of the electrodes. This is realized by the so-called *two wire* geometry [33].

For mass selection, the clusters are ionized using a pulsed F_2-excimer laser (1.25 mJ @

157 nm). Before ionization, the clusters pass an electronically controlled shutter, which allows for determining the intensity distribution of the clusters in arbitrary positions of the beam. After ionization, the cluster ions reach an orthogonal time of flight (TOF) mass spectrometer and are accelerated normal to the initial flight route. The final velocity of the accelerated ions varies with their individual masses. Hence, in combination with the electronically controlled shutter a mass- and position resolved separation of the cluster size distribution in the beam is realized. Subsequently, the ions reach an Even-Cup detector, where they are re-accelerated and impinge onto an aluminum plate, exciting electrons. These electrons are laterally accelerated through an aperture onto a scintillator plate, resulting in emitted photons which are detected by a photo-multiplier and conversed into electrical currents that are picked up by an oscilloscope.

The cluster velocities (up to 1000 m/s for Sn_1 - Sn_{20}) are determined using a shutter, which is positioned right after the cluster source and is used to gradually interrupt the cluster beam [33,34]. In principle, the ionization time is kept constant, while the closure time of this shutter is varied. Together with the known dimensions of the apparatus, the velocities can be determined according to

$$v = \frac{l}{t_{ion} - \tau}, \tag{1.80}$$

where l represents the flight route of the clusters, t_{ion} the ionization time and τ the moment where the shutter is fully closed. The deflection of the cluster beam is determined by comparison of the mass resolved beam profile with and without the applied field.

Chapter 2

Clusters

2.1 Definition and Types

In chemistry, an aggregate of a countable number of particles (i.e. atoms or molecules) lacking translational symmetry is considered a cluster. The constituent particles can be of the same kind, resulting in homo-atomic (or homo-molecular) clusters (N_n), or they may be of two or more different species, leading to hetero-atomic (or hetero-molecular) clusters ($N_n M_m$). There are many different types of clusters, such as metallic clusters, fullerenes, semiconductor clusters, molecular clusters, rare-gas clusters and ionic clusters. The features and properties of these distinct physical objects may be studied in the gas phase, in a cluster molecular beam, adsorbed onto a surface or trapped in an inert matrix.

2.2 Size Effects and Experimental Synthesis

Both theoretical and experimental investigations on the size-dependent evolution of cluster properties and geometric and electronic structures represent a major area of current research [1,6,7,35–37] and are rooted in the fundamental interest in these nano-particles and also in the potential to fine tune cluster properties for technological applications by carefully controlling their size and the type of particles they are composed of. Important questions that are addressed with this respect are:

- Is a distinct growth-pattern for the geometric structures observable and if so, does it give insight into the crystal growth at the microscopic level?
- How rapidly do cluster structures and properties converge towards the bulk limit?

- Is the nature of bonding in discrete clusters the same as in the bulk solid?
- Can phase transitions be observed and are they of the same type as in bulk solids or surfaces?
- When does the onset of metallic behavior occur in finite-sized clusters of metals?[1]

The synthesis of clusters may be performed in a number of ways, depending for instance on the type of clusters under investigation, the required size range, production intensity and temperature and can be divided into three main stages: cluster generation, cluster investigation and cluster detection. The most important cluster sources are:

- **Seeded supersonic nozzle sources** produce metal vapor in a hot oven, which is seeded into an inert carrier gas[2]. The mixture is then expanded into a high vacuum resulting in a supersonic beam. This adiabatic expansion cools the vapor which becomes saturated and condenses into clusters and continues until its density becomes too low, which results in clusters with hundreds to thousands of atoms. These sources produce continuous, intense cluster beams with narrow velocity distributions. The molar mass of the inert gas, its temperature and the nozzle aperture cross-section are the main factors that determine the size and distribution of clusters.
- **Gas-aggregation sources** generate metal vapor by evaporation or sputtering and utilize supersaturation of the vapor introduced into a flow of cold inert gas to introduce aggregation of (alkali metal) clusters with usually more than 20000 atoms. The low temperature of the inert gas ensures the addition of one atom at a time, ignoring the relative stabilities of the clusters.
- **Ion sputtering sources** produce clusters by bombarding a metal surface with high-energy inert gas ions (i.e. Kr and Xe) and may be used to generate clusters of high-melting metals. The clusters are initially very hot and cool by evaporation of atoms, thus giving rise to abundance spectra reflecting the relative stabilities of the cluster sizes. This source typically produces small, singly ionized clusters.

[1]The use of the term metallic can be problematic for clusters, but in general a closure of the band gap, i.e. smaller than kT, is understood by this.

[2]Usually He or Ar.

- **Spray sources** are used to produce clusters from liquids and solutions. In thermospray sources, a liquid or a solution of a usually involatile sample is partially pyrolyzed before expansion through a needle into a stagnation chamber with a flowing inert carrier gas, whereupon a subsonic beam containing neutral and charged clusters is generated. Electrospray sources work in a similar fashion, however, the needle may carry a relative negative or positive potential.

- **Laser vaporization sources**[3] are used to produce small and medium-sized clusters of any type of metal, carbon and silicon for instance. Here, a plasma with a temperature of around 10^4 K is produced by focusing a pulsed excimer or Nd:YAG laser on the surface of a rotating metal rod. Introducing the plasma into a cold helium pulse results in rapid cooling and induces cluster formation. Adiabatic cooling occurs as in the seeded supersonic nozzle source, but much lower temperatures can be achieved. Neutral and ionic clusters are generated in this way.

- **Pulsed-arc cluster-ion sources** are very similar to the laser vaporization sources, however an intense electrical discharge is used instead of a laser.

[3]This source was used to produce small tin clusters as described in section (1.3.2).

Chapter 3

Global Optimization

3.1 Genetic Algorithm

The global minima and energetically lowest-lying isomers of all clusters presented in this thesis were obtained utilizing a genetic algorithm code BELPHEGOR, which was developed in this work, as described in detail below. In the research of clusters, obtaining the *global minimum* (GM) structure, i.e. the geometric structure with the lowest energy, is one of the most fundamental and challenging problems. Challenging, due to the fact that the number of local minima increases exponentially with the number of atoms, giving rise to at least 988 local minima for a homo-nuclear cluster containing 13 atoms for instance [38]. Fundamental, because clusters corresponding to the GM are the most likely candidates for most probable structures formed in a cluster experiment. *Genetic algorithms* (GA) present an efficient solution to this problem. The main functionalities of BELPHEGOR are inspired by R. L. Johnston's review article on genetic algorithms [39] to which the reader is referred for background. Technically, GAs are inspired by the Darwinian evolution process in which only the fittest candidates of a population can survive permanently [40]. Numerically, they represent an iterative, stochastic algorithm maintaining a population of individuals.

The application of GAs to clusters was pioneered by Hartke, who investigated the global minimum of Si_4 clusters using an empirical potential energy surface [41]. Zeiri introduced a GA that employed the real-valued Cartesian coordinates of the clusters, hence removing the requirement of encoding and decoding binary genes [42]. The next step in the development of GAs used for optimizing cluster structures was introduced by

Deaven *et al.* [38]. In his approach each structure generated by the GA is subjected to a gradient driven local minimization.

Deaven's approach is very significant, as it represents Lamarckian rather than Darwinian evolution. Characteristics that are acquired by an individual in the course of its lifetime can be passed on to its offspring in the Lamarckian concept of evolution [43]. In the Darwinian concept of evolution the characteristics that are passed on to an offspring are the ones that the parent possessed when it was born. The former is preferable since the modified genetic information is passed from parents to offspring.

A GA can be divided into three essential steps: selection, mating (or crossover) and mutation. Figure (3.1) depicts a flow chart of the operation of BELPHEGOR. The initial population (typically ranging from 10 - 20 individual structures) in the 'mating pool' is generated in part randomly by placing the atoms in a cubic box, with edge lengths a that are given by

$$a = 1.2N^{\frac{1}{3}}d_{min}, \tag{3.1}$$

where N represents the number of atoms and d_{min} the minimal distance between any two atoms. Further initial structures were constructed from global minima Lennard-Jones structures with adapted bond lengths according to the cluster type in question. Moreover, great effort has been made to extract the predicted lowest-lying minima of the clusters in question from various publications. These empirical structures represent the final part of the initial population. All structures in the initial population are then relaxed into their nearest local minimum using DFT and the Los Alamos minimum basis set and corresponding shape-consistent scalar-relativistic pseudopotential (LANL2MB). In the algorithm the fitness of each minimum structure is determined based on its energy V_i (total electronic energy plus nuclear-nuclear repulsion energy). The structure with the lowest energy in a population is assigned a fitness of 1 and that with the highest energy a fitness of 0. The fitness f_i of each local minimum of the evolving population is calculated using a dynamically scaled potential energy ρ_i,

$$\rho_i = \frac{V_i - V_{min}}{V_{max} - V_{min}}, \tag{3.2}$$

where V_{max} and V_{min} are the highest and lowest energies in the current population, respectively. Using the roulette wheel selection method [39] two members of the current population are chosen for mating (i.e. to be parents) according to their fitness. BELPHEGOR uses an exponential type fitness function, thus favoring the choice of parents towards

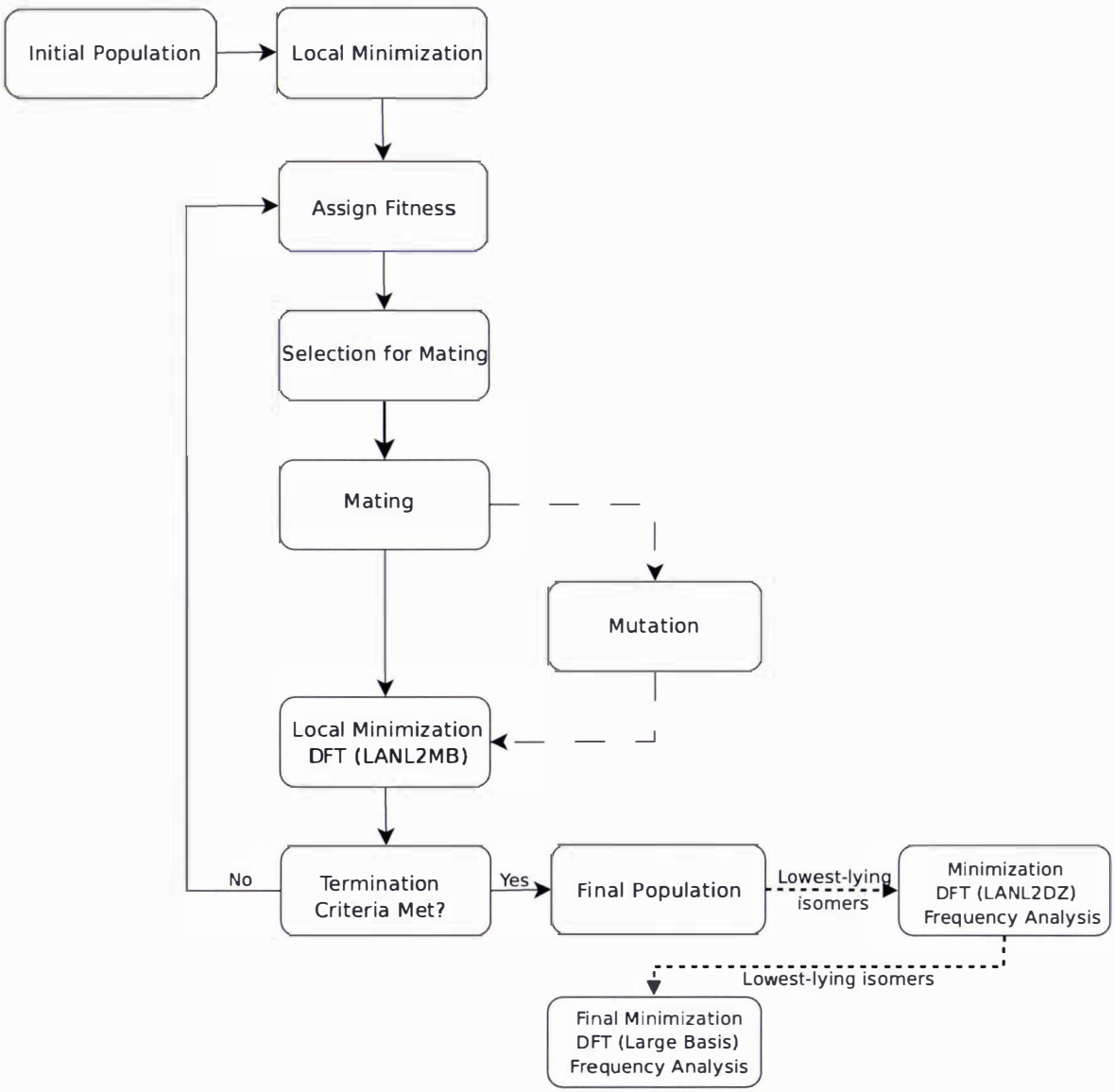

Figure 3.1: Flow chart for the genetic algorithm program BELPHEGOR used in the search for the global minima of cesium, tin, gold and copper nonamer clusters.

those clusters with low energy.

$$f_i = e^{-\alpha\rho_i} = e^{-3\rho_i} \tag{3.3}$$

In the process of mating, the chosen parent structures are first aligned according to their main axis of inertia, then both are rotated randomly about the same angle and finally cut horizontally through their mass centers into halves as depicted in figure (3.2). Complementary halves are then merged to form an offspring, ensuring that the number of atoms remains constant and that the lengths of the newly formed bonds are similar to the bond lengths in the parent structures. This operation is a variant of the so called 'cut and splice' crossover operation introduced by Deaven *et al.* [38]. The offspring is then relaxed into its local minimum. The structural rearrangements during the minimization step are greatest in the region of the splice between the fragments 'inherited' by its parents and it is ensured that the minimal (d_{min}) and maximal (d_{max}) bond lengths are not exceeded.

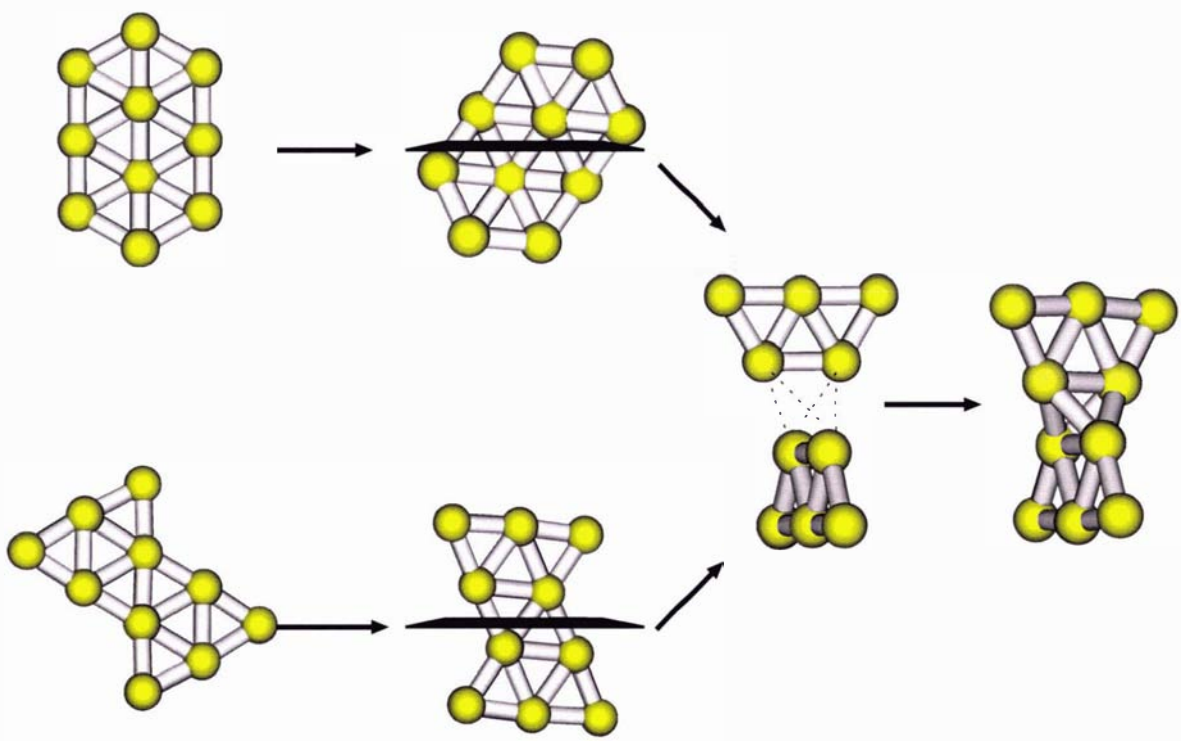

Figure 3.2: Pictorial representation of the cut and splice method. Two structures, here two Au_{10} isomers, are selected for mating according to their fitness, rotated randomly about the same angle and cut horizontally through their mass centers. Complementary halves are then merged, employing a random dihedral angle, to form an offspring.

After an optimized offspring has been obtained, a selection operation is performed to decide its fate. If its energy is lower than that of any cluster in the mating pool, a new pair of mates are selected and the process is repeated. The cluster with the highest energy in the mating pool is discarded once the population has reached 50. An optimized offspring is, however, discarded if its energy is within the minimum energy difference δV_i of a member of the pool in order to maintain structural diversity within the pool. Structural diversity is furthermore increased by allowing members of the mating pool to mutate. The percentage mutated is initially 10 % and is increased to 20 % for the last 50 mating steps. In a mutation the atomic coordinates of a chosen number of the atoms, typically surface atoms, are given randomly generated values. The termination criteria for BELPHEGOR is set between 100 and 200 mating and local minimization steps.

Once the termination criteria is reached, typically four to ten of the most stable isomers are further optimized from a Los Alamos double-zeta basis set and corresponding shape-consistent scalar-relativistic pseudopotential (LANL2DZ) calculation, and a subsequent harmonic vibrational analysis is carried out. From this set of structures, typically two to six energetically lowest-lying isomers are further optimized using the extensive STUTTGART valence basis set together with the energy-consistent scalar-relativistic pseudopotential for the respective cluster type in question. Finally, a harmonic vibrational analysis is performed for all isomers.

The uniqueness of the present GA approach towards the global minimum should be stressed. Other studies using GAs to obtain a global minimum structure usually utilize two-body or many-body potentials or semi-empirical methods. These approaches are highly questionable, as such model potentials cannot describe the bonding nature of metal clusters reliably [44]. Empirical methods are usually parameterized according to certain bulk material properties, but there are unpredictable differences in geometric structures and chemical and physical properties between bulk materials and their clusters. In fact, this is one of the inspirations for the study of these nano-materials. As a result, first-principle methods like wave-function based *ab initio* or density based DFT treatments should be used [45].

It has to be mentioned, however, that the DFT approach presented in this work is orders of magnitude more computationally expensive than utilizing empirical methods. Hence, although *ab initio* and DFT methods describe the interactions much more accurately, the number of mating operations in the GA approach required to establish a high

probability of having obtained the global minimum structure cannot be realized necessarily. As many as 5000 mating operations were required to obtain the ideal icosahedral buckyball structure of C_{60} using a tight-binding method starting from four random initial candidates and disregarding the mutation operation [46].

In this work the number of mating operations and local minimization step varies typically between 100 - 200, where the limitation is only due to availability of computing power. This might seem significantly too small. Not to be sneezed at, however, is that the initial populations in this work do not only consist of random structures, but also of published best candidates for lowest-lying minima evaluated at the *ab initio* and/or DFT level. This drastically reduces the required number of mating steps to find the GM. Furthermore, the cluster sizes in this work are markedly smaller than the buckyball C_{60}, resulting in significantly less structural possibilities. A thorough description of the parameterization of BELPHEGOR for each cluster type investigated in this work is given in the respective chapters.

Chapter 4

Cesium Clusters

4.1 Motivation

Due to their basic electronic structure, with only one valence electron, the first main group clusters represent the simplest metal clusters to study theoretically and, hence, have been used as an antetype system for understanding size effects in metal clusters. Indeed, the synthesis of sodium clusters by Knight *et al.* and detection of electronic shell structure [48, 49], as well as the measurement of their static electric dipole polarizabilities [29] and interpretation in terms of the jellium model [30, 50] can be regarded as one of the triggers for the extensive research activities that today form the field of modern metal cluster physics.

In the lowest approximation, the jellium picture [6], an alkali-metal cluster can be regarded as a microscopic metallic droplet, consisting of ionic cores and a delocalized electron cloud, which results from the weakly bound valence electrons. For an ideal conductor ($\epsilon \rightarrow \infty$) with spherical shape, the polarizability, for this approximation, is simply given as [6]

$$\alpha_{classical} = R^3, \tag{4.1}$$

where the positive background formed by the ions is denoted by a uniformly charged sphere of radius R. The application of this expression to microscopic clusters provides correct order-of-magnitude estimates of cluster polarizabilities.

Alkali-metal clusters are amongst the most polarizable particles in existence [51] and Knight's *et al.* [29] pioneering experimental studies on sodium clusters revealed that the polarizabilities, depending on the cluster size n, are enhanced towards the classical value,

reaching values of up to $\approx 2R^3$, and then slowly decrease to the bulk value. Phenomenologically, this enhancement has been attributed to the electron *spill-out* effect[1]. The electron spill out ultimately increases the effective radius of the particle and thus, the polarizability can be approximated by

$$\alpha_{classical} \cong (R + \delta)^3, \tag{4.2}$$

where $R = r_{ws} N_e^{\frac{1}{3}}$ and δ denotes the effective radius enhancement. r_{ws} is the bulk Wigner-Seitz radius and N_e the total number of valence electrons.

Displaying the largest relativistic correction (decrease of α_{iso} by 16 % [52]) and core electron contribution (decrease of α_{iso} by 4 % [53]) to the polarizability of the stable alkali atoms, cesium enjoys a rather exceptional position within the group of alkali metals. This is furthermore confirmed by the substantial amount of experimental and theoretical studies of the polarizabilities and structural properties of homonuclear and heteronuclear lithium [55–63, 69–72], sodium [29, 48, 51, 54, 56, 58, 63, 64, 73, 74, 76–82] and potassium clusters [63, 65–68, 83, 84], to name a few, whereas there is no experimental or theoretical polarizability studies of small neutral cesium clusters[2]. There is also scarce theoretical work done on the structural properties of small cesium clusters. Stevens *et al.* calculated the polarizabilities of polyhedral clusters and compared them to linear clusters up to 8 and 10 atoms, respectively, [85]. Borstel *et al.* studied the electronic-, atomic structure and inhomogeneous contraction of the interatomic distances in Cs_n clusters up to $n = 70$ using the spherical average pseudopotential (SAPS) method [86, 87]. Blaisten-Barojas *et al.* [88] and Lai *et al.* [89] investigated the structure of alkali-metal clusters (Na, K, Rb, Cs) employing the Gupta potential fitted to the local density approximation database to account for the interactions between atoms in the cluster.

Since Blaisten-Barojas *et al.* report only selected structures of cesium clusters in their publication and do not mentioned how they actually obtained these structures systematically, it is not clear if the displayed Cs_n structures given by them correspond to the lowest energy minima. In contrary, Lai *et al.* obtained their structures by utilizing the genetic algorithm- and the basin hopping method. They find the same predicted global minima for both methods.

[1] The conduction electrons in a large metallic particle are essentially located in the interior (except for a thin surface layer). In a finite cluster, however, a considerable fraction of these electrons are located near the surface. As a result, a significant portion of the electron cloud spills-out beyond the edge of the jellium background.

[2] To my best knowledge

Maity *et al.* looked into the geometrical and electronic properties of cesium clusters up to ten atoms employing density functional and second-order Møller-Plesset perturbation theory [90]. They, however, were not looking for global minima structures, neither conducted a frequency analysis for their reported structures nor investigated polarizabilities.

Regarding the generation of cesium clusters, only the work of Gspann is mentioned in the literature [91]. He generated clusters with up to 2500 atoms per cluster from pure vapor expansion and investigated the velocities of them. Avoiding the use of a carrier gas means that the metal vapor cannot cool down sufficiently to produce small and medium-sized clusters in a high abundance and Gspann also stated that "...the clusters have been predicted to remain liquid when resulting from pure vapor expansions...". It appears that the higher susceptibility of cesium to oxidation and explosive nature towards water (even to ice) lead to great experimental challenges for beam deflection techniques.

There are, however, some experimental and theoretical studies on the cesium atom, dimer and trimer (negatively charged) available for spectroscopy [75], ionization potentials [92–96], the polarizability [52, 53, 97–101], lifetime measurements [102], Stark shift measurements [103–106], and photoabsorption spectra [107–109].

This work is hence inspired by the lack of experimental measurements and theoretical calculations of polarizabilities and structural- and electronic data for small cesium clusters ranging up to twenty atoms (Cs_2 - Cs_{20}).

4.2 Methods

The predicted low-spin global minima (GM) of cesium clusters (Cs_{2-20}) were obtained utilizing the genetic algorithm code BELPHEGOR as described in detail in section (3.1). The initial populations[3] of the clusters up to six atoms were generated randomly, whereas those for the larger clusters consisted both of randomly generated structures as well as predicted low-lying minima structures of sodium clusters from the literature [80,82]. The minimum energy difference $\delta_i V$ was set to 0.002 eV[4], d_{min} and d_{max} parameters were fixed at 2.8 Å and 8-10 Å, respectively. The termination criteria for BELPHEGOR was 150 mating and local minimization steps for clusters up to ten atoms and 100 steps for the remaining clusters. The mutation probability was first set to 10 % and then increased

[3] Ranging typically from ten to twelve different structures for Cs_{7-20} clusters.

[4] The energy difference between the isomers of the larger cesium clusters is often marginal (see table (4.1)).

to 60 % for the last 20 mating steps. Depending on the cluster energy distribution, the energetically lowest-lying six to ten isomers were then further optimized from LANL2DZ basis set and pseudopotential calculations.

Four to six of the energetically lowest-lying true minima structures obtained by this means were then further optimized using the extensive STUTTGART valence basis set together with the energy-consistent relativistic pseudopotential for cesium [110]. Finally, a harmonic vibrational analysis was performed for all clusters in order to discriminate between minima and transition states on the potential energy surface. All reported properties were calculated based on these structures. All calculations were performed with the GAUSSIAN03 program package [331]. For the exchange-correlation potential, the generalized gradient approximation (GGA), according to the parameterization suggested by Becke [111] and Perdew [112] (bp86), was applied in a self-consistent fashion. No symmetry constraints were applied during the optimization procedure.

Several DFT functionals comprising different exchange and correlation functions such as b3p86, b3lyp, b3pw91, blyp, bp86, pw91pw91, svwn, svwn5, pbepbe, mpw1pw91, b1b95 and pbe1pbe were tested in the case of the cesium atom to look for the best DFT functional reproducing the experimental (59.43 A^3 [53]) and highly accurate CCSD(T) calculation in the *Douglas-Kroll-Hess* (DKH) transformation (58.69 A^3 [52]) for the polarizability. As depicted in figure (4.1), the exchange-correlation potential (bp86) within the generalized gradient approximation (GGA), combined with the extensive STUTTGART valence basis set and pseudopotential for cesium [110], gives excellent agreement with the aforementioned experimental and calculated results. All structures are singlet states for even-numbered cesium clusters and doublet states for the odd-numbered ones.

4.3 Results and Discussion

4.3.1 Structural Data

The following figures (4.2-4.7) and table (4.1) show the structures, relative energies, average neighbor distances[5], vertical ionization potentials (VIP), vertical electron affinities (VEA)[6] and cohesive energies per atom of the the lowest-energy isomers and global minima predicted by the simulations for Cs_n clusters with $2 \leq n \leq 20$. The VIPs (VEAs)

[5]Calculated as the arithmetic mean of all distances ($d \leq 6$ Å).

[6]Vertical detachment energy (VDE)

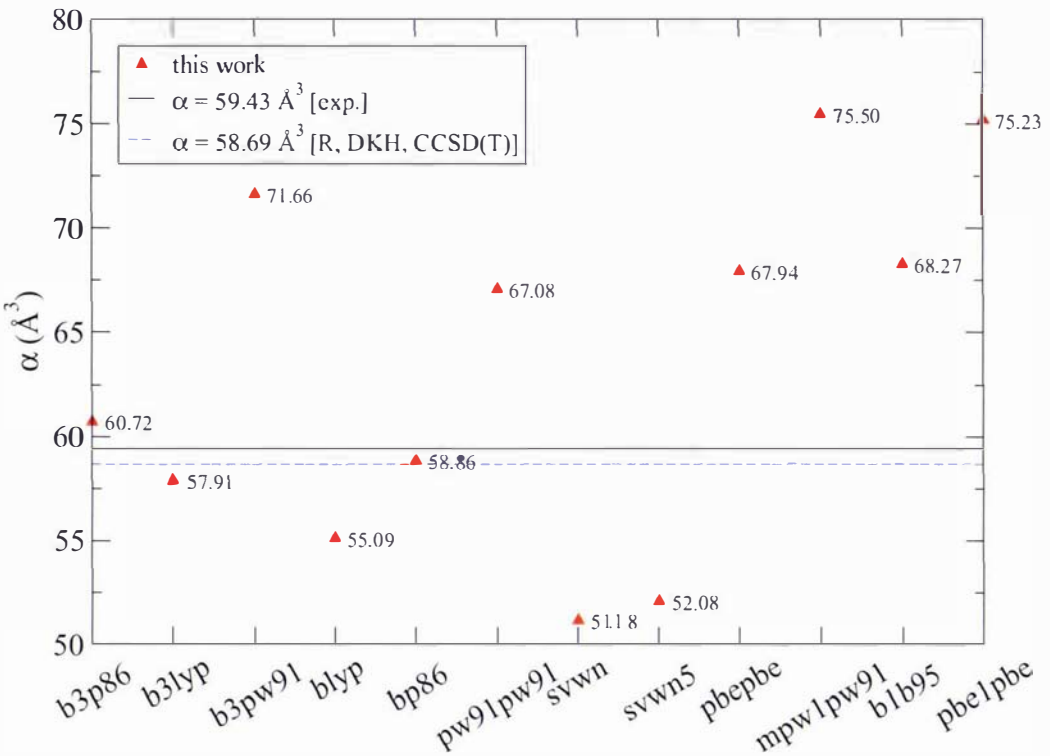

Figure 4.1: Static electric dipole polarizabilities of the cesium atom in Å^3 as a function of different DFT exchange-correlation functionals and compared to experimental [53] and calculated [52] values.

are calculated as the energy difference between the neutral cluster and the cation (anion). The clusters are labelled as n_m, where n indicates the number of atoms and m gives the rank in increasing energy order.

Due to the considerable sampling of trial geometries taken from the literature of sodium clusters [80, 82] together with random structures and most importantly the genetic algorithm approach, as discussed in section (3.1), there is great confidence that the most stable ground state structures have been found[7]. As can be seen from the relative energies (table (4.1)) of the respective isomers, a clear distinction between the global minimum and low-energy isomers cannot always be made. The relative total energy difference between

[7]In saying that, it must however be noted, that it is impossible to search for *all* possible local minima even for these small clusters, as the number of minima increases exponentially with cluster size.

Table 4.1: Average neighbor distances, relative energies, vertical ionization potentials, vertical electron affinities and cohesive energies (not corrected for zero-point vibrational energy) of the lowest-energy Cs_n cluster isomers $2 \leq n \leq 20$. The geometry notation is that of figure (4.2). The notation $/n$ implies the value is given per atom.

Cluster	d (Å)	ΔE (eV)	VIP (eV)	VEA (eV)	E_{Coh} (eV/n)	Cluster	d (Å)	ΔE (eV)	VIP (eV)	VEA (eV)	E_{Coh} (eV/n)
1_0	-	-	4.053	0.576	-	12_3	5.441	0.099	3.057	1.001	0.356
2_0	4.695	-	3.855	0.602	0.198	12_4	5.485	0.142	2.945	1.085	0.352
3_0	4.925	0.000	3.505	0.987	0.192	13_0	5.417	0.000	2.901	1.119	0.367
3_1	4.920	0.006	3.375	0.809	0.190	13_1	5.385	0.024	2.914	1.112	0.365
3_2	4.968	0.006	3.481	0.945	0.190	13_2	5.378	0.058	2.940	1.120	0.362
4_0	5.432	0.000	3.296	0.811	0.234	13_3	5.403	0.061	2.980	1.153	0.362
4_1	4.874	0.050	3.402	1.034	0.221	13_4	5.42	0.122	-	-	0.357
5_0	5.221	0.000	3.264	0.983	0.263	14_0	5.401	0.000	2.985	1.004	0.374
5_1	4.936	0.209	3.251	1.240	0.222	14_1	5.402	0.010	2.947	0.997	0.373
5_2	5.451	0.238	3.252	0.807	0.216	14_2	5.376	0.030	2.954	1.009	0.372
6_0	5.246	0.000	3.383	0.837	0.299	14_3	5.441	0.064	2.919	1.046	0.369
6_1	5.223	0.002	3.347	0.844	0.299	14_4	5.485	0.095	2.935	1.059	0.367
6_2	4.917	0.400	3.182	1.279	0.232	15_0	5.495	0.000	2.929	1.125	0.380
7_0	5.337	0.000	3.236	0.910	0.330	15_1	5.407	0.092	2.900	1.131	0.374
7_1	5.324	0.096	3.209	0.911	0.317	15_2	5.455	0.099	2.922	1.161	0.373
7_2	5.282	0.305	3.077	1.039	0.287	15_3	5.413	0.163	2.954	1.179	0.369
8_0	5.285	0.000	3.281	0.783	0.353	16_0	5.462	0.000	2.941	1.177	0.386
8_1	5.393	0.075	3.196	0.837	0.344	16_1	5.440	0.035	2.906	1.173	0.384
8_2	5.312	0.089	3.291	0.781	0.342	16_2	5.421	0.046	2.956	1.184	0.383
8_3	5.356	0.096	3.211	0.861	0.341	16_3	5.401	0.103	2.962	1.113	0.380
8_4	5.258	0.471	3.047	1.060	0.294	17_0	5.486	0.000	3.064	1.291	0.396
9_0	5.318	0.000	3.077	1.023	0.343	17_1	5.405	0.020	2.953	1.195	0.395
9_1	5.409	0.010	2.908	0.918	0.342	18_0	5.391	0.000	3.003	1.161	0.403
9_2	5.328	0.019	2.913	0.901	0.341	18_1	5.491	0.017	3.004	1.188	0.402
10_0	5.343	0.000	2.995	0.954	0.349	19_0	5.403	0.000	2.935	1.252	0.405
10_1	5.393	0.001	2.979	0.924	0.349	19_1	5.430	0.035	2.834	1.170	0.403
11_0	5.400	0.000	2.993	1.102	0.356	19_2	5.428	0.046	2.970	1.316	0.403
11_1	5.366	0.030	2.967	1.071	0.353	19_3	5.398	0.053	2.920	1.251	0.402
11_2	5.376	0.035	2.976	1.055	0.353	20_0	5.431	0.000	2.801	1.162	0.408
12_0	5.431	0.000	2.995	1.056	0.364	20_1	5.392	0.004	2.962	1.070	0.408
12_1	5.439	0.039	3.032	1.016	0.361	20_2	5.482	0.140	2.893	1.077	0.401
12_2	5.399	0.072	3.022	0.995	0.358	20_3	5.642	0.217	2.871	1.117	0.397
						20_4	5.426	0.275	2.994	1.095	0.394

the cesium hexamer isomers (Cs_{6_0} and Cs_{6_1}), for instance, adds up to only 0.002 eV, which is clearly too small to appoint either of them as the global minimum structure of Cs_6. The relative energy differences of the isomers which are mentioned in the tables are less than 0.5 eV and those of the isomers illustrated in the diagrams less than 0.1 eV. 0.5 eV is considered to represent an error bar for relative energies computed with GGA functionals [113].

Rather than discussing all the cesium clusters structurally in detail and comparing them to clusters of other calculated alkali-metal clusters, only selected structures, with distinct features or abnormalities to other alkali-metal clusters, are discussed here. As aforementioned, the relative energy differences for the isomeric clusters is less or equal to 0.5 eV, thus making it moot to discuss only one isomer.

For the clusters Cs_3 to Cs_6 it is very interesting to note, that linear structures are true local minima for up to six atoms, with alternating bond lengths for the Cs_4, Cs_5 and Cs_6 isomers. While the relative energy difference for the linear tetramer to the parallelogram (C_s) is a marginal 0.05 eV, that of the linear hexamer compared to the trapezoidal structure (D_{3h}) is already 0.4 eV. The transition from planar (2D) to three-dimensional structures (3D) is ambiguous, but most probably occurs at cluster size seven, as the pentagonal bipyramid (Cs_{7_0}, D_{5h}) is energetically more stable than the bicapped planar trapezoidal structure (Cs_{7_2}, C_s) by 0.305 eV. In contrast, for the pentamer the isosceles trapezoid (Cs_{5_0}, C_{2v}) is energetically favored by 0.238 eV over the trigonal bipyramid (Cs_{5_2}, D_{3h}). The relative energy difference between the capped trapezoidal structure (triangle surrounded by three other triangles) (Cs_{6_0}, D_{3h}) and the pentagonal pyramid (Cs_{6_1}, C_{5h}) is extremely small.

Thus, in the light of relative energy differences, cesium pentamers formed in an experiment should be mostly planar, while the heptamers should be mostly three-dimensional. For the hexamer, without consideration of any kinetically driven factors, an almost equal mixture of both planar and 3D structures should be expected. The transitions from 2D to 3D structures for lithium, sodium and potassium clusters are therefore somewhat ambiguous. This is, however, also due to the fact that some publications only mention one isomer per cluster size or have utilized a computational approach that is regarded as inaccurate nowadays.

For comparison, Li_5 is claimed to have a trigonal bipyramidal structure [59,70]. Hutter *et al.* established this structure (3D) to be more stable than the isosceles trapezoid (2D)

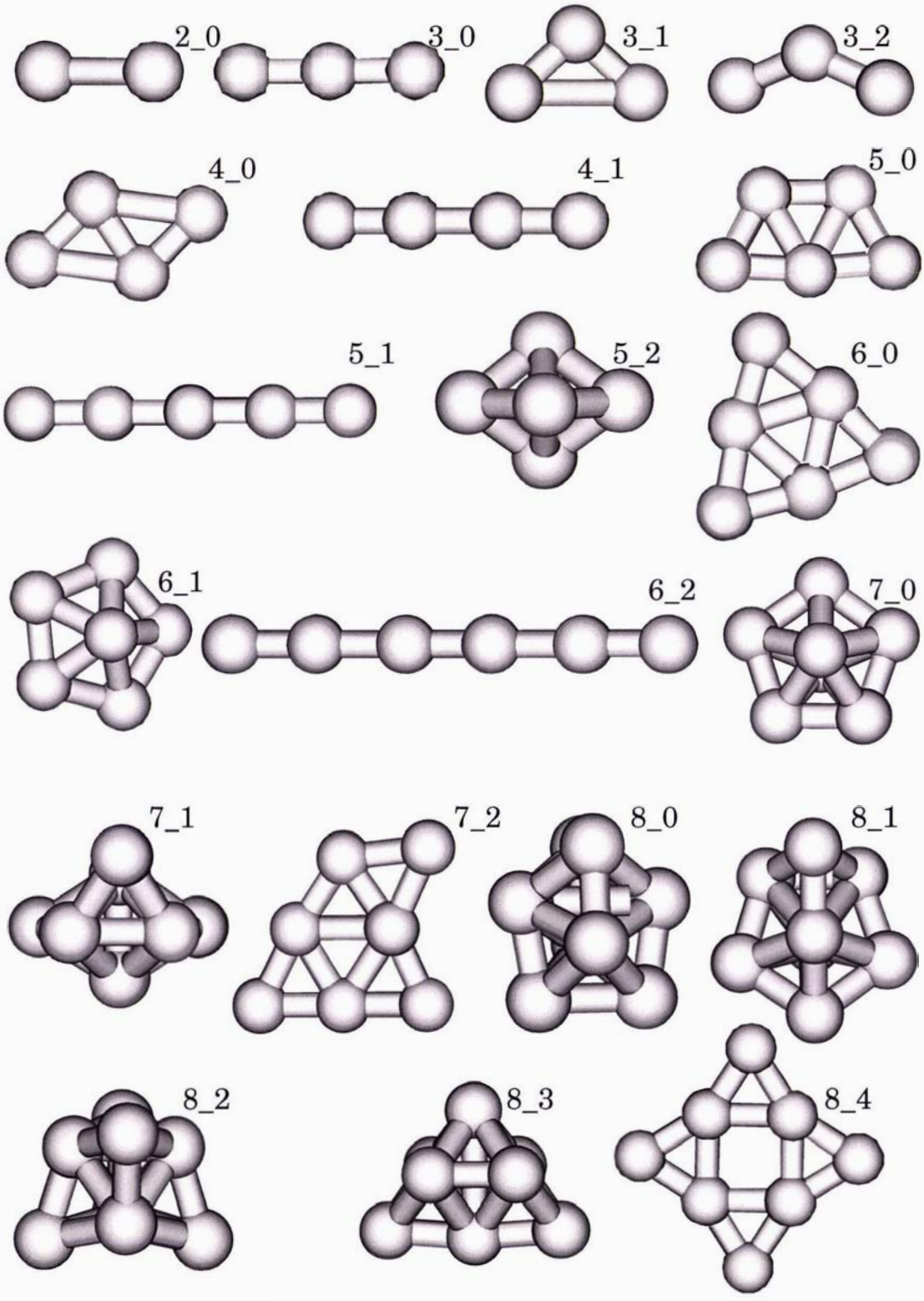

Figure 4.2: Predicted global minima and lowest-energy isomers of Cs_{2-8}, ordered (from left to right and top to bottom) by increased size and energy. The cluster n_m is the mth energetic isomer with n atoms.

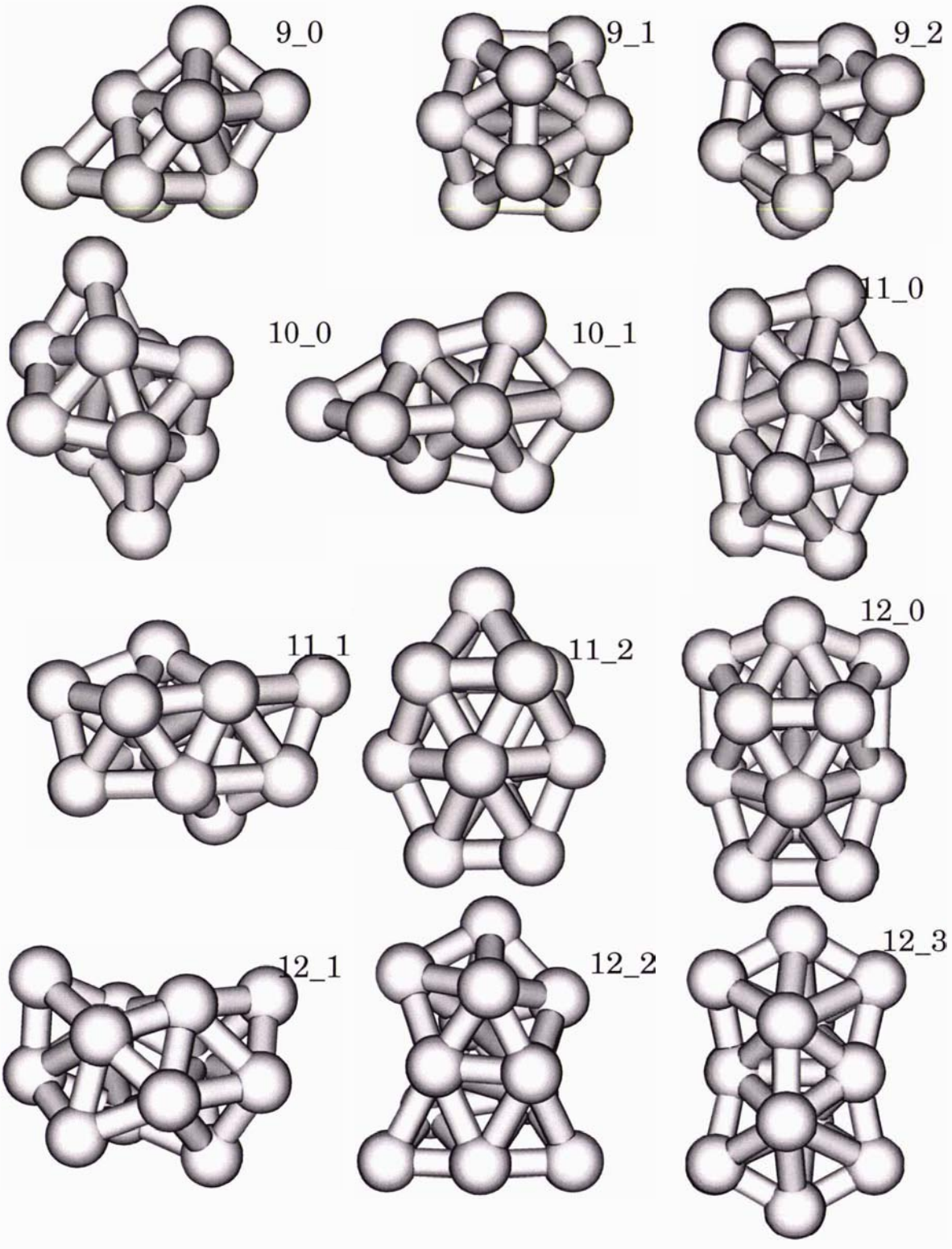

Figure 4.3: Predicted global minima and lowest-energy isomers of Cs_{9-12}, ordered (from left to right and top to bottom) by increased size and energy. The cluster n_m is the mth energetic isomer with n atoms.

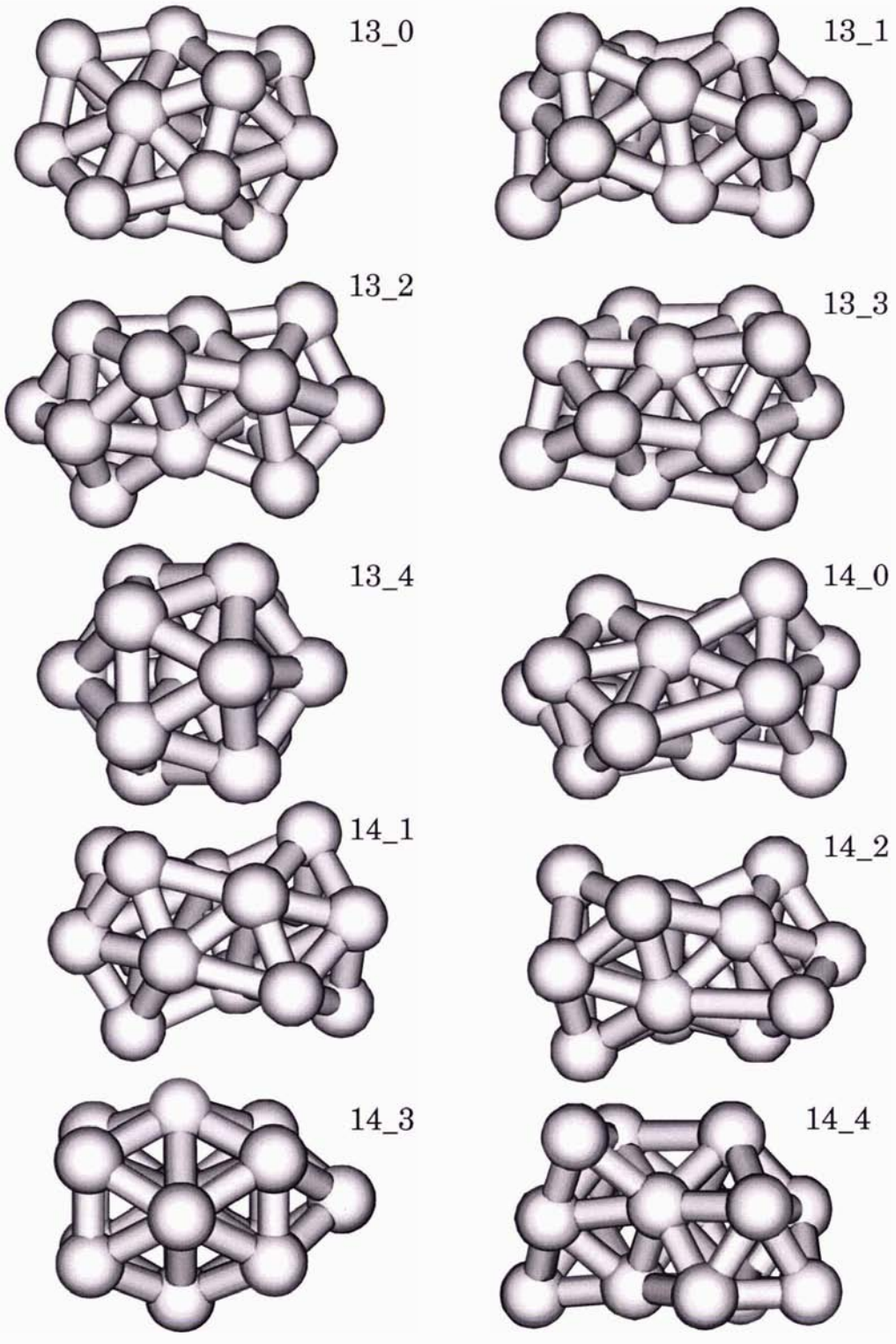

Figure 4.4: Predicted global minima and lowest-energy isomers of Cs_{13-14}, ordered (from left to right and top to bottom) by increased size and energy. The cluster n_m is the mth energetic isomer with n atoms.

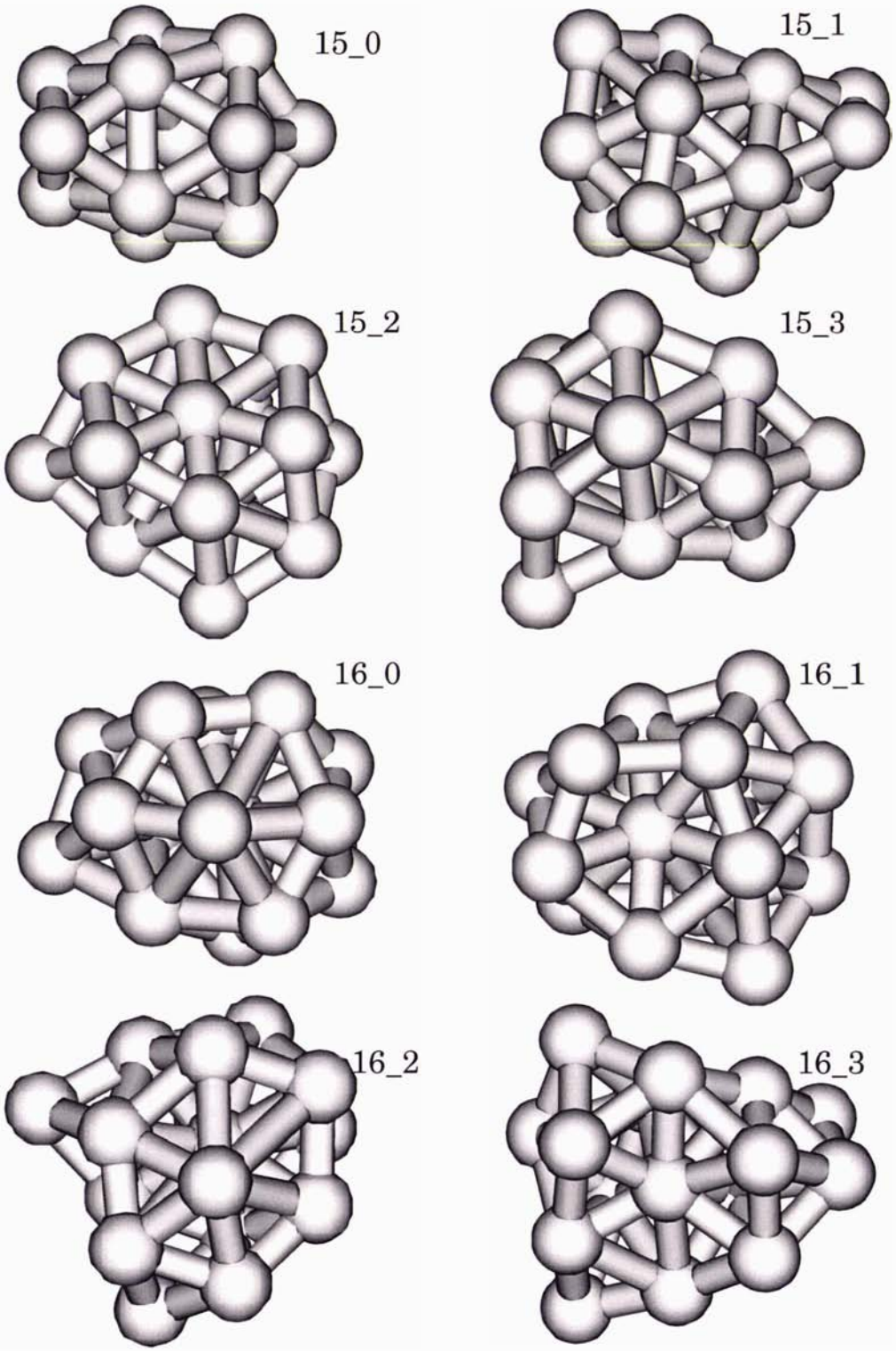

Figure 4.5: Predicted global minima and lowest-energy isomers of Cs_{15-16}, ordered (from left to right and top to bottom) by increased size and energy. The cluster n_m is the mth energetic isomer with n atoms.

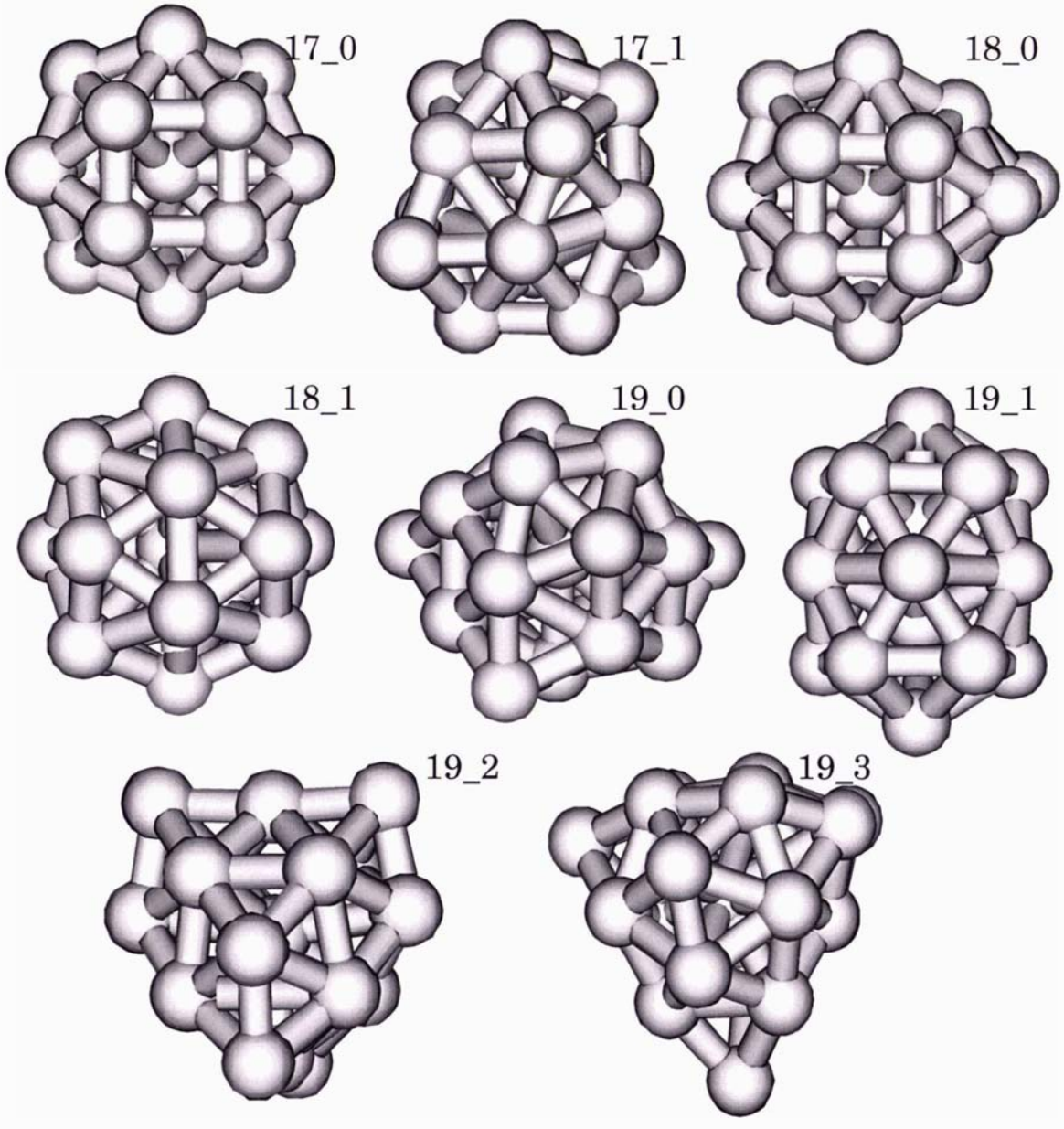

Figure 4.6: Predicted global minima and lowest-energy isomers of Cs_{17-19}, ordered (from left to right and top to bottom) by increased size and energy. The cluster n_m is the mth energetic isomer with n atoms.

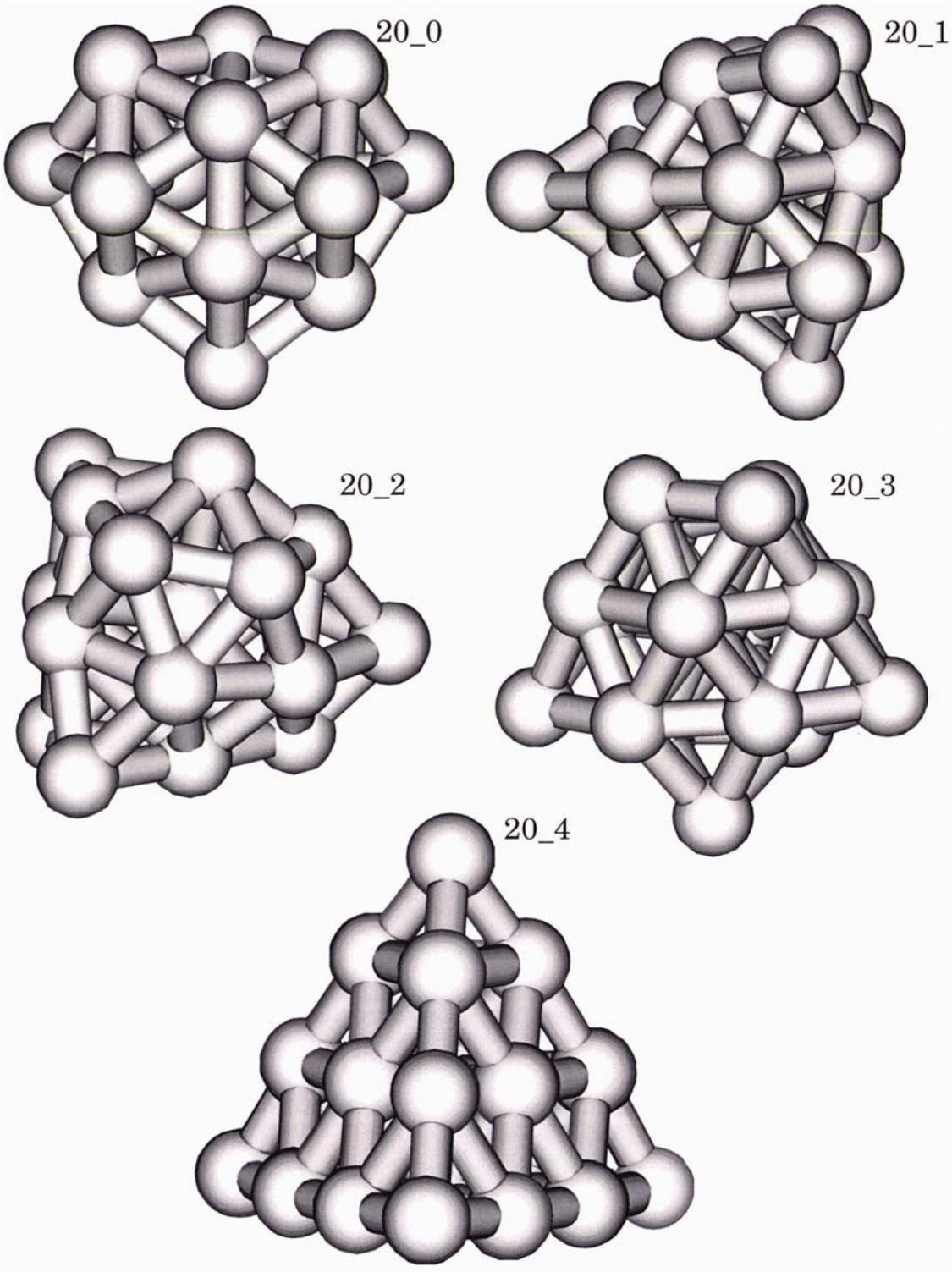

Figure 4.7: Predicted global minimum and lowest-energy isomers of Cs_{20}, ordered (from left to right and top to bottom) by increased size and energy. The cluster n_m is the mth energetic isomer with n atoms.

by 0.22 eV. Greiner *et al.* [80] claim that the pentagonal pyramid of Na_6 is more stable than the triangular Na_6 isomer by 0.22 eV, while Buttet *et al.* calculated an energy difference between these two structures of 0.124 eV. Na_6 is also mentioned to be 3D with a pentagonal pyramidal structure by at least three other publications [59,73,82]. Altekar *et al.* calculated the relative energy difference between the more stable pentagonal pyramid of K_6 and the triangular K_6 isomer to be merely 0.06 eV. All this indicates that there is a shift towards higher nuclearity in the transition from 2D to 3D down the group of the alkali clusters and that the triangular and pentagonal pyramidal hexamers become more and more degenerate in energy going down the group 1 series of elements.

The four 3D isomers of Cs_8 lie within a relative energy difference of less than 0.1 eV, with the Cs_{8_1} isomer assuming a dodecahedral geometry and the Cs_{8_2} structure (a tetrahedron surrounded by four other tetrahedra, T_d) being the most symmetric and also most polarizable isomer. Some of the unusual cluster geometries mentioned in Maity's *et al.* work [90], namely the rectangular tetramer (labelled $Cs_{4\_}a$), the cubic and twisted cubic octamer (labelled Cs_{8_a} and Cs_{8_b}), were optimized according to the author's geometries. The harmonic vibrational analysis of these structures revealed that they are all higher order saddle points. This underlines the absolute necessity of discriminating between true minima and saddle points on the potential energy surface.

It is very interesting to compare the predicted global minima structures from this work to those published by Lai *et al.* [89], who also employed a genetic algorithm approach based on the Gupta potential [114]. Although this potential includes all n-body forces in an effective many-body potential depending only on the pairwise atomic distances r_{ij}, the predicted global minima structures of Lai *et al.* favor compact cluster structures that are similar to those obtained using a two-body potential like the Lennard-Jones potential [115]. This is also reflected by the transition from 2D to 3D structures as early as possible and the icosahedral growth-pattern. Hence, the many-body effects in the Gupta potential are not accurately described. Lai *et al.* predict the global minimum of the tetramers of sodium, potassium, rubidium, cesium and even the tetravalent lead clusters to have a triangular pyramidal[8] structure with at least C_s symmetry.

Geometry optimization for the tetrahedral symmetry of the tetramer results in distortions, due to the first-order Jahn-Teller effect[9], into its geometric analogons with C_{2v}

[8]Unfortunately, the discrimination between the triangular pyramid (C_{3v}) and the tetrahedron (T_d) is not always clear-cut in the publication.

[9]Which is a many-body effect.

and C_s symmetry. The distorted tetraeder with C_s symmetry optimizes for the singlet spin-state into a rhombus, which is a transition state. For the triplet state, it further distorts to a 3D "parallelogram", where two atoms are raised equally from the plane. This structure is less stable than the parallelogram (Cs_{4_0}) by 0.205 eV. The structure remains intact for the quintet state, but is less stable than (Cs_{4_0}) by 0.753 eV.

These results confirm that for the low-spin state of tetrameric cesium the parallelogram (Cs_{4_0}) is clearly more stable than any possible 3D structure. For the pentamer, the flat Cs_{5_0} is more stable than Cs_{5_2} by 0.346 eV. The latter is the predicted global minimum by Lai *et al.*. The predicted global minimum for the hexamer by Lai *et al.* is an octahedron. This geometry is for cesium in the singlet spin-state a saddle point of fourth order, a transition state in the triplet state and a local minimum for the quintet state, which is less stable by about 0.5 eV than the predicted ground-state structures reported in this work.

Their global minima for the heptamer and octamer are the same as those in this work. In Lai's *et al.* work, the structural growth of the sodium, potassium, rubidium and cesium clusters is based on motifs of the tetrahedral pyramid and the pentagonal bipyramid, resulting in an icosahedral-like growth-pattern. It is striking that this growth-pattern, with only a few exceptions, is apparently the same for these four alkali-metal clusters. Although key isomers like the Cs_{13} (icosahedron), Cs_{19} (double icosahedron) and Cs_{20} (capped double icosahedron) are found to be energetically low-lying isomers in this work, there are, however, unsymmetric isomers that have almost the same stability as these highly symmetrical structures. The unsymmetric Cs_{13_0} isomer for instance is 0.112 eV more stable than the icosahedron Cs_{13_4} (I_h). The unsymmetric Cs_{19_0} isomer is only 0.035 eV more stable than the double icosahedron Cs_{19_1}. The relative energy difference between the Cs_{20_0} and the unsymmetric Cs_{20_1} is merely 0.004 eV.

This fact is a clear and strong indication against claiming explicit growth-patterns based on geometric magic numbers and predicted global minima structures obtained via employment of potentials for small-sized alkali-metal clusters or metallic clusters in general. In a recent study by Schwerdtfeger *et al.* it was found that for metallic or covalent interactions in small clusters, empirical potentials such as the Gupta potential fail to describe the cluster's geometry accurately as opposed to *first-principles* wavefunction- and density functional based methods [44]. Since the parameters of the Gupta potential are optimized to reproduce certain bulk material properties, the application of such a

potential to small clusters is doubtful anyway.

4.3.2 Polarizabilities and other Electronic Properties

The main results in this work concerning the static response properties in conjunction with some selected electronic structure properties of small cesium clusters are collected in table (4.2). Structural properties and vertical ionization potentials and vertical detachment energies are displayed in table (4.1).

As illustrated in figure (4.8), the polarizability of cesium clusters per atom as a function of size approaches the bulk limit from above, as is also the case for measured and calculated lithium and sodium polarizabilities. While the deviation from the classical bulk limit (equation (4.1)) for Cs_{20} is about 26 %, that of Li_{20} and Na_{20} are about 42 % and 40 %, respectively. Hence, cesium clusters approach their bulk value of polarizability faster than lithium and sodium clusters. The atomic polarizability and polarizability in general of cesium (58.85 $Å^3$)[10] is far greater than those of lithium (24.4 $Å^3$) [59], sodium (24.12 $Å^3$) [64], potassium (43.51 $Å^3$) [98] and rubidium (47.41 $Å^3$) [98]. This is qualitatively attributed to the stronger screening of the valence s electrons down the group and relativistic effects which are not large enough to change this trend. As in the case of lithium and sodium clusters, there is a marked decrease in polarizability from the cesium atom to its dimer. The two energetically lowest-lying isomers of trimeric cesium (Cs_{3_0} and Cs_{3_1}) show higher polarizabilities than the cesium atom. Cs_{3_2} is more compact than the aforementioned isomers, is less polarizable and hence displays the strong geometrical dependency of the polarizability. The transition from planar to 3D structures in cesium results also in a significant decrease in polarizabilities (compare values for 2D Cs_{6_0} and 3D Cs_{6_1}). This transition is not evident in the measured data for sodium and occurs for lithium at cluster size six. In general, the energetically lowest-lying isomers Cs_{n_0} also exhibit the smallest isotropic polarizabilities per atom with increasing cluster size.

The solid line in figure (4.8) corresponds to the polarizability calculated for a finite metallic sphere according to the jellium model, equation (4.2) fitted to the Cs_{n_0} data, and agrees nicely for the heavier clusters with the calculated values. From this fit, the spill-out of the electrons from the surface of the metallic sphere adds to 0.96 Å and a Wigner-Seitz radius of 3.07 Å is obtained. This agrees very nicely with the Wigner-Seitz

[10] this work

Table 4.2: Calculated static response and electronic structure properties of low-spin DFT-optimized Cs_n clusters. The second difference in cluster energy is denoted by $\Delta_2 E_n$ and $\Delta\epsilon$ stands for the HOMO-LUMO gap. The mean static polarizability per atom α_{iso} and the polarizability anisotropy per atom were calculated analytically. The absolute value of the dipole moment is denoted by μ. The notation $/n$ implies the value is given per atom. The bp86 functional is used throughout.

Cluster	$\Delta_2 E_n$ (eV)	$\Delta\epsilon$ (eV)	α_{iso} (Å$^3/n$)	α_{aniso} (Å$^3/n$)	μ (D)	Cluster	$\Delta_2 E_n$ (eV)	$\Delta\epsilon$ (eV)	α_{iso} (Å$^3/n$)	α_{aniso} (Å$^3/n$)	μ (D)
1_0	-	0.469	58.854	0.0	0.0	12_3	-	0.442	45.006	31.466	0.0
2_0	0.214	0.760	51.003	38.848	0.0	12_4	-	0.210	41.865	15.632	0.507
3_0	-0.178	0.314	65.014	84.725	0.0	13_0	-0.074	0.186	43.414	22.605	0.191
3_1	-	0.337	56.527	46.146	0.120	13_1	-	0.206	44.263	28.901	0.281
3_2	-	0.324	62.654	71.756	0.481	13_2	-	0.214	44.201	28.285	0.544
4_0	-0.022	0.464	55.241	56.944	0.0	13_3	-	0.197	42.349	20.580	0.192
4_1	-	0.442	71.472	114.091	0.0	13_4	-	0.229	38.205	0.204	0.0
5_0	-0.097	0.291	52.991	44.886	0.033	14_0	0.008	0.416	41.957	19.951	0.161
5_1	-	0.494	89.911	170.426	0.0	14_1	-	0.390	41.281	18.780	0.126
5_2	-	0.346	49.088	8.727	0.0	14_2	-	0.383	43.438	22.594	0.887
6_0	-0.042	0.716	52.642	38.599	0.0	14_3	-	0.288	40.663	21.173	0.605
6_1	-	0.585	47.954	29.769	0.056	14_4	-	0.337	43.685	21.657	0.523
6_2	-	0.314	98.244	199.456	0.0	15_0	-0.015	0.206	38.774	11.557	0.312
7_0	0.007	0.340	42.291	14.976	0.0	15_1	-	0.213	42.213	20.157	0.418
7_1	-	0.325	44.838	14.998	0.0	15_2	-	0.207	43.107	20.986	0.259
7_2	-	0.266	57.299	52.923	0.226	15_3	-	0.213	42.877	17.860	0.862
8_0	0.251	0.633	41.827	12.673	0.0	16_0	-0.075	0.195	38.182	11.369	0.423
8_1	-	0.518	42.360	12.759	0.119	16_1	-	0.195	41.409	17.301	0.193
8_2	-	0.713	44.826	0.0	0.119	16_2	-	0.224	40.192	12.568	0.157
8_3	-	0.522	42.919	13.205	0.479	16_3	-	0.224	43.281	18.760	0.638
8_4	-	0.356	57.956	47.703	0.0	17_0	0.025	0.207	36.104	6.727	0.0
9_0	-0.144	0.250	43.938	24.902	0.210	17_1	-	0.207	39.556	13.663	0.281
9_1	-	0.219	42.693	16.106	0.417	18_0	0.089	0.327	37.236	8.271	0.444
9_2	-	0.236	43.069	16.224	0.799	18_1	-	0.296	36.907	5.952	0.250
10_0	-0.013	0.323	46.738	31.567	0.0	19_0	-0.029	0.210	37.905	5.280	0.227
10_1	-	0.347	43.129	24.058	0.235	19_1	-	0.173	41.822	1.342	0.018
11_0	-0.036	0.210	43.514	28.270	0.332	19_2	-	0.164	39.015	5.963	0.0
11_1	-	0.220	44.112	28.440	0.239	19_3	-	0.204	39.170	7.451	0.607
11_2	-	0.225	42.751	25.616	0.849	20_0	-	0.167	37.387	7.194	0.178
12_0	0.059	0.312	43.661	26.745	0.423	20_1	-	0.473	39.731	1.275	0.436
12_1	-	0.423	46.630	29.957	0.031	20_2	-	0.420	42.307	3.637	0.260
12_2	-	0.419	43.496	23.503	0.382	20_3	-	0.473	42.815	5.814	0.949
						20_4	-	0.533	45.042	0.0	0.0

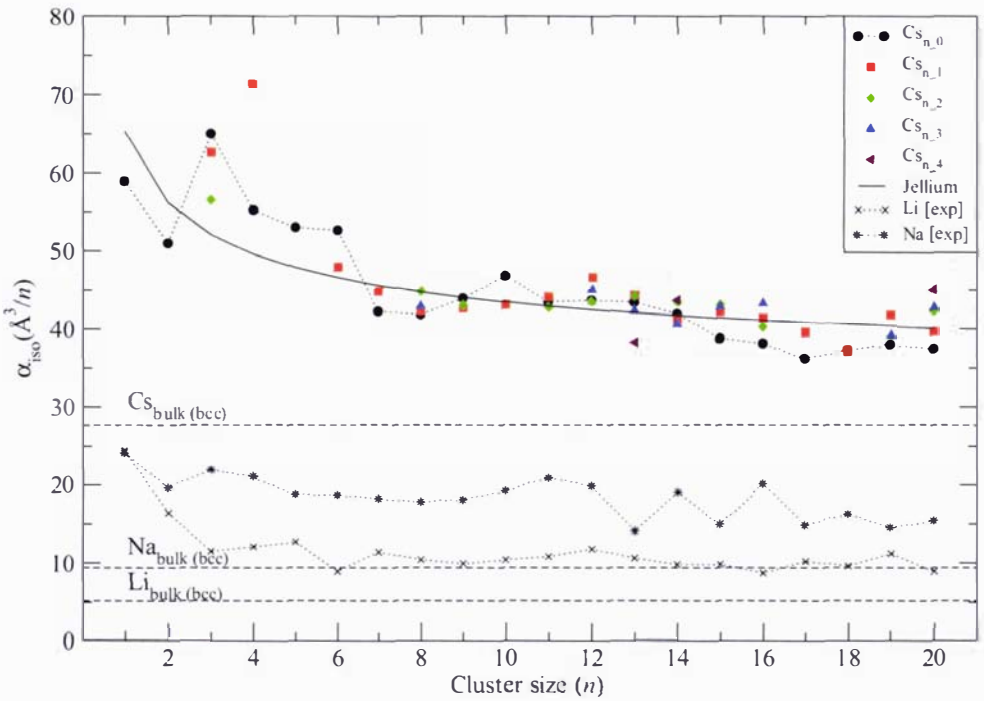

Figure 4.8: Isotropic static electric dipole polarizabilities per atom of Cs_n clusters as a function of cluster size compared to the classical value of bulk *bcc* Cs. The black line represents the prediction from the classical metallic sphere (jellium model, equation (4.2)). The measured polarizabilities of Li_n (extracted from [58,59]) and Na_n (extracted from [58,64]) clusters are also plotted and compared to their classical bulk *bcc* polarizabilities.

radius derived from crystallographic data of *bcc* Cs:

$$r_{WS} = \sqrt[3]{\frac{3}{4\pi}\frac{a^3}{N}} = \sqrt[3]{\frac{3}{4\pi}\frac{6.14^3\text{Å}^3}{2}} = 3.02\ \text{Å} = \sqrt[3]{\alpha_{iso}} \tag{4.3}$$

Here, a and N represent the length and the number of atoms in the cubic unit cell. For lithium and sodium clusters it is also found that the jellium-picture nicely describes the evolution of the polarizability per atom with increasing cluster size [59][11].

Despite the fact that the jellium model in the spill-out approximation predicts on average the trend of the polarizability per atom as a function of the cluster size, it can of course not account for the more interesting quantum mechanical effects. In this respect, deviations of the calculated polarizabilities from the prediction in equation (4.2) can be regarded as 'true' quantum effects. The anisotropy to the polarizability α_{aniso} per atom, according to equation (1.56), is given in table (4.2) and is also plotted in figure (4.9). α_{aniso} increases rapidly from monomeric to trimeric cesium and then decreases towards Cs_8. It is worthy to mention the difference in anisotropies for the Cs_3 isomers, where the linear structure (Cs_{3_0}) shows an anisotropy that is almost twice as large as that of the isosceles triangle (Cs_{3_1}). The transition to 3D structures (Cs_6 - Cs_7) is followed by a significant decrease in α_{aniso}. The anisotropy is per definition strongly dependent on the geometric structures of the respective isomers and approaches zero for spherically shaped isomers. The general decreasing trend for clusters $10 \leq n \leq 20$ underlines the fact that the evolution of cesium clusters tends towards more compact and more spherically shaped clusters towards the solid state.

Figure (4.10) depicts the ionization potentials and electron affinities of the ground state cesium atom as a function of DFT exchange-correlation functionals and shows clearly that DFT can reproduce the experimental values very satisfyingly. The experimental IP of cesium (3.894 eV) [116] is reconfirmed theoretically by Kaldor *et al.* (3.903 eV) using the Dirac-Coulomb-Breit Hamiltonian framework within a Fock-space coupled-cluster approach in a large basis set [93]. The bp86 functional, which is used throughout all cesium calculations in this work, does not perform as well as other functionals for these properties. Indeed, it deviates from the experimental electron affinity by about 18 %. The choice of the bp86 functional is, however, as discussed in section (4.2), not founded on a

[11] Note, that the authors in ref [59] rather 'assumed' values for r_{WS} and δ than to fit their data to $\alpha_{iso} = (r_{WS}N_e^{1/3} + \delta)^3$ properly. (Li: $r_{WS} = 1.75$ Å and $\delta = 0.75$ Å; Na: $r_{WS} = 2.12$ Å and $\delta = 0.69$ Å.)

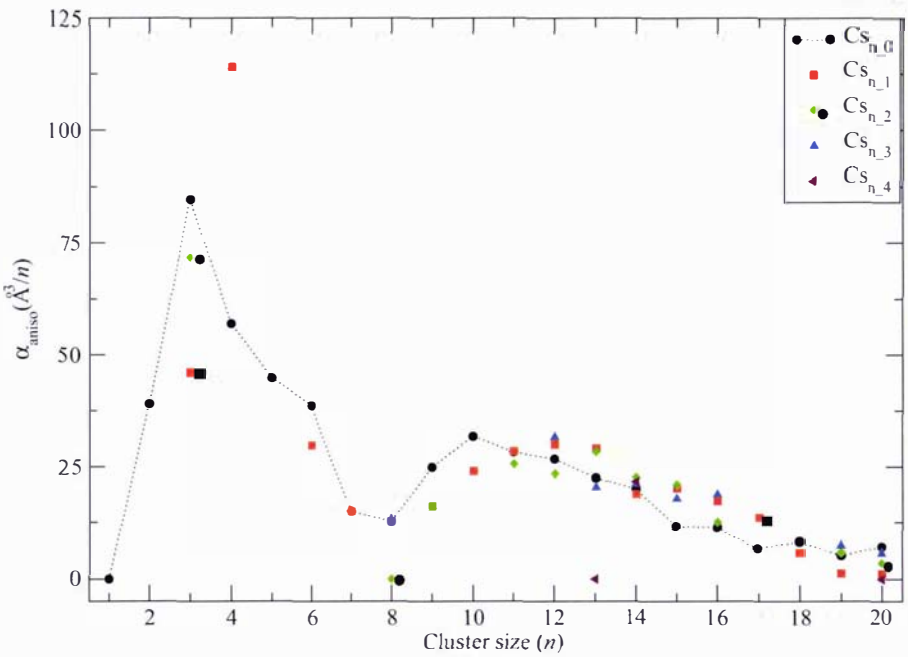

Figure 4.9: Anisotropy to the static electric dipole polarizability per atom, according to equation (1.56), as a function of cluster size for cesium.

the reproduction of the experimental ionization potential and electron affinity, but on the reproduction of the polarizability of the ground state cesium atom. The vertical ionization potentials of the cesium clusters as a function of cluster size together with available experimental data are displayed in figure (4.11). The workfunction (1.93 eV) [119] is, as is often the case for metals, almost half of the experimental atomic VIP (3.894 eV). Even for Cs_{20}, the VIP is about 45 % larger than the bulk limit. The VIP decreases rapidly towards Cs_4 and then follows a smaller decrease up to Cs_{10}. There is no continuous odd-even oscillation with respect to the cluster size for the predicted global minima (Cs_{n_0}) and the VIP shows an approximately constant behavior for the Cs_{10} to Cs_{16} clusters. Its dependency on the isomers of Cs_{10} to Cs_{16} is rather small, but is significant for the clusters Cs_{19}, Cs_{20}, Cs_3 and Cs_9. This underlines that the ionization potential is not a good measure for geometric differences in isomers at all, as is evident from the values for Cs_6 and Cs_{15} for instance. For the former, there is only a marginal change in VIP for the

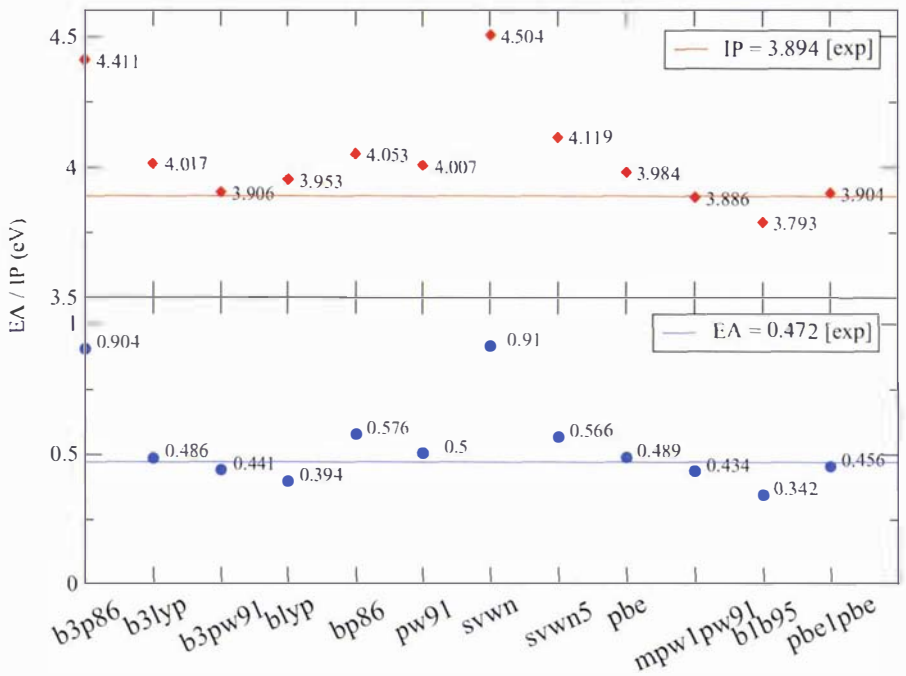

Figure 4.10: Ionization potentials and electron affinities of the ground state cesium atom in eV as a function of DFT exchange-correlation functionals and compared to experimental (IP) [116] (EA) [117, 118] values.

2D and 3D structures, respectively, and the same applies to the latter isomers (Cs_{15_0}, Cs_{15_1}, Cs_{15_2}, Cs_{15_3}), which show distinctively different geometric structures.

The dashed black line in figure (4.11) represents scaled values of the Cs_{n_0} isomers from the atomic calculation of the VIP using the bp86 functional and the pbe1pbe functional, respectively. The calculated VIPs are in good agreement, especially for the scaled case of Cs_{n_0}, with the available experimental data (experimental references for: Cs_1 [116], Cs_2 [96] and Cs_{9-15} [94])[12].

It is worthwhile to note that the interpretation of photoionization spectra as well as photoelectron spectra of clusters is far from straightforward due to uncertainties in the

[12]Maity *et al.* [90] compare their calculated VIPs for Cs_3 to Cs_8 with experimental ionization potentials. They fail, however, to cite the source of the experimentally observed IPs for these clusters and could not respond on enquiry to this issue adequately.

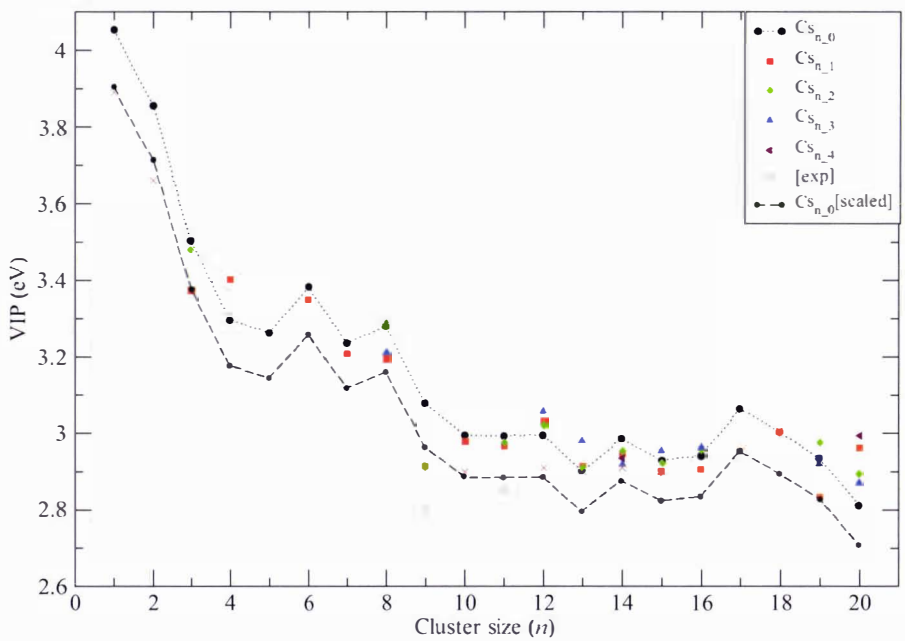

Figure 4.11: Vertical ionization potentials of cesium clusters as a function of cluster size n. The geometry notation is that of figure (4.2). Experimental data for $n = 2$ and $9 \leq n \leq 15$ are extracted from references [96] and [94], respectively.

temperatures of the clusters, Franck-Condon factors, isomerization and fragmentation [95]. A clear odd-even oscillation is observed for the vertical electron affinities, where, as expected, the closed-shell clusters (even n) show smaller electron affinities, due to the electron pairing effect (see figure (4.12)). The calculated VEAs of Cs_2 and Cs_3 are in good agreement with experimental photoabsorption spectra data obtained for Cs_2^- (0.511 eV) and Cs_3^- (0.987 eV) [107]. Experimental photoabsorption spectra for Cs_4 to Cs_9 were measured by Martin *et al.* [108]. However, the emphasis in that work was put on the spectral region 1.3 - 1.7 eV and hence no conclusion can be drawn upon the first electron affinities. It should be noted that a low (high) electron affinity of a cluster is generally identified as a signature of a closed-shell (open-shell) pattern of electronic configuration with large (small) electronic gap.

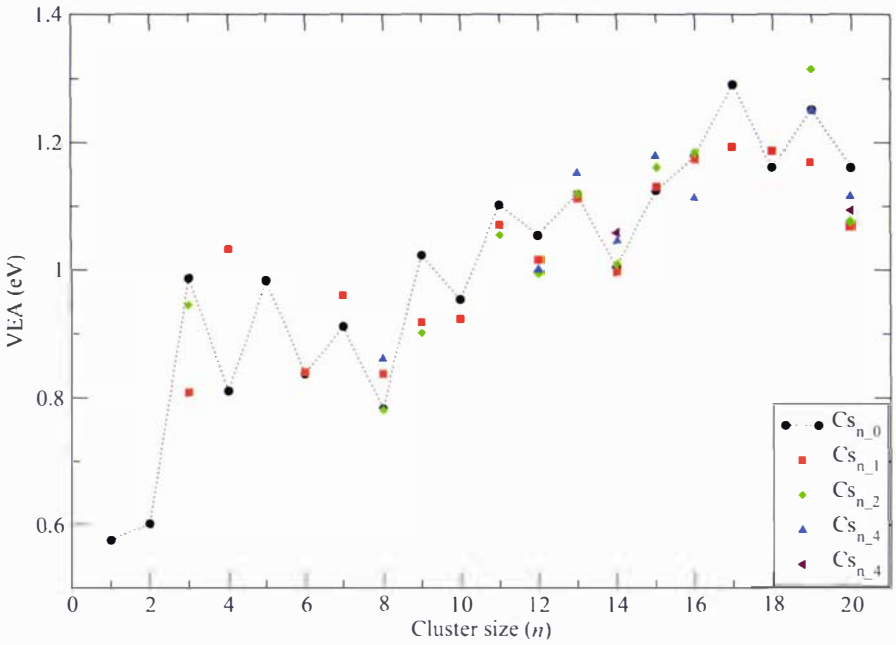

Figure 4.12: Vertical electron affinities of cesium clusters as a function of cluster size n.

According to the scaling laws of cluster properties, the VIP and VEA can be plotted against the cluster size ($n^{-1/3}$) and fitted linearly to $G(n) = g(\infty) + A_0 x$, where $g(\infty)$ denotes here the workfunction of bulk cesium (1.93 eV) [119]. As depicted in figure (4.13), the vertical ionization potentials (vertical electron affinities) decrease (increase) towards the W_f of bulk cesium as expected and the evolution of both properties can be approximated satisfyingly by linear regressions according to $G(n) = 1.93 + A_0 x$. The second difference in cluster energy, which is defined as

$$\Delta_2 E_n(n) = E_{n+1} + E_{n-1} - 2E_n, \tag{4.4}$$

where E_n is the total calculated energy of the cluster with n atoms, is displayed in figure (4.14). $\Delta_2 E_n$ represents the relative stability of a cluster with n atoms in comparison to clusters with $n+1$ and $n-1$ atoms and consequently a peak in $\Delta_2 E_n$ indicates that the cluster with size n is very stable[13]. With the exception of Cs_6 and Cs_{16}, a clear

[13]These clusters are termed magic clusters.

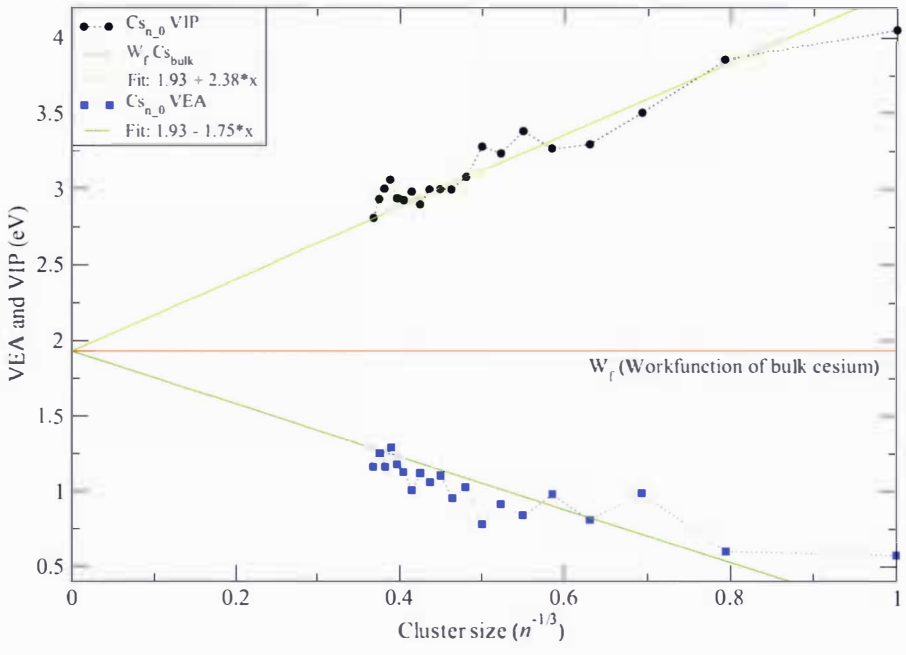

Figure 4.13: Vertical electron affinities and vertical ionization potentials of cesium clusters as a function of cluster size ($n^{-1/3}$). The evolution of both properties is approximated by a linear regression of the type $G(n) = 1.93 + A_0 x$, where 1.93 denotes the workfunction of bulk cesium [119].

odd-even oscillation is present in the $\Delta_2 E_n$, where due to the electron pairing effect, the even sized clusters are more stable than the odd ones. While the deviant behavior of Cs_6 from the odd-even oscillation is due to the transition from 2D to 3D structures, the low stability of Cs_{16} with respect to its neighbors is peculiar. Perhaps there exists a more stable isomer. $\Delta_2 E_n$ shows that clusters with $n = 2, 8, 12$ and 18 have particularly stable configurations. The driving force behind the stability of Cs_2, Cs_8 and Cs_{18} is the electronic shell structure [48]. The relative higher stability is usually, as can be seen from figure (4.8), followed by a decrease in polarizability. The electron pairing effect also explains the oscillatory trend in the HOMO-LUMO gaps ($\Delta\epsilon$) of cesium clusters in figure (4.15). Odd- (even-) sized clusters have an odd (even) total number of s valence electrons and the HOMO is singly (doubly) occupied. The electron in a doubly occupied HOMO feels a

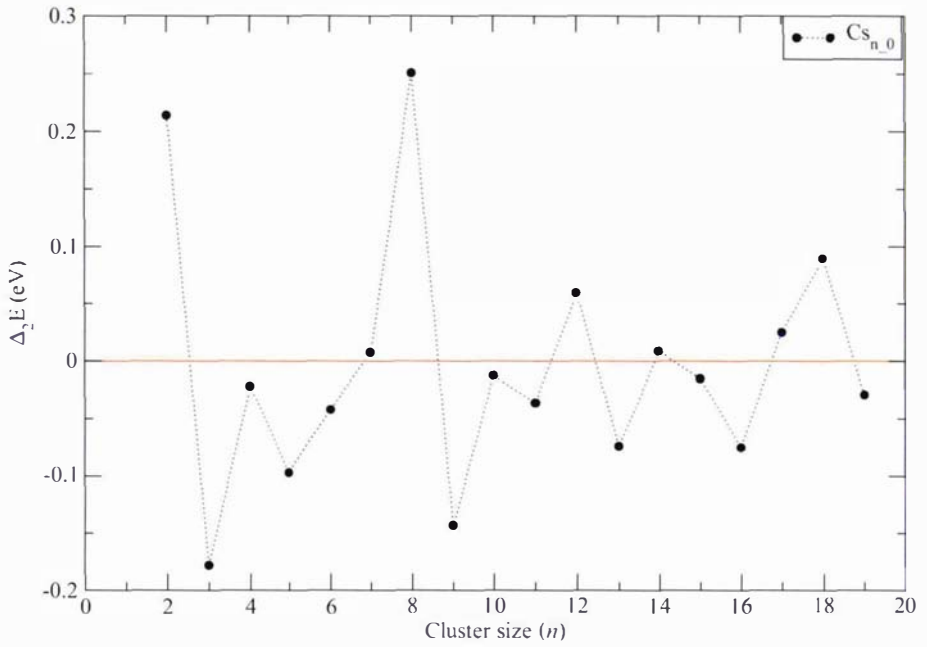

Figure 4.14: Second difference in cluster energy ($\Delta_2 E_n$) as a function of cluster size.

stronger effective core potential since the electron screening is weaker for electrons in the same orbital of a valence electron than for inner-shell electrons. Therefore, the binding energy of a valence electron in a cluster of even size is larger than that of an odd one, thus exhibiting a larger gap.

Comparison between figure (4.15) and figure (4.14) reveals a resemblance between cluster stability and HOMO-LUMO gap. Clusters that show higher stability ($n = 2, 8, 12, 18$) also exhibit large $\Delta\epsilon$ gaps. Cs_6 is an exception to that, exhibiting a large gap, but no peak in the second difference in cluster energy. The missing peak is, however, due to the transition from planar structures to three dimensional structures. The predicted global minima of Cs_5 is definitely planar and that of Cs_7 definitely three dimensional, making the interpretation of $\Delta_2 E$ for Cs_6 ambiguous. As mentioned before, no clear distinction between the energetically lowest-lying planar and three dimensional isomers of Cs_6 can be made, as the energy differences are marginal. The pentagonal pyramid displays, however, a notably smaller $\Delta\epsilon$ than the planar triangle isomer of Cs_6. However, the magnitude

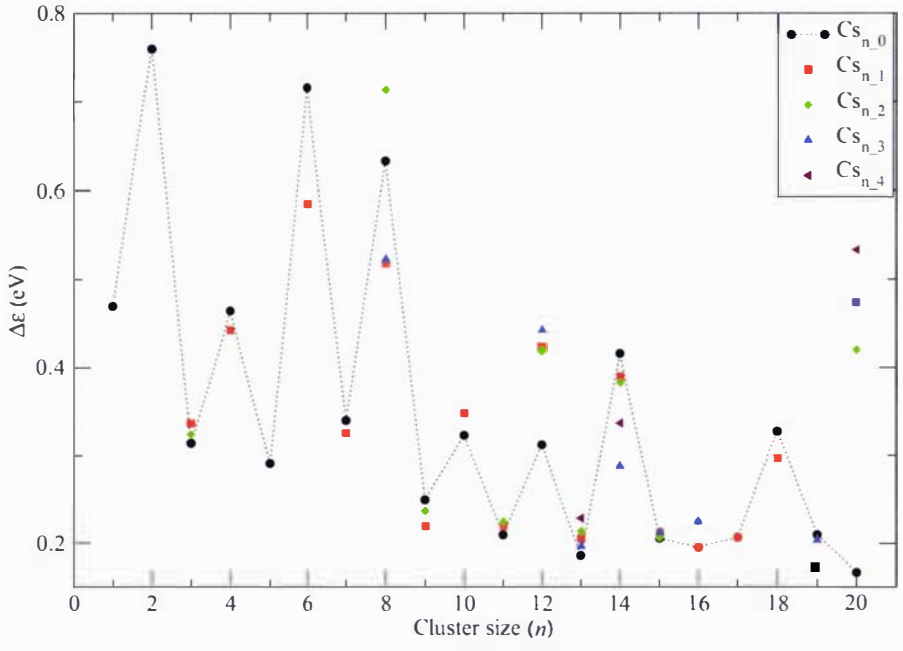

Figure 4.15: The calculated HOMO-LUMO gaps ($\Delta\epsilon$) of cesium clusters versus the cluster size n.

of $\Delta\epsilon$ gives at most a good lead for cluster stabilities and should not be used solely to comment on the stability of a cluster.

No obvious relation between the HOMO-LUMO gap and the dipole moments of the clusters can be found. For most of the germanium clusters ($n = 11 - 25$), a close relation between these two properties was found, where a large HOMO-LUMO gap corresponds to a large dipole moment [120]. The dipole moments are listed in table (4.2). There is also no stringent relationship between dipole moments and the isotropic polarizability or its anisotropy. In general, the clusters with near-spherical structures have lower dipole moments compared with those of prolate structures[14].

In figure (4.16), the nearest-neighbor bond lengths of all presented cesium clusters are plotted against the cluster size. There is an abrupt increase from Cs_2 to Cs_3, from

[14]For reasons of comparison, the dipole moment of water is 1.85 D and that of hydrogen chloride 1.05 D.

Cs_{5_0} to Cs_{6_1} and from Cs_{6_0} to Cs_{7_0}, respectively. The former is a consequence of the structural transition from one dimension 1D to 2D and the latter from 2D to 3D. Moreover, the calculated bond length in the cesium dimer (4.695 Å[3]) agrees nicely with the experimental value (4.65 Å[3]) and in general, the nearest-neighbor bond length approaches to the experimental value of the shortest equilibrium interatomic distance in *bcc* cesium solid (5.32 Å) as the cluster size increases. In contrast to Cs_{20_0} or Cs_{20_1}, Cs_{20_2} and Cs_{20_3} already show shortest bond distances that are larger than that in the cesium solid, see table (4.1). Note that in table (4.1) the average neighbor distances[15] are listed and not the nearest-neighbor distance. The latter excludes surface effects, which play a major role in clusters, as most of the atoms in the clusters investigated in this work belong to the surface, and allows for a comparison with the nearest-neighbor distance in the *bcc* cesium solid.

The cohesive energy[16] (binding energy per atom) of the cesium clusters, defined as,

$$E_{coh} = \frac{n \cdot E(Cs_1) - E(Cs_n)}{n}, \tag{4.5}$$

where $E(Cs_1)$ denotes the calculated total electronic energy of the cesium atom, is reported in figure (4.17). Due to the small energy difference between the respective cesium cluster isomers, of course the cohesive energy is also relatively independent of the cesium cluster isomers. With the exception of the linear isomers of Cs_4 and Cs_5, the E_{coh} increases approximately linearly from Cs_3 to Cs_8. It then decreases to Cs_9 and then increases again almost linearly, with a considerably smaller slope than before, towards Cs_{20}. The onset of this change is drastic and correlates strongly with the HOMO-LUMO gaps of the respective clusters. In general, clusters with nine to twenty atoms exhibit smaller gaps than those with three to eight atoms and this is reflected by the cohesive energies. The cohesive energy up to Cs_{20} is 0.408 eV, which is about 50 % of the experimental bulk cohesive energy (0.83 eV) [123]. Averill [124] calculated the cohesive energy of bulk cesium (0.8299 eV) and confirmed the experimental value. The calculated cohesive energies in this work are by about 30 % larger than those published by Maity *et al.* [90][17], but the trend is analogous. Plotting the cohesive energy as a function of cluster size to the power of $(n^{-1/3})$ yields a slightly different picture and allows for fitting of the data towards bulk cesium

[15]Calculated as the arithmetic mean of all distances (d $\leq$ 6 Å).

[16]The cohesive energy is defined as the energy required to separate the most stable form of a cluster into its constituent atoms, and is usually expressed as an energy per atom.

[17]Reported cohesive energies of Cs_2 to Cs_{10} lie within 0.16 eV and 0.25 eV

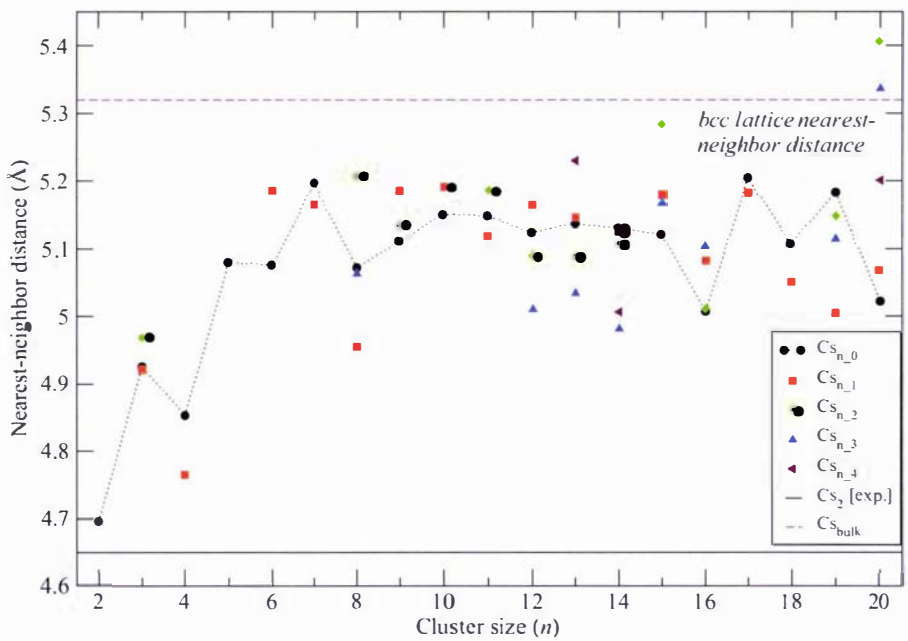

Figure 4.16: Nearest-neighbor distances plotted against the cluster size. The solid line represents the experimental cesium dimer bond length (4.65 Å [92, 121]) and the dashed line symbolizes the experimental value of the shortest equilibrium interatomic distance in bulk *bcc* cesium (5.32 Å [122]).

(see figure (4.18)). The dashed lines represent linear regressions towards the bulk limit for the cohesive energies for clusters Cs_3 to Cs_{20} and clusters Cs_9 to Cs_{20}. Considering the fact that there is still a very long way from Cs_{20} to bulk cesium, the linear approximation yields a satisfying result. It should be noted, however, that different DFT functionals will characterize the binding situations differently and hence result in quite different cohesive energies.

For Li_{10}[18], for instance, the vwn [125] approach yields a cohesive energy of 1.38 eV and the bp86 approach a value of 1.18 eV [71]. Chermette *et al.*, also utilizing the bp86 functional, report the cohesive energy of Li_{10} to be 0.84 eV and that of the biggest cluster they investigated, Li_{13}, to be 0.88 eV [70]. They also report cohesive energies for various

[18]The biggest cluster studied in that reference.

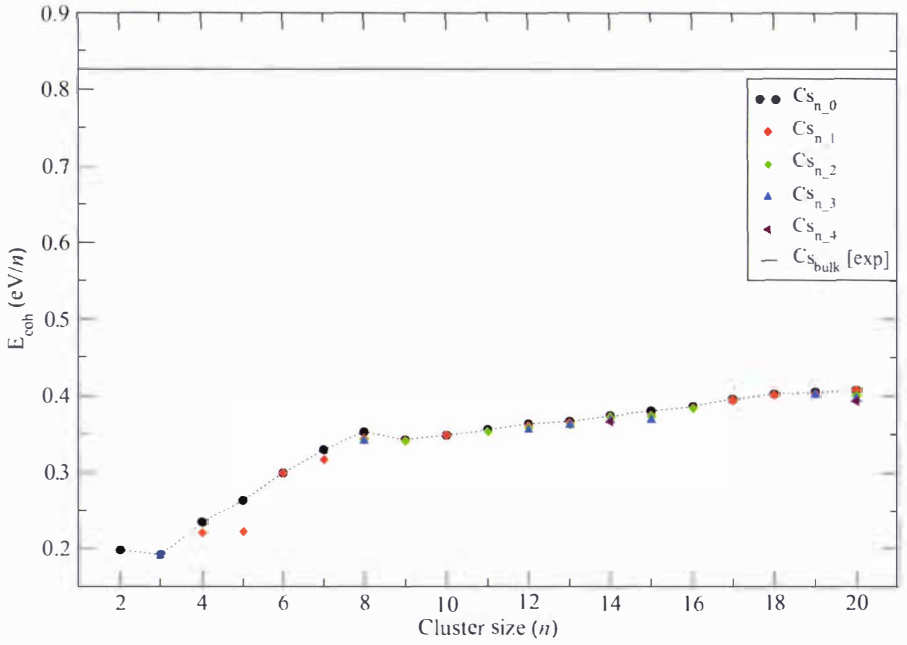

Figure 4.17: The calculated cohesive energies of cesium clusters as a function of size and in comparison to the experimentally obtained cohesive energy of the cesium bulk.

DFT functionals. The experimental cohesive energy of bulk lithium is reported to be 1.65 eV [123].

Calculated DFT, b3lyp cohesive energies of neutral sodium clusters up to 20 atoms show also a very shallow convergence towards the bulk value [80]. The cohesive energy of Na_{20} is about 55 % of the experimental bulk cohesive energy of sodium (1.13 eV) [124]. In the case of potassium clusters, the cohesive energy reported for the largest potassium cluster is 0.33 eV for K_7, which is about 35 % of the bulk cohesive energy of potassium (0.94 eV) [124]. In figure (4.19), the calculated zero-point vibrational energies (ZPVE) per atom are plotted against the cluster size to the power of $(n^{-1/3})$ and fitted linearly. This approach estimates the ZPVE per atom of bulk cesium to be 0.006 eV/n, which is unknown experimentally.

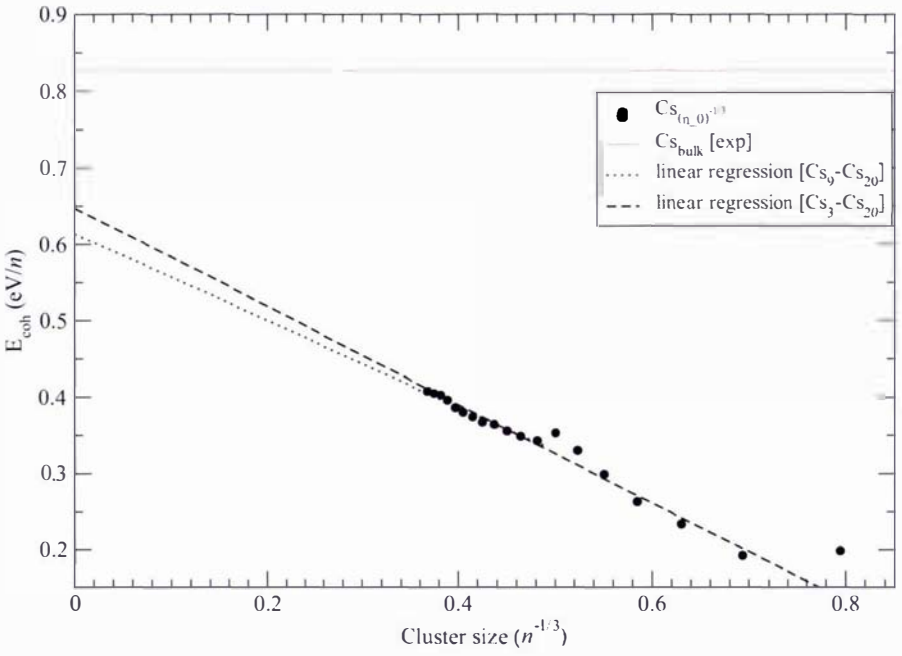

Figure 4.18: Calculated cohesive energies of cesium clusters as a function of cluster size to the power of ($n^{-1/3}$). The dashed lines represent linear regressions towards the bulk limit for Cs_3 to Cs_{20} and Cs_9 to Cs_{20}.

4.4 Conclusions

For the first time, the lowest order static response of small cesium clusters up to 20 atoms to a static electric field is calculated. The predicted low-spin geometric structures are believed to be the energetically lowest-lying structures reported so far. This conclusion is based on the considerable sampling rate of initial geometric structures combined with a genetic algorithm approach, which is based on density functional methods rather than using empirical n-body potentials. A comparison with previously undertaken genetic algorithm and basin hopping studies based on the Gupta potential shows clearly, that this approach is superior and necessary, hence underlining its originality. The energetic separation of isomers is in most cases marginal, resulting often in totally unsymmetric isomers to be more stable or as stable as highly symmetric structures. Therefore, no obvious growth-pattern can be predicted. However, the relative energy differences, the

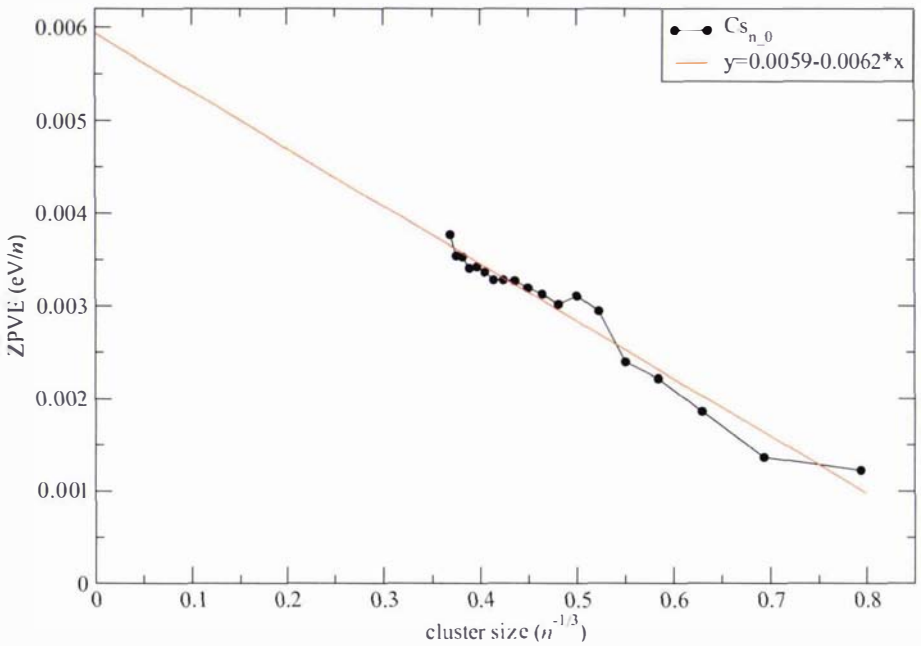

Figure 4.19: Calculated zero-point vibrational energies (ZPVE) per atom of cesium clusters as a function of cluster size to the power of $(n^{-1/3})$. The dashed line represents a linear regression towards the bulk limit.

isotropic- and anisotropic polarizabilities indicate that the clusters' geometric growth tends towards more compact and spherically shaped structures with increasing size. The onset of the transition from planar to three dimensional structures is ambiguous, with the pentamer preferring a planar structure, the heptamer a three dimensional structure and the hexamer showing the same energetic preference for the planar triangular shape and the three dimensional pentagonal pyramid.

The isotropic polarizability per atom of cesium clusters approaches the bulk value from above, which is also the case for lithium and sodium clusters. However, this trend occurs faster for cesium than for lithium and sodium clusters, with the Cs_{20} cluster exhibiting a deviation from the bulk of about 26 %. The jellium model in the electron spill-out approximation can be applied very satisfyingly to the isotropic polarizability. Moreover, the energetically most stable isomers (Cs_{n_0}) exhibit the smallest isotropic polarizabilities

per atom with increasing cluster size, indicating that cluster growth tends towards more compact and spherically shaped structures.

The vertical ionization potentials agree well with the available experimental data and show no continuous even-odd oscillations. The vertical electron affinities show clear even-odd oscillations with the odd-numbered clusters exhibiting higher affinities. Both these properties approach the workfunction of the bulk cesium slowly and approximately linearly. Dominant peaks in the second difference in cluster energy as a function of cluster size are obtained for Cs_2, Cs_8 and Cs_{18}, and are due to electron shell- illing e fect.

A band gap closure to the metallic state ($\Delta\epsilon < kT$) is not observed yet. The cohesive energy per atom increases very slowly towards the bulk value and shows linear dependency for Cs_3 to Cs_8 and Cs_9 to Cs_{20}. The latter interval displays a much smaller slope and correlates strongly with the HOMO-LUMO gaps. These oscillate and show larger gaps for even-sized clusters than for odd-sized clusters and, more importantly, display a clear overall decrease in the HOMO-LUMO gaps for the cluster size interval Cs_9 to Cs_{20}. By means of linear regression, the bulk zero point vibrational energy per atom of bulk cesium is estimated to be about 0.006 eV/n.

4.5 Further Work

In further work, a genetic algorithm approach for high-spin states, with special attention to the triplet states of even-sized cesium clusters, should be undertaken to study the band gap in more detail. Furthermore, it would be very interesting to investigate the magnetic moments of the clusters as a function of size. Bulk cesium is paramagnetic, displaying a molar magnetic susceptibility of ($\chi_m = +29 \cdot 10^{-6}$ cm^3 mol^{-1}) [116]. Recently "unexpected" magnetism has been found in small clusters of the otherwise diamagnetic bulk silver ($\chi_m = -19.5 \cdot 10^{-6}$ cm^3 mol^{-1}) [126].

Chapter 5

Tin Clusters

5.1 Motivation

The physical and chemical properties of isolated, small clusters of the semiconducting group 14 elements (Si_n, Ge_n, Sn_n) have been the subject of intense research due to the fundamental interest and the possibility of diverse applications in nano-technologies [127]. The electric dipole moment and dipole polarizability are especially interesting properties to probe, because they provide both a characterization of the geometrical and the electronic structure of these small nano-sized particles. Particularly tin clusters have become the center of focus due to their occurrence in both covalent and metallic bulk phases [128] and their abnormal higher melting temperatures as compared to the bulk value [129, 130]. The higher ratio of surface to bulk atoms was believed to always cause size-dependent melting temperature depression of nanoclusters [131–133][1]. However, Sn_{10} was the first reported example of a nano-particle melting at a higher temperature than its bulk phase and contradicted the above mentioned standard paradigm based on thermodynamic arguments. Melting properties measured by nanocalorimetry and ion mobility measurements and calculated by density functional methods and molecular dynamics simulations are reported in [129, 130, 134–138].

In conclusion, significantly higher melting temperatures than that of bulk tin (505 K) were found for most of the tin clusters and were attributed to the covalent nature of bonding and to geometrical factors[2].

[1] For instance, Au clusters with a radius of 3 nm (around 700 atoms) melt at about 800 K, compared to a bulk melting point of 1337 K [132].

[2] The reported melting temperature of Sn_{10}, for instance, is around 2000 K [136].

The normal allotrope of tin under ambient conditions (β-Sn, white tin) is a metal with a body-centered tetragonal lattice, as opposed to its lighter congeners, Si and Ge which are already semiconductors at room temperature. Below 286 K, there is a stable semiconducting phase (α-Sn, grey tin) with a small band gap of 0.1 eV and a cubic, diamond structure similar to Si and Ge.

Due to the high relevance of silicon clusters in the nano-electronic industry, a vast range of theoretical investigations into the geometric stable structures of neutral and charged, small and mid-sized silicon clusters have been published [139–153]. Jackson *et al.* [154] and Maroulis *et al.* [155] calculated their response to an external static electric field. The former group found the per atom polarizability of Si_{20-28} for compact structures to decrease towards the bulk limit, whereas prolate structures become increasingly polarizable. Since jellium-based models for the polarizability captured this trend nicely, the response to the applied field is claimed to be metallic. The latter group focused on cluster sizes three to seven and found that, for the differential mean polarizability per atom[3], *ab initio* and density functional theory based calculations yield distinctively different pictures. Earlier, Schäfer *et al.* measured the polarizabilities of Si_n clusters by a laser vaporation beam deflection method at a nozzle temperature of 300 K ($9 \leq n \leq 120$) and found a very strong variation of the polarizabilities per atom around the bulk value of 3.71 A^3 [156,200]. These variations about the bulk value were not found by Jackson *et al.* [154] and have not been reported by theoretical methods so far. A very revealing study is the spectroscopic evidence for the tricapped trigonal prism structure (TTP), which is a dominating structural motif in small, neutral Si, Ge and Sn clusters, for anionic silicon clusters [157].

Germanium clusters have attracted similar theoretical and experimental interest compared to silicon in the past two decades. They belong to the most important microelectronics materials and understanding their growth-habit and various electronic properties is of fundamental and substantial practical relevance. A vast range of theoretical studies on the structures of neutral and charged germanium clusters up to 40 atoms have been reported [140, 158–164]. In general, the claimed ground-state structures were obtained using a genetic algorithm combined with tight-binding methods or a basin-hopping algorithm coupled with plane-wave pseudopotential density functional calculations.

Polarizabilities were calculated by Zhao *et al.* [120] and Chelikowsky *et al.* [165]. The

[3] $\alpha_{diff,iso}/n = \alpha_{iso}(Si_n)/n - \alpha_{iso}(Si)$

former group calculated the polarizabilities of Ge_n ($n = 2 - 25$) from B3LYP Los-Alamos pseudopotential calculations using a valence double-zeta basis set (LANL2DZ) and concluded that in general, the polarizabilities per atom *increase* with increasing cluster size, but show various fluctuations around 5.4 $Å^3/n$ for the cluster sizes 5 to 25. These fluctuations are claimed to correspond to clusters with large HOMO-LUMO gaps, resulting in smaller polarizabilities. These findings are, however, in contradiction[4] with those of the latter group. Chelikowsky *et al.* [165] investigated the polarizabilities of silicon, germanium and germanium-arsenide clusters up to ten atoms and find these to *decrease* with increasing size towards the bulk limit. They find identical geometrical structures for Si_{2-10} and Ge_{2-10}, where the germanium clusters show an average increase of interatomic distances by about 4 %, and exhibit about 10 % higher polarizabilities per atom than Si clusters. Ion mobility measurements of germanium cluster ions revealed that clusters with about 10 to 40 atoms follow a one-dimensional growth-pattern to give prolate geometries, those with 40 to 70 atoms retain roughly the same aspect ratio and at about 70 atoms, the clusters reconstruct to a more spherical geometry [166][5].

Early studies on tin clusters date back to 1953. Honig identified ionic clusters of up to five tin atoms upon vaporization of tin [167]. The atomization energies of tin cluster with up to seven atoms and the evaluation of their stability under equilibrium conditions were investigated by Gingerich *et al.* [168]. Anderson calculated the binding energies of tin clusters with different geometric structures and compared them to the aforementioned study [169]. The energetic separation and geometries of a variety of different neutral and positively charged tin clusters[6] (Sn_2, Sn_3, Sn_4, Sn_4^+, Sn_5, Sn_5^+) were reported by Balasubramanian *et al.* [170–175].

The ground state vibrational frequency and equilibrium molecular constants of Sn_2 were measured by Miller *et al.* [176]. Measured photoionization and -emission spectra are reported in [177–179]. No regions of unusual high stability were observed in the mass spectra of cationic silicon[7], germanium and tin clusters by Schaber *et al.* [180]. Studies on the reaction of tin cluster anions with oxygen revealed that no oxide products were observed for clusters larger than Sn_5 [181]. Calculated dissociation energies, bond lengths

[4] Although otherwise stated by Zhao *et al.*, who unfortunately do not compare their results with the bulk limit polarizability.

[5] An indication for metallic clusters.

[6] In most cases respective germanium and lead clusters are also reported.

[7] The produced silicon clusters contained a significant amount of hydrogen.

and harmonic frequencies of silicon, germanium and tin dimers are compared with experimental results in ref. [182]. Jarrold *et al.* characterized the structures of tin cluster cations up to $n = 68$ by ion mobility measurements and summarized that up to $n \approx 35$, tin cluster cations show a prolate growth-pattern [183]. They also probed structures of lead cluster cations up to $n = 32$ by the same means and concluded that these clusters adopt near-spherical geometries, indicating the expected growth-pattern for metallic clusters [184]. According to these findings, the transition to "normal" metal cluster growth in the group-14 of singly positively charged clusters occurs between tin and lead. Lee *et al.* calculated the ionization potentials and binding energies of small germanium and tin clusters with up to 13 atoms using a semi-empirical tight binding method and found reasonable agreement with experimental results [185]. Much better agreement with experimental results for these properties were found by Majumder *et al.*, who calculated the ground state geometries and energetics of neutral and singly positively charged tin clusters up to 20 atoms using the ultrasoft pseudopotential plane-wave method with generalized gradient approximations [186]. With respect to collision induced fragmentation processes of small tin cluster cations (Sn_{4-20}) in the energy range of 0-300 eV, Tai *et al.* concluded that smaller clusters ($n \leq 11$) fragmented by the atom loss process and the larger ones decayed by fission. Furthermore, they found that these favored fragmentation paths resembled those for respective Si and Ge cluster ions, hence, confirming the structural similarities. They also backed their experimental results by theoretical calculations utilizing various DFT methods [187, 188].

By starting with high-symmetry structures and distorting them according to their unstable modes, Pushpa *et al.* calculated low-energy structures of M_n (M = Sn, Al, As; $n = 4, 6, 13$) using DFT methods [189]. Although this is a conceptionally simple way to search for low-energy structures, and it also mimics the way in which the Jahn-Teller effect leads to particularly low-symmetry structures, it does not provide a proper route to search for global minima. Majumder *et al.* investigated the structures, energetics and fragmentation behavior of tin clusters up to 20 atoms by means of DFT methods and reported a different growth behavior to that of germanium and silicon clusters for tin clusters with more than 7 atoms [190]. A comparative theoretical study with different exchange-correlation functionals of geometric structures and some electronic properties of tin clusters up to 20 atoms was published by Majumder *et al.* in 2005 [191]. A stable closed-shell icosahedral (I_h) Sn_{12}^{2-} cluster, synthesized in the form of KSn_{12}^{-}, was found by

photoelectron spectroscopy recently [192].

Considering the vast amount of theoretical and experimental studies undertaken on small tin clusters, it becomes evident that neither calculated, nor experimentally evaluated static electric dipole polarizabilities have been published. Furthermore, all reported theoretical work on geometric structures was undertaken by using low-lying isomer structures of silicon and germanium clusters as an initial structure and then relaxing them into their local minima, rather than undertaking an unbiased search. Moreover, the theoretical approaches mentioned here, investigated only the lowest spin state of tin clusters. These three arguments are the main motivation for the present work.

5.2 Methods

The predicted singlet and triplet global minima (GM) structures of tin clusters ranging from seven up to twenty atoms were obtained utilizing the genetic algorithm code BELPHEGOR as described in detail in section (3.1). The initial populations[8] consisted of randomly generated structures, predicted Lennard-Jones global minima and predicted low-lying minima structures from tin [190] and silicon clusters [147, 193] from the literature. The minimum energy difference $\delta_i V$ was set to 0.01 eV, d_{min} and d_{max} parameters were fixed between 2.2 Å and 3.8 Å, respectively. The termination criteria was 150 mating and local minimization steps for clusters up to 12 atoms and 100 steps for the remainder. The mutation probability was varied between 10 % and and 20 %.

In contrast to cesium and gold clusters, the quest for the GM was performed in combination with the ultrasoft pseudopotential plane-wave method, leaving $5s^2 5p^2$ valence electrons, within the local spin-density approximation (LDA) as implemented in the VASP program package [194][9]. The cut-off energy for the plane-wave expansion was chosen to be 6 Ry. The clusters were placed in a cubic cell of side 16 Å with periodic boundary conditions. During the global optimization the cell was dynamically adapted, ensuring a distance of greater than 8 Å between the clusters.

Typically, eight to ten of the thus obtained energetically lowest-lying isomers were then further relaxed from LANL2DZ basis set and pseudopotential calculations to their local minima as implemented in the GAUSSIAN03 program package [331]. Depending on the

[8] Typically ranging from 10 to 15 different structures.

[9] VASP makes a better compromise between a realistic treatment of the electronic structure and the computational cost than GAUSSIAN03 for these systems.

energy distribution, two to four of the energetically lowest-lying true minima structures obtained by these means were then further optimized using the extensive STUTTGART valence basis set together with the energy-consistent relativistic pseudopotential for tin [195]. Finally, harmonic vibrational frequencies were computed to ensure that the relaxed geometries are true minima on the potential energy surface. For the exchange-correlation potential, the hybrid functional b3p86, according to the parameterization suggested by Becke [196] and Perdew [112], was applied in a self-consistent fashion as implemented in the GAUSSIAN03 program package. No symmetry constraints were applied during the optimization procedure.

The same approach was adopted to find the best DFT functional reproducing the mean static dipole polarizability as mentioned in the cases of gold and cesium clusters. At first, the polarizability of the ground state ($^3P_0$) tin atom was calculated in the framework of CCSD(T) from the uncontracted and extensive STUTTGART valence basis set (labelled Basis A [195]) with a respective energy-consistent relativistic pseudopotential. Then, this basis set was contracted and reduced (labelled Basis B [195]), and several DFT functionals, comprising different exchange and correlation functions such as b3p86, b3lyp, b3pw91, blyp, bp86, pw91pw91, svwn, svwn5, pbepbe, mpw1pw91, b1b95 and pbe1pbe were tested to probe the best one reproducing the aforementioned CCSD(T) value (8.04 A^3). As depicted in figure (5.1), the b3p86 functional yields the smallest deviation and hence was applied for all optimizations and calculations of electronic properties of the tin clusters presented in this work.

5.3 Results and Discussion

5.3.1 Structural Data

Figures (5.2-5.6) depict the predicted global minima and lowest-energy isomers of Sn_{2-20}, where singlet and triplet states of isomers with relative energy differences of up to about 0.5 eV are shown. As discussed in chapter (4), the relative energy differences of some isomers are too small to appoint a distinct global minimum (see table (5.1)). Quintet spin states were calculated for a variety of different structures of Sn_{2-7} and it is found that they all lie higher in energy by 1-1.86 eV and thus are expected not to play a role in the characterization of the global minima. Relative energies, average neighbor distances, VIPs, VEAs and cohesive energies are shown in table (5.1).

Table 5.1: Average neighbor distances, relative energies, vertical ionization potentials, vertical electron affinities and cohesive energies of the lowest-energy Sn_n cluster isomers $2 \leq n \leq 20$. The geometry notation is that of figure (5.2). The notation $/n$ implies the value is given per atom.

Cluster	d (Å)	ΔE (eV)	VIP (eV)	VEA (eV)	E_{Coh} (eV/n)	Cluster	d (Å)	ΔE (eV)	VIP (eV)	VEA (eV)	E_{Coh} (eV/n)
1_t_0	-	0.0	7.885	0.867	-	12_s_2	3.092	0.083	6.728	2.563	2.652
2_t_0	2.757	0.0	8.026	2.238	1.250	12_s_3	3.082	0.235	6.711	2.768	2.633
3_t_0	2.841	0.0	8.048	2.589	1.777	12_t_4	3.072	0.546	6.494	3.220	2.607
3_s_1	2.920	0.160	7.785	2.541	1.724	13_s_0	3.105	0.0	6.776	2.834	2.674
4_s_0	2.862	0.0	8.051	2.482	2.187	13_t_1	3.113	0.499	6.487	3.483	2.636
5_s_0	3.180	0.0	7.751	2.142	2.347	14_s_0	3.094	0.0	6.932	2.586	2.718
5_t_1	2.977	0.493	7.646	2.936	2.248	14_s_1	3.105	0.272	7.033	2.695	2.699
6_s_0	3.042	0.0	7.674	2.200	2.525	15_s_0	3.093	0.0	6.682	3.033	2.721
6_t_1	3.037	0.523	7.358	2.868	2.438	15_s_1	3.102	0.093	6.706	2.376	2.715
7_s_0	3.030	0.0	7.728	2.455	2.647	15_s_2	3.088	0.253	6.790	2.781	2.704
8_s_0	3.059	0.0	6.971	2.447	2.576	15_t_3	3.094	0.368	6.281	3.430	2.696
8_s_1	3.085	0.190	6.898	2.411	2.552	16_s_0	3.110	0.0	6.985	2.415	2.732
8_t_2	3.074	0.249	6.752	2.890	2.545	16_s_1	3.098	0.131	6.786	2.828	2.723
9_s_0	3.064	0.0	6.964	2.265	2.627	17_s_0	3.114	0.0	6.471	2.820	2.711
9_t_1	3.069	0.432	6.993	3.470	2.579	17_s_1	3.087	0.085	6.571	2.946	2.706
10_s_0	3.051	0.0	7.300	2.404	2.716	17_s_2	3.100	0.140	6.641	2.666	2.703
11_s_0	3.067	0.0	6.695	2.660	2.658	17_t_3	3.100	0.377	6.078	3.649	2.689
11_s_1	3.080	0.020	6.560	2.354	2.657	18_s_0	3.110	0.0	6.641	2.671	2.725
11_s_2	3.098	0.102	6.663	2.498	2.649	19_s_0	3.060	0.0	6.664	3.186	2.724
11_t_3	3.072	0.255	6.642	2.807	2.635	19_s_1	3.130	0.034	6.629	3.015	2.722
12_s_0	3.094	0.0	6.716	2.827	2.652	20_s_0	3.070	0.0	6.707	3.337	2.741
12_s_1	3.092	0.059	6.713	2.617	2.647	20_t_1	3.120	0.391	6.421	3.872	2.721

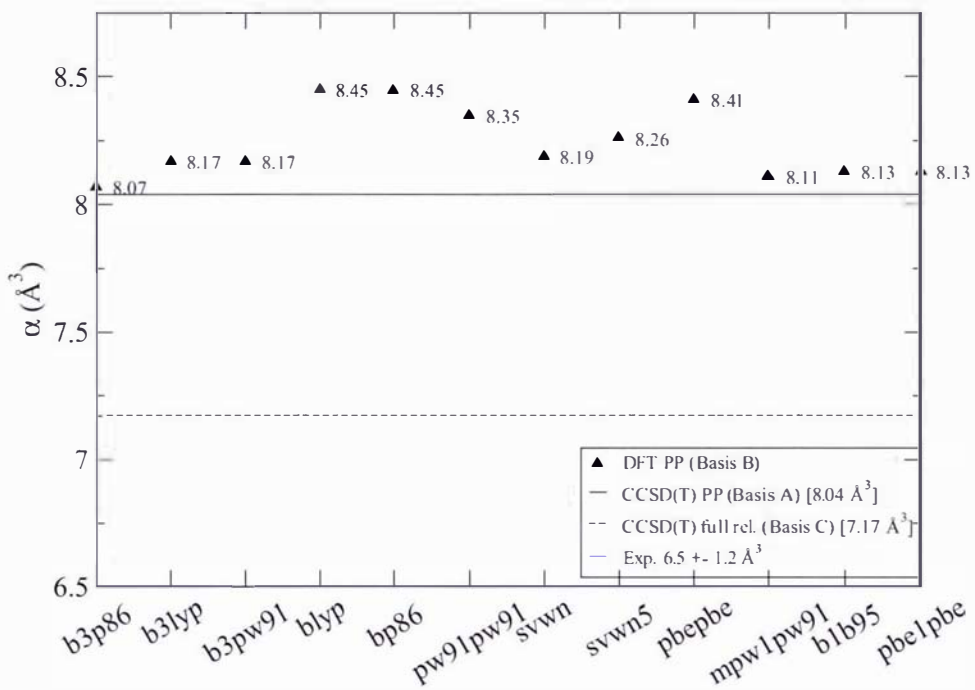

Figure 5.1: Static electric dipole polarizabilities of the $^3P_0$ tin atom in Å^3 as a function of different DFT exchange-correlation functionals and compared to experimental [198], scalar relativistic CCSD(T) ($^3P_0$) and 4-component relativistic CCSD(T) ($J = 0$) calculations.

The presented global minima of clusters with $n \leq 7$ have the same structures as those of Si and Ge and have been also reported previously [141, 162, 165, 190, 197]. Except for the Sn_2 and Sn_3, all ground state clusters are singlet states. The singlet state of Sn_2 is less stable than its triplet by 0.68 eV. The global minimum of Sn_3 is represented by a triplet C_{2v} triangle. Their linear structures are less stable by 0.70 eV (singlet) and 1.29 eV (triplet), thus underlining the particularly interesting scenario for linear cesium clusters up to six atoms as discussed in chapter (4). Sn_4 adopts a singlet D_{4h} rhombus and Sn_5 a singlet distorted trigonal bipyramid. The transition from planar to three-dimensional structures clearly occurs from $n = 4$ to $n = 5$, the flat singly capped rhombus (C_{2v}) is less stable than the trigonal bipyramid by 1.09 eV at the LANL2DZ level[10]. The distorted

[10]By LANL2DZ level, calculations from LANL2DZ basis set and respective shape-consistent pseudopo-

octahedron in the singlet spin state is more stable than the triplet one by 0.52 eV. Sn_7 adopts a pentagonal bipyramid structure (D_{5h}).

In accordance with references [165, 190, 197], the global minimum for the octamer is an edge-capped pentagonal bipyramid and not a doubly-edge-capped octahedron which is found as the global minimum for Si_8 and Ge_8. The nonamer ground state structure is a distorted singlet bicapped pentagonal bipyramid, which is more stable than the tricapped trigonal prism (TTP) in the triplet state by 0.43 eV. The structure of Sn_{9s_0} is also found as the global minimum for Si_9 and Ge_9 [141, 142, 165][11]. Majumder *et al.* [190] report the tin nonamer global minimum to adopt the TTP structure, which is contradicting the results in this work. At the LANL2DZ level, the structure in Sn_{9s_0} is more stable than the TTP structure in the triplet spin state by 0.43 eV and by 0.27 eV in the singlet spin state, respectively. The global minima of Sn_{10}, which is the same as for Si_{10} and Ge_{10}, and Sn_{11} show, however, clearly the trigonal prism motif and represent symmetrical tetra- and pentacapped derivatives of it.

The energetically lowest-lying structures for Sn_{11}, Sn_{12} and Sn_{13} are more stable than the ones reported in reference [190]. The same structure was found for Ge_{11}, but a different one for Si_{11} [197]. The optimization of an icosahedral structure for Sn_{13} yields various distorted versions of it that all are less stable than Sn_{13s_0} by around 0.8 eV at the LANL2DZ level. Interestingly, the stacked structures of Sn_{14s_0} and Sn_{15s_0}, which are also reported as the ground state structures in [190], are also essentially found for Si_{14}, Si_{15} [141,162] and Ge_{14}, Ge_{15} [120]. The predicted global minimum Sn_{17} adopts a spherical structure rather than a prolate one. It is quite different than the ones found for Ge_{17} and Si_{17}, which are reported in [141, 160–162]. The Sn_{17} structure reported in ref. [190] is less stable than Sn_{17s_0} by 0.22 eV at the LANL2DZ level. The predicted global minima with 18, 19 and 20 atoms are stacked prolate structures, each displaying at least one trigonal prism motif. Sn_{18s_0} is identical to that found in reference [190], while the structures for Sn_{19} and Sn_{20} represent more stable distorted versions. Sn_{19s_0} consists of a distorted tricapped trigonal prism prolately connected to a distorted tetracapped trigonal prism. The structure of Sn_{20s_0} is based on two identical tetracapped trigonal prisms twisted by 180° with respect to each other.

tentials as implemented in GAUSSIAN03 are meant.

[11] In reference [120], the germanium nonamer is reported to be a tricapped trigonal prism.

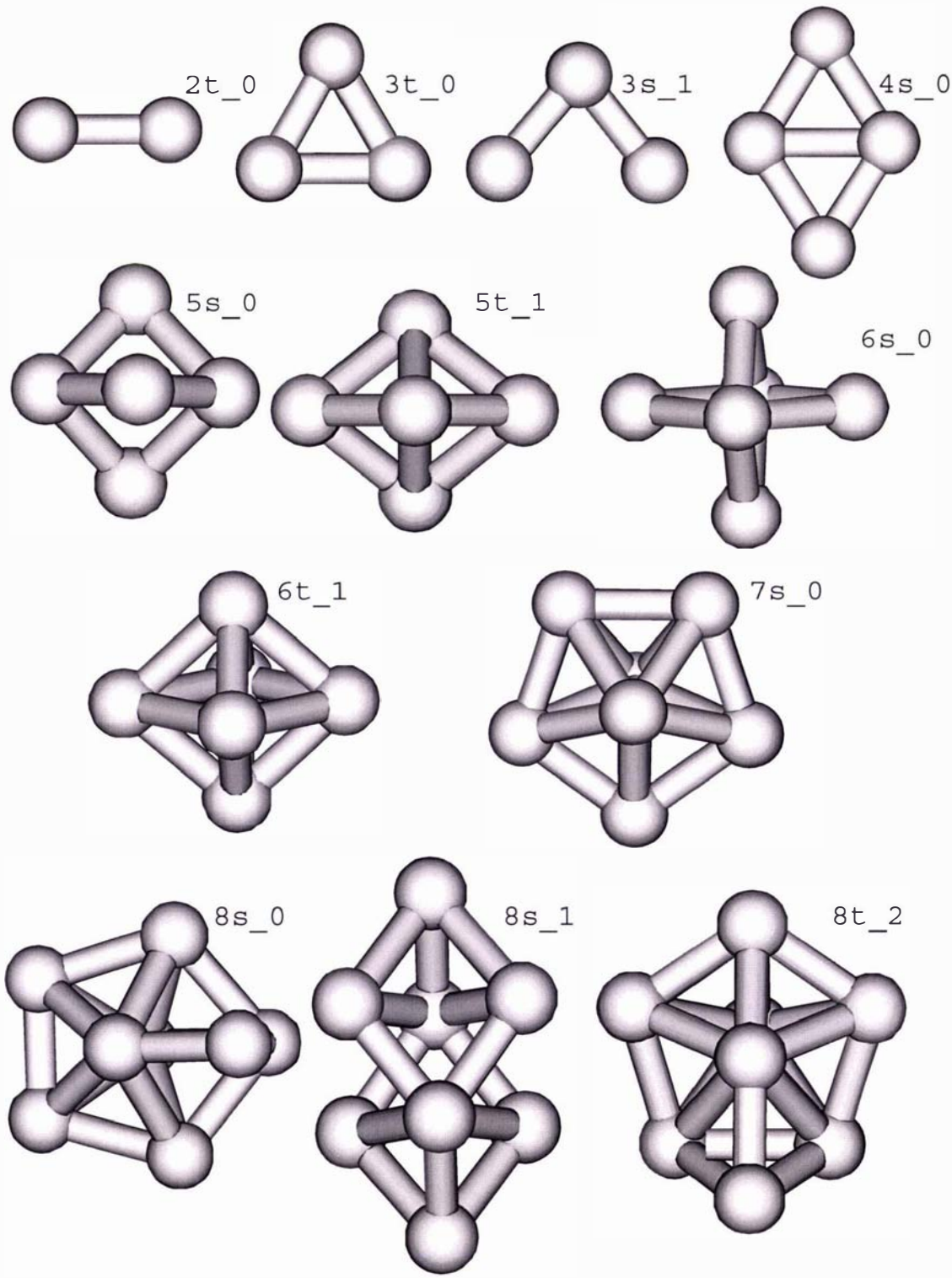

Figure 5.2: Predicted global minima and lowest-energy isomers of Sn_{2-8}, ordered (from left to right and top to bottom) by increased size and energy. The cluster n_m is the mth energetic isomer with n atoms. (s) denotes a singlet and (t) a triplet spin multiplicity.

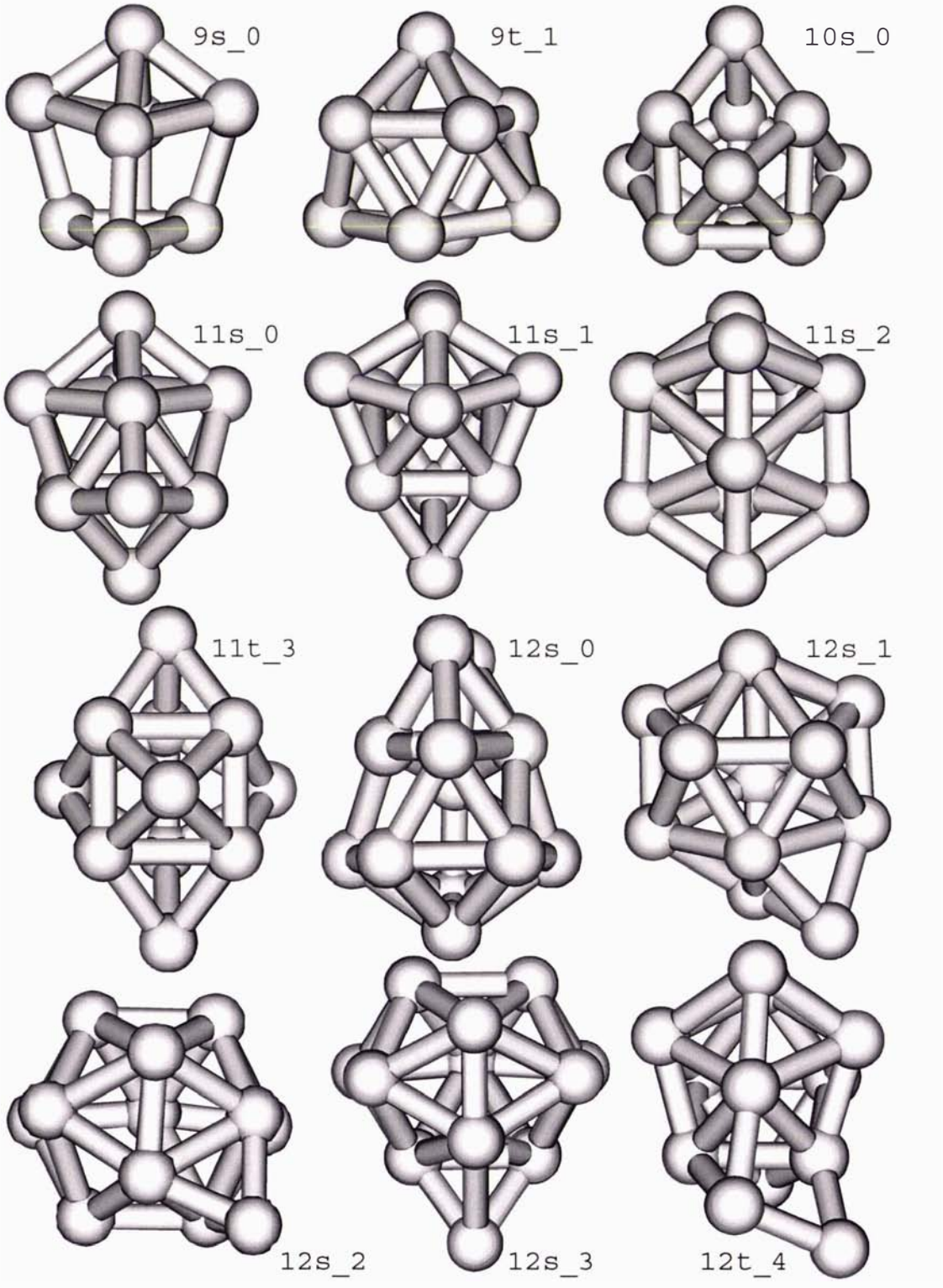

Figure 5.3: Predicted global minima and lowest-energy isomers of Sn_{9-12}, ordered (from left to right and top to bottom) by increased size and energy. The cluster n_m is the mth energetic isomer with n atoms. (s) denotes a singlet and (t) a triplet spin multiplicity.

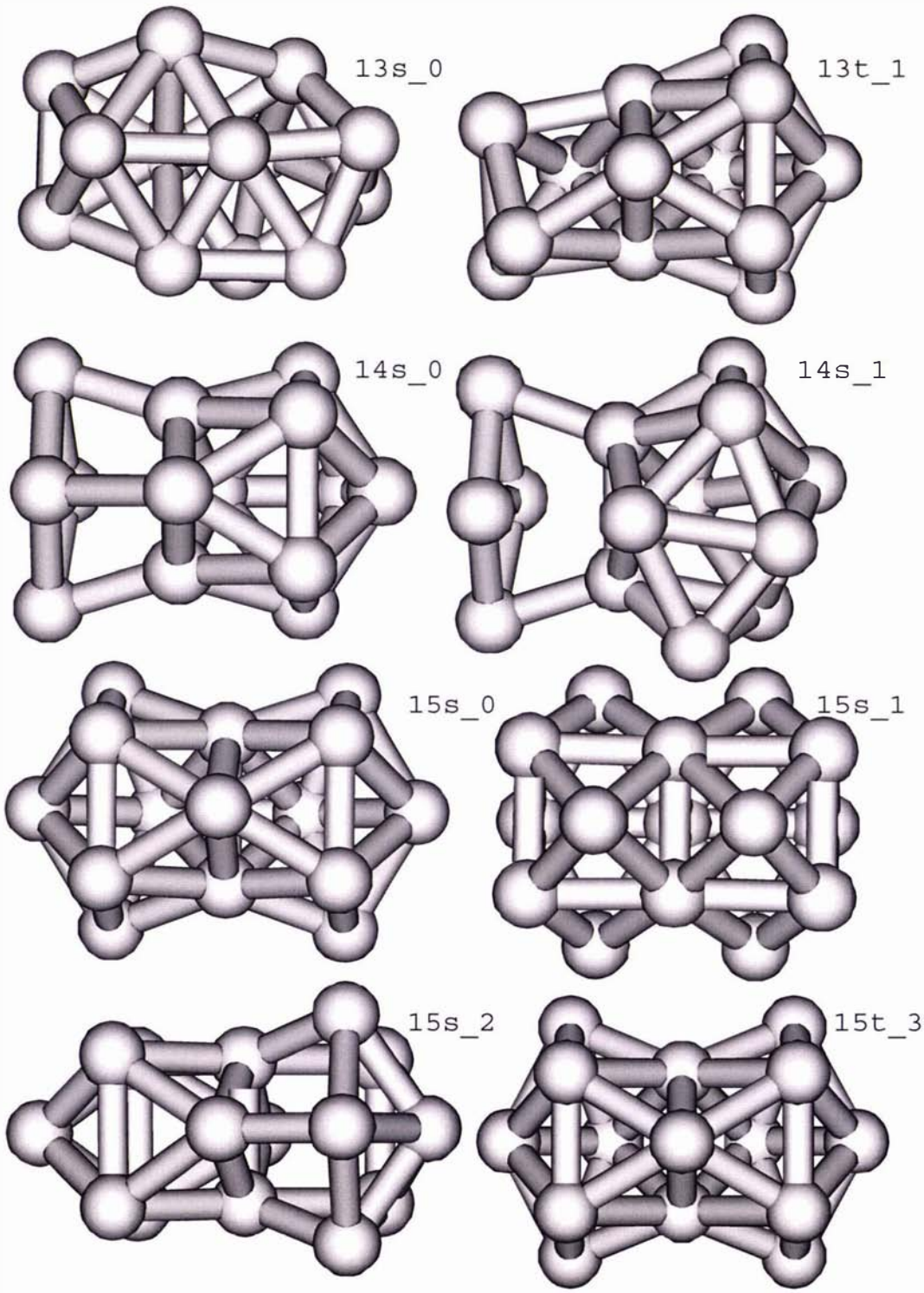

Figure 5.4: Predicted global minima and lowest-energy isomers of Sn_{13-15}, ordered (from left to right and top to bottom) by increased size and energy. The cluster n_m is the mth energetic isomer with n atoms. (s) denotes a singlet and (t) a triplet spin multiplicity.

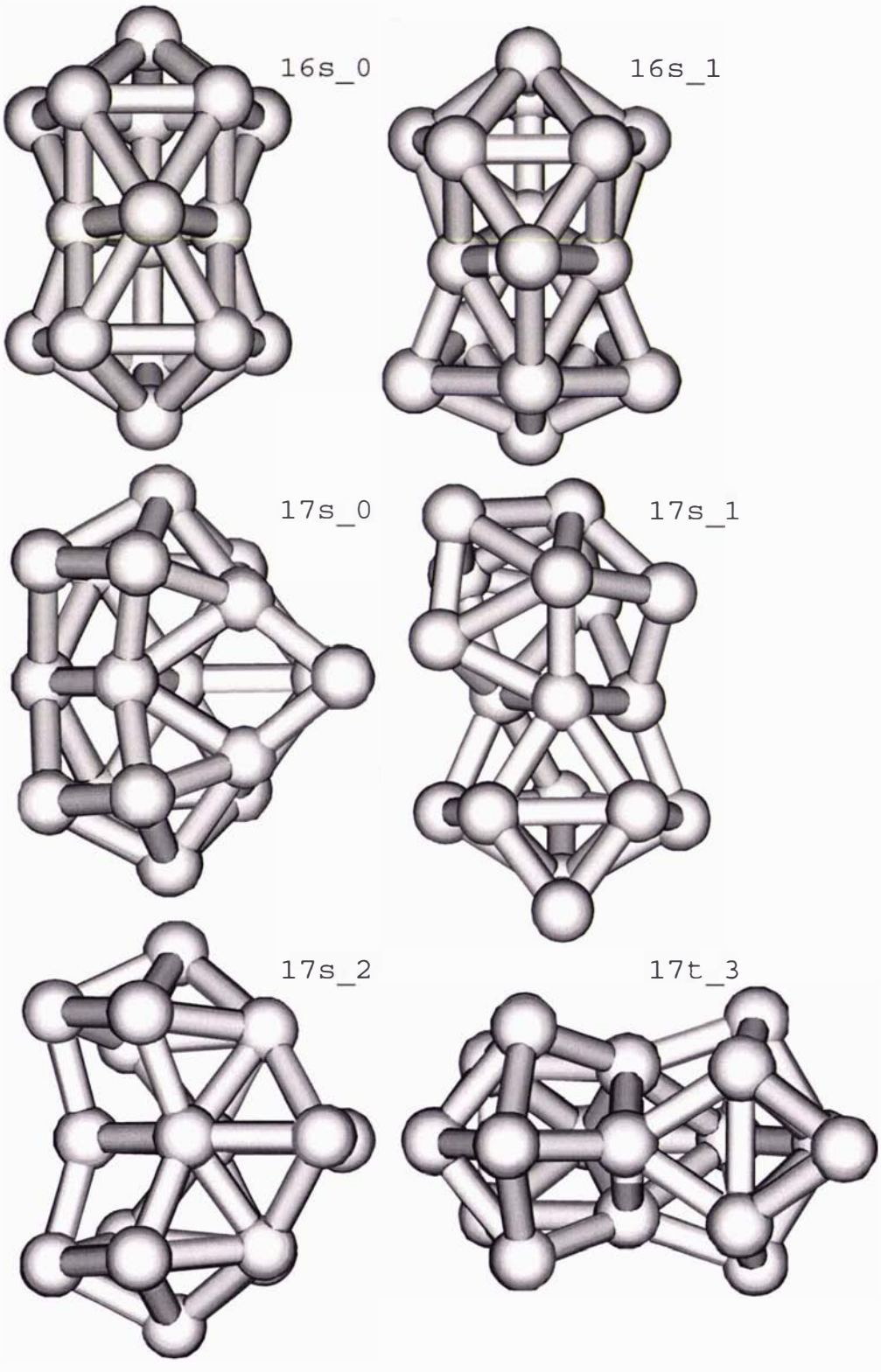

Figure 5.5: Predicted global minima and lowest-energy isomers of Sn_{16-17}, ordered (from left to right and top to bottom) by increased size and energy. The cluster n_m is the mth energetic isomer with n atoms. (s) denotes a singlet and (t) a triplet spin multiplicity.

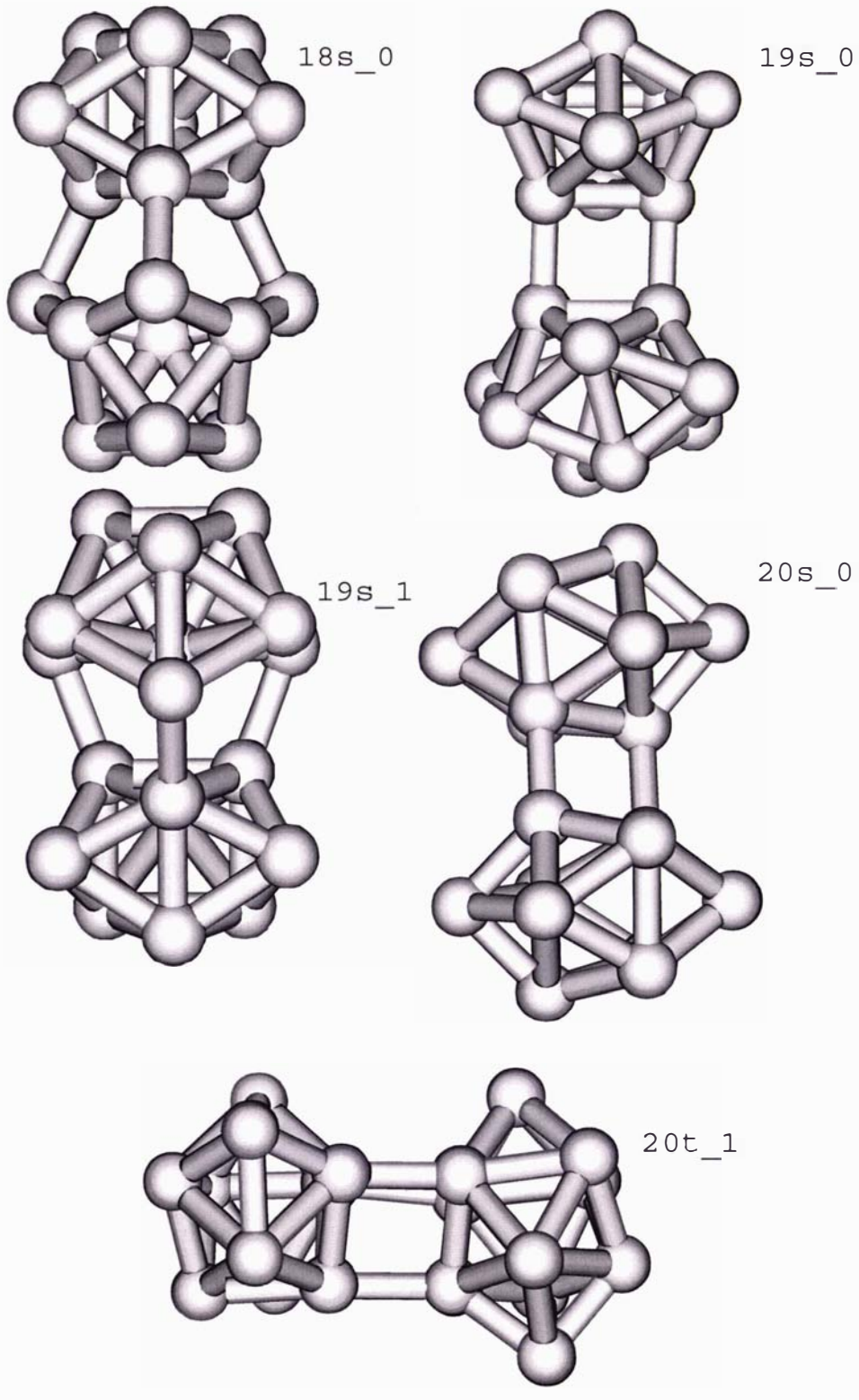

Figure 5.6: Predicted global minima and lowest-energy isomers of Sn_{18-20}, ordered (from left to right and top to bottom) by increased size and energy. The cluster n_m is the mth energetic isomer with n atoms. (s) denotes a singlet and (t) a triplet spin multiplicity.

5.3.2 Polarizabilities and other Electronic Properties

In order to gain insight into the marked deviation of the recently experimentally observed polarizability (6.5 $\text{Å}^3 \pm 1.2\ \text{Å}^3$ [198]) of atomic Sn and the calculated scalar-relativistic CCSD(T) value (8.04 Å^3) (see figure (5.1)), a 4-component relativistic calculation with an optimized 33s/27p/18d/5f (labelled Basis C [195]) in the framework of CCSD(T), where correlation of all states between -10 and 500 a.u. was taken into account for, was undertaken. The total electronic energy of the ground-state tin atom was calculated in an external, homogeneous electric field with a strength of up to $\pm 2 \cdot 10^{-3}$ a.u. (figure (5.7)). The polarizability was obtained by a quadratic fit to the total electronic energy. It is worthwhile to mention that the scalar relativistic calculation at the CCSD(T) level presented in this work already denotes the most accurate evaluation of the polarizability of atomic tin. Previous evaluations were done at the DFT level [7]. It is found that the inclusion of spin-orbit coupling reduces the polarizability by about 11 %. This value is then within the error margin of the experiment. In comparison the ground-state indium atom, a decrease in polarizability due to spin-orbit coupling of about 8 % was found [199]. The calculated static response and electronic structure properties of the tin clusters are presented in table (5.2). The calculated isotropic polarizabilities per atom are presented in figure (5.8) and compared to approximated values of bulk α- and β-Sn. A significant decrease is observed for the transition from flat to three-dimensional structures, but more importantly, already the hexamer shows the same polarizability per atom as the bulk value for α-Sn. The bulk polarizabilities per atom of the tin modifications that are present under ordinary conditions are approximated according to the Clausius-Mossotti equation (i.e. picturing the tin clusters as little dielectric or metallic droplets, respectively)[12]:

$$\alpha_{iso} = \frac{\epsilon - 1}{\epsilon + 2} r_{ws}^3 \tag{5.1}$$

β-Sn is metallic, has a tetragonal lattice with lattice parameters $a = 5.8318\ \text{Å}^3$, $c = 3.1818\ \text{Å}^3$ and $Z = 4$ atoms per unit cell [116]. Its classical polarizability per atom (α/n) can thus be approximated according to $\alpha_{iso} = r_{ws}^3$ and yields:

$$r_{ws}^3 = \frac{a^2 \cdot c}{Z} \cdot \frac{3}{4\pi} = 6.46 \frac{\text{Å}^3}{n} \tag{5.2}$$

[12]For metals, $\epsilon \to 0$, this equation becomes analogues to equation (4.2).

Table 5.2: Calculated static response and electronic structure properties of DFT-optimized Sn_n clusters. The second difference in cluster energy is denoted by $\Delta_2 E_n$ and $\Delta\epsilon$ represents the HOMO-LUMO gap. (The mean static polarizability per atom α_{iso} and the polarizability anisotropy per atom were calculated analytically.) The absolute value of the dipole moment is denoted by μ. The notation $/n$ implies the value is given per atom. The b3p86 functional is used throughout.

Cluster	$\Delta_2 E_n$ (eV)	$\Delta\epsilon$ (eV)	α_{iso} (Å$^3/n$)	α_{aniso} (Å$^3/n$)	μ (D)	Cluster	$\Delta_2 E_n$ (eV)	$\Delta\epsilon$ (eV)	α_{iso} (Å$^3/n$)	α_{aniso} (Å$^3/n$)	μ (D)
1_t_0	-	2.017	8.073	2.159	0.0	12_s_2	-	1.849	7.196	1.737	1.129
2_t_0	-0.328	1.919	9.261	7.033	0.0	12_s_3	-	1.632	7.214	1.313	2.253
3_t_0	-0.590	1.976	8.005	4.019	0.0	12_t_4	-	1.033	7.638	2.873	0.839
3_s_1	-	1.804	8.300	4.793	0.620	13_s_0	-0.354	1.699	7.276	2.479	0.749
4_s_0	0.434	2.111	8.101	5.869	0.0	13_t_1	-	0.768	7.398	2.677	1.384
5_s_0	-0.429	2.575	7.659	0.606	0.0	14_s_0	0.540	2.185	7.345	2.414	0.981
5_t_1	-	1.371	7.512	1.523	0.052	14_s_1	-	2.116	7.360	2.341	1.275
6_s_0	0.031	2.557	7.263	1.913	0.0	15_s_0	-0.140	1.506	7.303	2.774	0.070
6_t_1	-	1.547	7.168	0.749	0.0	15_s_1	-	2.146	7.123	1.703	0.0
7_s_0	1.307	2.466	7.106	2.840	0.0	15_s_2	-	1.863	7.341	2.988	0.847
8_s_0	-0.959	1.923	7.306	2.155	0.563	15_t_3	-	1.623	7.353	2.552	0.0
8_s_1	-	1.878	7.494	3.974	0.0	16_s_0	0.516	2.187	7.290	2.437	0.864
8_t_2	-	1.217	7.319	2.525	0.224	16_s_1	-	1.854	7.322	2.503	0.940
9_s_0	-0.475	2.137	7.203	1.203	0.208	17_s_0	-0.587	1.573	7.267	1.606	0.927
9_t_1	-	0.983	7.120	1.526	0.056	17_s_1	-	1.589	7.639	3.982	1.164
10_s_0	1.426	2.426	7.020	0.241	0.634	17_s_2	-	1.904	7.256	1.834	1.311
11_s_0	-0.499	1.659	7.140	1.415	1.592	17_t_3	-	1.518	7.593	3.533	0.390
11_s_1	-	1.825	7.268	1.985	0.535	18_s_0	0.265	1.955	7.517	3.581	1.941
11_s_2	-	1.767	7.147	1.227	1.308	19_s_0	-0.370	1.558	8.005	4.900	0.974
11_t_3	-	1.519	7.300	2.430	0.0	19_s_1	-	1.562	7.489	3.459	2.880
12_s_0	-0.355	1.605	7.260	2.399	2.251	20_s_0	-	1.498	8.003	5.175	0.126
12_s_1	-	1.780	7.277	2.544	1.395	20_t_1	-	1.613	8.339	6.200	0.331

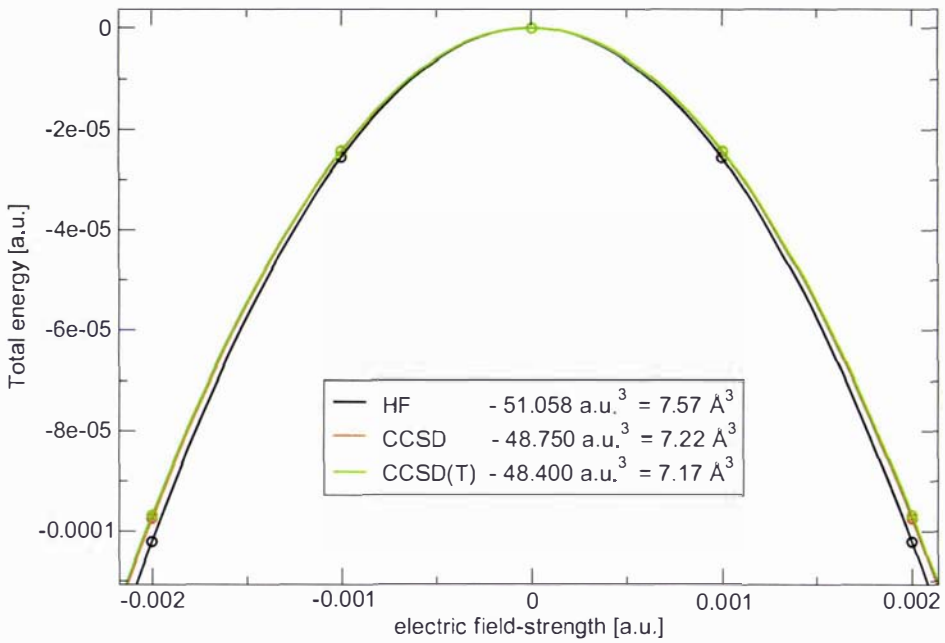

Figure 5.7: Full relativistic calculation of the polarizability of the ground state tin atom with an optimized basis (Basis C: 33s/27p/18d/5f [195]) in the finite field approach. Correlation of all states between -10 and 500 a.u. were taken into account.

α-Sn is a semiconductor with a diamond lattice and parameters $a = 6.4892$ Å^3, $Z = 8$ and a dielectric constant of 24 [116], which gives for the Wigner-Seitz radius

$$r_{ws}^3 = \frac{a^3}{Z} \cdot \frac{3}{4\pi} = 8.168 \frac{\text{Å}^3}{n}. \tag{5.3}$$

Thus, the classical polarizability per atom for bulk α-Sn is obtained to be 7.23 Å$^3/n$. The polarizabilities per atom of the predicted global minima of Sn_{6-17} resemble this value and only small deviations are observed. This may be another indication, that small tin clusters adopt rather a covalent bonding nature than a metallic one, as already suggested by melting temperature measurements and calculations for small clusters [129, 130, 134–138]. The structures of Sn_{18-20} are distinctively prolate which explains the increase in polarizability. Clearly, the evolution of α/n as a function of cluster size is more complicated than

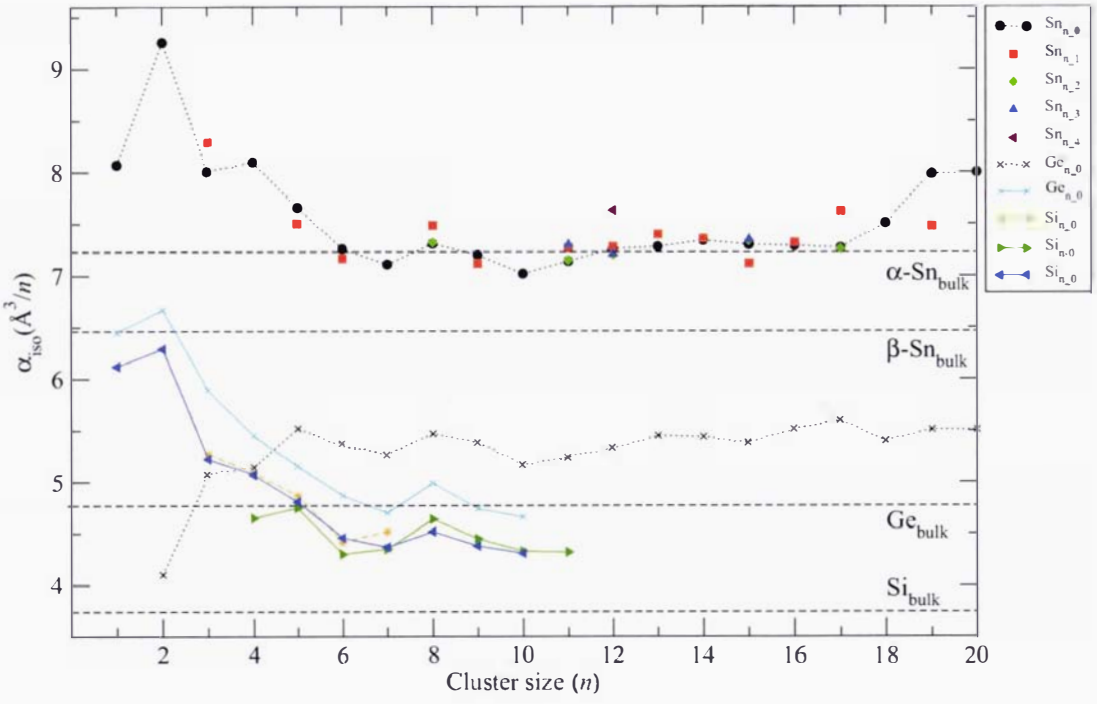

Figure 5.8: Isotropic static electric dipole polarizabilities per atom of Sn_n clusters as a function of cluster size compared to the classical values of bulk α- and β-Sn. Polarizabilities of Ge_2 - Ge_{20} are extracted from [120], Ge_1 - Ge_{10} from [165] and (Si_{3-7} [155], Si_{4-11} [142], Si_{1-10} [165]) are also plotted and compared to their classical bulk polarizabilities for reasons of comparison.

those for simple metallic clusters like cesium for instance and it would be very interesting to evaluate the cluster sizes at which the bulk value for β-Sn is resembled. The magic cluster Sn_{10} stands out, exhibiting the smallest polarizability per atom within the range of clusters presented here. In comparison to the tetracapped trigonal prism structure of Sn_{10}, all following clusters, with the exception of Sn_{17}, can be regarded as elongated and from Sn_{18} - Sn_{20} as prolate. This structural transition is reflected by a slight increase in α/n and a significant one for the prolate structures. Taking this into account one may speculate that at some stage the geometric structures of the tin clusters will adopt more compact, spherical shapes, resulting in a decrease of α/n. This could lead to a convergence towards the bulk value of the metallic allotrope of tin.

Tin clusters are more polarizable than germanium and silicon clusters. Moreover, it becomes apparent that the approach of α/n for Si-cluster towards their respective bulk limit[13] is significantly slower than that of Sn-cluster. As mentioned in section (5.1), however, beam deflection experiments by Schäfer *et al.* suggest that the α/n of Si-cluster of at least nine atoms vary about the bulk value of Si and do not show a convergence behavior [156, 200]. The data of Ge_2 - Ge_{20} are extracted from reference [120] and were calculated from b3lyp/LANL2DZ calculations. The α/n increase with n and show no convergence behavior towards the bulk limit[14]. This trend is contrary to the ones observed for Si and Sn cluster of similar sizes and puts a question mark behind the accuracy of the data, because it has been established that the structure of Si and Ge cluster of up to around nine to ten atoms are equal (see (5.3.1)). Moreover, the LANL2DZ basis set will not suffice to describe the polarizability in the valence region, where it is most pronounced, accurately enough. Furthermore, the α/n of the germanium dimer is expected to be larger than the atomic one, as it is observed for Si and Sn. In contrast, the atomic polarizability of Ge is reported to be 6.07 Å^3 [7], which is about 50 % larger than the one calculated for Ge_2 by Zhao *et al.* [120] and thus indicating that the reported absolute value for Ge_2 by Zhao *et al.* is questionable. The trend and absolute values of polarizabilities per atom for Ge_1 - Ge_{10} reported by Chelikowsky *et al.* [165] seem to be much more reliable and support the Sn data reported here. They also find that at Ge_6 the bulk limit is reached and small variations about this value are observed until Ge_{10}.

[13]Bulk Si at ambient conditions has a diamond structure and parameters $a = 5.4307$ Å, $\epsilon = 11.8$ and $Z = 8$ [116].

[14]Bulk Ge at ambient conditions has a diamond structure and parameters $a = 5.657$ Å, $\epsilon = 16$ and $Z = 8$ [116].

Very accurate calculations at the CCSD(T) level by Maroulis *et al.* [155], DFT calculations by Zeng *et al.* [142] and DFT calculations by Chelikowsky *et al.* [165] suggest that small silicon clusters show polarizabilities per atom that are larger than their bulk value but converge from above towards the bulk value. Since the reported absolute values of Si_3 to Si_7 are essentially the same for references [155] and [165], the published data for the germanium clusters by [165] are reconfirmed.

The α/n of the predicted global minima cannot be meaningfully fitted by the jellium-model (see section (4.1)), since any good fit of the data according to

$$\alpha = \frac{(n \cdot N_e^{1/3} \cdot r_{ws} + \delta)^3}{n} \tag{5.4}$$

yields a product of parameters for the number of electrons ($N_e^{1/3}$) and the Wigner-Seitz radius of tin that is four times smaller than it should be. In other words, the absolute values of α/n for the predicted global minima cannot be fitted by the jellium function and assuming four valence electrons and the crystallographically obtained Wigner-Seitz radius of α-Sn for instance.

In figure (5.9), the calculated *permanent* dipole moments of the predicted global minima are compared with the estimated *effective* dipole moments from a recent beam deflection experiment (see section (1.3.2), [198]). The calculated dipole moments from this work are scaled down by a factor of 40 for reasons of better comparison. The experimental evaluation of the effective dipole moments is based on the spherical rigid rotator model and obtained from the broadening of the deflected molecular beam profile [198]. The quantitative agreement between experiment and theory is very poor and can be ascribed mainly to the dynamics of the clusters in the experiment, to the model adopted to evaluate the effective dipole moments from the experiment or to other, unknown reasons. The measured effective dipole moments are strongly temperature dependent and increase significantly with decreasing cluster temperature. The measured effective dipole moment of Sn_{12} is for instance 12 times larger measured at a nozzle temperature of 50 K compared to the one measured at a nozzle temperature of 310 K, indicating a more body-fixed moment at lower temperature. The observed effective dipole moments in figure (5.9) are obtained at a nozzle temperature of 310 K and are therefore significantly smaller than the calculated permanent dipole moments from this work. However, the qualitative resemblance is very satisfactory, showing exceptions only for Sn_{11}, Sn_{16} and Sn_{18}, and thus confirming most of the geometric structures of the predicted global minima.

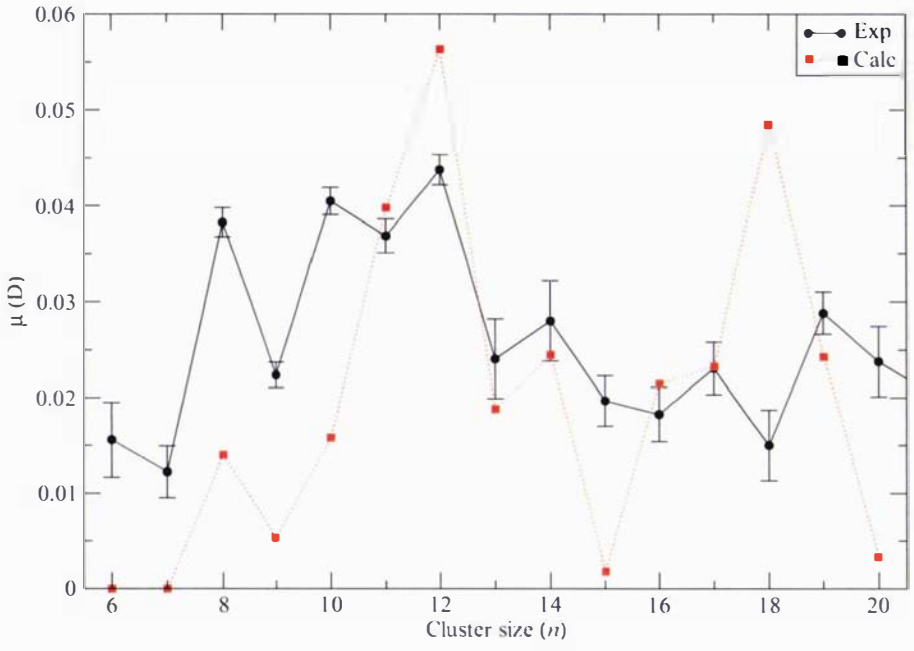

Figure 5.9: Comparison between calculated permanent dipole moments and experimentally obtained effective dipole moments. The calculated values are scaled down by a factor of 40 for reasons of better comparison. (See text for details).

The calculated polarizabilities per atom are compared to a recent temperature dependent beam deflection experiment in figure (5.10) [198]. The calculated values are scaled by a factor of 1.65 for better comparison. The experimentally obtained α/n are all larger than the calculated ones. As described below, this discrepancy is perhaps due to fact that observed effective polarizabilities represent an upper bound to the electronic polarizability. The qualitative agreement with the experiment at a nozzle temperature of 310 K is, however, very satisfying. Clearly, the experimentally obtained values have converged towards a limit and vary about 12 $\text{Å}^3/n$, which is approx. 1.65 times higher than the bulk value of α-Sn. Furthermore, a significant temperature dependent polarizability per atom is observed for Sn_8, Sn_{10-13}, Sn_{16-17}, Sn_{19-20}. The most pronounced dependence is

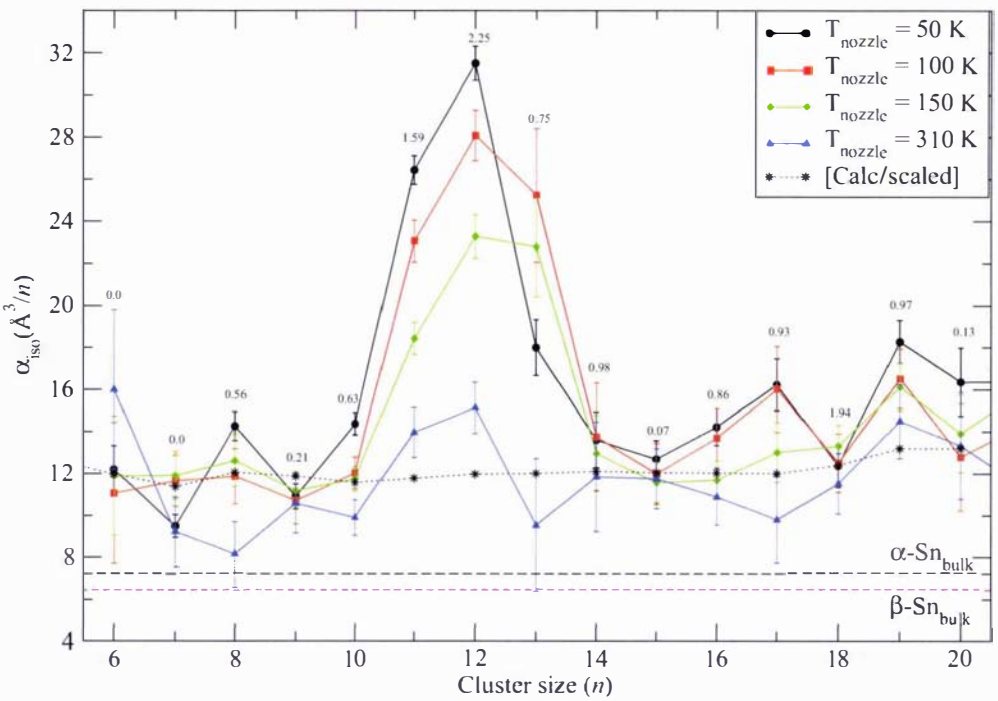

Figure 5.10: Comparison between calculated and experimentally obtained isotropic polarizabilities per atom at different nozzle temperatures. The calculated values are scaled up by a factor of 1.65 for better comparison. The calculated dipole moments (in D) are indicated for the respective clusters (See text for details).

observed for Sn_{11-13}[15].

In the experiment, as described in detail in section (1.3.2), the displacement of the beam profile is directly proportional to the polarizability. However, within the weak-field limit ($\mu_0 F \ll k_B T_{rot}$, where F denotes the electric field, k_B the Boltzmann constant and T_{rot} the rotational temperature), measured polarizabilities represent upper limits to the electronic polarizability as permanent dipole moments and the rotational temperature of the clusters contribute to the effective polarizability. For symmetric tops with principal

[15]For Sn_{13}, the α/n at 50 K is for unknown reasons smaller than that for for 100 K and 150 K.

moments of inertia I_1 $(=I_2)$ and I_3, the effective polarizability is given by [200]

$$\alpha_{\text{eff}} = \alpha + \frac{2}{9}\frac{\mu_0^2}{k_B T_{rot}}\left(1 + \frac{1}{5}\kappa\right), \tag{5.5}$$

where $\kappa = I_3/I_1 - 1$ denotes the deviation from sphericity. Hence, experimentally an effective polarizability is measured, which also depends on the permanent dipole moments and rotational temperatures of respective clusters, and explains why usually larger polarizabilities are obtained in experiments than predicted from theoretical evaluations. Furthermore, for clusters with large permanent dipole moments (i.e. $n = 8, 10-13, 17, 19$, see figure (5.9)), also a strong temperature dependence of α/n is observed. It can be argued that the dynamics of clusters at high temperature may lead to a partly or total cancellation of the permanent dipole moment and that at low temperature, this moment becomes more body-fixed, thus resulting in a greater displacement of the beam. This qualitative argument explains the strong temperature dependence for clusters with large dipole moments.

The calculated dipole moments are denoted in figure (5.10) and clearly, when taking the experimental margin of errors into account, the trend of the magnitude of the temperature dependence of α/n is satisfyingly confirmed by the calculated permanent dipole moments. The only distinct exceptions are for $n = 18$ and 20. It must however be noted that the magnitude of the temperature dependence depends also on the rotational temperature, which is probably different for different cluster sizes, and that further effects may also be operative.

The anisotropy to the polarizability per atom α_{aniso}, according to equation (1.56) is given in table (5.2) and is also plotted in figure (5.11). For the singlet spin-states, a small α_{aniso} can be (solely) regarded as an indication for compact (spherical) symmetry. This is reflected for instance by low values for Sn_5, Sn_{10} and Sn_{17} as compared to their less compact neighbors. As expected, the prolate clusters with $n = 18, 19$ and 20 exhibit larger anisotropies per atom.

Figure (5.12) depicts the ionization potentials and electron affinities of the ground state tin atom as a function of DFT exchange-correlation functionals and shows clearly that bp86 reproduces the experimental values extremely well. The b3lyp, b3pw91 and blyp functionals underestimate the electron affinity drastically while the b3p86, the functional employed for all tin cluster calculations, overestimates the ionization potential by about 7 % and underestimates the electron affinity by about 22 %. The calculated verti-

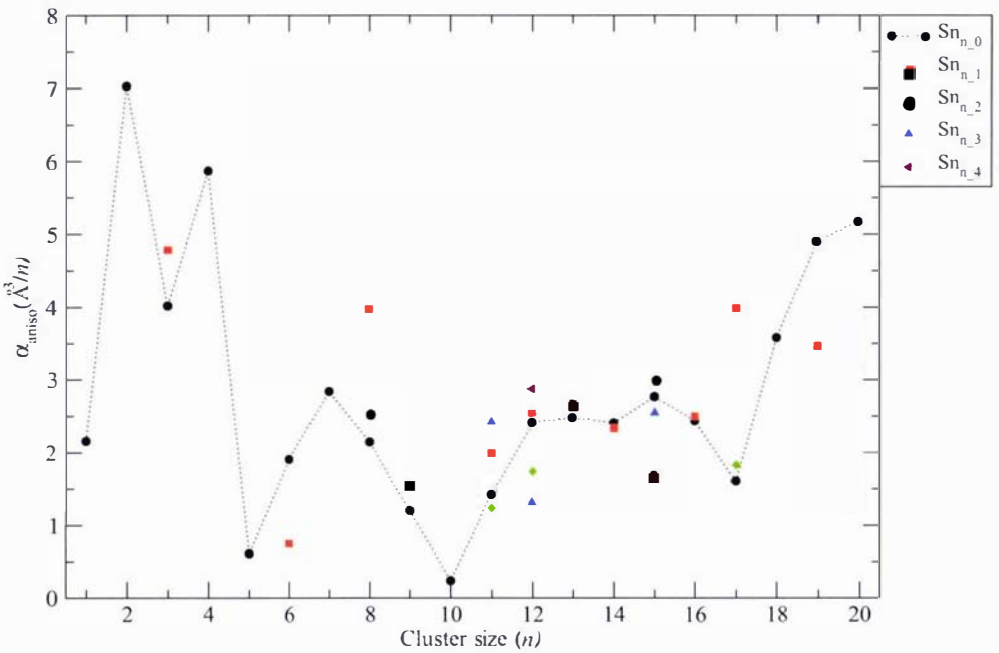

Figure 5.11: Anisotropy per atom to the static electric dipole polarizability, according to equation (1.56), as a function of cluster size for tin.

cal ionization potentials and electron affinities as a function of cluster size are displayed in figure (5.13) and compared to experimental values and the work function of tin. Experimental values for ionization energies are extracted from [179][16], those for electron affinities from [178]. Experimental values for the workfunction, atomic ionization energy and atomic electron affinity are extracted from [116]. The trend of the calculated VIP graph agrees very nicely with the experimental results and would give a better match for the actual values if it was scaled down by approximately 0.5 eV. This results from the fact that the b3p86 functional, according to figure (5.12), overestimates the atomic IP by about 0.5 eV and does not perform as well as the bp86 functional for instance[17]. The experimental electron affinities in figure (5.13) are obtained from photoemission spectra

[16]The upper and lower bounds of the experimental ionization potentials are given in figure (5.13).

[17]The choice of the b3p86 functional is, however, not founded on the reproduction of the experimental ionization potential and electron affinity, but on the polarizability of the ground state tin atom.

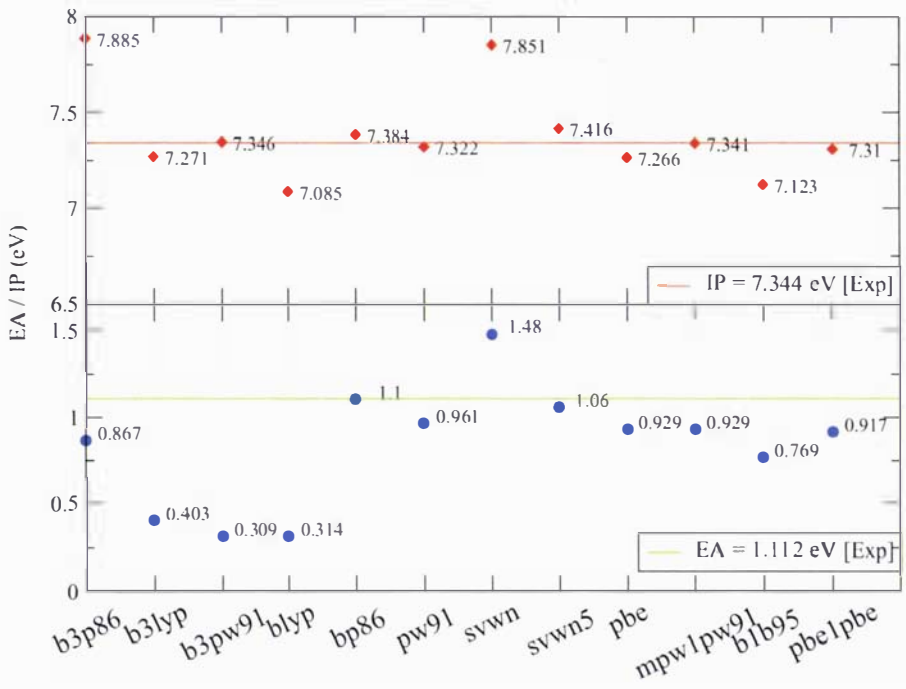

Figure 5.12: Ionization potentials and electron affinities of the ground state tin atom ($^3P_0$) in eV as a function of DFT exchange-correlation functionals and compared to experimental values [116].

of anionic tin clusters and, besides for the Sn_4 case, are resembled satisfyingly by the calculated values.

Peaks in the second difference energy ($\Delta_2 E_n$) according to equation (4.4) (see figure (5.14)) indicate magic cluster sizes (i.e cluster sizes that are very stable and may give rise to higher intensities in cluster synthesis experiments). Interestingly, most even-numbered clusters of the predicted global minima with the exception of Sn_8 and Sn_{12} are more stable than odd-sized ones. In alkali clusters, electronic shell effects are mainly responsible for magic cluster sizes [49] (see also section (4.3.2)) and the even-odd oscillation of higher stability for even-sized clusters can be explained by the spin-pairing effect. The latter argument does not hold for the tin clusters presented here, because other than the dimer and trimer clusters all predicted global minima represent closed-shell singlet states. A simple electronic shell filling effect as in the case of the alkali clusters is also out of question,

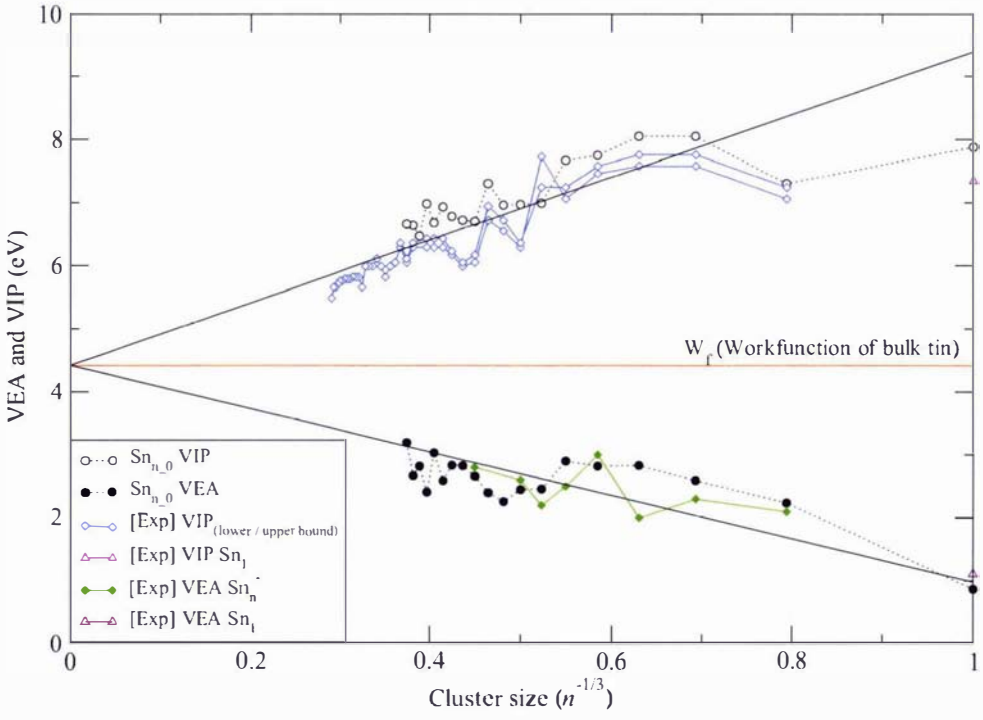

Figure 5.13: Vertical electron affinities and vertical ionization potentials of tin cluster as a function of cluster size ($n^{-1/3}$). The evolution of both properties is approximated by a linear regression according to $G(n) = 4.42 + bn^{-1/3}$, where 4.42 eV denotes the workfunction of bulk tin [116]. Open symbols denote ionization potentials and filled symbols electron affinities. (see text for details).

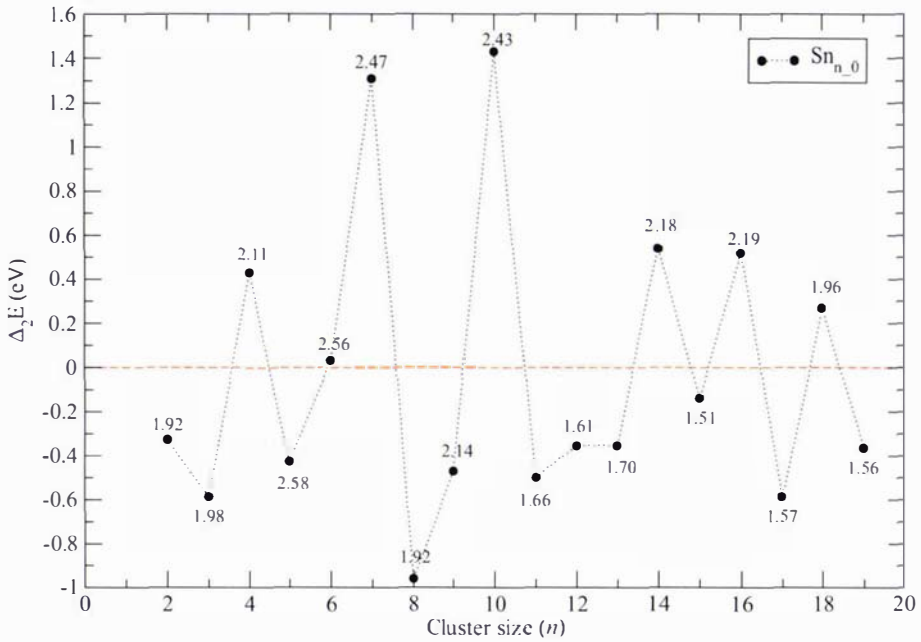

Figure 5.14: Second difference in Sn cluster energy as a function of cluster size as denoted in equation (4.4). Respective HOMO-LUMO gaps in eV are shown.

otherwise distinct peaks at Sn_2, Sn_8 and Sn_{18} should be observed. The low stability of Sn_8 is probably a result of geometric effects. While Sn_{7_0} adopts a pentagonal bipyramid (D_{5h}) and Sn_{9_0} a symmetrically bicapped version of it (D_{2h}), Sn_8 lies structurally in-between and does not adopt a planar pentagonal motif (C_1). Higher stabilities for even-sized germanium, silicon and tin clusters to this extent have not been reported so far, although there is some indication for this phenomenon in tin clusters [191][18]. Peaks that stand out in particular are the ones for Sn_{10}, Sn_7, Sn_{14} and Sn_{16}. It is seen that magic clusters with $n \geq 10$ are also more tightly bound than their neighbors (see figure (5.15)). For smaller cluster sizes, where geometric effects play a more dominant role, larger HOMO-LUMO gaps do not coincide with the pattern in figure (5.14). It becomes thus clear that HOMO-LUMO gaps cannot be used solely to discuss stabilities of clusters.

[18]Obviously, the trend in $\Delta_2 E$ can only be interpreted reasonably, when the global minima structures have been found. This may be one explanation as to why this oscillation has not been reported so far.

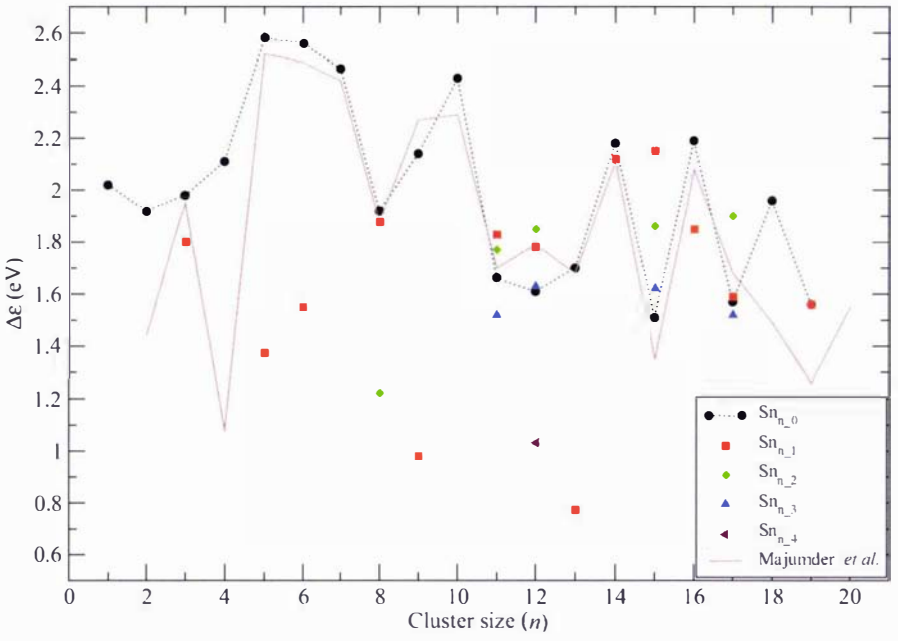

Figure 5.15: Calculated HOMO-LUMO gaps $\Delta\epsilon$ of tin clusters versus the cluster size n. The solid line represents extracted values from Majumder *et al.* [191].

Arguments based on the tricapped trigonal prism motif cannot explain the extremely high stability of Sn_{10} either, because Sn_{11} shows a tetracapped trigonal prism and is relatively less stable than Sn_{12} which does not show this motif. Moreover, the predicted global minimum of Sn_9 adopts a distorted bicapped pentagonal bipyramid rather than a tricapped trigonal prism by 0.23 eV at the LANL2DZ level. Hence, if the unusual high stability of Sn_{10} was solely based on the geometric structure of capped derivatives of the trigonal prism, the global minimum of Sn_9 should adopt this motif as well.

HOMO-LUMO gaps are presented in figure (5.15) and compared to those calculated by Majumder *et al.* [191]. In most cases, the trend and also the absolute values are similar to those in ref. [191]. Triplet states exhibit much lower gaps. The gaps for the global minima of Sn_5, Sn_6 and Sn_{10} are similarly large, however, Sn_{10} exhibits a magic cluster (see figure (5.14)), whereas the others do not. This shows again, that HOMO-LUMO gaps should not be used solely to discuss stabilities of clusters. The HOMO-LUMO evolution

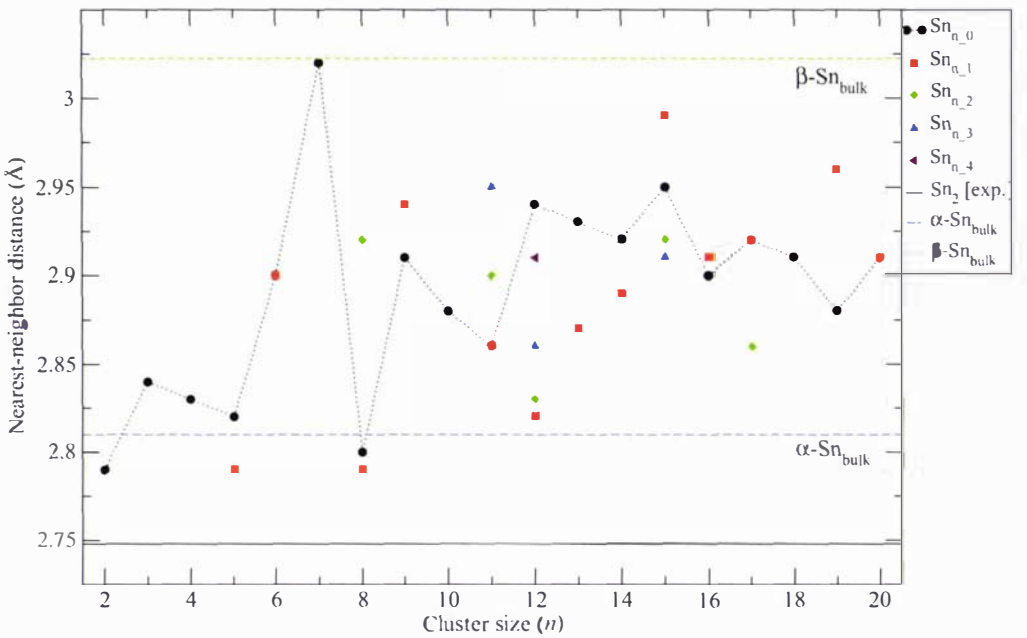

Figure 5.16: Nearest-neighbor distances plotted against the cluster size n. The solid line represents the experimental tin dimer bond length (2.75 Å [176]) and the dashed lines symbolize the experimental value for the shortest equilibrium interatomic distances in α-Sn (2.81 Å) and β-Sn (3.02 Å) [116].

with cluster size also shows a rather slow convergence towards the metallic state.

In figure (5.16), the nearest-neighbor distances are plotted as a function of cluster size n and compared to the nearest-neighbor distances in bulk α- (2.81 Å) and β-Sn (3.02 Å). Note that in table (5.1) the average neighbor distances[19] are listed and not the nearest-neighbor distance. The latter excludes surface effects, which play a major role in clusters. Most clusters exhibit nearest-neighbor distances that are in-between the shortest equilibrium interatomic distances in bulk α- and β-Sn. There is a general trend for this bond length in the global minima structures to increase towards that of β-Sn up to Sn_{15}, but no coherent information can be extracted. The cohesive energies as a function of cluster size to the power of $(n^{-1/3})$ are depicted in figure (5.17) and compared to the

[19]Calculated as the arithmetic mean of all distances ($d \leq 3.5$ Å).

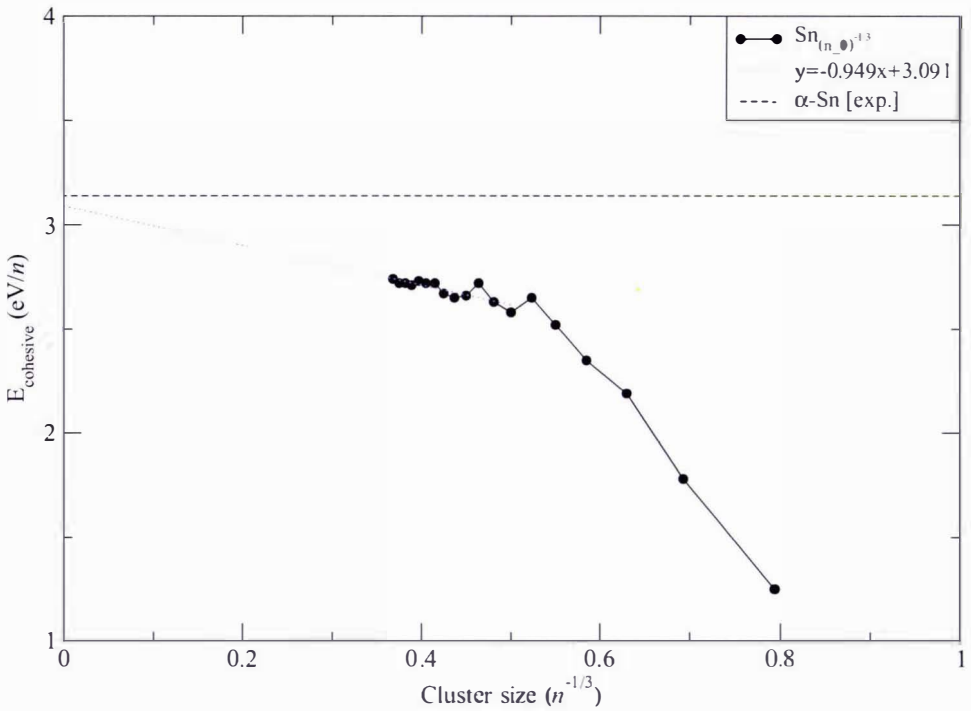

Figure 5.17: Calculated cohesive energies of tin clusters as a function of cluster size to the power of $(n^{-1/3})$. The experimental cohesive energy of α-Sn (solid line) is reported to be 3.140 eV/n. For β-Sn, 3.100 and 3.140 eV/n are reported, respectively [202].

experimental bulk value for α-Sn (3.140 eV/n)[20]. The progression towards the bulk value can be described by two almost linear intervals (i.e. from Sn_2 to Sn_7 and Sn_8 to Sn_{20}). Sn_{20} shows only a 12.7 % deviation from the bulk value and the linear fit from Sn_8 to Sn_{20} estimates the bulk cohesive energy as 3.09 eV/n. Considering the fact that the small cluster sizes discussed here are very far away from the macroscopic solid state, it is an astonishing result that the bulk cohesive energy of tin can be estimated within a deviation of less than 2 % by this means.

In figure (5.18), the calculated zero-point vibrational energies (ZPVE) per atom are

[20]The bulk cohesive energy of β-Sn is reported as 3.100 and 3.130 eV/n [202] and are not displayed in figure (5.17) for reasons of simplicity.

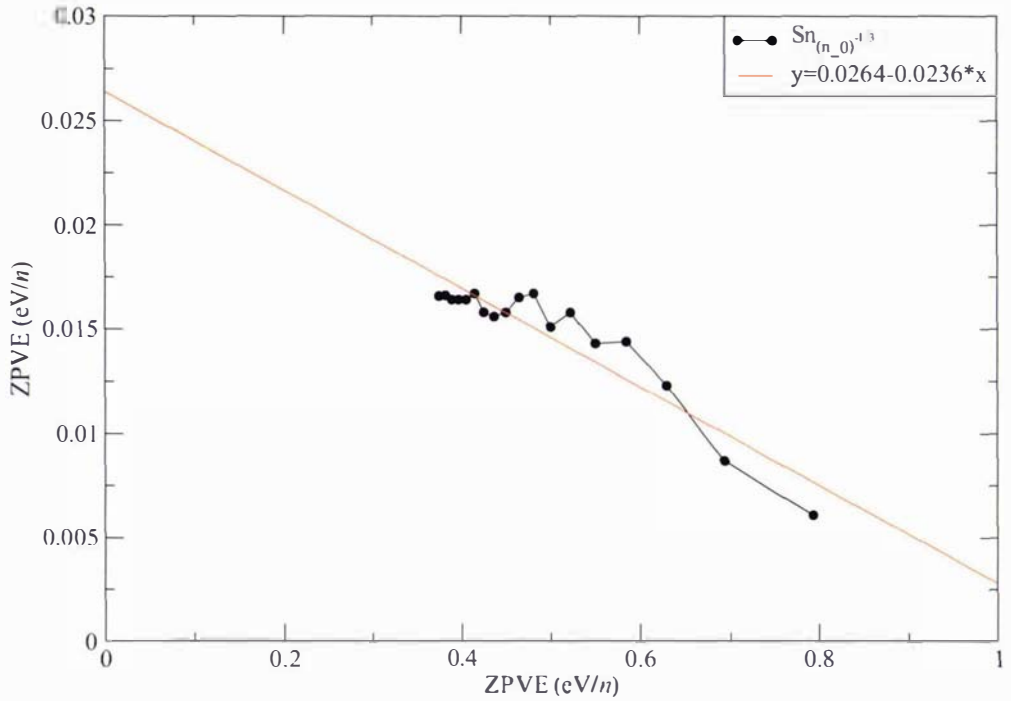

Figure 5.18: Calculated zero-point vibrational energies (ZPVE) per atom of tin clusters as a function of cluster size to the power of ($n^{-1/3}$). The dashed line represents a linear regression towards the bulk limit.

plotted against the cluster size to the power of ($n^{-1/3}$) and fitted linearly. This approach estimates the ZPVE per atom of bulk tin, which is unknown experimentally, to be between 0.02 and 0.03 eV.

5.4 Conclusions

In conclusion, it is found that singlet spin-states clearly dominate the energetically lowest-lying isomers of small tin clusters up to 20 atoms, and that triplet and quintet spin-states do not play a role in their global minima structures. The GM of Sn_2 to Sn_7 are identical to those found for germanium and silicon clusters, respectively. Tri- and tetracapped trigonal prism motifs are found as a major structural motif in the GM of Sn_{10}, Sn_{11}, Sn_{18},

Sn_{19} and Sn_{20}. The GM of Sn_{15} and Sn_{16} adopt distinct stacked structures displaying an A, B, A stacking. For $n \geq 9$, some predicted global minima are reconfirmed, while seven new structures are found that are lower lying in energy than previously reported, thus underlining the performance of the genetic algorithm developed in this work.

The static electric dipole polarizability of the tin atom in its ground state is evaluated for the first time at the scalar-relativistic and 4-component relativistic CCSD(T)-level, and compared to the recently experimentally evaluated polarizability of the tin atom. It is found that inclusion of spin-orbit effects reduces the polarizability by about 11 % and that the value obtained by this means lies within the error margin of the experiment. However, spin-orbit effects should become smaller for larger cluster sizes.

The qualitative agreement of the calculated dipole moments and polarizabilities with recent beam deflection experiments is very satisfying, indicating firstly that the general trend of the polarizability as a function of cluster size is correct, secondly that most global minima structures are found and thirdly that clusters with large permanent dipole moments result in significantly larger beam deflections at low rotational temperatures, thus explaining why in experiments usually larger, effective polarizabilities are obtained than from theory.

5.5 Further Work

It would be very interesting to investigate the evolution of the isotropic polarizability per atom for larger cluster sizes and identify the re-transition from prolate structures, that clearly start at Sn_{18}, to spherical ones and evaluate when the polarizabilities resemble that of bulk β-Sn.

Chapter 6

Gold Clusters

6.1 Motivation

While inert as a bulk material or as supported gold layers, nano-scale gold particles in form of clusters adsorbed on various metal oxide supports (i.e. MgO, TiO_2, Al_2O_3, Fe_2O_3) exhibit remarkable heterogeneous catalytic activity for several technological important reactions such as the low-temperature oxidation of CO, selective hydrogenation, oxidation and epoxidation of hydrocarbons, reduction of nitrogen oxides and hydrogenation of carbon dioxides [203]. The dramatic breakthrough in the heterogeneous catalysis of gold came when Haruta *et al.* succeeded in depositing small (5 <nm) gold clusters on metal surfaces in 1987 and discovered that for suitable metal oxide supports and cluster sizes, CO oxidation occurred well below room temperature [204–206].

Since then gold nanoclusters and nano-crystalline gold compounds have been the subject of intense research. The rapid growth of this interest in the past decades is demonstrated in figure (6.1), which denotes the number of published theoretical studies as a function of time. Applications of gold nanoparticles are vast and comprise areas of materials science, medicine and catalysis [208, 209]. In contrast to its lighter congeners in group 11, copper and silver, gold shows distinctively different structural and electronic properties both at the microscopic and macroscopic level. The stronger tendency of gold to form close metal-metal interactions (aurophilicity) [210] (see chapter (8)) is for instance one example for the exceptional position of gold in group 11 and among the transition metals for that matter. These differences are attributed to large relativistic effects in gold [23, 211, 212].

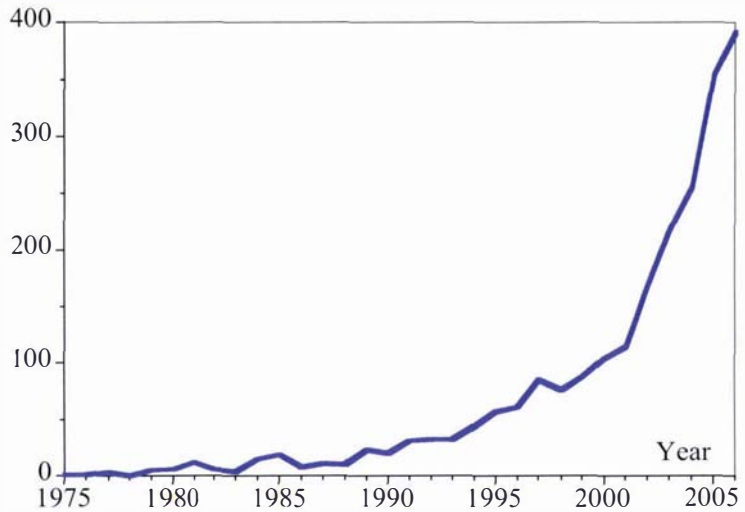

Figure 6.1: Number of papers published on gold clusters and gold compounds using computational methods as a function of time [207].

Due to the vast amount of studies on gold clusters, in the following, only a brief summary of recent investigations on homo-nuclear, small-sized (Au_{2-20}) clusters by computational and experimental methods is given. Furthermore, since gold cluster structures obtained from model potential optimizations favor maximum number of close atom-atom contacts and it is well established that the global minima of metallic and covalent systems obtained by these means are energetically higher lying than those obtained from DFT and *ab initio* calculations, studies based on empirical interaction potentials are not mentioned here [44].

Rabin *et al.*, who also investigated the ionization potentials of small gold clusters [213], observed concentration maxima for singly charged Au_n^+ with $n = 3, 9, 19, 21, 35$ in agreement with previous work by Katakuse *et al.* [214], and the predictions from the electronic shell model [215]. Photoelectron spectroscopy of negatively charged gold clusters up to five atoms were undertaken by Lineberger *et al.* [216]. The first benchmark calculations on atomic and dimeric gold were carried out by Schwerdtfeger, who studied correlation and relativistic effects [217]. Rösch *et al.* calculated ionization potentials, electron affinities, structural properties and binding energies of Au_n clusters ($n = 6, 13, 19, 38, 44, 55, 147$) with octahedral, cuboctahedral and icosahedral symmetry from LDA and GGA scalar-relativistic all-electron DFT calculations and compared their results with bulk values. They obtained good agreement for the GGA extrapolation of the VIP and VEA to the

bulk limit [218]. Landman *et al.* studied electronic properties and structures of neutral and anionic gold clusters up to ten atoms from scalar-relativistic pseudopotential GGA DFT calculations and found neutral clusters up to seven atoms and anionic ones up to 6 atoms to adopt planar structures [219]. Zhao *et al.* report the structural transition from 2D to 3D to take place at the size of 7 atoms and discuss electronic and structural properties of gold clusters up to 20 atoms based on LSDA calculations [220]. They obtained their structures from a genetic algorithm simulation, where the structural relaxation is performed from a tight-binding potential. From ion mobility measurements, Weis *et al.* concluded that anionic clusters up to 11 atoms adopt flat structures, while their DFT calculations predicted planar structures for up to Au_{13}^-, thus indicating that DFT may overestimate the stability of planar structures [221]. Bonačić-Koutecký *et al.* find from their DFT studies that neutral gold clusters of up to ten atoms adopt planar structures and compare them with bimetallic silver-gold clusters [222].

The exceptional stability of planar anionic clusters, which is found to be correlated to strong hybridization of the atomic $5d$ and $6s$ orbitals due to relativistic effects, is addressed and compared to respective copper and silver clusters in the study by Landman *et al.* [223] and Grönbeck *et al.* [224]. In a photoelectron study, Wang *et al.* discovered that the HOMO-LUMO energy gap of Au_{20} is even greater than that in C_{60}. From relativistic DFT studies they found the Au_{20} cluster to possess a tetrahedral structure [225][1]. Hou *et al.* investigated in DFT calculations the polarizabilities among other electronic and structural properties of planar, neutral gold clusters up to 20 atoms [230]. Trends in the structure and bonding of singly positively, negatively and neutral noble metal clusters up to 20 atoms are reported by Fernández *et al.* [231], who also calculated the static electric dipole polarizabilities of their structures in ref. [232]. From DFT calculations including spin-orbit coupling, Wang *et al.* conclude that gold clusters up to 15 atoms adopt a planar geometry [233].

Theoretical rearrangement collisions between gold clusters were studied by Kiwi *et*

[1] This sensational structure represents the lowest-lying minimum of Au_{20} and all other reported isomers lie much higher in energy. For Cu_{20}, however, a less symmetrical, more compact and energetically lower lying isomer is found [226]. A comparative DFT study of various metal clusters consisting of 20 atoms with T_d and lower symmetry is presented in [227]. The static electric dipole polarizability and first hyperpolarizability, together with the UV-Vis spectrum of this structure is evaluated by Li *et al.* [228]. The tetrahedral structure is reconfirmed in an extensive search for other low-lying isomers within a DFT basin-hopping approach [229] and also in this work.

al. [234]. In a study comprising Gaussian-based and plane-wave DFT, MP2 and CCSD(T) calculations, it is found that the neutral gold octamer, optimized at the DFT level, adopts a 3D structure in the framework of the two latter methods and a 2D at the DFT level [235]. This result is in contradiction with the studies of Han and Kim *et al.*, who both also employed DFT, MP2 and CCSD(T) methods and report a planar structure of Au_8 for all three methods to be most stable [236, 237]. Remacle *et al.* [238] and Walker [239] re-established that the size threshold for the 2D-3D coexistence is lower for cationic gold clusters than for neutral ones in their DFT study of charged and neutral gold clusters, where Walker calculated structures and energetics of neutral and positively charged gold clusters up to the nonamer employing three different DFT functionals and three basis sets. Xiao *et al.* calculated various electronic properties and magnetic moments of gold clusters Au_n ($n = 2 - 14,\ 20,\ 55$), also including linear and zig-zag chains. They report the transition from 2D to 3D at Au_{13} and that cluster stabilities calculated with the Sutton-Chen potential disagree with those yielded from DFT calculations [240]. Dong *et al.* studied the vibrational breathing modes of clusters up to 16 atoms employing all-electron DFT calculations, and they predict the Au_{13} cluster to be more stable in a 3D arrangement [241, 242]. A global-minimum search for Au_n ($n = 15 - 19$) by means of a basin-hopping method coupled with DFT, was undertaken by Zeng *et al.* [243]. By photo-dissociation experiments, Vogel *et al.* determined the unimolecular decay rates and monomer-dimer branching ratios of Au_n^+ ($n = 7 - 27$) clusters and observed only direct fragments Au_{n-1}^+ for all even-sized clusters and those containing more than 16 atoms. For the remaining odd-sized clusters, dimeric fragmentation is found to be in general preferred [244]. Wang *et al.* calculated structural and electronic properties of gold clusters up to 14 atoms from DFT LANL2DZ theory and found the turnover point from 2D to 3D to occur at Au_{12}. They also report the static electric dipole polarizabilities per atom and find them to oscillate with cluster size, giving smaller values for even cluster sizes [245]. Jellinek and coworkers investigated the dipole polarizabilities and optical absorption spectra of low energy structures of Au_n clusters, $n = 2 - 14$ and 20, obtained from static (GGA and LDA) and time-dependent DFT (LDA) calculations [246]. They employed a valence double-zeta basis set including d polarization functions and a large core pseudopotential, leaving 11 valence electrons. Their obtained polarizabilities per atom computed with the finite-field method exhibit odd-even oscillation and increase with cluster size for the planar clusters (Au_4 - Au_{13}). Those obtained from the TDLDA

excitation energies and oscillator strengths show the same trend but give absolute values that are smaller by at least 10 %.

Further photoemission, -ionization and other spectroscopic studies on small gold clusters can be found in refs. [247–252]. A variety of sophisticated theoretical calculations on atomic, dimeric and trimeric gold are reported in [211, 217, 253–270]. Finally, extremely stable gold coated nano-clusters of the form $M@Au_n$ (M = various transition metals, $n = 6,\ 12$) were found recently and are reported in refs. [271–273].

The motivation for this work was to systematically search for the lowest-lying isomers of small gold clusters up to 20 atoms, employing a DFT based genetic algorithm and to accurately calculate the static electric dipole polarizability of the clusters among other electronic and structural properties. To my best knowledge, there are only four reports on calculated polarizabilities of gold clusters [230, 232, 245, 246] and no experimental measurements are available. In all these theoretical approaches, however, no systematic search for the lowest-lying isomers was undertaken. Furthermore, Hou *et al.* only investigated the polarizabilities of planar structures and Wang *et al.* employed solely the rather small LANL2DZ basis set and pseudopotential, which were used in this work for preliminary calculations only.

6.2 Methods

The predicted low spin global minima structures of gold clusters consisting from four up to twenty atoms were obtained utilizing the genetic algorithm code BELPHEGOR as described in detail in section (3.1). The initial populations of respective cluster sizes consisted of the Lennard-Jones global minima, from at least ten randomly generated structures and from published energetically lowest-lying structures [219, 220, 222, 225, 230, 231, 233, 239, 240, 243]. The minimum energy difference dV_i was set to 0.005 eV, d_{min} and d_{max} parameters were fixed between 2.4 Å and 4.5 Å, respectively. The termination criteria was 150 mating and local minimization steps for clusters up to ten atoms and 100 steps for the remainder. The mutation probability was varied between 10 % and 20 %.

Typically, ten of the thus obtained energetically lowest-lying isomers were then further relaxed from LANL2DZ basis set and pseudopotential calculations to their local minima. Depending on the relative energy distribution, two to four of the energetically lowest-lying true minima isomers obtained by these means were then further optimized using

the extensive STUTTGART valence basis set together with the energy-consistent scalar-relativistic pseudopotential (labelled large basis) for gold [274]. Finally, in each case, the nature of the stationary point was determined by calculating and diagonalizing the matrix of energy second derivatives (Hessian). For the exchange-correlation potential, the hybrid functional b3pw91, according to the parameterization suggested by Becke [196] and Perdew and Wang [275], was employed in a self-consistent fashion as implemented in the GAUSSIAN03 program package. No symmetry constraints were applied during the optimization procedure. The large basis set, which was used for the accurate calculations, contains 58 basis functions, whereas the LANL2DZ basis set which was used for preliminary calculations contains only 22. Since DFT scales with N^3, where N denotes the number of basis functions, calculations from the large basis are extremely computer-time demanding and could not be finished by the completion of this thesis, as the computer resources at Massey University were rather limited. More accurate results from large basis set calculations are only reported up to the decamer, and LANL2DZ calculations are reported for the whole range of gold clusters studied in this work. It will, however, become apparent that the deviations for most electronic properties and also for structural properties from LANL2DZ and large basis set calculations are less than 5 %. It should also be noted that many publications on gold clusters only employ the LANL2DZ basis set and pseudopotential. It is, however, found that the relative energy differences between respective isomers obtained at the LANL2DZ level can be quite different from those obtained from the extensive basis set.

The static electric dipole polarizability of the ground state gold atom was calculated utilizing several DFT functionals comprising different exchange and correlation functions such as b3p86, b3lyp, b3pw91, blyp, bp86, pw91pw91, svwn, svwn5, pbepbe, mpw1pw91, b1b95 and pbe1pbe. As depicted in figure (6.2), where calculated polarizabilities of atomic gold are plotted against various DFT functionals, the b3pw91 functional yields the smallest deviation from the benchmark all-electron, relativistic CCSD(T) calculation in the framework of the Douglas-Kroll-Hess transformation, and was thus employed for all gold cluster calculations.

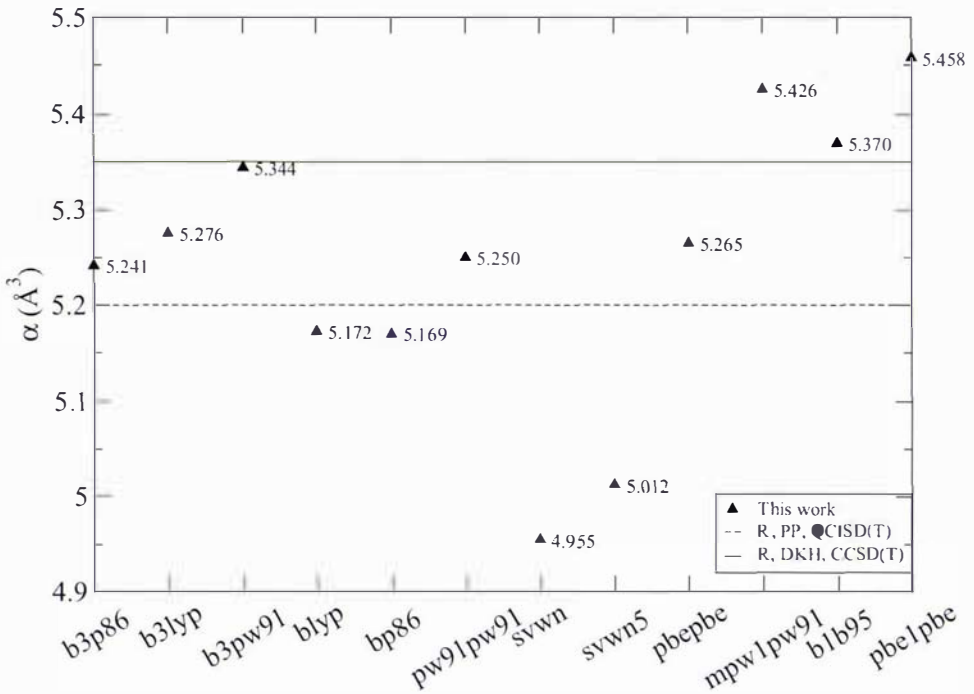

Figure 6.2: Static electric dipole polarizability of the ground state gold atom in $Å^3$ as a function of different DFT exchange-correlation functionals and compared to benchmark calculations. 5.20, $Å^3$ R, DKH, CCSD(T) [276] and 5.35 $Å^3$, R, PP, QCISD(T) [277]

6.3 Results and Discussion

6.3.1 Structural Data

Figures (6.3-6.7) depict the predicted low-spin global minima of neutral gold clusters up to 20 atoms. In table (6.1), the average neighbor distance, δE, VIPs, VEAs and cohesive energies of these clusters are presented.

For clusters up to ten atoms, planar structures are found to represent the energetically lowest-lying isomers. Essentially the same structures are reported as global minima by Wang *et al.* [245], Xiao *et al.* [240], Walker[2] [239], Jellinek *et al.* [246] and Fernández *et al* [231], thus confirming the efficiency of BELPHEGOR and the employed methods in this

[2]Only clusters up to the nonamer are considered in Walker's study

Table 6.1: Average neighbor distances, relative energies, vertical ionization potentials, vertical electron affinities and cohesive energies (not corrected for zero-point vibrational energy) of the lowest-energy Au_n cluster isomers $2 \leq n \leq 20$. The geometry notation is that of figure (6.3). The notation $/n$ implies the value is given per atom. Values in parenthesis are obtained from LANL2DZ and those without from large basis set calculations.

Cluster	d (Å)	ΔE (eV)	VIP (eV)	VEA (eV)	E_{Coh} (eV/n)	Cluster	d (Å)	ΔE (eV)	VIP (eV)	VEA (eV)	E_{Coh} (eV/n)
1_0	-	-	9.353	2.093	-	(11_1)	(2.766)	(0.267)	(7.092)	(3.656)	(1.687)
(1_0)	-	-	(9.340)	(2.101)	-	(11_2)	(2.836)	(0.389)	(6.814)	(3.134)	(1.676)
2_0	2.519	-	9.273	1.785	1.021	(12_0)	(2.768)	(0.0)	(7.449)	(3.278)	(1.746)
(2_0)	(2.547)	-	(9.450)	(1.887)	(0.951)	(12_1)	(2.858)	(0.018)	(7.565)	(2.836)	(1.745)
3_0	2.564	0.0	8.195	3.136	1.029	(12_2)	(2.804)	(0.098)	(7.325)	(2.768)	(1.737)
(3_0)	(2.611)	(0.0)	(8.461)	(3.382)	(0.942)	(12_3)	(2.819)	(0.205)	(7.321)	(2.393)	(1.728)
4_0	2.675	0.0	7.743	2.347	1.337	(13_0)	(2.804)	(0.0)	(6.594)	(3.405)	(1.741)
(4_0)	(2.719)	(0.0)	(7.915)	(2.472)	(1.235)	(13_1)	(2.820)	(0.053)	(6.525)	(3.399)	(1.737)
5_0	2.687	0.0	7.355	2.825	1.478	(13_2)	(2.768)	(0.160)	(6.700)	(3.512)	(1.728)
(5_0)	(2.737)	(0.0)	(7.517)	(2.994)	(1.363)	(14_0)	(2.839)	(0.0)	(7.452)	(2.428)	(1.804)
6_0	2.685	0.0	8.219	1.897	1.713	(14_1)	(2.839)	(0.163)	(7.232)	(2.783)	(1.793)
(6_0)	(2.733)	(0.0)	(8.482)	(2.000)	(1.596)	(15_0)	(2.824)	(0.0)	(6.381)	(3.150)	(1.794)
7_0	2.696	0.0	7.046	2.993	1.662	(15_1)	(2.849)	(0.021)	(6.753)	(3.410)	(1.793)
(7_0)	(2.748)	(0.0)	(7.238)	(3.179)	(1.538)	(15_2)	(2.852)	(0.032)	(6.971)	(3.657)	(1.792)
8_0	2.670	0.0	8.012	2.535	1.786	(15_3)	(2.774)	(0.266)	(6.956)	(3.928)	(1.777)
(8_0)	(2.717)	(0.0)	(8.139)	(2.636)	(1.663)	(16_0)	(2.831)	(0.0)	(7.194)	(2.883)	(1.846)
9_0	2.712	0.0	6.904	3.188	1.757	(16_1)	(2.845)	(0.218)	(6.889)	(2.784)	(1.832)
(9_0)	(2.766)	(0.0)	(7.106)	(3.403)	(1.621)	(16_2)	(2.852)	(0.242)	(7.032)	(2.954)	(1.8310
9_1	2.710	0.135	7.421	3.589	1.742	(17_0)	(2.826)	(0.0)	(6.947)	(3.708)	(1.850)
(9_1)	(2.766)	(0.156)	(7.553)	(3.826)	(1.604)	(17_1)	(2.861)	(0.037)	(6.327)	(3.124)	(1.848)
10_0	2.714	0.0			1.838	(18_0)	(2.827)	(0.0)	(7.139)	(2.944)	(1.889)
(10_0)	(2.766)	(0.0)	(7.626)	(2.770)	(1.695)	(18_1)	(2.830)	(0.034)	(6.999)	(2.809)	(1.887)
10_1	2.718	0.259			1.812	(19_0)	(2.864)	(0.0)	(6.584)	(3.497)	(1.920)
(10_1)	(2.767)	(0.049)	(7.798)	(2.105)	(1.690)	(19_1)	(2.869)	(0.471)	(6.379)	(3.356)	(1.895)
(10_2)	(2.774)	(0.063)	(7.051)	(2.481)	(1.688)	(20_0)	(2.875)	(0.0)	(7.438)	(2.419)	(1.969)
(11_0)	(2.762)	(0.0)	(6.138)	(2.888)	(1.712)						

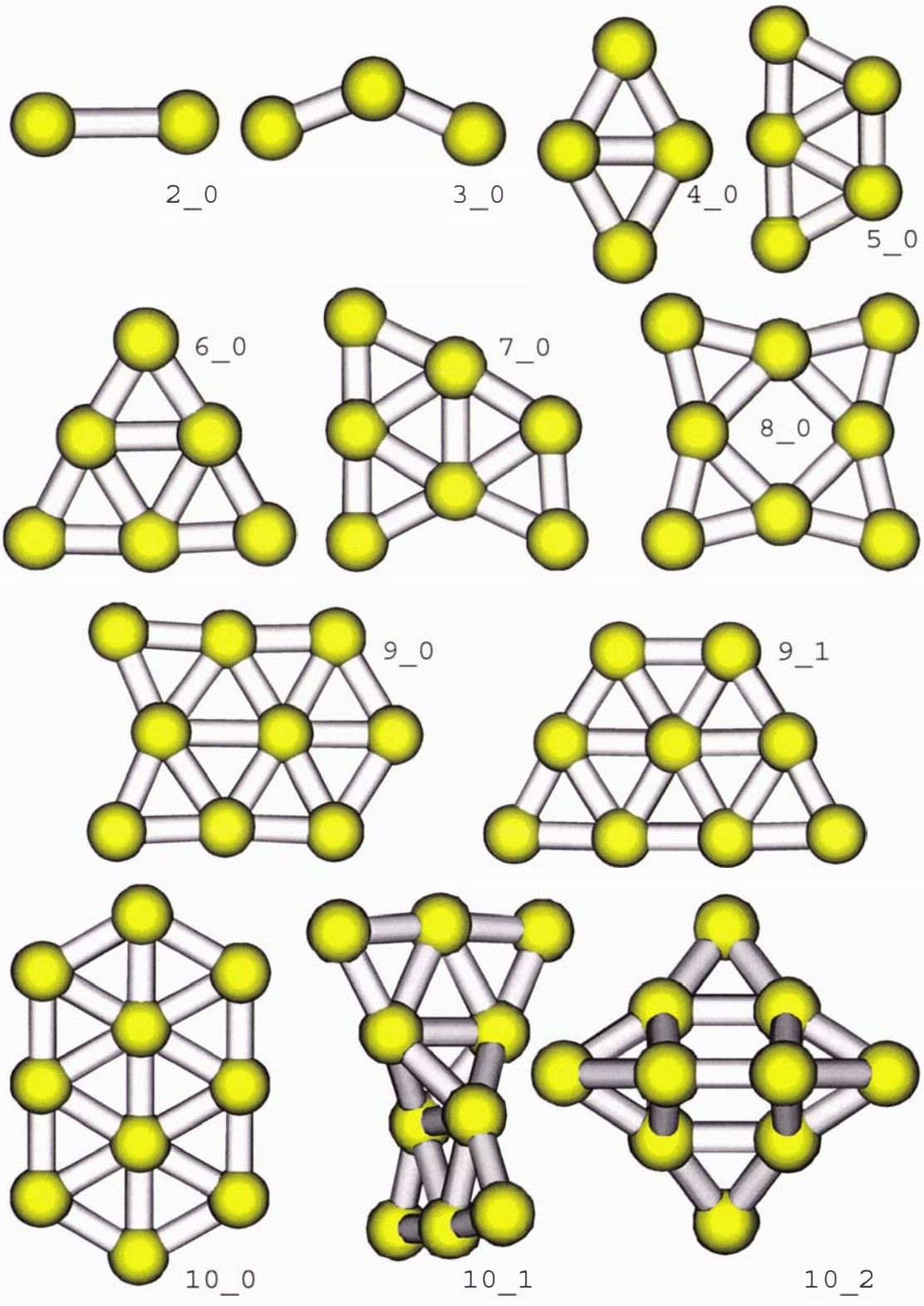

Figure 6.3: Predicted global minima and lowest-energy isomers of Au_{2-10}, ordered (from left to right and top to bottom) by increased size and energy. The cluster n_m is the mth energetic isomer with n atoms.

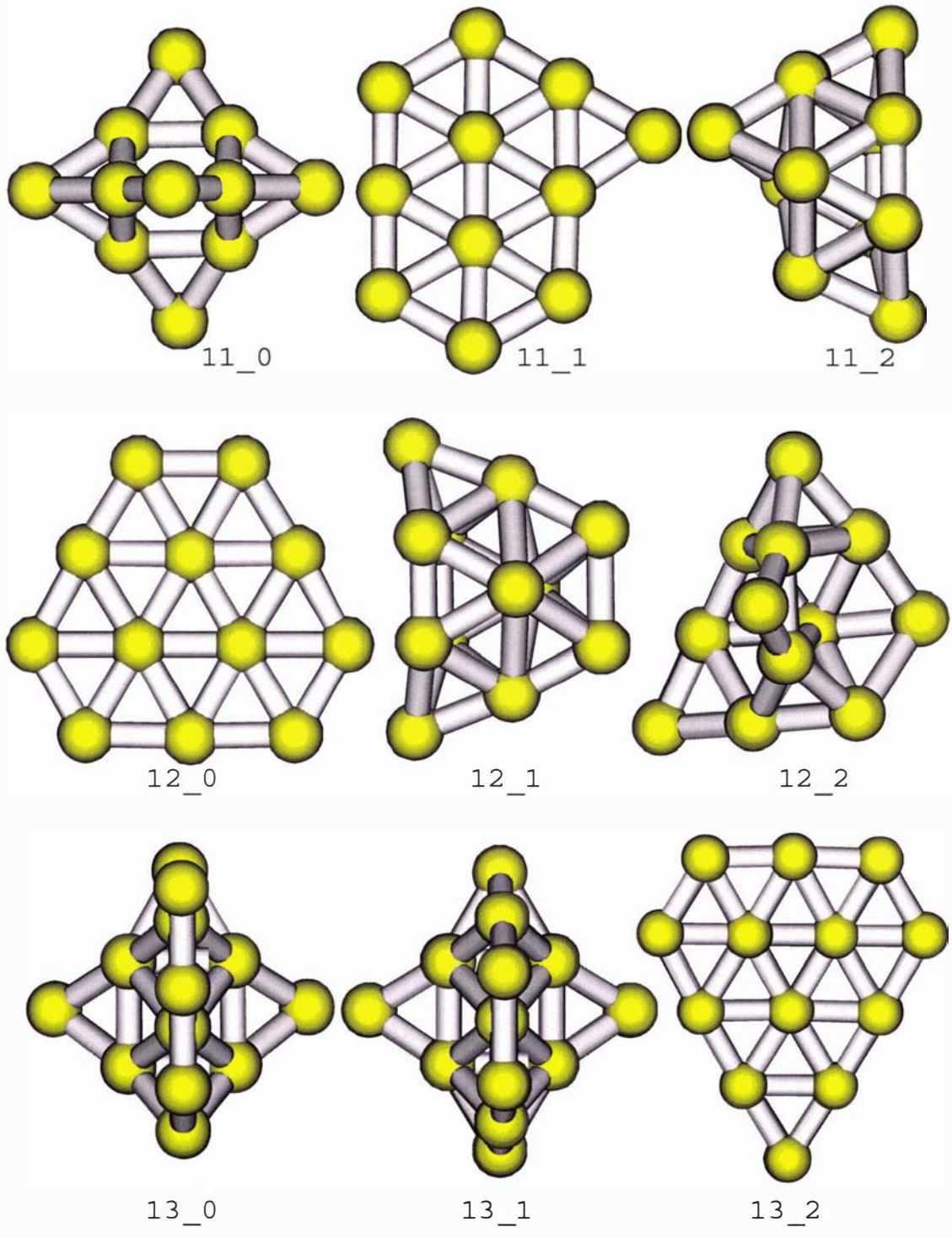

Figure 6.4: Predicted global minima and lowest-energy isomers of Au_{11-13}, ordered (from left to right and top to bottom) by increased size and energy. The cluster n_m is the mth energetic isomer with n atoms.

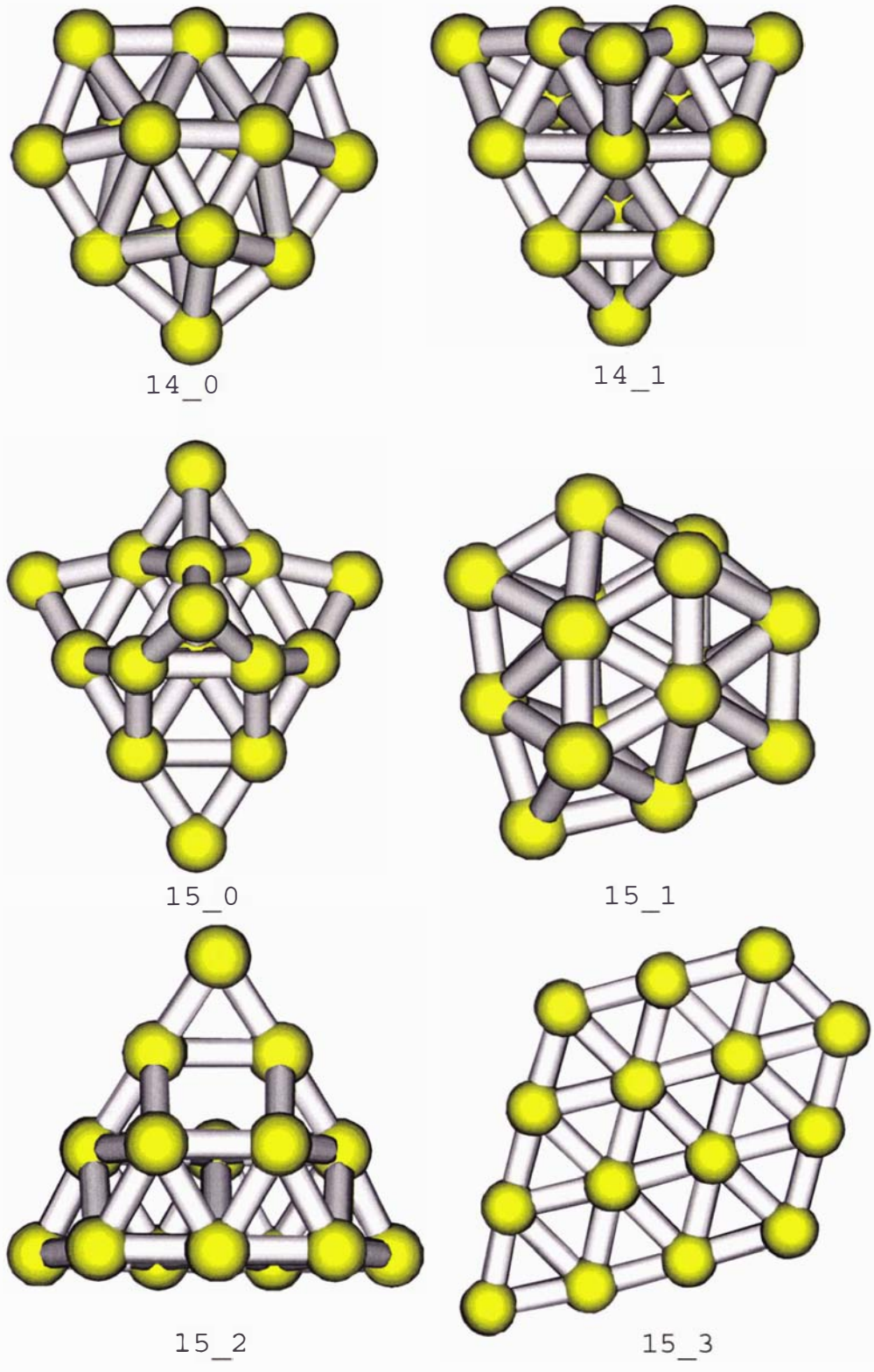

Figure 6.5: Predicted global minima and lowest-energy isomers of Au_{14-15}, ordered (from left to right and top to bottom) by increased size and energy. The cluster n_m is the mth energetic isomer with n atoms.

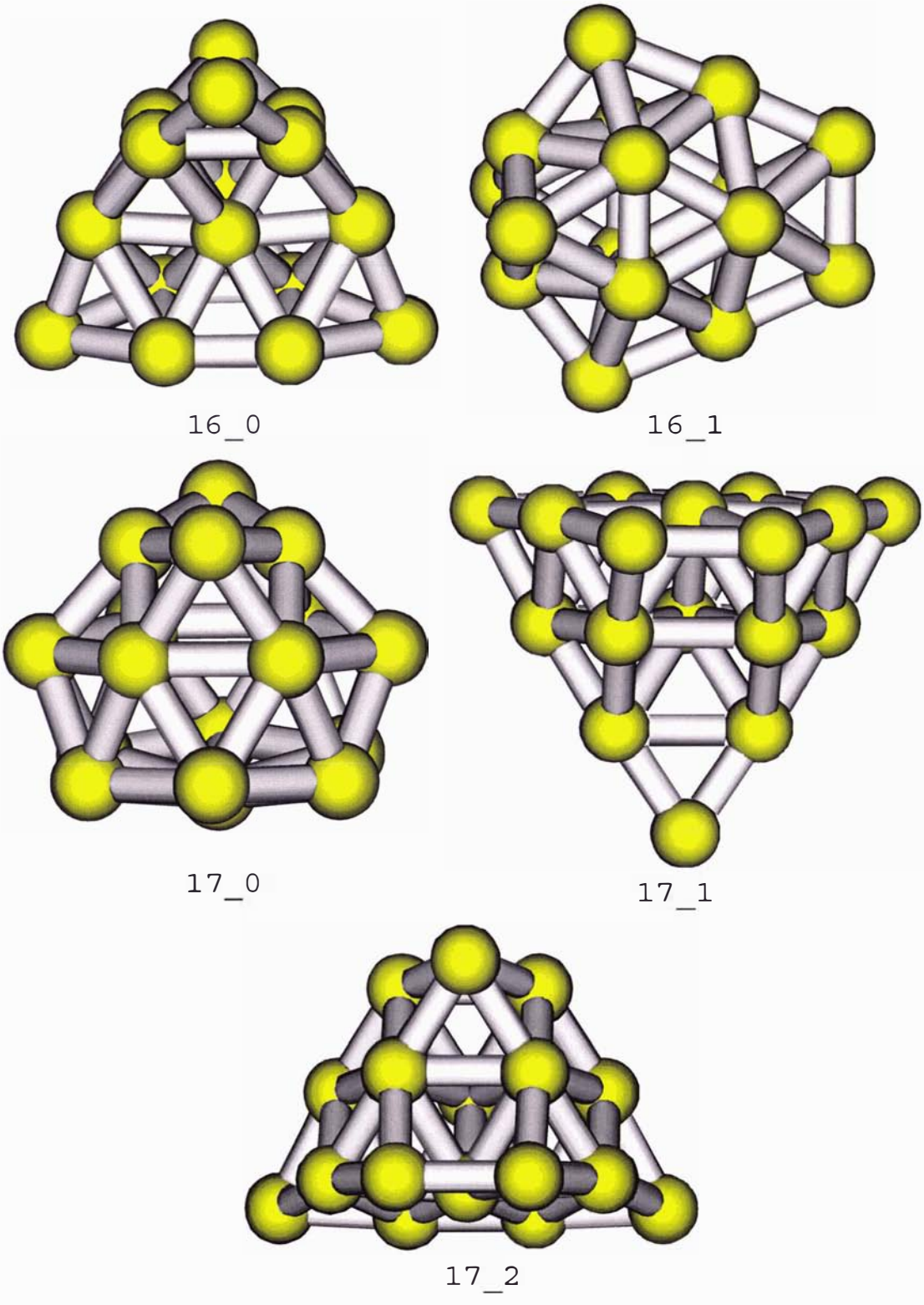

Figure 6.6: Predicted global minima and lowest-energy isomers of Au_{16-17}, ordered (from left to right and top to bottom) by increased size and energy. The cluster n_m is the mth energetic isomer with n atoms.

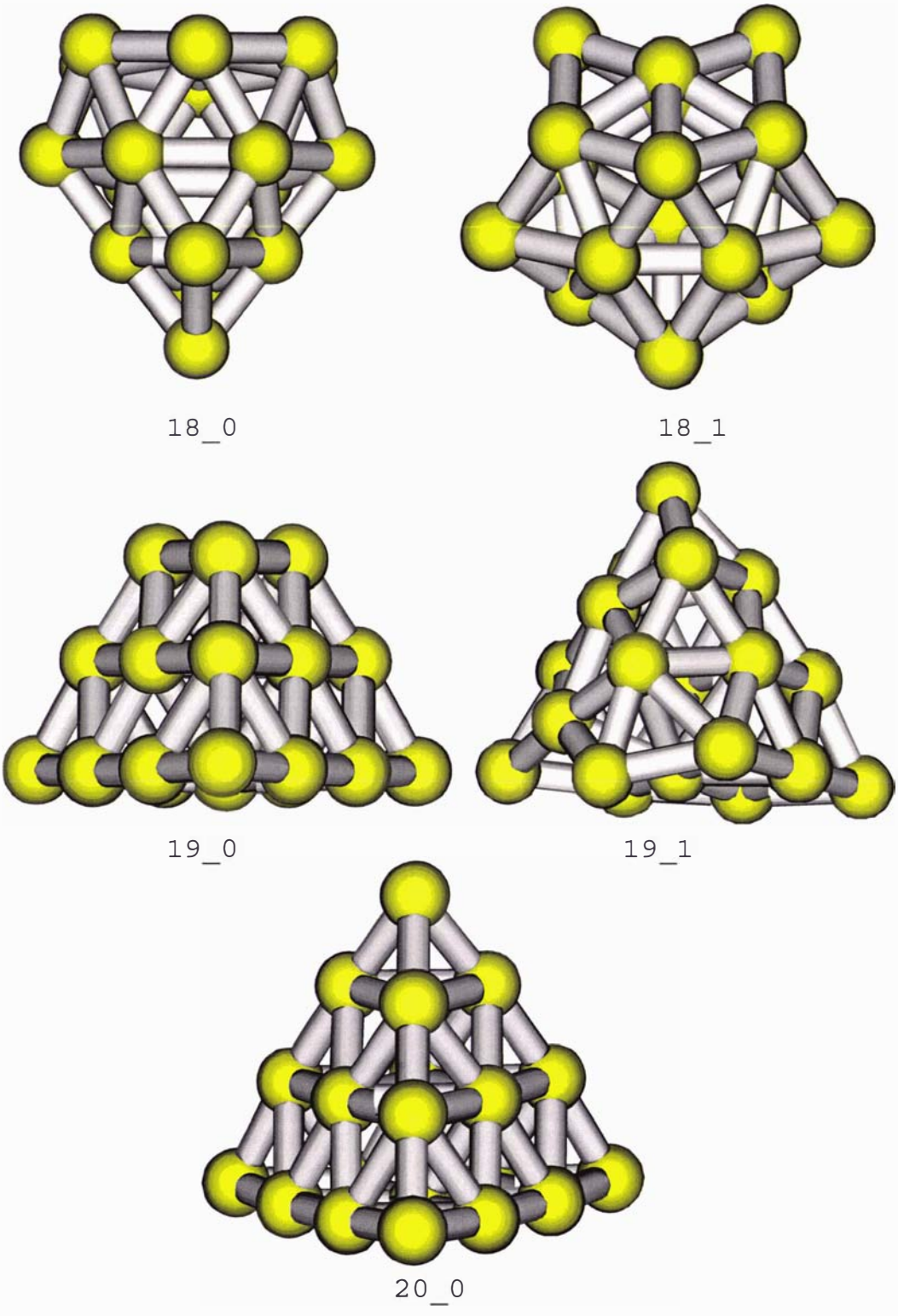

Figure 6.7: Predicted global minima and lowest-energy isomers of Au_{18-20}, ordered (from left to right and top to bottom) by increased size and energy. The cluster n_m is the mth energetic isomer with n atoms.

work. Many isomers for this set of clusters and relative energy differences are reported in the above-mentioned studies and are therefore not discussed here again. The global minimum of the trimer is represented by an obtuse triangle (C_{2v}), a trapezoid (D_{2h}) for the tetramer, a W-shaped structure (C_{2v}) for the pentamer, an isosceles D_{3h} triangle for the hexamer, a capped (C_s) triangle for the heptamer, a tetra-capped (D_{4h}) rhombus for the octamer, a di-capped (C_{2v}) hexagon for the nonamer and a tri-capped (D_{2h}) hexagon for the decamer.

To my best knowledge the three-dimensional structure of Au_{10_1} has never been reported before for the gold decamer and is only 0.049 eV less stable than the two-dimensional structure of Au_{10_0} at the LANL2DZ level. Au_{10_1} is based on two W-shaped pentamer fragments tetrahedrally linked together. Calculations employing the large basis set reveal, however, that Au_{10_1} is less stable than Au_{10_0} by 0.259 eV. Therefore, relative energy differences obtained from LANL2DZ calculations should be regarded as preliminary calculations. A new 3D structure is also found for the undecamer (Au_{11_0}), which is more stable than the 2D Au_{11_1} by 0.267 eV at the LANL2DZ level. The latter isomer is predicted as the most stable undecamer in the above mentioned references (i.e. [231,240,241,245]). This new structure indicates that the transition from planar to three-dimensional structures in neutral gold clusters appears at cluster size Au_{11}, contradicting many recent DFT studies addressing this transition. Wang and coworkers, Xiao and coworkers and Dong and coworkers predict clusters up to 12 atoms to be planar [240, 241, 245], Fernández and coworkers predict clusters up to 13 atoms to adopt planar geometries [231]. Walker, however, who studied structures of neutral and singly positively charged gold clusters up to 9 atoms, predicted the 2D-3D transition based on his findings on positively charged clusters to occur at Au_{11} [239].

For the dodecamer, however, the most stable structure found is again planar. This structure is also predicted as the global minimum by [231,240,245]. A variety of capped versions of the Au_{11_0} isomer were relaxed to their local minima and it was found that they are all less stable than Au_{12_0} by around 0.1 eV. Due to the close structural resemblance between Au_{12_0} and Au_{11_1}, there is some indication that the global minimum of Au_{12} has not been found yet. Au_{13_0} denotes another structure that has not been reported before and is more stable than the planar Au_{13_2} by 0.160 eV at the LANL2DZ level. For the tetradecamer, the same structure as reported by Xiao *et al.* [240] is found. Au_{15_0} has not been reported before either and is more stable than the global minimum predicted

by Zeng *et al.* [243] by merely 0.021 eV[3]. The two lowest-lying isomers for Au_{16} are the ones reported also by Zeng *et al.* [243], but in this work, it is found that Au_{16_0} is more stable than Au_{16_1} by 0.218 eV. Zeng *et al.* report Au_{16_1} as the global minimum and report only are marginal (0.02 eV) relative energy difference between these two structures. The lowest-lying isomers of clusters containing 17 and 18 atoms are the ones reported by Zeng *et al.* [243] and were not found by BELPHEGOR. These isomers are, however, only insignificantly more stable (less than 0.04 eV) than the ones found in this work. The most stable isomer of Au_{19}, also reported by Zeng *et al.*, denotes the tetrahedral Au_{20} structure, lacking one corner atom. Energetically lower-lying isomers of the perfect tetrahedral Au_{20_0} were not found. Isomers of the tetrahedral structure were less stable by at least 0.8 eV at the LANL2DZ level of theory.

6.3.2 Polarizabilities and other Electronic Properties

Results in this work concerning the static response properties in conjunction with some selected electronic properties are collected in table (6.2). Structural properties and vertical ionization potentials and vertical detachment energies are displayed in table (6.1). For reasons of comparison, the atomic and dimeric polarizabilities per atom (in $\text{Å}^3/n$) of the coinage metals are given in the following:

$$Cu_1 = 6.89; \qquad Cu_2 = 7.09$$

$$Ag_1 = 7.78; \qquad Ag_2 = 8.65$$

$$Au_1 = 5.20; \qquad Au_2 = 6.07$$

The atomic values are obtained from R, DKH, CCSD(T) calculations extracted from ref. [7] and the dimeric values from all electron 4-component relativistic Hartree-Fock calculations from ref. [266]. The smaller polarizabilities per atom of gold in comparison to silver are attributed to the enhanced screening of the s electrons by the d electrons in gold.

Figures (6.8) and (6.9) denote the evolution of the mean dipole polarizability as a function of cluster size. In figure (6.8), the polarizabilities of all gold isomers presented

[3]As highlighted in the case of the decamer, however, calculations employing the large basis and corresponding scalar-relativistic pseudopotential are ultimately inevitable in order to determine the most stable isomer in those cases where the relative energy differences at the LANL2DZ level are rather small.

Table 6.2: Calculated static response and electronic structure properties of DFT-optimized Au_n clusters. The second difference in cluster energy is denoted by $\Delta_2 E_n$ and $\Delta\epsilon$ represents the HOMO-LUMO gap. α_{iso} denotes the mean static polarizability per atom, α_{aniso} the polarizability anisotropy per atom and μ the absolute value of the dipole moment. The notation $/n$ implies the value is given per atom. Values in parenthesis are obtained from LANL2DZ and those without from large basis set calculations. The b3pw91 functional is used throughout.

Cluster	$\Delta_2 E_n$ (eV)	$\Delta\epsilon$ (eV)	α_{iso} (Å$^3/n$)	α_{aniso} (Å$^3/n$)	μ (D)	Cluster	$\Delta_2 E_n$ (eV)	$\Delta\epsilon$ (eV)	α_{iso} (Å$^3/n$)	α_{aniso} (Å$^3/n$)	μ (D)
1_0	-	2.290	5.345	0.0	0.0	(11_1)	-	(1.016)	(6.723)	(6.274)	(0.237)
(1_0)	-	(2.172)	(5.648)	(0.0)	(0.0)	(11_2)	-	(1.119)	(5.641)	(3.263)	(1.117)
2_0	0.998	3.476	5.598	3.807	0.0	(12_0)	(0.458)	(1.796)	(6.728)	(6.291)	(0.0)
(2_0)	(0.980)	(3.407)	(5.806)	(4.229)	(0.0)	(12_1)	-	(2.041)	(5.530)	(3.098)	(0.012)
3_0	-1.218	1.515	6.857	7.820	0.370	(12_2)	-	(2.159)	(5.778)	(2.476)	(2.131)
(3_0)	(-1.191)	(1.458)	(7.036)	(8.664)	(0.427)	(12_3)	-	(2.535)	(5.945)	(2.608)	(2.270)
4_0	0.224	2.072	5.951	5.324	0.0	(13_0)	(-0.960)	(0.913)	(6.231)	(1.931)	(1.229)
(4_0)	(0.238)	(2.062)	(5.841)	(5.433)	(0.0)	(13_1)	-	(0.854)	(6.229)	(1.581)	(1.378)
5_0	-0.855	1.450	6.066	4.906	0.070	(13_2)	-	(0.921)	(7.137)	(7.156)	(1.012)
(5_0)	(-0.883)	(1.385)	(5.982)	(5.087)	(0.033)	(14_0)	(0.978)	(2.556)	(5.475)	(3.258)	(0.285)
6_0	1.543	3.445	5.774	3.998	0.0	(14_1)	-	(2.098)	(5.569)	(2.265)	(1.981)
(6_0)	(1.572)	(3.556)	(5.689)	(4.098)	(0.0)	(15_0)	(-0.963)	(0.992)	(5.969)	(2.356)	(2.179)
7_0	-1.309	1.266	6.245	5.353	0.369	(15_1)	- (0.955)	(5.393)	(2.608)	(0.257)	
(7_0)	(-1.354)	(1.233)	(6.204)	(5.567)	(0.387)	(15_2)	-	(0.994)	(5.845)	(3.178)	(1.339)
8_0	1.272	2.870	5.812	4.288	0.0	(15_3)	-	(0.857)	(7.294)	(8.214)	(0.175)
(8_0)	(1.411)	(2.878)	(5.731)	(4.391)	(0.0)	(16_0)	(0.698)	(2.231)	(5.577)	(0.980)	(1.229)
9_0	-1.046	1.136	6.443	5.622	0.216	(16_1)	-	(1.779)	(5.438)	(2.367)	(0.911)
(9_0)	(-1.069)	(1.112)	(6.421)	(5.806)	(0.199)	(16_2)	-	(1.793)	(5.547)	(2.119)	(2.233)
9_1	-	1.167	6.578	6.252	1.132	(17_0)	(-0.634)	(0.892)	(5.088)	(0.285)	(0.898)
(9_1)	-	(1.095)	(6.619)	(6.548)	(1.172)	(17_1)	-	(0.996)	(5.760)	(1.574)	(1.179)
10_0		2.315	6.437	6.112	0.0	(18_0)	(0.082)	(1.933)	(5.165)	(1.111)	(0.278)
(10_0)	(0.475)	(2.357)	(6.469)	(6.384)	(0.0)	(18_1)	-	(1.936)	(5.212)	(1.596)	(0.304)
10_1	-	3.112	6.180	3.363	0.014	(19_0)	(-0.430)	(0.920)	(5.539)	(1.003)	(0.296)
(10_1)	-	(3.199)	(6.092)	(3.328)	(0.020)	(19_1)	-	(0.860)	(5.567)	(1.034)	(0.574)
(10_2)	-	(2.079)	(5.719)	(2.307)	(1.343)	(20_0)	-	(2.911)	(5.535)	(0.0)	(0.0)
(11_0)	(-0.250)	(0.920)	(6.523)	(1.653)	(0.020)						

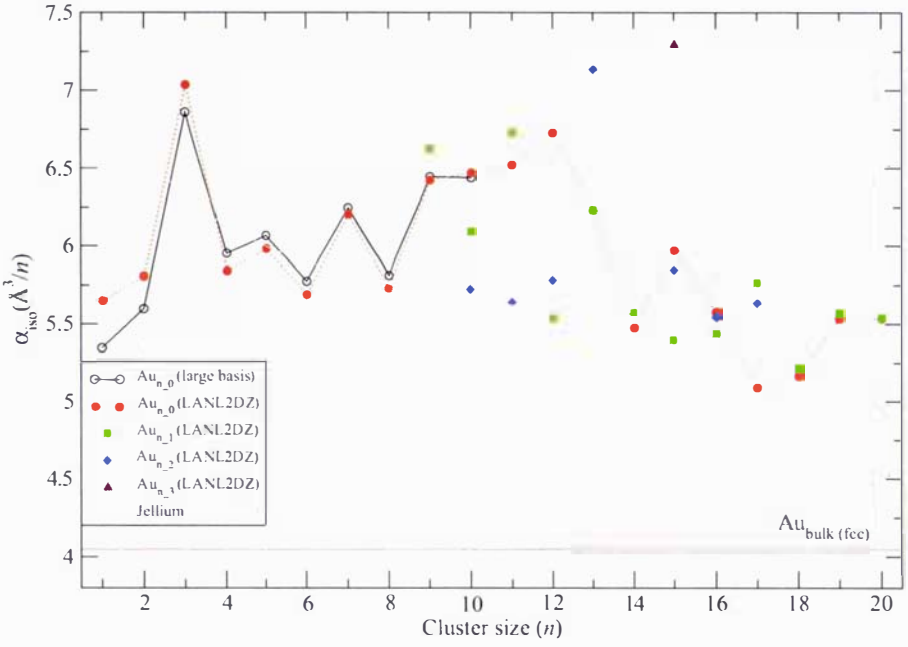

Figure 6.8: Isotropic static electric dipole polarizabilities per atom of Au_n clusters as a function of cluster size compared to the classical values of bulk gold and to the prediction from the jellium model.

here are represented along with the prediction of the jellium model (see equation (4.2)). Bulk gold adopts an *fcc* lattice with parameters $a = 4.0782$ Å and $Z = 4$ atoms per unit cell [116]. Its classical polarizability ($\alpha_{classical} = r_{ws}^3$) can thus be approximated according to:

$$r_{ws}^3 = \frac{a^3}{Z} \cdot \frac{3}{4\pi} = 4.05 \frac{\text{Å}^3}{n}. \tag{6.1}$$

The trend in polarizability per atom is distinctively different from the trends obtained for cesium clusters (see section (4)) and tin clusters (see section (5)). The convergence of the dipole polarizability from above to the approximated bulk value is very slow and displays an alternating behavior, where in most cases the odd-sized clusters exhibit larger α/n than even-sized clusters. Exceptions arise from structural factors. The obtuse triangular structure of Au_3 ($\angle 133.84°$) displays unsurprisingly the largest α/n[4]. One exception to

[4]Note that the spin-orbit effect cancels out the first-order Jahn-Teller effect in Au_3 [270].

the aforementioned odd-even oscillation occurs at Au_{10_0}, where the decamer displays a larger α/n than the nonamer. This is however not surprising, because Au_{10_0} is obtained from prolate capping of Au_{9_0}. Au_{12_0} displays also a larger α/n than its neighboring odd-sized clusters. This is also explained by the fact that the lowest-lying dodecamer isomer is planar, while those for the undecamer and tridecamer adopt three-dimensional structures. The strong dependence of the dipole polarizability on geometric factors is also reflected in the general increasing trend in the α/n from Au_1 to Au_{12} and the general downward trend for the remainder. With the exception of Au_{11}, which denotes a strongly expanded structure, Au_2 to Au_{12} adopt planar structures. From a two-dimensional growth-pattern of a cluster, one would expect a general increase in α/n. A three-dimensional growth-pattern towards more compact structures on the other hand should exhibit a decrease in α/n.

Obviously, the absolute values of the α/n cannot be fitted nicely by a smooth decaying function according to the jellium model (see equation (5.4)). The best fit yields an r_{ws} of 1.65 Å^3 and an electron spill-out (δ) of 0.281 Å^3 and illustrates that the decay to the classical bulk polarizability occurs very slowly. The crystallographically obtained Wigner-Seitz radius is 1.59 Å. However, since δ cannot be measured and the above mentioned jellium fit function contains r_{ws} and δ both as parameters, together with the fact that the absolute values in figure (6.8) are rather widespread, the jellium fit can only be regarded as a rough approximation. Interestingly, the discrepancy between polarizabilities calculated from the LANL2DZ and large basis with respective pseudopotentials decreases towards larger cluster sizes. In the case of the nonamer and decamer, the discrepancy is less than 1%. Diffuse functions, which are missing in the LANL2DZ basis set, become apparently less relevant in the evaluation of polarizabilities of gold clusters with increasing cluster size. This is qualitatively reflected by stabilization of the HOMOs with increasing cluster size.

In figure (6.9), the mean dipole polarizabilities per atom of the predicted global minima from this work are compared to previously reported values by Wang *et al.* [245], Fernández *et al.* [232], Hou *et al.* [230] and Jellinek *et al.* [246]. α/n from this work are in excellent agreement with those from Wang *et al.*, who obtained the polarizabilities from LANL2DZ calculations, up to cluster size 11. However, they report Au_{11_1} as the global minimum for the undecamer. In this work, Au_{11_0} yields an α/n which is 0.2 Å^3 larger than that of Au_{11_1}. For the dodecamer, the discrepancy is again due to the different assignment

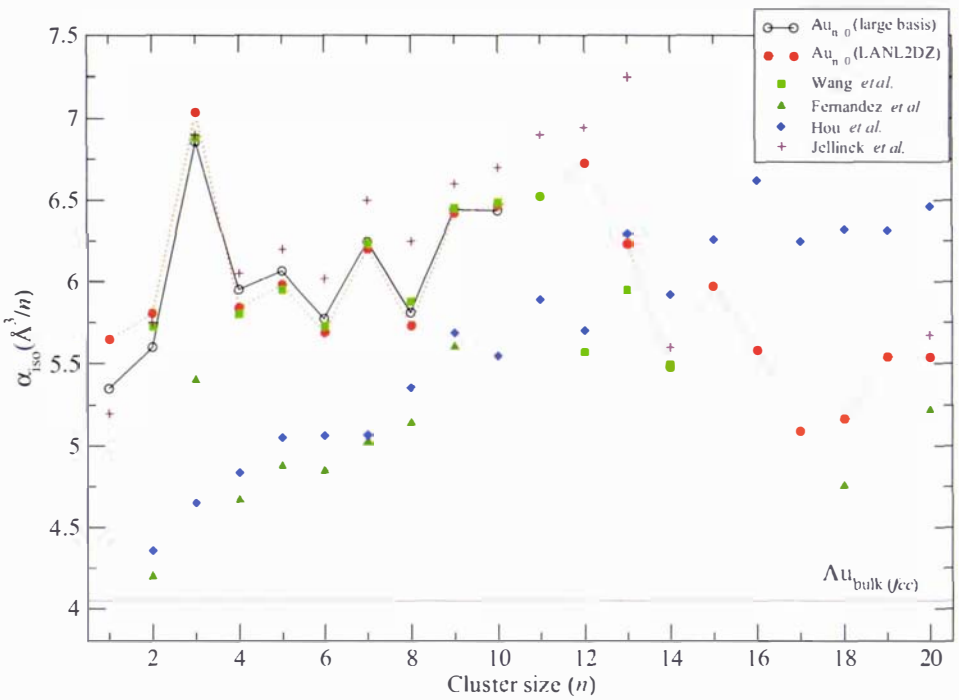

Figure 6.9: Isotropic static electric dipole polarizabilities per atom of Au_{n_0} clusters as a function of cluster size compared to the classical value of bulk gold and to previously reported values by Wang *et al.* [245], Fernández *et al.* [232], Hou *et al.* [230] and Jellinek *et al.* [246].

of the global minimum. Wang *et al.* find Au_{12_1} to be the global minimum and Au_{12_0} the energetically closest-lying isomer with a relative energy difference of 0.022 eV. In this work, the α/n of Au_{12_1} is 5.530 A^3, which is essentially the value as reported by Wang. For the tridecamer, the discrepancy is again due to the different assignment of the global minimum. In the case of the tetradecamer, the same structures are found for the global minimum in this and Wang's work, and the agreement is excellent. Good agreement is also found with the polarizabilities per atom published by Jellinek *et al.* [246], who have employed a finite field method based on LDA and GGA DFT using a large core pseudopotential and double-zeta valence basis set with diffuse *d*-functions. Although the absolute values of α/n reported in ref. [246] are slightly larger than the ones obtained in

this work, the general trend is very similar. Exceptions are the Au_{11} and Au_{13} clusters and result from the fact that more stable, three-dimensional isomers were found in this work. The most stable isomer in ref. [246] for the undecamer is the planar structure denoted as Au_{11_1} in this work and gives proportionally a larger α/n than the more stable three-dimensional isomer Au_{11_0}. The same holds for Au_{13}, where the most stable isomer found in ref. [246] is the planar structure denoted as Au_{13_2}.

In conclusion, this work confirms the absolute values of mean polarizabilities per atom together with their oscillating and general trend as a function of cluster size found by Wang and coworkers, and improves on their results, as lower-lying isomers have been found, larger cluster sizes were considered and a much more extensive basis set and corresponding pseudopotential was employed. This work also agrees nicely with the absolute values and general trend of α/n reported by Jellinek and coworkers. Fernández *et al.* [232] calculated the mean polarizabilities of gold clusters Au_n $(n = 2 - 9, 18, 20)$, within the finite-field approximation, employing a plane-wave, double-zeta valence basis set and a norm-conserving scalar-relativistic pseudopotential at the density functional level of theory. Although they studied the same global minima structures up to Au_9 as presented in this work, they obtain much smaller α/n and report a strong increasing trend with much less pronounced odd-even oscillation. Fernández and coworkers employed a large core pseudopotential, leaving apparently 11 valence electrons $5d^{10}6s^1$ [232]. This could perhaps lead to systematic errors in the absolute values of the dipole polarizability but does not explain the pronounced increasing trend they report. The deviations in α/n from this work and that of Fernández and coworkers become, however, smaller as the cluster size increases. They also acknowledge that their calculated mean polarizability of atomic gold is, within their applied method, smaller than the most precise relativistic all-electron CCSD(T) calculation within the framework of a Douglas-Kroll-Hess (DKH) transformation [276] by ca. 43%. Hou and coworkers [230], studied the mean polarizability per atom of planar gold clusters up to 20 atoms, from DFT calculations employing an all-electron scalar-relativistic corrected basis set. Their values are in good agreement with those by Fernández *et al.* up to Au_9. They also observe an odd-even oscillation, which is, however, less pronounced as presented in this work, and yield increasing α/n with increasing cluster size. This is not surprising, however, as Hou *et al.* only studied planar structures which also explains why they obtain much higher α/n for Au_{18} and Au_{20} than Fernández *et al.* Relativistic all-electron CCSD(T) calculations within the

DKH transformation represent quantum mechanical calculations at the highest, feasible, level of theory and therefore are accepted as the most accurate evaluation of structural and electronic properties of clusters. The fact that relativistic CCSD(T) calculations, either within the DKH transformation or in combination with pseudopotentials, represent benchmark calculations for atomic polarizabilities is for instance nicely illustrated in ref. [7], where atomic polarizabilities of 119 elements are tabulated along with levels of theory employed. Since CCSD(T) calculations are not feasible even for the small cluster sizes presented in this work, a DFT approach is inevitable. However, it is assumed that calculated atomic polarizabilities at the DFT level of theory should resemble those at the CCSD(T) level of theory.

The anisotropy per atom (α_{aniso}) to the dipole polarizability is plotted against the cluster size in figure (6.10). Clusters up to the decamer and the dodecamer reveal large anisotropies per atom. These are in general almost as large as the isotropic polarizability itself and result from the high stability of planar structures. The predicted transition from planar to three-dimensional structures at the undecamer is reflected by a strong decrease in α_{aniso}.[5] Moreover, the general decreasing trend in α_{aniso} for clusters $12 \leq n \leq 20$ gives some indication that the evolution of gold clusters tends towards more compact and more spherically shaped clusters towards the solid state. This trend is, however, not as marked as in the case for cesium clusters (see section (4)). The calculated atomic electron affinities and ionization potentials as a function of DFT exchange-correlation functionals are depicted in figure (6.11) and compared to experimental values [116]. The b3pw91 functional[6], which was used for all gold cluster calculations, underestimates the EA by about 10 % and overestimates the IP by circa 1.5 %. Calculated vertical ionization potentials (VIPs) and vertical electron affinities (VEAs) from large basis set and LANL2DZ calculations are plotted against the cluster size $n^{-1/3}$ and compared to experimentally observed IPs and EAs in figure (6.12). A distinct odd-even oscillation is observed in both cases, where the even-sized clusters exhibit larger IPs and smaller EAs, which is due to the spin-pairing effect. The only exception is for the VIP of Au_3. LANL2DZ calculations overestimate the VIPs and VEAs slightly compared to larger basis set calculations. The agreement with experimental values is good for the IPs and slightly better for the EAs.

[5] As aforementioned, an energetically lower-lying three-dimensional isomer of the planar Au_{12-0} was not found.

[6] The choice of the b3pw91 functional is not founded on the reproduction of the experimental ionization potential and electron affinity, but on the polarizability of the ground state gold atom.

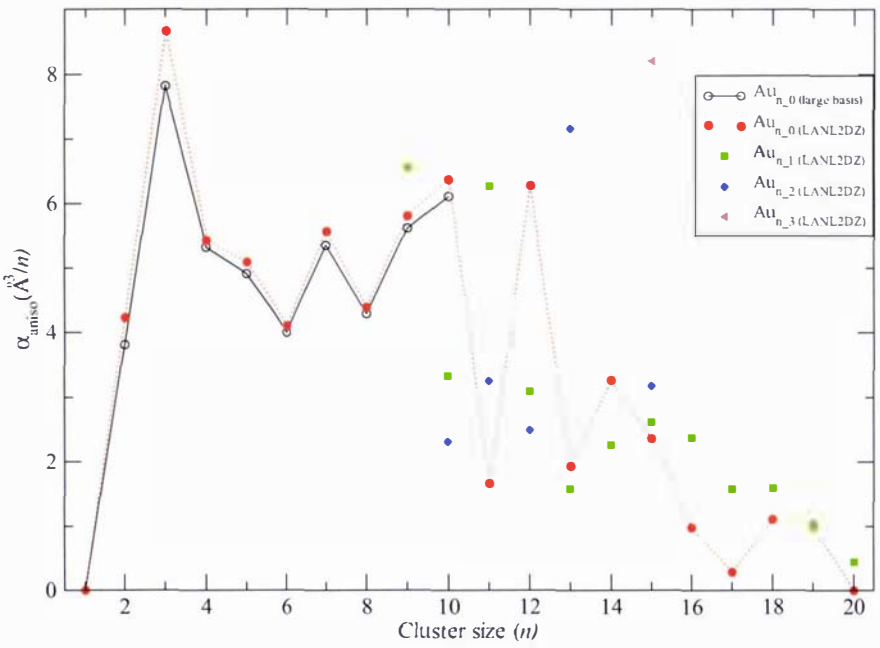

Figure 6.10: Anisotropy per atom to the static electric dipole polarizability, according to equation (1.56), as a function of cluster size.

Linear regressions fitted to the values calculated with the large basis, i.e. Au_{1-10}, according to $G(n) = A_0 x + 5.38$, where 5.38 eV denotes the average workfunction of solid gold [116], yield satisfying agreement to the data. For the VIPs it is seen that the extrapolation of the cluster data converges nicely to the workfunction of bulk gold, while a linear fit of the experimentally observed IPs would not converge that nicely. The opposite situation is evident in the VEAs case. It must be noted, however, that since experimentally obtained electronic workfunctions of bulk metals are dependent on the cleanliness of the bulk surface, on the surface plane and the type of experiment, measurements reported in the literature often cover a considerable range. In the case of bulk gold, 5.47 eV, 5,37 eV and 5.31 eV are reported for photoelectric measurements of the 100, 110 and 111 bulk plane, respectively [116].

Both the second difference of the cluster energies $\Delta_2 E(n)$ (see figure (6.13)) and the HOMO-LUMO gaps $\Delta\epsilon(n)$ (see figure (6.14)) exhibit odd-even oscillations, indicating

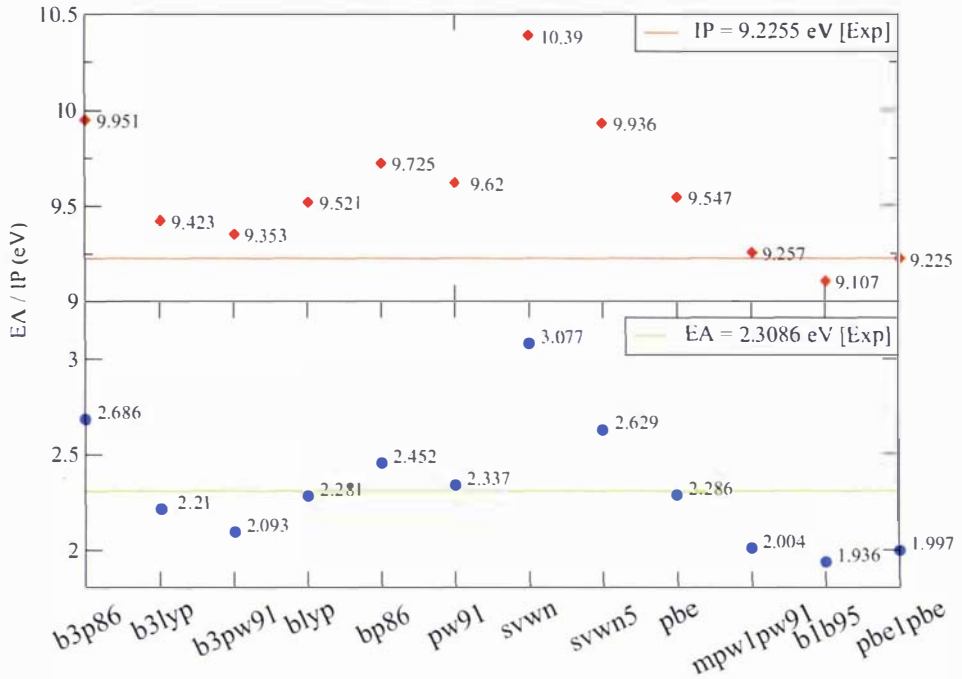

Figure 6.11: Ionization potentials and electron affinities of the ground state gold atom in eV as a function of DFT exchange-correlation functionals and compared to experimental values [116].

that the even-numbered clusters are bound more strongly and are relatively more stable than their odd-numbered neighbors. This alternation is due to the spin-pairing effect and is also found in Ag, Cu and alkali metal clusters. Since the coinage metal atoms Cu, Ag, and Au possess filled d-shells, they display electronic structures determined in a large part by the half-filled bands of nearly free s electrons. Thus, it is not surprising that coinage metal clusters exhibit size dependencies in physical properties (i.e. IP, EA, $\Delta_2 E$, $\Delta\epsilon$) that are similar to those observed in alkali metal clusters, and are thus more akin to alkali clusters than open d-shell transition element clusters [49] (see also section (4.3.2)).

The even-odd oscillation is, however, much more pronounced in gold clusters as in cesium clusters. Every even-sized gold cluster would be classified as a magic cluster as they all exhibit second difference cluster energies larger than zero. Therefore, the electron shell filling observed for alkali metal clusters (i.e. M_2, M_8, M_{18}, where M represents an

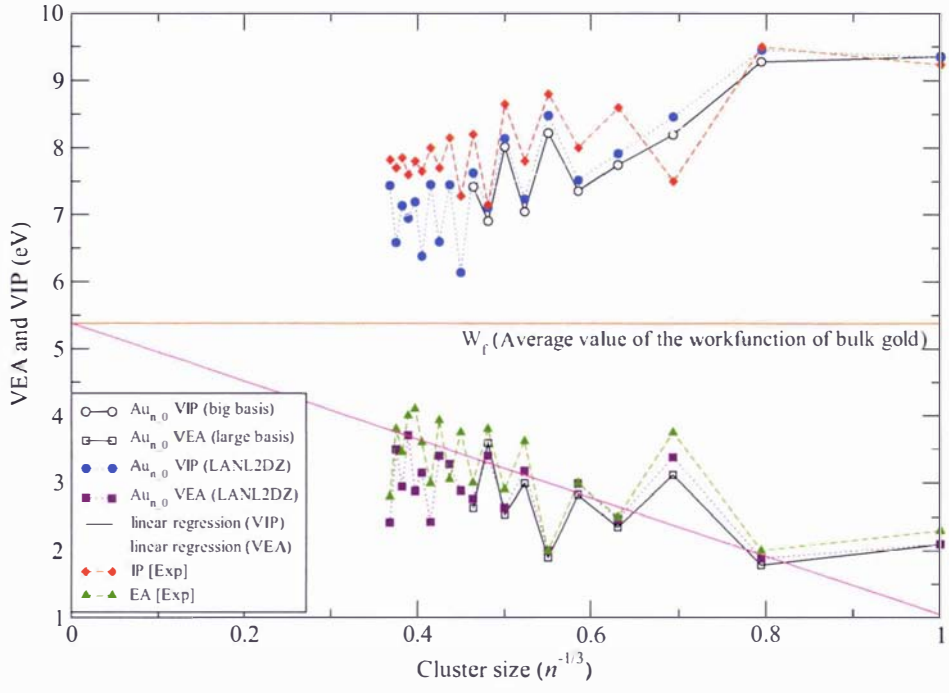

Figure 6.12: Vertical electron affinities and vertical ionization potentials of gold clusters as a function of cluster size ($n^{-1/3}$). The evolution of both properties is approximated by a linear regression according to $G(n) = 4.15x + 5.38$ and $G(n) = -4.33x + 5.38$, where 5.38 eV denotes the average workfunction of bulk gold [116]. Open symbols denote calculations from the large basis set [274] and filled symbols calculations from LANL2DZ. Experimental IP are extracted form [213] and experimental EA from [250] (see text for details).

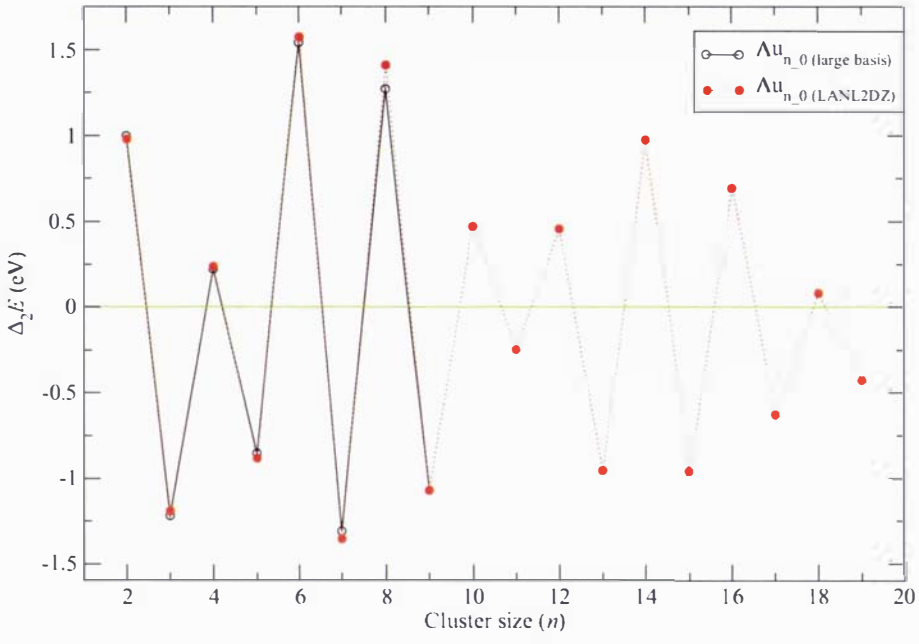

Figure 6.13: Second difference in the Au cluster energy as a function of cluster size n as denoted in equation (4.4).

alkali metal) [48], is less pronounced in gold clusters than in cesium clusters for instance. Au_2, Au_6, Au_8, Au_{14} and Au_{20} exhibit rather large HOMO-LUMO gaps, which coincide with rather large peaks in the second difference of the energies for these cluster sizes. Interestingly, the three dimensional Au_{10_1} isomer exhibits a $\Delta\epsilon$ gap, which is 0.83 eV larger than that of the planar Au_{10_0} isomer. Less pronounced, but still significantly stronger bound are also the three-dimensional Au_{12_1} and Au_{12_2} compared to the planar Au_{12_0} isomer. The discrepancies for $\Delta_2 E$ and $\Delta\epsilon$ with respect to calculations at the LANL2DZ and STUTTGART level of theory for the available data is less than 2%.

In figure (6.15), the nearest-neighbor bond lengths of all presented gold clusters are plotted against the cluster size. Nearest-neighbor distances exclude surface effects, which play a major role in clusters. For instance, all atoms in Au_{20_0} are located on the surface, and allow for a comparison with the nearest-neighbor distance in the *fcc* bulk gold (2.884 Å) [116]. Calculations at the LANL2DZ level of theory overestimate the nearest-neighbor

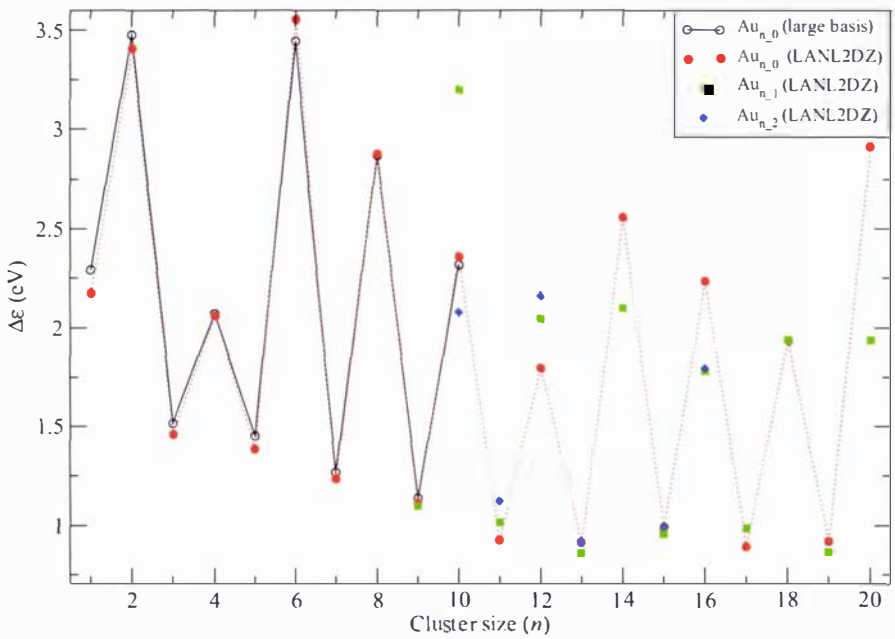

Figure 6.14: Calculated HOMO-LUMO gaps of gold clusters versus the cluster size n.

and average bond lengths (see also table (6.1)) by about 2%. The calculated dimer bond length (2.519 Å) is in good agreement with the experimental bond length (2.472 Å) [116].

Plotting the cohesive energy as a function of cluster size to the power of $(n^{-1/3})$ allows for fitting of the data towards bulk gold (figure (6.16)). Calculations from LANL2DZ give smaller cohesive energies than from the large basis by about 8%. Extrapolation of the large basis data yields a bulk cohesive energy of 3.47 eV, which is in good agreement with the observed one of 3.8 eV [278]. The extrapolation of the cohesive energies per atom obtained from the large basis is at this stage insufficient, as a change in the slope of the linear regression is expected for the transition from 2D to 3D structures. A significant decrease in this slope, which does not coincide sharply with the onset of the 2D-3D transition, is obtained in the cases of cesium (see figure (4.18)) and tin (see figure (5.17)). Interestingly, in the case of gold, an *increase* in the slope is apparent in the LANL2DZ data starting at Au_{15}. Cohesive energies obtained from the large basis are needed for the larger cluster sizes in order to address this point further. It should be noted, that

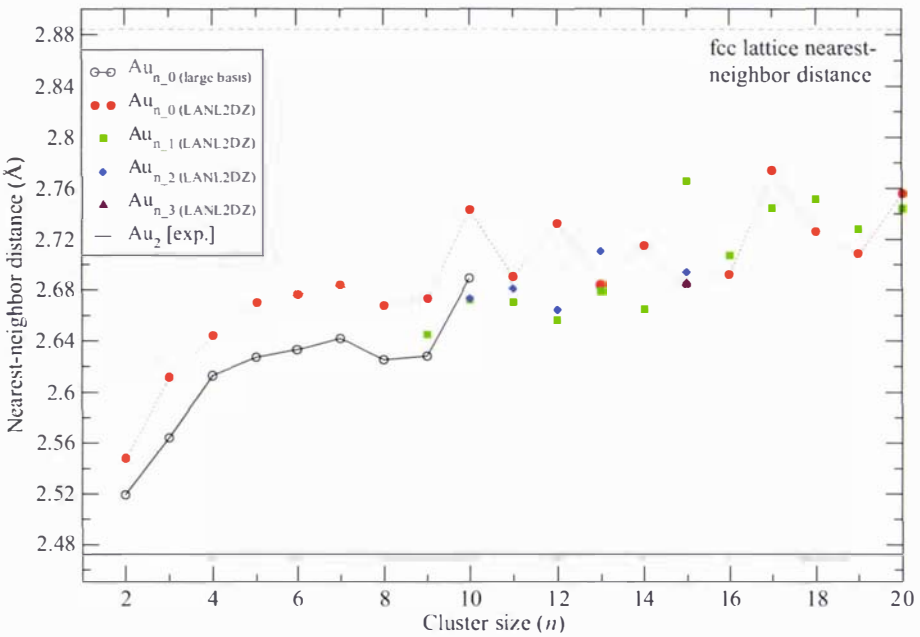

Figure 6.15: Nearest-neighbor distances in gold clusters plotted against the cluster size n. The solid line represents the experimental gold dimer bond length (2.472 Å [261]) and the dashed line symbolizes the experimental value for the shortest equilibrium interatomic distances in bulk gold (2.88 Å) [116]

different DFT functionals characterize the binding situations differently and hence result in quite different cohesive energies. Calculated cohesive energies of bulk gold within the framework of DFT yield values around 3.2 eV [279]. In that reference it is also noted that the discrepancy from experiment may be attributed to a general deficiency of DFT in describing the bulk cohesive energies. In figure (6.17), the calculated zero-point vibrational energies (ZPVE) per atom are plotted against the cluster size to the power of $(n^{-1/3})$ and fitted linearly. This approach estimates the ZPVE per atom of bulk gold to be 0.024 eV/n, which is unknown experimentally.

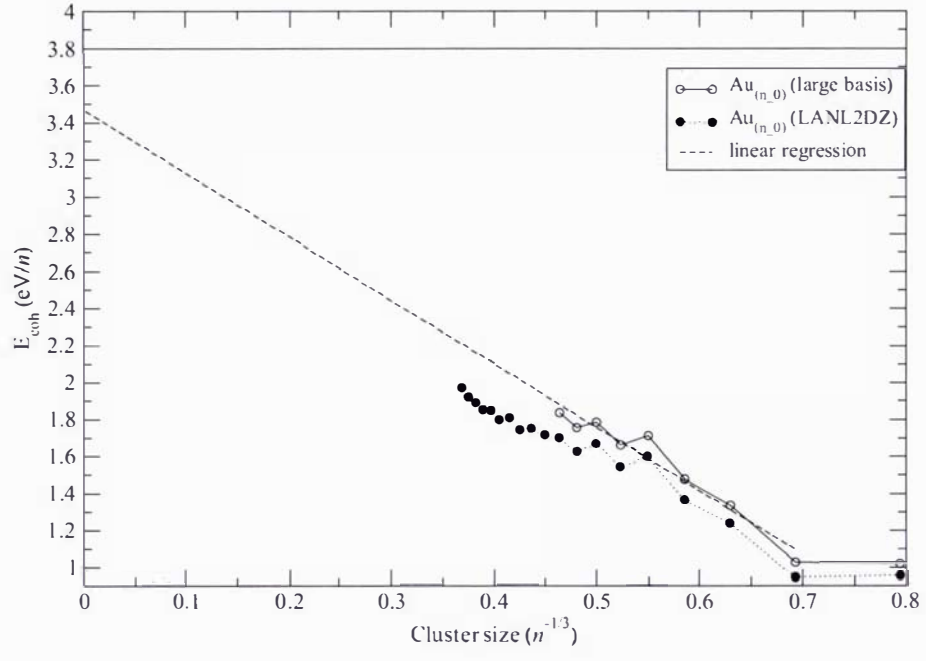

Figure 6.16: Calculated cohesive energies of gold clusters as a function of cluster size to the power of $(n^{-1/3})$. The experimental cohesive energy of bulk gold is reported to be 3.8 eV [278].

6.4 Conclusions

Within a unique genetic algorithm approach, a systematic search for the energetically lowest-lying low-spin gold cluster isomers up to 20 atoms was undertaken. A number of previously predicted global minima structures are reconfirmed, while more stable isomers are found for Au_{11}, Au_{13} and Au_{15}. The structure of the undecamer throws new light into the discussion of the onset of the transition from planar to three-dimensional structures. At the LANL2DZ level, previously reported planar undecamers are less stable than the three-dimensional structure presented in this work by at least 0.25 eV, indicating that three-dimensional structures in neutral gold clusters are more stable than planar ones from the undecamer onwards. Previous DFT studies on this matter claimed this transition to occur at Au_{13} or at an even larger cluster size. Therefore, it may be that the planar

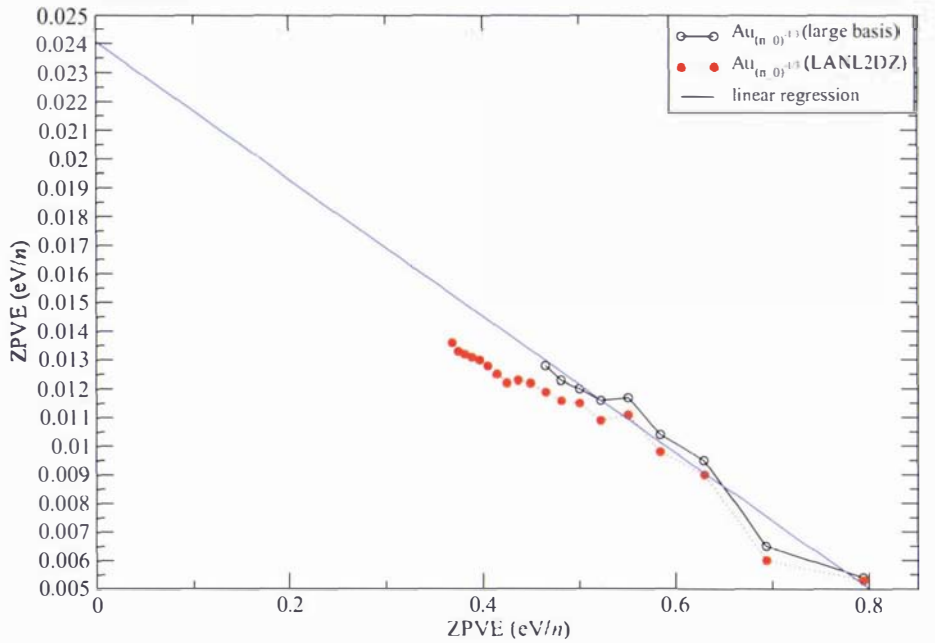

Figure 6.17: Calculated zero-point vibrational energies (ZPVE) per atom of gold clusters as a function of cluster size to the power of $(n^{-1/3})$. The solid line represents a linear regression towards the bulk limit.

Au_{12_0}, which is also the most stable isomer found in previous studies, is not the global minimum of the dodecamer. With increasing size, the three-dimensional clusters evolve to more compact structures. Electronic properties, such as the VEA, VIP, $\Delta_2 E$, E_{coh} and $\Delta\epsilon$ show a distinct odd-even oscillation reflecting the spin-pairing effect (i.e. reflecting the electronic configuration of gold $[Xe]4f^{14}5d^{10}6s^1$). This alternation is so strong, that the electronic shell filling effect is disguised in the $\Delta_2 E$ spectrum. With respect to dipole polarizabilities, this work improves on previous studies since a larger range of clusters were studied and the atomic polarizability of gold was evaluated within the DFT framework in excellent agreement with relativistic all-electron CCSD(T) calculations. Interestingly, the strong odd-even oscillation of electronic properties in small, neutral gold clusters is also apparent in the evolution of polarizabilities per atom as a function of cluster size. Odd-sized clusters, i.e. doublet spin-state, show in general significantly larger polarizabilities

than even-sized clusters. A convergence towards the classical bulk polarizability is not yet evident for the cluster sizes presented in this work.

6.5 Further Work

Final structural optimizations and calculations of electronic properties with the large basis for Au_{11} - Au_{20} are pending and are needed to assign the most stable isomers for this set of clusters. Although it is not expected that calculations from the large basis will yield significantly different results than from the LANL2DZ basis, they are more accurate and are also needed for a better extrapolation of electronic properties towards the bulk limit. Furthermore, it is assumed that the presented lowest-lying isomer of the dodecamer is not the global minimum and further evaluations from BELPHEGOR should be undertaken.

Chapter 7

Copper Nonamer Clusters

7.1 Motivation

The determination of the structure and properties of transition metal clusters has received considerable attention, both theoretically and experimentally, because of the importance of such clusters in nano-science and their potential use as catalysts [1,36,37,203]. Particularly the electric dipole moment and polarizability are interesting properties to consider, as they provide a characterization of the electronic structure, and they can be probed by experiment.

Since the coinage metal atoms (Cu, Ag, and Au) possess filled d shells, they display electronic structures determined in a large part by the half-filled bands of nearly free s electrons. Thus, it is not surprising that coinage metal clusters exhibit size dependencies in some physical properties that are similar to those observed in alkali metal clusters (see section (6.1)) and are thus more akin to alkali clusters than open d-shell transition element clusters. For instance, an odd-even alternation is observed for experimentally observed ionization potentials of clusters up to 114 atoms, together with large decreases in the ionization potential (IP) corresponding to electronic shell and subshell closings predicted for systems of n valence electrons confined to a spherical or spheroidal potential [280].

For neutral and ionized copper clusters in particular, there are many theoretical investigations of the geometrical and electronic structure [281–296][1]. In a recent experimental beam deflection study of neutral Cu_n clusters with $9 \leq n \leq 61$, Knickelbein [297] observed a polarizability per atom for Cu_9 (16.2 ± 0.8 Å^3), more than than three times

[1] And references therein.

larger than the one predicted by density functional theory calculations (4.9 $Å^3$) [288]. This discrepancy is surprising since the theoretical approach presented in [288] predicts polarizabilities for realistic, geometry-optimized alkali clusters that are similar to those experimentally measured, indicating that effects of the electron spill-out are accurately accounted for by the DFT approach [297].

As aforementioned, one expects Cu, Ag and Au clusters to have properties that are similar to those of alkali metals. The experimental polarizability values for the smaller Cu clusters in this size range lie significantly higher than the classical predictions for conducting ellipsoids, and convergence to the classical predictions is only achieved for $n \geq 45$ [297]. However, as Knickelbein points out, within the weak-field limit ($\mu_0 F \ll k_B T_{rot}$, where F denotes the electric field, k_B is Boltzmann's constant and T_{rot} the rotational temperature), the experimentally measured "effective" polarizabilities represent an upper limit to the electronic polarizability as the permanent dipole moment contributes to the effective polarizability in a way that depends on temperature (see equation(5.5)). Knickelbein did not state sufficiently enough, if he observed any symmetric broadening of the molecular beam spatial profiles upon application of the deflection field, from which the dipole moment can be evaluated, but stresses that the rotational temperatures remain intractable.

Jackson *et al.* [293] calculated polarizabilities of copper clusters consisting of up to 32 atoms from all-electron calculations using a small basis set (7s5p4d) and employing the pbepbe functional. They also found a large discrepancy with experiment and confirmed the α/n values from ref. [288]. In addition they obtained good agreement with the predictions of the classical model already at cluster sizes as small as six atoms. Furthermore, they tested their DFT approach against wavefunction based theories and tested basis set and electron correlation effects at different geometries for smaller copper clusters. They found that these effects are too small to account for the aforementioned discrepancy. They conclude, however, that according to equation (5.5), low rotational temperatures combined with non-negligible permanent dipole moments can in some cases explain the observed difference between theory and experiment.

The motivation of this work was to find the global minimum of Cu_9, i.e. testing the efficiency of the genetic algorithm BELPHEGOR, and to calculate accurately the static electric dipole polarizabilities and dipole moments of the respective isomers from density functional methods utilizing a large basis set. Dipole moments and polarizabilities strongly depend on the geometric structure and the delocalization of the valence electrons.

None of the aforementioned studies systematically searched for the ground state structures employing DFT or *ab initio* approaches. Furthermore, in order to exclude that the discrepancy between experimentally and theoretically obtained polarizabilities is due to the use of too small basis sets, an extensive valence basis set (10s10p8d3f2g) (see section (7.2)), which is considerably larger than any basis set utilized for copper clusters so far, was employed.

7.2 Methods

The global minimum and energetically lowest-lying isomers of copper nonamer clusters were obtained utilizing the genetic algorithm code BELPHEGOR as described in detail in section (3.1). The initial population consisted of ten random structures, the Lennard-Jones global minimum structure, predicted global minima and energetically low-lying isomers of Cs_9, Sn_9 and Au_9 and predicted global minima from the literature [281, 290, 291, 293–295], giving rise to 23 different initial geometries. The minimum energy difference δV_i was set to 0.002 eV, d_{min} and d_{max} parameters were fixed at 2.0 and 3.3 Å, respectively. The termination criteria for BELPHEGOR was 200 mating and local minimization steps. The mutation probability was first set to 10 % and then increased to 20 % for the last 80 mating steps. The energetically lowest-lying three- and two-dimensional isomers were then further optimized from LANL2DZ basis set and pseudopotential calculations.

From this set of structures, the six energetically lowest-lying isomers and one planar isomer were further optimized using the extensive STUTTGART valence basis set together with the energy-consistent relativistic pseudopotential for copper [298]. Finally, a harmonic vibrational analysis was performed for all isomers in order to discriminate between minima and transition states on the potential energy surface. All calculations were performed with the GAUSSIAN03 program package [331]. For the exchange-correlation potential, the generalized gradient approximation, according to the parameterization suggested by Perdew, Burke and Erzenhof [299] (pbe1pbe), was applied in a self-consistent fashion. No symmetry constraints were applied during the optimization procedure.

The most accurate evaluations of the static electric dipole polarizability published for the copper atom are 6.67 $Å^3$ [7, 302] and 6.89 $Å^3$ [303], where the former is obtained from relativistic pseudopotential QCISD(T) calculations and the latter from relativistic all electron CCSD(T) calculations within the DKH transformation, respectively. In figure

(7.1), calculated polarizabilities from different DFT functionals, comprising different exchange and correlation functions such as b3p86, b3lyp, b3pw91, blyp, bp86, pw91, svwn, svwn5, pbe, mpw1pw91, b1b95 and pbe1pbe, are compared to the most precise DKH value of Sadlej and co-workers [303]. The hybrid functional (pbe1pbe) within the GGA, in combination with the extensive STUTTGART basis set and pseudopotential, gives good agreement with the aforementioned value and thus has been used throughout all calculations of the copper nonamer isomers. For the copper dimer this method gives a bond length of 2.232 Å, a dissociation energy of 1.88 eV and a harmonic frequency of 258.09 cm^{-1} to be compared with experimental values of 2.219 Å, 2.08 eV [300] and 266.43 cm^{-1} [301]. In general, DFT tends to underestimate the polarizability. It should be noted that increasing the Hartree-Fock exchange within the b3lyp hybrid DFT functional should yield better agreement of the polarizability with the relativistic DKH CCSD(T) calculation. While the b3lyp functional yields a value of 5.912 $Å^3$ and pure Hartree-Fock gives 10.284 $Å^3$, mixing into the exchange 50 % Hartree-Fock (the so-called Becke half-and-half lyp functional) yields a value of 6.703 $Å^3$.

7.3 Results and Discussion

7.3.1 Structural Data

Due to the considerable sampling of trial geometries taken from the literature of Cu_9 clusters, together with random structures and most importantly the genetic algorithm approach, there is great confidence that the lowest energy structures have been found (see figure (7.2). The energetic separation between the Cu_{9_0}, Cu_{9_1} and Cu_{9_2} structures is however too small to appoint either one of them as the global minimum structure (see table (7.1)). In previous publications, the Cu_{9_0} isomer with C_{2v} or C_s symmetry, where the reduction in symmetry stems from a distortion of the pentagonal bipyramid, was predicted as the ground state structure [288,290,291,293–295,304]. Interestingly enough, Cu_{9_0} is the predicted Lennard-Jones global minimum structure for a nonamer cluster; it has C_{2v} symmetry and is obtained by double capping of two adjacent lower triangles of a pentagonal bipyramid. Cu_{9_1} has also C_{2v} symmetry and is obtained by double capping of two adjacent upper and lower triangles of a pentagonal bipyramid. The predicted GM by Calaminici *et al.* [296] is the Cu_{9_2} isomer of this work. It has C_s symmetry and can be regarded as a capped octamer which consists of two slightly distorted, intersecting

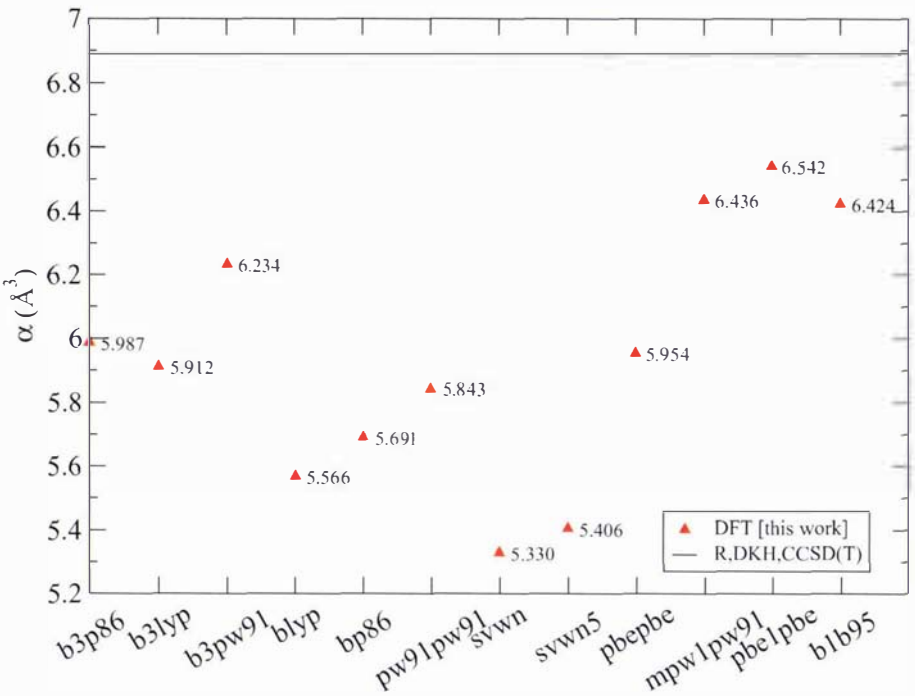

Figure 7.1: Static electric dipole polarizabilities oft he ground state copper atom in $Å^3$ as a function of different DFT exchange-correlation functionals and compared to a relativistic all-electron DKH CCSD(T) [303] calculation.

squares that are rotated by 90° to each other. Cu_{9_3} represents a C_1 derivative of the Cu_{9_2} isomer. Cu_{9_4} and Cu_{9_5} are again based on the pentagonal bipyramid structural motif. The copper nonamer cluster clearly adopts a three-dimensional structure and all flat structures obtained from the genetic algorithm are found to be less stable by more than 1.0 eV. The average bond length d for all directly bonded Cu atoms are listed together with electronic properties in table (7.1). Interestingly, the planar high-energy structure Cu_{9_6} has a rather small average bond distance. Vibrational frequencies and zero-point vibrational energies are given in table (7.2). It is found that the differences in zero point vibrational energies (ZPVE) of all isomers are less than 0.002 eV/n and thus cannot be drawn on in determining the relative stabilities of isomers.

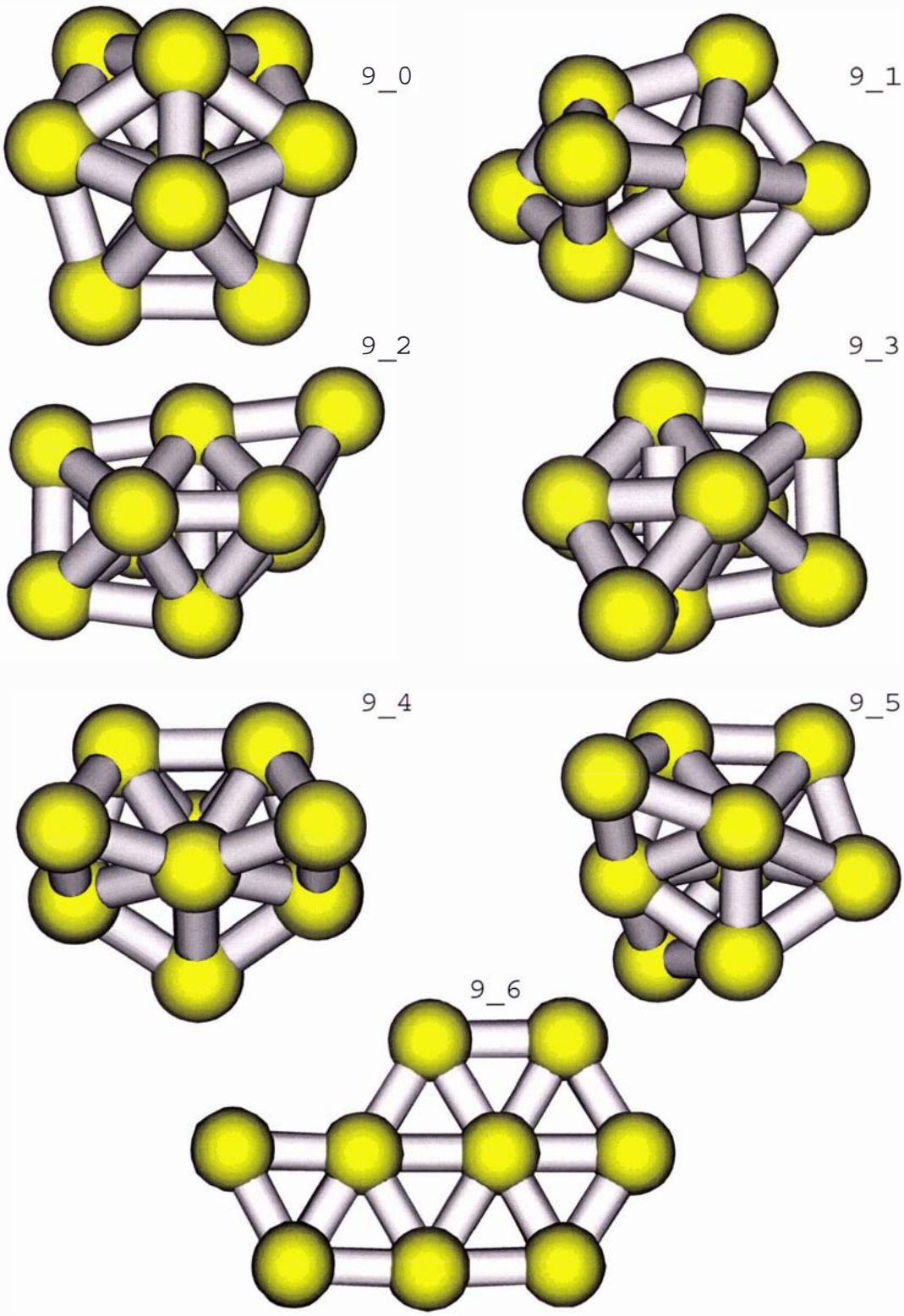

Figure 7.2: Global minimum and lowest-energy isomers of Cu_9, ordered (from left to right and top to bottom) by energy. The cluster 9_m is the mth energetic isomer with 9 atoms.

7.3.2 Polarizabilities and other Electronic Properties

The isotropic, static electric dipole polarizability per atom, the anisotropy, the dipole moment and other electronic properties for the Cu_9 isomers are given in table (7.1). The first data set refers to the large basis set [298] and the second to the LANL2DZ basis set. It is seen that even the smaller basis set calculations with LANL2DZ give satisfactory results, except perhaps for the dipole moment where the largest absolute difference between the two calculations is 0.08 D.

Table 7.1: Calculated static response and electronic structure properties of DFT-optimized Cu_{9_0} clusters. ΔE denotes the relative energy differences between isomers, $\Delta\epsilon$ the HOMO-LUMO gap, α_{iso} the isotropic static electric dipole polarizability, α_{aniso} its anisotropy, μ the absolute value of the dipole moment, d the average neighbor distances, VIP and VEA the vertical ionization potentials, respectively, E_{Coh} the cohesive energies (not corrected for zero-point vibrational energy). The geometry notation is that of figure (7.2). The notation $/n$ implies the value is given per atom.

Cluster	ΔE (eV)	$\Delta\epsilon$ (eV)	α_{iso} (Å$^3/n$)	α_{aniso} (Å$^3/n$)	μ (D)	d (Å)	VIP (eV)	VEA (eV)	E_{Coh} (eV/n)
Stuttgart basis set and pp									
Cu_{9_0}	0.000	1.486	4.939	1.490	0.124	2.469	5.440	1.438	1.76
Cu_{9_1}	0.013	1.501	5.188	1.977	0.280	2.457	5.286	1.366	1.76
Cu_{9_2}	0.064	1.512	5.010	2.422	0.379	2.448	6.059	1.979	1.76
Cu_{9_3}	0.145	1.526	4.999	1.722	0.201	2.451	5.366	1.328	1.75
Cu_{9_4}	0.201	1.487	5.082	1.352	0.338	2.463	5.282	1.328	1.74
Cu_{9_5}	0.242	1.386	5.336	2.039	0.178	2.462	5.184	1.379	1.74
Cu_{9_6}	1.105	1.510	5.815	5.504	0.332	2.409	5.856	1.981	1.64
LANL2DZ									
Cu_{9_0}	0.000	1.426	5.230	1.547	0.177	2.539	5.249	1.327	1.81
Cu_{9_1}	0.004	1.432	5.504	2.242	0.306	2.521	5.101	1.269	1.81
Cu_{9_2}	0.048	1.457	5.287	2.577	0.398	2.568	5.874	1.854	1.81
Cu_{9_3}	0.111	1.469	5.282	1.898	0.277	2.544	5.172	1.219	1.80
Cu_{9_4}	0.187	1.446	5.377	1.428	0.432	2.514	5.099	1.223	1.79
Cu_{9_5}	0.242	1.354	5.622	2.287	0.180	2.513	5.029	1.264	1.79
Cu_{9_6}	1.132	1.454	6.138	5.907	0.409	2.470	5.622	1.801	1.69

In table (7.3), calculated electronic properties from this work are compared to those of other theoretical and experimental studies for Cu_{9_0} and it is found that the theoretically yielded α/n are very similar and more than three times smaller than the published experimental one by Knickelbein. With respect to dipole moments, only Jackson *et al.* [293]

Table 7.2: Zero-point vibrational energy per atom (in eV/n) and harmonic frequencies (in cm^{-1}) of the neutral copper cluster nonamers obtained using the Stuttgart basis set and pp.

Cluster	ZPVE	Frequencies
Cu_{9_0}	0.0203	63.1, 66.9, 75.7, 92.9, 102.6, 108.2, 112.9, 115.9, 121.4, 124.1, 124.7
		127.4, 143.1, 145.0, 167.9, 177.8, 190.3, 197.1, 221.1, 223.5, 246.2
Cu_{9_1}	0.0205	54.0, 55.5, 64.5, 88.5, 88.7, 103.4, 110.5, 125.7, 134.9, 135.8, 136.5
		142.8, 150.4, 152.3, 157.9, 175.3, 187.2, 219.8, 225.7, 229.2, 232.6
Cu_{9_2}	0.0205	58.3, 64.8, 74.6, 94.8, 100.9, 106.2, 106.8, 116.5, 116.6, 119.4, 137.5
		138.0, 161.3, 164.1, 172.1, 173.9, 193.7, 205.2, 211.2, 220.8, 236.2
Cu_{9_3}	0.0201	40.7, 58.5, 69.4, 85.5, 89.7, 103.9, 112.0, 113.4, 117.9, 123.5, 124.5
		137.2, 153.3, 170.3, 175.2, 182.5, 197.0, 206.6, 215.4, 219.7, 228.2
Cu_{9_4}	0.0198	38.4, 59.2, 61.5, 74.6, 96.8, 96.8, 105.3, 107.3, 116.8, 122.5, 131.7
		143.7, 149.5, 152.2, 167.6, 171.7, 190.3, 199.8, 216.6, 227.1, 253.3
Cu_{9_5}	0.0199	39.8, 52.7, 59.6, 72.7, 86.7, 100.1, 107.5, 115.8, 119.9, 126.3, 136.6
		140.3, 143.6, 152.3, 156.7, 174.5, 182.8, 209.8, 227.4, 229.2, 259.8
Cu_{9_6}	0.0185	17.6, 20.1, 31.0, 42.1, 46.3, 51.7, 67.8, 93.4, 101.3, 114.8, 127.1
		143.8, 150.3, 156.0, 183.1, 185.1, 194.1, 216.7, 228.5, 251.3, 262.8

report a value which is almost 35 % smaller than the one reported here. But given the rather small value of μ, the absolute discrepancy is only 0.03 D. The agreement with the experimental vertical ionization potential [280] is rather good. The calculated cohesive energy per atom is 1.765 eV for Cu_{9_0} which is perhaps larger than the experimentally estimated value (1.4±0.5 eV) [305], but within the experimental uncertainty. The discrepancy between the absolute values of the theoretically evaluated binding energies is due to the use of different DFT functionals and basis sets. In general, calculated cluster binding energies are larger than those observed in experiments. This error arises most probably from the calculated total energy of the atom [294].

The disagreement between experiment and theory with respect to the isotropic polarizability per atom remains, however, an open question. In accordance with arguments from Knickelbein [297] and Jackson *et al.* [293] one could utilize equation (5.5), use the theoretically obtained dipole moments and parameterize the rotational temperature until agreement is reached. As nicely shown by Jackson *et al.*, non-negligible dipole moments combined with low rotational temperatures can lead to much higher effective polarizabilities, but do not explain the general disagreement between experiment and theory. Since rotational temperatures and dipole moments vary with cluster size and morphology, and the dynamics of the dipole moments are also unknown, equation (5.5) is inadequate to

Table 7.3: Comparison of electronic properties of Cu_{9_0} from this work with those of available theoretical and experimental studies. The notation $/n$ implies the value is given per atom.

Method	Ref.	α_{iso} (Å$^3/n$)	α_{aniso} (Å$^3/n$)	μ (D)	VIP (eV)	VEA (eV)	E_{Coh} (eV/n)	ZPVE (eV/n)	$\Delta\epsilon$ (eV)
pbe1pbe	[This work]	4.939	1.490	0.124	5.440	1.438	1.76	0.0203	1.486
pbepbe	[295]	-	-	-	5.62	-	1.98	-	-
LDA	[294]	-	-	-	-	-	2.44	-	-
pbepbe	[293]	5.05	-	0.092	-	-	2.0	-	1.143
b3pw91	[291]	5.15	-	-	-	-	1.772		1.24
LDA	[290]	-	-	-	6.07	1.8	2.12	0.022	-
bp86	[288]	4.86	-	-	-	-	-	-	
Exp.	[297]	16.2 ± 0.8	-	-	-	-	-	-	
Exp.	[305]	-	-	-	-	-	1.25	-	-
Exp.	[280]	-	-	-	5.35	-	-	-	-

fully explain the general discrepancy between theory and experiment. Employing equation (5.5) with the calculated dipole polarizability, dipole moments, highest I_1 and lowest I_3 principal moments of inertia, and use of Knickelbein's observed effective polarizability, the following rotational temperatures are obtained for the three lowest-lying isomers.

$$T_{\rm rot}(Cu_{9\_0}) \approx 3 \text{ K}; T_{\rm rot}(Cu_{9\_1}) \approx 15 \text{ K}; T_{\rm rot}(Cu_{9\_2}) \approx 29 \text{ K}.$$

The rotational temperature in Knickelbein's experiment is estimated as being 58 K. No clear conclusion can be drawn from this except to say that perhaps the measured effective polarizability may indicate that the isomer Cu_{9_2} is the global minimum.

In order to obtain more insight into the huge discrepancy between theory and experiment, polarizability measurements of atomic and dimeric copper are needed; for atomic and dimeric copper, where equation (5.5) does not apply, one would infer very large static polarizabilities per atom from the reported trend of figure 2 in ref. [297]. These would be much higher again compared to Saue and Jensen [266] who obtained an isotropic α/n for Cu_2 of 7.09 Å^3 using the 4-component relativistic random phase approximation (anisotropy per atom of 3.10 Å^3). This is close to the coupled cluster [CCSD(T)] value of Maroulis [306] who obtained an isotropic polarizability of 6.95 Å^3 per atom. Temperature dependent measurements would also be of great interest, in order to determine the contribution of the dipole moment to the effective polarizability. It should also be noted that Knickelbein did not calibrate the beam deflection apparatus to atomic copper, but used the aluminum atoms as a calibrant.

7.4 Conclusions

For the first time, a systematic approach in the framework of DFT was employed to find the global minimum of the copper cluster nonamer. It is found that the isomers labelled Cu_{9_0}, Cu_{9_1} and Cu_{9_2} lie energetically too close to adopt either of them as the global minimum. Moreover, the static electric dipole polarizability and other electronic properties are calculated with a basis set that is significantly larger than any other employed for the copper nonamer so far. While previously reported polarizabilities per atom obtained from theory are confirmed, i.e. it is shown that the larger basis set does not yield significantly different values, the dipole moments of a set of copper cluster nonamer isomers are reported for the first time. Finally, it is argued that the origin of the large discrepancy between theoretically and experimentally obtained polarizabilities per atom is rather due to a systematic error in the experiment than large permanent dipole moments and small rotational temperatures of the respective clusters.

7.5 Further Work

Measurements of the polarizability per atom of atomic and dimeric copper, together with temperature dependent measurements of polarizabilities of copper clusters are needed to clarify the significant discrepancy between theory and experiment. Equation (5.5) should be generalized to cover asymmetric top molecules.

Chapter 8

Metallophilicity, the Performance of DFT

8.1 Motivation

The attractive interaction between closed-shell species of group 11, also known as metallophilic interactions, is well established experimentally and theoretically. For a generic and comprehensive review of strong closed-shell interactions (CSIs) in inorganic chemistry see ref. [210]. Due to their interesting chemical and physical properties [307–309] and strongest CSI[1] in group 11, particularly gold(I) phosphine complexes have been studied experimentally in the past [310–315]. This is so mainly, because phosphine ligands stabilize gold-gold bonding [316] and hence allow for the formation of a large variety of gold clusters [317] like $[Au_{55}(PPh_3)_{12}]Cl_6$ [312,318]. Phosphine ligands also stabilize otherwise unstable gold compounds such as $AuCH_3$ [317]. Moreover, gold phosphine cluster compounds can also exhibit photo-physical properties such as the luminescence behavior observed in $[Au(dppn)_2]Cl$ derivatives [319] (dppn = diphenlyphosphinonaphthaline) or related species [320].

The theoretical work in this area was pioneered by Hoffmann *et al.* [321] and reinvestigated by Pyykkö *et al.* [322]. Pyykkö used HF and MP2 methods to investigate the aurophilicity in $[Cl\text{-}Au\text{-}PH_3]_2$ and $[X\text{-}Au\text{-}PH_3]_2$ dimers (X=H, CH_3, CN, SCH_3, F, Cl, Br and I). Since the interaction energy curves were repulsive at the HF level and attractive at

[1]The attractive aurophilic attraction (up to 50 kJ/mol) can be comparable with strong hydrogen bonds or weak covalent bonds.

the MP2 level, he concluded that aurophilicity is a correlation effect and cannot be satisfactorily explained by classical theory, such as hybridization. Moreover, he concluded that the aurophilicity is further enhanced by relativistic effects and that its strength increases from the hardest ligand to the softest ligand by a factor of 2.

In order to partition the local correlation contributions to the metal-metal interaction energy into different excitation classes, local MP2 calculations were performed by Werner *et al.* [323,324]. The target systems here were $[X\text{-}M\text{-}PH_3]_2$ (M = Cu, Ag, Au; X = H, Cl). In addition to Pyykkö's conclusions, they summarized that for $[Cl\text{-}M\text{-}PH_3]_2$ the strength of metallophilicity increases by almost 40 % from Cu (22 kJ/mol) to Au (35 kJ/mol). They also discovered that the attractive intermolecular correlation contributions arise from both dispersive (van der Waals) and ionic excitations[2].

While dispersion contributions, as expected, dominate the long-range behavior of the interaction curves for these systems and the ionic contributions decay exponentially with respect to r_{M-M}, they are of about the same importance as dispersion in $[H\text{-}M\text{-}PH_3]_2$ and of about 60 % in $[X\text{-}M\text{-}PH_3]_2$ at equilibrium [324]. They also report that metallophilicity does not solely arise from $M(d^{10})$ - $M(d^{10})$ interactions. Pure Au(5d)-Au(5d) pair correlation is responsible for only ca. 40 % of the attraction in $[Cl\text{-}Au\text{-}PH_3]_2$ and is further decreased to ca. 15 % for M = Cu. Pair correlation involving only one or neither $M(d^{10})$ center make up the bulk of the attractive part of the correlation; for the copper compound, pair correlations involving neither of the $Cu(3d^{10})$ centers are the leading term.

It is worthwhile to mention, that Magnko *et al.* acknowledge a potential problem with the MP2 approach, i.e. the overestimation of van der Waals attractions, and state that their MP2 results may well be too large by anything between 0 and 25 % [324]. Pyykkö noted that this area will require further investigation, since the interaction energies oscillate quite strongly as the higher levels of theory are introduced [334]. Recently, Kaltsoyannis *et al.* studied compounds of the type $[Cl\text{-}M\text{-}PH_3]_{n=1,2}$ (M = Cu, Ag, Au, [111]) using *ab initio* and density functional methods in the light of the question: Does metallophilicity increase or decrease down group 11? [325].

They reproduce the MP2 results from previous studies and complement them by DFT, QCISD and CCSD(T) data for the first time. Their DFT, QCISD and CCSD(T) results

[2]Dispersion effects originate from simultaneous mono-excitations at both monomers, each mono-excitation promoting an electron from the occupied space to the virtual space of the same monomer (A → A', B → B'). Ionic effects originate from mono-excitations from the occupied space of both monomers into the virtual space of only one of the monomers (A → A', B → A' and A → B', B → B').

reveal, however, that, contrary to MP2 results, the strength of metallophilic interaction in these systems increases negligibly from Cu to Ag, but decreases from Ag to Rg. Thus stating that metallophilicity does decrease down group 11.

Since there are no pairs of analogous free dimers for this series of compounds, Kaltsoyannis' results cannot be tested experimentally easily. For this purpose, Pyykkö probed comparative calculations for the A-frame molecules $[S(MPH_3)_2]$ [326], applying full geometry optimization at the MP2-MP4, CCSD and CCSD(T) level, and concluded that the oscillations of the metal-metal distance, as a function of theoretical level, are large and in the following order: Cu > Au > Ag. Thus, qualitatively agreeing with Kaltsoyannis, that MP2 may not be the appropriate method for investigating the metallophilicity. By performing local MP2 and CCSD calculations, he ascertained that dispersion terms dominate the silver and gold systems, while the ionic terms dominate the Cu compound. Furthermore, he stated that there is still a too large discrepancy between the optimized and experimental geometric data even at the CCSD(T) level.

The motivation of this work was to further probe the performance of DFT in the field of metallophilicity, to investigate a greater range of ligands than Kaltsoyannis [325] and to include for the first time also the trimers of the $[X\text{-}M\text{-}PH_3]_{n=1-3}$ systems (X=Cl, Br, I; M=Cu, Ag, Au). More extensive basis sets were employed and in contrast to Kaltsoyannis' study, all monomer, dimer and trimer structures were fully optimized at the DFT level[3].

8.2 Methods

When investigating metallophilicity, the choice of basis set is particularly important due to a combination of basis set superposition error (BSSE) [327] and the inherent weakness of the effect itself. Furthermore, it is imperative to treat the coinage metals and the bromine and iodine atoms relativistically and on the same footing. It has been shown that relativistic effects cannot be neglected in accurate calculations of bond lengths and energies in copper compounds [332,333]. Therefore, the extensive and well proven STUTTGART valence basis sets and energy-consistent small-core pseudopotentials[4], where scalar-relativistic effects are implicitly included, were used for Cu, Ag, Au, Br and I [337,338].

[3]Van der Waals-like interactions are not reliably described by the current DFT schemes [210,324] however, DFT has a reputation for producing the correct answer for unreliable reasons.

[4]Relativistic large-core pseudopotentials overestimate the attraction between coinage metals [334,335].

The heteroatoms of all compounds, i.e. H, P and Cl, were treated with all-electron aug-cc-pVDZ[5] basis sets as implemented in the GAUSSIAN03 program package [331]. All calculations were performed with the GAUSSIAN03 program package [331].

As in all other related theoretical studies cited here, the PR_3 (R=alkyl, aryl) groups, which are present in the experimental compounds, were replaced by PH_3 in order to simplify the calculations. Table (8.1) shows, that PH_3 is a good model for the larger PR_3 ligands, as far as structural properties are concerned. The structures of all monomeric, dimeric and trimeric compounds of the type $[X\text{-}M\text{-}PH_3]_{n=1-3}$ (M=Cu, Ag, Au; X=Cl, Br, I) were fully optimized at the DFT level, only constraining the dihedral angle (d_{XMMX}) to 90°, according to figure (8.1 (b) and (c)) (see table (8.2) for geometric data). The latter restriction was made to reduce electrostatic interactions between the monomers by minimizing the leading dipole-dipole term, and hence to allow more unencumbered focus on the metallophilicity. It has been shown that by lifting this restriction, significantly bigger interaction energies and in almost all cases smaller metal-metal distances are obtained [325], hence illustrating the need for the 90° restriction when investigating metallophilicity in these systems.

For the exchange-correlation potential, the generalized gradient approximation, according to the parameterization suggested by Becke [111] and Perdew [112] (bp86), was applied in a self-consistent fashion.

The BSSEs were accounted for using the counterpoise correction according to [10],

$$\begin{aligned} \Delta E_{complex} &= E^*_{AB}[ab] - E_A[a] - E_B[b] \\ \Delta E_{CP} &= E^*_A[ab] + E^*_B[ab] - E^*_A[a] - E^*_B[b] \\ E_{CPC} &= \Delta E_{complex} - \Delta E_{CP}, \end{aligned} \tag{8.1}$$

where $\Delta E_{complex}$ denotes the complexation energy, ΔE_{CP} the counterpoise correction energy and E_{CPC} the counterpoise corrected complexation energy of the dimer $[X\text{-}M\text{-}PH_3]_2$, respectively. A and B represent the monomers, AB the dimer complex, a and b the basis sets of the respective monomers and * the optimized complex geometry.

[5]Dunning's correlation consistent, double-zeta basis sets augmented with diffuse functions.

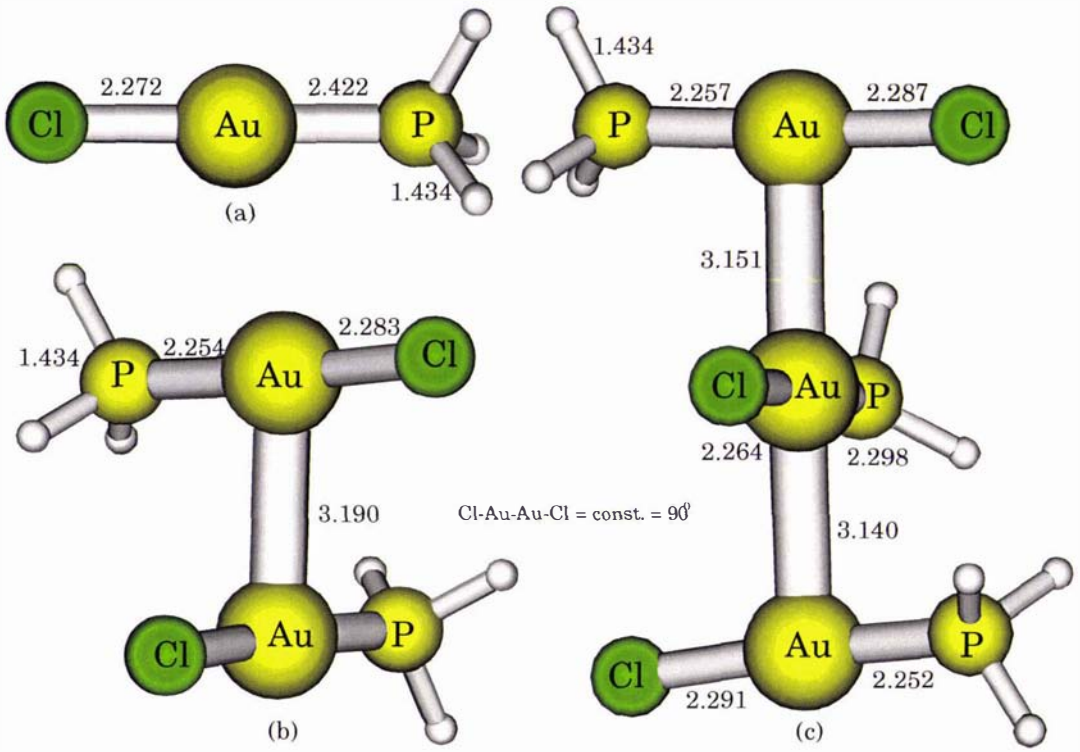

Figure 8.1: Optimized structures of $[Cl\text{-}Au\text{-}PH_3]_{n=1-3}$: bond lengths in Å.

8.3 Results and Discussion

A wide range of theoretical and experimental geometric data of the monomers of [X-M-PH_3] are compared in table (8.1). Clearly, the simplification of the different alkyl and aryl phosphine groups, which are present in the experimental studies, to the phosphane (PH_3) group is justified[6], as the discrepancies between the calculated and experimental bond lengths r_{M-X} and r_{M-P} for the monomers come to less than 3 % for all the studied compounds. It further becomes evident, when comparing the available theoretical work with the experimental, that both MP2 and DFT perform very satisfyingly. However, no clear conclusion can be drawn as to which method performs best, as there is no experimental data available for the optimized compounds.

The isostructural series of phosphine substituted compounds [X-M-(TMPP)]

[6]At least as far as geometric properties are concerned.

Table 8.1: Comparison of geometric data of [X-M-PH_3] (M=Cu, Ag, Au; X= Cl , Br, I); angles in deg and bond lengths in Å.

Molecule	Method	r_{M-X}	r_{M-P}	$\angle_{X-M-P}$	Ref.
[$ClCuPH_3$]	bp86	2.084	2.143	180.0	this work
[$ClCuPH_3$]	bp86	2.094	2.143		[325]
[$ClCuPH_3$]	b3lyp	2.106	2.175		[325]
[$ClCuPH_3$]	b3lyp	2.123	2.207		[324]
[$ClCuPH_3$]	MP2	2.097	2.159	180.0	[317]
[ClCu(TMPP)]	exp	2.118	2.117	173.0	[328]a
[$BrCuPH_3$]	bp86	2.213	2.151	180.0	this work
[BrCu(TMPP)]	exp	2.259	2.197	172.0	[328]b
[$ICuPH_3$]	bp86	2.393	2.163	180.0	this work
[ICu(TMPP)]	exp	2.417	2.188	171.0	[328]b
[$ClAgPH_3$]	bp86	2.283	2.312		this work
[$ClAgPH_3$]	bp86	2.294	2.319		[325]
[$ClAgPH_3$]	bp86	2.299	2.333		[339]
[$ClAgPH_3$]	b3lyp	2.310	2.364		[325]
[$ClAgPH_3$]	MP2	2.306	2.372	180.0	[317]
[ClAg(TMPP)]	exp	2.342	2.379	175.0	[329]
[$BrAgPH_3$]	bp86	2.405	2.325	180.0	this work
[BrAg(TMPP)]	exp	2.440	2.370	174.4	[329]
[$IAgPH_3$]	bp86	2.579	2.342	180.0	this work
[IAg(TMPP)]	exp	-	-	-	
[$ClAuPH_3$]	bp86	2.272	2.242	180.0	this work
[$ClAuPH_3$]	bp86	2.289	2.241	-	[325]
[$ClAuPH_3$]	bp86	2.227	2.222	-	[339]
[$ClAuPH_3$]	B3LYP	2.302	2.262	-	[325]
[$ClAuPH_3$]	B3LYP	2.325	2.283	-	[341]
[$ClAuPH_3$]	MP2	2.300	2.249	180.0	[317]
[ClAu(TMPP)]	exp	2.304	2.253	176.0	[330]
[$ClAuPPh_3$]	exp	2.279	2.235	179.6	[342]
[$ClAuPEt_3$]	exp	2.305[a]	2.233[a]	178.7[a]	[344]
[$ClAuPMe_3$]	exp	2.309[b]	2.234[b]	180.0[b]	[343]
[$BrAuPH_3$]	bp86	2.395	2.253	180.0	this work
[BrAu(TMPP)]	exp	2.413	2.255	175.9	[330]
[$IAuPH_3$]	bp86	2.562	2.269	180.0	this work
[IAu(TMPP)]	exp	2.586	2.240	177.7	[330]

[a] Average for two crystallographically inequivalent molecules

[b] Average for three crystallographically inequivalent molecules

(M = Cu(I), Ag(I), Au(I); X= Cl, Br, I)[7], with the exception of the AgI[8] complex, all form isomorphous solids in which the metals display the linear P-M-X structure, which is normally only characteristic to the gold(I) complexes [328–330]. The crystallographic data on the Chloro(triphenyl-, triethyl- and trimethylphosphine)gold(I) complexes all show the linear P-M-X structure as well and negligible deviations in their bond lengths r_{M-X} and r_{M-P}, respectively.

On the basis of the size of the phosphine ligands, the Chloro(trimethylphosphine)gold(I) complex is the most closest related to the Chloro(phosphane)gold(I) complex investigated in this work. This is reflected by the fact that, while the monomers of [ClAuPMe$_3$] are aggregated to form a helical chain through fairly short alternating Au $\cdots$ Au contacts of 3.271, 3.356, and 3.386 Å [343], the closest Au $\cdots$ Au contacts in the crystal lattice of [ClAuPEt$_3$] is 3.615 Å [344]. Such Au $\cdots$ Au contacts are not present in the Chloro(tripropylphosphine)gold(I) complex at all [343]. The calculated Au-Au distances for the dimers and trimers of [ClAuPH$_3$] are 3.190 and 3.146 Å, respectively, and resemble the ones of the [ClAuPMe$_3$] nicely.

The trends in geometric data, going from the monomers to the trimers, can be summarized as follows: While the r_{P-H} bond lengths are rather constant at 1.43 Å in all compounds, the metal-halide and metal-phosphorus bond lengths, r_{M-X} and r_{M-P}, increase slightly when comparing the monomers of a respective metal complex with its dimers and trimers. Within the halide series, both r_{M-X} and r_{M-P} increase almost linearly towards the softest halide. The gold complexes show the highest tendency towards linearity for the $\measuredangle_{X-M-P}$ angle, which decreases slightly going from the harder halides to the softer ones (see table (8.2)).

The r_{M-X} and r_{M-P} bond distances within all calculated compounds increase from copper to silver and decrease from silver to gold (see figures (8.2 and 8.3)). Note, that the r_{M-X} distances are quite similar for the silver and gold complexes, but the r_{M-P} distances in the gold complexes are significantly shorter than those of the silver compounds. This contraction is due to the large relativistic effects at gold [23] and is confirmed by comparison of relativistic and non-relativistic calculations for these and similar compounds [317,339]. Bowmaker *et al.* give two possible reasons, why the decrease in r_{M-P} bond lengths is more pronounced than that of the r_{M-X} bond lengths [339]. The first one

[7]TMPP [tris(2,4,6)methoxyphenylphosphine] is a strongly sterically hindered phosphine ligand that allows for overcoming the preferred tetrahedral four-coordination for copper(I) and silver(I) compounds.

[8]Experimental data is not available.

Table 8.2: Optimized geometric data for $[X\text{-}M\text{-}PH_3]_n$ [M=Cu, Ag, Au and X=Cl, Br, I], angles in deg and distances in Å.

Monomers		r_{M-X}	r_{M-P}	r_{P-H}	$\measuredangle_{X-M-P}$
M=Cu; X=Cl		2.084	2.143	1.436	180.0
M=Cu; X=Br		2.213	2.151	1.436	180.0
M=Cu; X=I		2.393	2.163	1.436	180.0
M=Ag; X=Cl		2.283	2.312	1.434	180.0
M=Ag; X=Br		2.405	2.325	1.434	180.0
M=Ag; X=I		2.579	2.342	1.434	180.0
M=Au; X=Cl		2.272	2.242	1.434	180.0
M=Au; X=Br		2.395	2.253	1.434	180.0
M=Au; X=I		2.562	2.269	1.434	180.0
Dimers[a]	r_{M-M}	r_{M-X}	r_{M-P}	r_{P-H}	$\measuredangle_{X-M-P}$
M=Cu; X=Cl	2.616	2.100	2.167	1.435	167.2
M=Cu; X=Br	2.596	2.231	2.176	1.435	166.5
M=Cu; X=I	2.572	2.412	2.189	1.435	165.4
M=Ag; X=Cl	2.970	2.297	2.328	1.434	171.7
M=Ag; X=Br	2.952	2.421	2.343	1.434	171.1
M=Ag; X=I	2.940	2.588	2.362	1.434	170.2
M=Au; X=Cl	3.190	2.283	2.254	1.434	174.3
M=Au; X=Br	3.154	2.407	2.265	1.434	173.7
M=Au; X=I	3.124	2.574	2.283	1.434	172.6
Trimers[a]	r_{M-M}	r_{M-X}	r_{M-P}	r_{P-H}	$\measuredangle_{X-M-P}$
M=Cu; X=Cl	2.634	2.114	2.176	1.435	170.3
	2.617				
M=Cu; X=Br	2.607	2.249	2.183	1.435	168.5
	2.589				
M=Cu; X=I	2.578	2.430	2.200	1.435	166.4
	2.564				
M=Ag; X=Cl	2.957	2.308	2.337	1.434	173.2
	2.943				
M=Ag; X=Br	2.950	2.435	2.353	1.434	171.7
	2.920				
M=Ag; X=I	2.943	2.607	2.374	1.434	169.8
	2.903				
M=Au; X=Cl	3.151	2.291	2.256	1.434	175.6
	3.140				
M=Au; X=Br	3.127	2.417	2.269	1.434	175.0
	3.110				
M=Au; X=I	3.107	2.586	2.287	1.434	174.4
	3.093				

[a] Averaged values where applicable

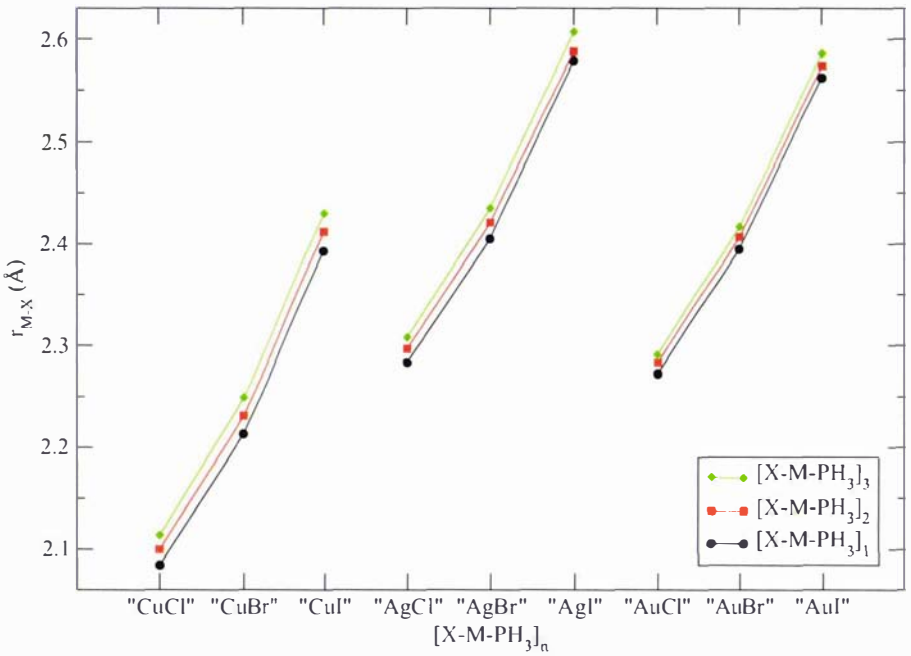

Figure 8.2: Comparison between the r_{M-X} bond lengths in optimized structures of $[X\text{-}M\text{-}PH_3]_{n=1-3}$.

deals with the fact that relativistic bond contractions are sensitive to the electronegativity of the ligand attached to gold [339,340] and, as the argument goes, results in larger bond length contractions where there is appreciable *ns* character to the bonding. Hence, for a completely ionic bonding situation (M^+X^-), with no *ns* character, there will be no relativistic bond length contraction[9]. The contraction would progressively increase through covalent Au-X to ionic Au^-X^+ (where, in this case, X is an alkali metal). Although this argument is in accordance with the geometric results presented in table (8.2), it must be noted that, while the relativistic contraction of orbitals and the relativistic contraction of bond lengths are parallel effects, the orbital contraction cannot be seen as the direct cause of the bond length contraction [19]. The second explanation involves the destabilization of the d orbitals (indirect relativistic effect) which would enhance π back-donation from

[9]There might even be a slight increase in the bond length, on account of the indirect relativistic expansion of the valence *d* orbitals.

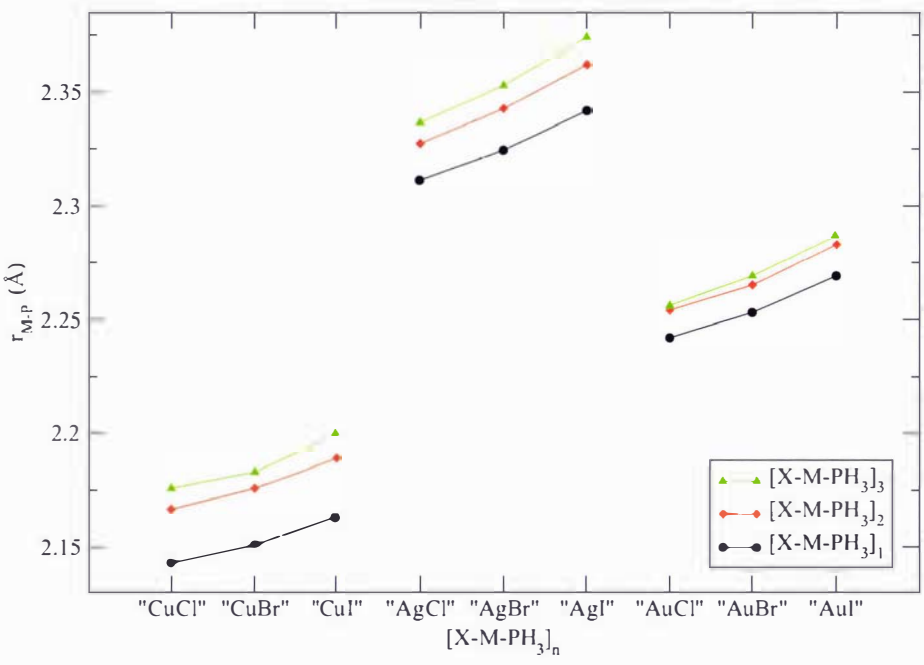

Figure 8.3: Comparison between the r_{M-P} bond lengths in optimized structures of $[X\text{-}M\text{-}PH_3]_{n=1-3}$.

the Au 5*d* orbitals to the PR_3 fragment, hence strengthening (and presumably shortening) the Au-P bond. This argument is also in agreement with the results presented in this work, however, the present methods do not permit a clear determination of the relative importance of the two mechanisms described above. It is worthwhile to mention that a significant relativistic bond length shortening has been found for RgH [345], compared to AuH, which indicates that metal-ligand π effects cannot be the only source for the relativistic M-P bond length shortening.

As displayed in figure (8.4), the metal-metal bond lengths (r_{M-M}) in these complexes, decrease almost linearly from the harder to the softer halides. The calculated r_{M-M} values are larger than the bond lengths of the metal dimers (Cu_2 = 2.22 Å; Ag_2 = 2.53 Å, Au_2 = 2.47 Å) [324], and are better comparable to the nearest-neighbor distances in the bulk metals (Cu: 2.55 Å; Ag: 2.88 Å; Au: 2.88 Å).

The striking result, however, is the degree of contraction of these metal-metal contacts

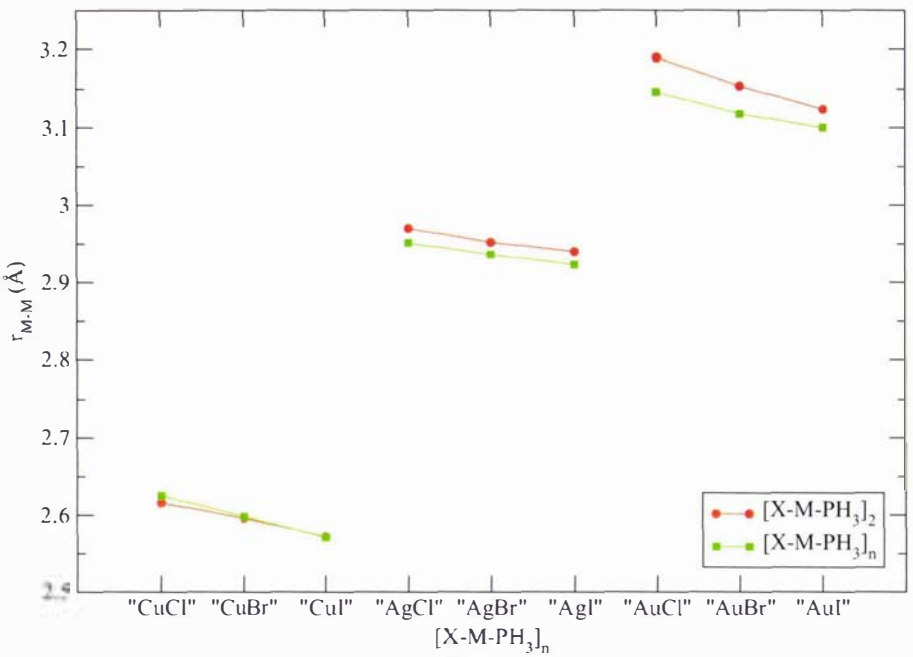

Figure 8.4: Comparison between the r_{M-M} bond lengths in optimized structures of [X-M-PH3]$_{n=2-3}$.

when going from the dimers to the respective trimers. While r_{Cu-Cu} remains rather constant, there is a distinct contraction for r_{Ag-Ag} and a substantial one for the r_{Au-Au} complexes (see also table (8.2)). This can be attributed to the increasing relativistic effects within the group of the coinage metals [346]. Another argument supporting this trend down the group is evident by the non-linear increase in r_{M-M} as a function of coinage metal dimers and trimers. For a linear increase, which has been found at the CCSD(T)-level[10] for [Cl-M-PH$_3$]$_2$ compounds [325], the contacts in the Chloro(phosphane)gold(I) dimers and trimers would be expected to be around 3.32 and 3.28 Å, respectively, rather than 3.19 and 3.15 Å.

Although the calculated metal-metal distances for the Chloro(phosphane)gold(I) dimers in this work are shorter than the ones obtained by Kaltsoyannis *et al.*, [325] (2.616,

[10] 3.00, 3.19, 3.36 Å for r_{Cu-Cu}, r_{Ag-Ag} and r_{Au-Au}, respectively.

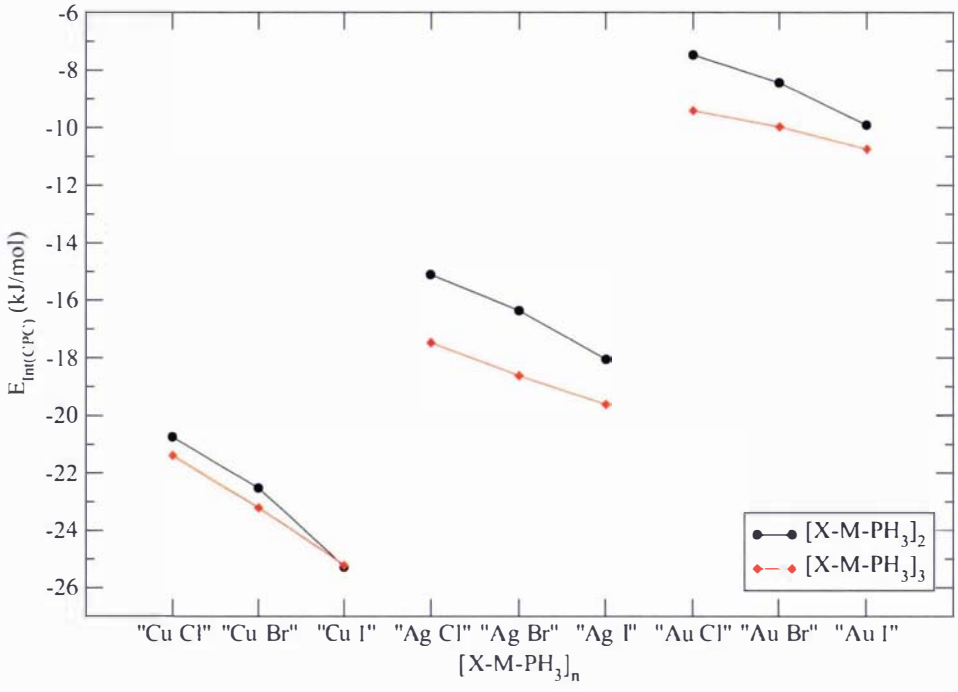

Figure 8.5: Counterpoise corrected interaction energies of $[X\text{-}M\text{-}PH_3]_{n=2,3}$ per metallophilic interaction.

2.970, 3.190 Å and 2.70, 3.04, 3.26Å)[11], the differences between these metal-metal bonds are quite similar. In particular, the bond length increase from silver to gold are the same in both studies. Thus, by only considering the geometric data, i.e. r_{M-M} contraction from dimers to trimers and the non-linear increase of r_{M-M} for the different coinage metals, it stands to reason that the attractive metal-metal interaction (metallophilicity) increases down group 11. In this regard, however, the crucial information lies within the counterpoise corrected interaction energies $E_{Int(CPC)}$ and not the structural data. A wide range of counterpoise corrected interaction energies, predicted at different levels of theory, are listed in table (8.3). The values for the dimers and trimers per metallophilic interaction from this work are also presented in figure (8.5).

[11]Latter three values obtained by Kaltsoyannis *et al*, also utilizing the bp86 functional. Distances in Å.

Table 8.3: r_{M-M} in A, counterpoise corrected interaction energies $E_{Int(CPC)}$ and non-counterpoise corrected in kJ/mol for $[X\text{-}M\text{-}PH_3]_n$ (dimers and trimers).

Dimers	Method	r_{M-M}	E_{Int}	$E_{Int(CPC)}$	Ref.
M=Cu; X=Cl	bp86	2.616	-22.836	-20.741	this work
M=Cu; X=Cl	bp86[a]	2.70	-18.9	-12.2	[325]
M=Cu; X=Cl	QCISD[a]	3.20	-25.3	-11.2	[325]
M=Cu; X=Cl	MP2[a]	3.13	-35.2	-13.5	[325]
M=Cu; X=Cl	HF[a]	4.13	-2.9	-1.5	[325]
M=Cu; X=Cl	CCSD(T)[a]	3.00	-33.1	-15.3	[325]
M=Cu; X=Cl	MP2[a]	2.77		-24.4	[324]
M=Cu; X=Cl	LMP2[a]	2.81		-22.1	[324]
M=Cu; X=Br	bp86	2.596	-24.755	-22.520	this work
M=Cu; X=I	bp86	2.572	-27.411	-25.284	this work
M=Ag; X=Cl	bp86	2.970	-16.650	-15.126	this work
M=Ag; X=Cl	bp86[a]	3.04	-15.9	-12.0	[325]
M=Ag; X=Cl	QCISD[a]	3.23	-36.1	-14.4	[325]
M=Ag; X=Cl	MP2[a]	3.11	-64.0	-21.2	[325]
M=Ag; X=Cl	HF[a]	4.21	-2.4	-1.2	[325]
M=Ag; X=Cl	CCSD(T)[a]	3.19	-38.3	-16.7	[325]
M=Ag; X=Cl	MP2[a]	2.90		-33.1	[324]
M=Ag; X=Cl	LMP2[a]	2.92		-30.7	[324]
M=Ag; X=Br	bp86	2.952	-17.877	-16.375	this work
M=Ag; X=I	bp86	2.940	-19.626	-18.060	this work
M=Au; X=Cl	bp86	3.190	-9.568	-7.874	this work
M=Au; X=Cl	bp86[a]	3.26	-9.4	-5.5	[325]
M=Au; X=Cl	QCISD[a]	3.45	-30.6	-13.2	[325]
M=Au; X=Cl	MP2[a]	3.17	-64.9	-25.5	[325]
M=Au; X=Cl	HF[a]	4.55	-2.0	-1.1	[325]
M=Au; X=Cl	CCSD(T)[a]	3.36	-33.6	-15.4	[325]
M=Au; X=Cl	MP2[a]	3.00		-37.0	[324]
M=Au; X=Cl	LMP2[a]	3.03		-34.8	[324]
M=Au; X=Cl	MP2[a]	3.37		-16.7	[322](b)
M=Au; X=Cl	MP2[a]	3.21		-24.7	[334]
M=Au; X=Cl	MP2[a]	3.26		-20.9	[336]
M=Au; X=Cl	MP2[a]	3.33		-16.5	[336]
M=Au; X=Br	bp86	3.154	-10.220	-8.435	this work
M=Au; X=I	bp86	3.124	-11.928	-9.913	this work
Trimers	Method	r_{M-M}[b]	E_{Int}	$E_{Int(CPC)}$	Ref.
M=Cu; X=Cl	bp86	2.625	-47.210	-42.771	this work
M=Cu; X=Br	bp86	2.598	-50.982	-46.417	this work
M=Cu; X=I	bp86	2.571	-55.279	-50.450	this work
M=Ag; X=Cl	bp86	2.951	-38.115	-34.975	this work
M=Ag; X=Br	bp86	2.936	-40.448	-37.260	this work
M=Ag; X=I	bp86	2.923	-42.738	-39.272	this work
M=Au; X=Cl	bp86	3.146	-22.271	-18.837	this work
M=Au; X=Br	bp86	3.118	-23.526	-19.950	this work
M=Au; X=I	bp86	3.100	-25.486	-21.495	this work

[a]Note, that the monomer geometry was optimized at the respective level of theory and the interaction of the monomers were investigated using the frozen monomer geometries and varying the r_{M-M} distance.

[b]averaged values

It is found that the counterpoise corrected interaction energies of dimers and trimers are not additive within the halogen series and that three-body terms may contribute up to almost 16 % ("AgCl") to the $E_{Int(CPC)}$ per metallophilic interaction. These interaction energies increase almost linearly towards the softer ligand for the trimers, whereas the dimers exhibit a marked increase going from the bromine to the iodine ligand. In general, when looking at the dimers and trimers independently, the metallophilicity is most pronounced in the copper- and least in the gold complexes, thus confirming Kaltsoyannis' *et al.* DFT results. Furthermore, it becomes apparent, when comparing the bp86 interaction energies presented in this work with the bp86 data of Kaltsoyannis *et al.* (compare counterpoise correction energies for the dimers in table (8.3)), that the basis sets used in this work are significantly less prone to BSSE and hence better suited for the study of these compounds. Moreover, the interaction energy of the $[Cl\text{-}Cu\text{-}PH_3]_2$ complex presented in this work is markedly higher to that predicted by Kaltsoyannis *et al.* [325].

8.4 Conclusions

The metallophilicity of the dimeric and trimeric complexes of the type $[X\text{-}M\text{-}PH_3]_n$ is studied at the DFT level employing the structures that are shown in figure (8.1) in the light of the question: Does metallophilicity increase or decrease down group 11?

Since the DFT calculations perform analogous to *ab initio* methods (QCISD, CCSD and CCSD(T)) employed in a recent study by Kaltsoyannis *et al.* [325], it appears that, for unknown reasons, DFT can reproduce metallophilic interactions at least in the present systems. For the monomers, dimers and trimers, there is an increase in r_{M-X} and r_{M-P} from copper to silver. The r_{M-X} bond distance remains approximately constant from silver to gold, however, there is a significant bond length contraction, attributed to relativity, in r_{M-P} when comparing the silver to the gold compounds. While the metal-metal distances (r_{M-M}) in the dimers and trimers of the copper compounds remain approximately constant, a r_{M-M} contraction is observed for the silver and the gold compounds. The latter ones showing the most pronounced contraction, and reflects the importance of unusually high relativistic effects in gold. Within the halogen series of the respective compounds, r_{M-X} and r_{M-P} increase almost linearly towards the softer halogen. r_{M-M} decreases towards the softer halogen and this is reflected in a stabilization of the interaction energies. The counterpoise corrected interaction energies per metallophilic interaction

reveal that the metallophilicity apparently decreases down group 11 (Cu > Ag > Au) for both the dimers and trimers of these compounds and are in accord with Kaltsoyannis *et al.* predicted trend for the dimers of these systems.

8.5 Further Work

Further work should include the study of the dependency of the interaction energies of dimers and trimers of Chloro(methylphosphine)gold(I) on geometric parameters. This compound is highly related to the systems studied here and in many other studies. Utilizing the experimental geometry on the one hand and optimizing the geometry on the other hand and comparing the differences in interaction energy would give a clearer picture on the magnitude of sensitivity of interaction energies to the geometry. As Pyykkö *et al.* noted, even at the CCSD(T) level of theory, the discrepancy between the optimized and experimental geometric data is too large [326]. One should also re-investigate relativistic effects.

Chapter 9

Summary and Conclusions

Conclusions for each chapter are already given in this thesis. The main conclusions are summarized in the following. For the first time, a systematic search for the global minima structures of homo-nuclear clusters of cesium, tin and gold clusters consisting of up to twenty atoms and of the copper nonamer clusters is undertaken within a Density Functional Theory based genetic algorithm approach. This approach outperforms all previous studies, as numerous new, more stable cluster isomers were found in this work. This thesis is further distinguished, as both the structural optimization of the most stable clusters and calculation of their electronic properties, with special focus on the static electric dipole polarizability, are performed employing extensive valence basis sets and corresponding scalar-relativistic energy-consistent pseudopotentials.

The energetic separation of the cesium isomers for the reported cluster sizes is in most cases marginal, and it is found that a large number of unsymmetric isomers are more stable than highly symmetric species, thus contradicting proposed icosahedral growth-patterns. An evolution towards more compact and spherically shaped structures is, however, indicated by the calculated isotropic and anisotropic polarizabilities. The transition from two-dimensional to three-dimensional structures is ambiguous, as the hexamer shows essentially the same energetic preference for planar and three-dimensional structures. The mean polarizability per atom can be approximated nicely by the jellium model, and it is found that the most stable isomers mostly exhibit the smallest mean polarizabilities per atom. A band gap closure is not observed yet for this size-range.

Singlet spin-states clearly dominate the energetically lowest-lying isomers of tin clusters, and the tetracapped trigonal prism is found as a major structural motif in many

isomers. Both the isotropic and anisotropic polarizabilities per atom indicate that the structural evolution of the proposed global minima with cluster size tends towards elongated and prolate morphologies. The static polarizability of atomic tin is calculated for the first time at the scalar-relativistic and 4-component relativistic CCSD(T)-level. The inclusion of spin-orbit effects reduces the atomic polarizability by about 11 %, and the final value is in good agreement with experimental measurements. The qualitative agreement of calculated dipole moments and mean polarizabilities with the observed values is very satisfying, indicating that most predicted global minima structures are found and thus confirms the methods employed to calculate the mean polarizabilities. Temperature dependent beam deflection measurements reveal that clusters with large permanent dipole moments result in significantly larger beam deflections and explain why in experiments usually larger, effective polarizabilities are obtained than from theory.

More stable isomers than previously reported are also found for the gold clusters, which throws new light into the controversial discussion of the crossover from planar to three-dimensional structures. Most recent studies predict the Au_{13} isomer to be the last planar structure, while on the contrary more stable, three-dimensional isomers are found for the Au_{11} and Au_{13} isomer in this study. Previously reported odd-even oscillations of the electronic properties of gold clusters are also calculated in the evolution of polarizabilities per atom as a function of cluster size, where odd-sized clusters exhibit usually larger polarizabilities.

The three most stable isomers of copper nonamer clusters lie energetically too close to adopt either of them as the preferred global minimum. The dipole moments of a set of clusters are reported for the first time. They are rather small, showing little charge separation. Previously calculated polarizabilities per atom are confirmed and the discrepancy between the calculated and observed polarizabilities are attributed to a possible systematic error in the experiment.

Within the halogen series of dimeric and trimeric complexes of the type [X-M-PH_3], it is found that DFT can reproduce metallophilic interactions in the present systems, and that the counterpoise corrected interaction energies reveal that the metallophilicity apparently decreases down group 11 for both dimers and trimers. This is in accord with the previously predicted trend for the dimers of these systems.

Chapter 10

Appendix

10.1 Basis Sets

Table 10.1: Basis set used for cesium

	Exponent	Coefficient		Exponent	Coefficient
S			P		
	132.350219	-0.000589		1.92919385	1.000000
	67.0303504	0.002513	P		
	33.4646400	-0.006236		0.81186955	1.000000
	7.45885112	-0.031642	P		
S				0.34691639	1.000000
	3.00149096	1.000000	P		
S				0.13384182	1.000000
	1.46108301	1.000000	P		
S				0.0516367	1.000000
	0.40220942	1.000000	P		
S				0.0199217	1.000000
	0.17558056	1.000000	P		
S				0.0076859	1.000000
	0.045835	1.000000	D		
S				0.91618110	1.000000
	0.02000918	1.000000	D		
S				0.34691639	1.000000
	0.008735	1.000000	F		
P				0.916181	1.000000
	38.6167425	0.000326			
	18.5150602	-0.001341			
	9.13909091	0.001814			
	4.12932541	0.043747			

Table 10.2: Basis set used for tin (Basis A)

	Exponent	Coefficient		Exponent	Coefficient
S			P		
	1586.593652	0.000303		0.817986	1.000000
	234.779089	0.001436	P		
	25.843943	-0.064023		0.384912	1.000000
	18.959130	0.210108	P		
	7.981470	-0.385796		0.178019	1.000000
	5.171401	-0.372267	P		
	2.308745	0.556666		0.080521	1.000000
S			P		
	1.252033	1.000000		0.035547	1.000000
S			P		
	1586.593652	-0.000120		0.015	1.000000
	234.779089	-0.000565	P		
	25.843943	0.022824		0.0075	1.000000
	18.959130	-0.078195	D		
	7.981470	0.172563		53.061191	0.001798
	5.171401	0.115604		10.022209	-0.036340
	2.308745	-0.255761		7.423631	0.059630
S				3.398105	0.243636
	1.252033	1.000000		1.777932	0.375303
S			D		
	0.657126	1.000000		0.905763	1.000000
S			D		
	0.271380	1.000000		0.439545	1.000000
S			D		
	0.123219	1.000000		0.191423	1.000000
S			D		
	0.054495	1.000000		0.06	1.000000
S			D		
	0.02	1.000000		0.02	1.000000
S			D		
	0.01	1.000000		0.01	1.000000
P			F		
	198.071811	0.000253		3.882	1.000000
	22.140282	0.006348	F		
	16.289158	0.061749		1.191	1.000000
	12.066043	-0.126788	F		
	7.008325	-0.142358		0.4	1.000000
	2.941000	0.354530	F		
	1.582025	0.516249		0.15	1.000000
P			F		
	0.817986	1.000000		0.075	1.000000
P			G		
	198.071811	-0.000074		2.915	1.000000
	22.140282	-0.001360	G		
	16.289158	-0.019290		1.0	1.000000
	12.066043	0.040441	G		
	7.008325	0.033729		0.3	1.000000
	2.941000	-0.113874	G		
	1.582025	-0.163307		0.15	1.000000

Table 10.3: Basis set used for tin (Basis B)

	Exponent	Coefficient		Exponent	Coefficient
S					
	1586.593652	0.000303	P		
	234.779089	0.001436		0.384912	1.000000
	25.843943	-0.064023	P		
	18.959130	0.210108		0.178019	1.000000
	7.981470	-0.385796	P		
	5.171401	-0.372267		0.080521	1.000000
	2.308745	0.556666	P		
	1.252033	.672586		0.035547	1.000000
S			D		
	1586.593652	-0.000120		53.061191	0.001798
	234.779089	-0.000565		10.022209	-0.036340
	25.843943	0.022824		7.423631	0.059630
	18.959130	-0.078195		3.398105	0.243636
	7.981470	0.172563		1.777932	0.375303
	5.171401	0.115604		0.905763	.3366632
	2.308745	-0.255761	D		
	1.252033	-.409739		0.439545	1.000000
S			D		
	0.657126	1.000000		0.191423	1.000000
S			D		
	0.271380	1.000000		0.06	1.000000
S					
	0.123219	1.000000			
S					
	0.054495	1.000000			
P					
	198.071811	0.000253			
	22.140282	0.006348			
	16.289158	0.061749			
	12.066043	-0.126788			
	7.008325	-0.142358			
	2.941000	0.354530			
	1.582025	0.516249			
P					
	198.071811	-0.000074			
	22.140282	-0.001360			
	16.289158	-0.019290			
	12.066043	0.040441			
	7.008325	0.033729			
	2.941000	-0.113874			
	1.582025	-0.163307			
P					
	0.817986	1.000000			

Table 10.4: Basis set used for tin (Basis C)

	Exponent	Coefficient		Exponent	Coefficient
S					
	7.9679550E+07	1.00000		1.0643468E+02	1.00000
	2.1111952E+07	1.00000		5.8879326E+01	1.00000
	7.1669636E+06	1.00000		3.2761215E+01	1.00000
	2.6922571E+06	1.00000		1.8087021E+01	1.00000
	1.0939261E+06	1.00000		1.0090743E+01	1.00000
	4.6648190E+05	1.00000		5.6311244E+00	1.00000
	2.0711902E+05	1.00000		3.0577847E+00	1.00000
	9.4950649E+04	1.00000		1.6085284E+00	1.00000
	4.4827047E+04	1.00000		8.2204937E-01	1.00000
	2.1739911E+04	1.00000		3.7962321E-01	1.00000
	1.0808631E+04	1.00000		1.7493628E-01	1.00000
	5.4996837E+03	1.00000		7.7726430E-02	1.00000
	2.8620699E+03	1.00000		3.3744350E-02	1.00000
	1.5236558E+03	1.00000	D		
	8.3025497E+02	1.00000		1.8146443E+04	1.00000
	4.6332252E+02	1.00000		4.6133170E+03	1.00000
	2.6511834E+02	1.00000		1.6313708E+03	1.00000
	1.5730929E+02	1.00000		6.8231586E+02	1.00000
	1.0446732E+02	1.00000		3.1716834E+02	1.00000
	7.1329590E+01	1.00000		1.5841390E+02	1.00000
	4.4743352E+01	1.00000		8.2994569E+01	1.00000
	2.7007722E+01	1.00000		4.5071562E+01	1.00000
	1.5893325E+01	1.00000		2.5018308E+01	1.00000
	9.7731771E+00	1.00000		1.4047922E+01	1.00000
	6.0199525E+00	1.00000		7.9655373E+00	1.00000
	3.7110616E+00	1.00000		4.4905065E+00	1.00000
	2.2706859E+00	1.00000		2.4753573E+00	1.00000
	1.3424342E+00	1.00000		1.3400768E+00	1.00000
	7.5165204E-01	1.00000		7.2142291E-01	1.00000
	3.5062253E-01	1.00000		3.9545442E-01	1.00000
	1.8509389E-01	1.00000		2.1573367E-01	1.00000
	9.2119430E-02	1.00000		8.8334165E-02	1.00000
	4.4348908E-02	1.00000	F		
P				3.88	1.00000
	4.3524067E+07	1.00000		1.2	1.00000
	9.9362626E+06	1.00000		0.4	1.00000
	2.6682617E+06	1.00000		0.15	1.00000
	8.0036417E+05	1.00000		0.075	1.00000
	2.6250825E+05	1.00000			
	9.3697913E+04	1.00000			
	3.5815467E+04	1.00000			
	1.4582743E+04	1.00000			
	6.3255199E+03	1.00000			
	2.9056573E+03	1.00000			
	1.4022722E+03	1.00000			
	7.0514880E+02	1.00000			
	3.6656695E+02	1.00000			
	1.9557480E+02	1.00000			

Table 10.5: Basis set used for gold clusters

	Exponent	Coefficient		Exponent	Coefficient		Exponent	Coefficient
S			P			F		
	55.684714	-0.006193		0.080759	-0.000667		0.15	1.000000
	35.989900	0.068959		0.038444	0.000807	G		
	24.637611	-0.280695		0.019695	-0.000392		0.4	1.000000
	16.991456	0.423086	P					
	5.352684	-0.818719		33.546791	-0.000417			
	1.663852	0.469411		22.937499	0.005072			
	1.138617	0.547926		15.739235	-0.015245			
	0.778700	0.160312		6.062878	0.062672			
	0.532166	0.212556		1.780863	-0.129327			
	0.162487	0.009912		0.922856	-0.137172			
	0.073074	-0.000969		0.456760	-0.003424			
S				0.187112	0.187462			
	55.684714	0.001446		0.080759	0.320966			
	35.989900	-0.020136		0.038444	0.384369			
	24.637611	0.091083		0.019695	0.234423			
	16.991456	-0.145680	P					
	5.352684	0.321145		0.038444	1.000000			
	1.663852	-0.311729	P					
	1.138617	-0.105361		0.019695	1.000000			
	0.778700	-0.403305	P					
	0.532166	0.056261		0.010294	1.000000			
	0.162487	0.524192	D					
	0.073074	0.527275		123.28225	0 0.000028			
S				14.529266	0.001999			
	0.162487	1.000000		9.946680	0.017169			
S				6.859780	-0.071160			
	0.073074	1.000000		1.818774	0.295063			
S				0.822603	0.455170			
	0.032891	1.000000		0.341105	0.352694			
P				0.126798	0.116879			
	33.546791	0.004887		0.05 0.00	1794			
	22.937499	-0.034127	D					
	15.739235	0.082581		0.126798	1.000000			
	6.062878	-0.288747	D					
	1.780863	0.488140		0.05	1.000000			
	0.922856	0.493544	F					
	0.456760	0.186631		0.5	1.000000			
	0.187112	0.017579						

Table 10.6: Basis set used for copper nonamers

	Exponent	Coefficient		Exponent	Coefficient
S			D		
	27.53091	-0.10565		0.74071	1.00000
	14.59263	0.29217	D		
	6.15443	0.62754		0.21651	1.00000
S			D		
	4.89927	1.00000		0.05492	1.00000
S			D		
	2.36351	1.00000		0.01500	1.00000
S			F		
	1.13720	1.00000		11.60973	0.11427
S				4.67063	0.33370
	0.50889	1.00000	F		
S				1.85482	1.00000
	0.26090	1.00000	F		
S				0.58635	1.00000
	0.12573	1.00000	G		
S				23.21669	0.13014
	0.06667	1.00000		7.84863	0.19765
S				2.78019	0.08969
	0.02409	1.00000	G		
S				1.00078	1.00000
	0.01	1.00000			
S					
	0.005	1.00000			
P					
	79.14552	0.00247			
	17.22254	-0.07389			
	7.69319	0.02583			
P					
	4.00736	1.00000			
P					
	1.86406	1.00000			
P					
	0.85030	1.00000			
P					
	0.36183	1.00000			
P					
	0.12873	1.00000			
P					
	0.04036	1.00000			
P					
	0.02	1.00000			
P					
	0.008	1.00000			
D					
	50.18287	0.02203			
	15.66677	0.10969			
	5.69954	0.25889			
D					
	2.13198	1.00000			

Bibliography

[1] R. L. Johnston, *Atomic and Molecular Clusters* (Taylor & Francis, 2002)

[2] C. R. Henry, *Surf. Sci. Rep.* **1998**, *31*, 231

[3] G. Padeletti, P. Fermo, *Appl. Phys. A* **2003**, *76*, 515

[4] I. Borgia, B. Brunetti, I. Mariani, A. Sgamellotti, F. Cariati, P. Fermo, M. Mellini, C. Viti, G. Padeletti, *Appl. Surf. Sci.* **2002**, *185*, 206

[5] D. J. Wales, *Energy Landscapes* (Cambridge University Press, 2003)

[6] K. D. Bonin, V. V. Kresin, *Electric-Dipole Polarizabilities of Atoms, Molecules and Clusters* (World Scientific Publishing, 1997)

[7] P. Schwerdtfeger, in *Computational Aspects of Electric Polarizability Calculations: Atoms, Molecules and Clusters*, ed. G. Maroulis, (Imperial College Press, London, 2006); pg.1-32.

[8] H. Schmidbaur, S. Cronje, B. Djordjevic, O. Schuster, *Chem. Phys.* **2005**, *311*, 151

[9] M. Bardají, A. Laguna, *J. Chem. Ed.* **1999**, *76*, 201

[10] F. Jensen, *Introduction to Computational Chemistry* (John Wiley & Sons, Ltd, 2003)

[11] C. J. Cramer, *Essentials of Computational Chemistry Theories and Models* (John Wiley & Sons, Ltd, 2002)

[12] A. Szabo, N. S. Ostlund, *Modern Quantum Chemistry Introduction to Advanced Electronic Structure Theory* (Dover Publications, Inc., 1996)

[13] C. Møller, M. S. Plesset, *Phys. Rev.* **1934**, *46*, 618

[14] R. J. Bartlett, *J. Phys. Chem.* **1989**, *93*, 1697

[15] K. Raghavachari, G. W. Trucks, J. A. Pople, M. Head-Gordon, *Chem. Phys. Lett.* **1989**, *157*, 479

[16] P. Hohenberg, W. Kohn, *Phys. Rev. B* **1964**, *136*, 864

[17] P Pyykkö, J. P. Desclaux, *Acc. Chem. Res.* **1979**, *12*, 276

[18] K. S. Pitzer, *Acc. Chem. Res* **1979**, *12*, 271

[19] P. Pyykkö, *Chem. Rev.* **1988**, *88*, 563

[20] P. Pyykkö, *Angew. Chem. Int. Ed.* **2004**, *43*, 4412

[21] P. Schwerdtfeger, G. A. Bowmaker, *J. Chem. Phys.* **1994**, *100*, 4487

[22] R. Wesentrup, T. Hunt, P. Schwerdtfeger, *J. Chem. Phys.* **2000**, *112*, 9356

[23] P. Schwerdtfeger, *Heteroat. Chem.* **2002**, *13*, 578

[24] H. Hellmann, *J. Chem. Phys.* **1935**, *3*, 61

[25] P. Gombàs, *Z. Phys.* **1935**, *94*, 473

[26] J. C. Phillips, L. Kleinmann, *Phys. Rev.* **1959**, *116*, 287

[27] http://www.theochem.uni-stuttgart.de/pseudopotentiale

[28] H. Stoll, B. Metz, M. Dolg, *J. Comput. Chem.* **2002**, *23*, 767

[29] W. D. Knight, K. Clemenger, W. A. de Heer, W. A. Saunders, *Phys. Rev. B* **1985**, *31*, 2539

[30] W. Ekardt, *Phys. Rev. Lett.* **1984**, *52*, 1925

[31] H. D. Cohen, C. C. J. Roothaan, *J. Chem. Phys.* **1965**, *43*, 534

[32] H. A. Bethe, R. Jackiw, *Intermediate Quantum Mechanics*, 3rd ed. (Benjamin, Menlo Park, 1986)

[33] S. Schäfer, Diplomarbeit, Technische Universität Darmstadt, **2004**
A. Kyriopoulos, Diplomarbeit, Technische Universität Darmstadt, **2006**

[34] L. Maguire, S. Szilagyi, R. Scholten, *Rev. Sci. Instrum.* **2004**, *75*, 3077

[35] W. Ekardt, *Metal Clusters* (Wiley & Sons, England, 1999)

[36] K. J. Klabunde, *Free Atoms, Clusters, and Nanoscale Particles* (Academic Press, 1994)

[37] J. Jellinek, *Theory of Atomic and Molecular Clusters* (Springer-Verlag, 1999)

[38] D. M. Deaven, N. Tit, J. R. Morris, K. M. Ho, *Chem. Phys. Lett.* **1996**, *256*, 195

[39] R. L. Johnston, *Dalton. Trans.* **2003**, 4193

[40] C. Darwin, *On The Origin of Species* (John Murray, 1859)

[41] B. Hartke, *J. Phys. Chem.* **1993**, *97*, 9973

[42] Y. Zeiri, *Phys. Rev. E* **1995**, *51*, R2769

[43] J. B. Lamarck, *Zoological Philosophy* (Paris, 1809)

[44] A. Hermann, R. P. Krawczyk, M. Lein, P. Schwerdtfeger, I. P. Hamilton, J. J. P. Steward, *Phys. Rev. A* **2007**, *76*, 013202

[45] B. Hartke, *Theor. Chem. Acc.* **1998**, *99*, 241

[46] D. M. Deaven, K. M. Ho, *Phys. Rev. Lett.* **1995**, *75*, 288

[47] P. Schwerdtfeger, *Relativistic Electronic Structure Theory Part 1. Fundamentals* (Elsevier, 2002)

[48] W. D. Knight, K. Clemenger, W. A. de Heer, W. A. Saunders, M. Y. Chou, M. L. Cohen, *Phys. Rev. Lett.* **1984**, *52*, 2141

[49] W. A. de Heer, *Rev. Mod. Phys.* **1993**, *65*, 611

[50] D. E. Beck, *Phys. Rev. B* **1984**, *30*, 6935

[51] G. Tikhonov, V. Kasperovich, K. Wong, V. V. Kresin, *Phys. Rev. A* **2001**, *64*, 063202

[52] I. S. Lim, M. Pernpointner, M. Seth, J. K. Laerdahl, P. Schwerdtfeger, *Phys. Rev. A* **1999**, *60*, 2822

[53] J. M. Amini, H. Gould, *Phys. Rev. Lett.* **2003**, *91*, 153001

[54] S. A. Blundell, C. Guet, R. R. Zope, *Phys. Rev. Lett.* **2000**, *84*, 4826

[55] K. R. S. Chandrakumar, T. K. Ghanty, S. K. Ghosh, *Int. J. Quantum Chem.* **2005**, *105*, 166

[56] P. Calaminici, A. M. Köster, A. Vela, *J. Chem. Phys.* **2000**, *113*, 2199

[57] R. Antoine, D. Rayane, A. R. Allouche, M. Aubert-Frécon, E. Benichou, F. W. Dalby, Ph. Dugourd, M. Broyer, *J. Chem. Phys.* **1999**, *110*, 5568

[58] D. Rayane, A. R. Allouche, E. Benichou, R. Antoine, M. Aubert-Frécon, Ph. Dugourd, M. Broyer, C. Ristori, F. Chandezon, B. A. Huber, C. Guet, *Eur. Phys. J. D* **1999**, *9*, 243

[59] E. Benichou, R. Antoine, D. Rayane, B. Vezin, F. W. Dalby, Ph. Dugourd, M. Broyer, C. Ristori, F. Chandezon, B. A. Huber, J. C. Rocco, S. A. Blundell, C. Guet, *Phys. Rev. A* **1999**, *59*, R1

[60] D. Plavšić, J. Koutecký, G. Pacchioni, V. Bonačić-Koutecký, *J. Phys. Chem.* **1982**, *87*, 1096

[61] I. Boustani, W. Pewestorf, P. Fantucci, V. Bonačić-Koutecký, J. Koutecký, *Phys. Rev. B* **1987**, *35*, 9437

[62] F. Wang, N. Andriopoulos, N. Wright, E. I. von Nagy-Felsobuki, *J. of Cluster Science* **1991**, *2*, 203

[63] M. Y. Chou, A. Cleland, M. L. Cohen, *Solid St. Commun.* **1984**, *52*, 645

[64] C. R. Ekstrom, J. Schmiedmayer, M. S. Chapman, T. D. Hammond, D. E. Pritchard, *Phys. Rev. A* **1995**, *51*, 3883

[65] C. Bréchignac, Ph. Cahuzac, *Chem. Phys. Lett.* **1985**, *117*, 365

[66] A. vom Felde, J. Fink, W. Ekardt, *Phys. Rev. Lett.* **1988**, *61*, 2249

[67] C. Bréchignac, Ph. Cahuzac, J. Ph. Roux, *J. Chem. Phys.* **1987**, *87*, 229

[68] A. K. Ray, S. D. Altekar, *Phys. Rev. B* **1990**, *42*, 1444

[69] C. Bréchignac, Ph. Cahuzac, F. Carlier, M. de Frutos, J. Ph. Roux, *Phys. Rev. B* **1993**, *47*, 2271

[70] G. Gardet, F. Rogemond, H. Chermette, *J. Chem. Phys.* **1996**, *105*, 9933

[71] R. O. Jones, A. I. Lichtenstein, J. Hutter, *J. Chem. Phys.* **1997**, 106, 4566

[72] S. E. Wheeler, K. W. Sattelmeyer, P. v. R. Schleyer, H. F. Schaefer III, *J. Chem. Phys.* **2004**, *120*, 4683

[73] P. Calaminici, K. Jug, A. M. Köster, *J. Chem. Phys.* **1999**, *111*, 4613

[74] J. Guan, M. E. Casida, A. M. Köster, D. R. Salahub, *Phys. Rev. B* **1995**, *52*, 2184

[75] W. E. Ernst, R. Huber, S. Jiang, R. Beuc, M. Movre, G. Pichler, *J. Chem. Phys.* **2006**, *124*, 024313

[76] I. Moullet, J. L. Martins, F. Reuse, J. Buttet, *Phys. Rev. B* **1990**, *42*, 11598

[77] I. Moullet, J. L. Martins, F. Reuse, J. Buttet, *Phys. Rev. Lett.* **1990**, *65*, 476

[78] K. B. Sophy, P. Calaminici, S. Pal, *J. Chem. Theory Comput.* **2007**, *3*, 716

[79] G. Durand, F. Spiegelman, A. R. Allouche, *Eur. Phys. J. D* **2003**, *24*, 19

[80] I. A. Solov'yov, A. V. Solov'yov, W. Greiner, *Phys. Rev. A* **2002**, *65*, 053203

[81] L. Kronik, I. Vasiliev, J. R. Chelikowsky, *Phys. Rev. B* **2000**, *62*, 9992

[82] S. Kümmel, T. Berkus, P.-G. Reinhard, M. Brack, *Eur. Phys. J. D* **2000**, *11*, 239

[83] A. Kornath, R. Ludwig, A. Zoermer, *Angew. Chem. Int. Ed.* **1998**, *37*, 1575

[84] W. A. Saunders, K. Clemenger, W. A. de Heer, W. D. Knight, *Phys. Rev. B* **1985**, *32*, 1366

[85] M. Krauss, W. J. Stevens, *Chem. Phys. Lett.* **1989**, *164*, 514

[86] U. Lammers, G. Borstel, A. Mañanes, J. A. Alonso, *Z. Phys. D - Atoms, Molecules and Clusters* **1990**, *17*, 203

[87] A. Mañanes, J. A. Alonso, U. Lammers, G. Borstel, *Phys. Rev. B* **1991**, *44*, 727

[88] Y. Li, E. Blaisten-Barojas, D. A. Papaconstantopoulos, *Phys. Rev. B* **1998**, *57*,15519

[89] S. K. Lai, P. J. Hsu, K. L. Wu, W. K. Liu, M. Iwamatsu, *J. Chem. Phys.* **2002**, *117*, 10715

[90] M. A. Basu, D. K. Maity, D. Das, T. Mukherjee, *J. Chem. Phys.* **2006**, *124*, 024325

[91] J. Gspann, *Z. Phys. D* **1991**, *20*, 421

[92] I. Moullet, W. Andreoni, P. Giannozzi, *J. Chem. Phys* **1989**, *90*, 7306

[93] E. Eliav, M. J. Vilkas, Y. Ishikawa, U. Kaldor, *Chem. Phys* **2005**, *311*, 163

[94] H. G. Limberger, T. P. Martin, *Z. Phys. D* **1989**, *12*, 439

[95] H. G. Limberger, T. P. Martin, *J. Chem. Phys.* **1988**, *90*, 2979

[96] P. Fayet, J. P. Wolf, L. Wöste, *Phys. Rev. B* **1986**, *33*, 6792

[97] M. S. Safronova, C. W. Clark, *Phys. Rev. A* **2004**, *69*, 040501

[98] A. Derevianko, W. R. Johnson, M. S. Safronova, J. F. Babb, *Phys. Rev. Lett.* **1999**, *82*, 3589

[99] R. W. Molof, H. L. Schwartz, T. M. Miller, B. Bederson, *Phys. Rev. A* **1974**, *10*, 1131

[100] W. D. Hall, J. C. Zorn, *Phys. Rev. A* **1974**, *10*, 1141

[101] G. E. Chamberlain, J. C. Zorn, *Phys. Rev.* **1963**, *129*, 677

[102] D. DiBerardino, C. E. Tanner, A. Sieradzan, *Phys. Rev. A* **1998**, *57*, 4204

[103] L. R. Hunter, D. Krause Jr., K. E. Miller, D. J. Berkeland, M. G. Boshier, *Opt. Commun.* **1992**, *94*, 210

[104] H. L. Zhou, D. W. Norcross, *Phys. Rev. A* **1989**, *40*, 5048

[105] L. R. Hunter, D. Krause, Jr., S. Murthy, T. W. Sung, *Phys. Rev. A* **1988**, *37*, 3283

[106] C. E. Tanner, C. Wiemann, *Phys. Rev. A* **1988**, *38*, 162

[107] K. M. McHugh, J. G. Eaton, G. H. Lee, H. W. Sarkas, L. H. Kidder, J. T. Snodgrass, M. R. Manaa, K. H. Bowen, *J. Chem. Phys.* **1989**, *91*, 3792

[108] H. Fallgren, K. M. Brown, T. P. Martin, *Z. Phys. D. - Atoms, Molecules and Clusters* **1991**, *19*, 81

[109] H. Fallgren, T. P. Martin, *Chem. Phys. Lett* **1990**, *168*, 233

[110] ECP46MDF + (8s8p2d1f) for **Cs**
I. S. Lim, P. Schwerdtfeger, B. Metz, H. Stoll, *J. Chem. Phys.* **2005**, *122*, 104103
Note, that the basis set from this reference is larger (8s8p5d3f2g), but otherwise identical (see Appendix for details on basis set).

[111] A. D. Becke, *Phys. Rev. A* **1988**, *38*, 3098

[112] J. P. Perdew, *Phys. Rev. B* **1986**, *33*, 8822

[113] S. Chrétien, D. R. Salahub, *Phys. Rev. B* **2002**, *66*, 155425

[114] R. P. Gupta, *Phys. Rev. B* **1981**, *23*, 6265

[115] J. E. Jones, A. E. Ingham, *Proc. R. Soc. London, A* **1925**, *107*, 636

[116] D. R. Lide, *CRC Handbook of Chemistry and Physics* (CRC Press LLC, 2001 - 2002)

[117] T. Andersen, H. K. Haugen, H. Hotop, *J. Phys. Chem. Ref. Data*, **1999**, *28*, 1511

[118] J. Slater, F. H. Read, S. E. Novick, W. C. Lineberger, *Phys. Rev. A* **1978**, *17*, 201

[119] A. J. Dekker, *Solid State Physics* (Macmillan & CO LTD, London, 1958)

[120] J. Wang, M. Yang, G. Wang, J. Zhao, *Chem. Phys. Lett.* **2003**, *367*, 448

[121] G. Höning, M. Czajkowski, M. Stock, W. Demtröder, *J. Chem. Phys.* **1979**, *71*, 2138

[122] C. E. Weir, G. J. Piermarini, S. Block, *J. Chem. Phys.* **1971**, *54*, 2768

[123] K. A. Gschneidner, Jr., *Solid State Phys.* **1964**, *16*, 275

[124] F. W. Averill, *Phys. Rev. B* **1972**, *6*, 3637

[125] The parametrization of the exchange-correlation energy of the homogeneous electron gas (*local density approximation*) given by S. H. Vosko, L. Wilk, M. Nusair, *Can. J. Phys.* **1980**, *58*, 1200

[126] M. Pereiro, D. Baldomir, J. E. Arias, *Phys. Rev. A* **2007**, *75*, 063204

[127] F. Baletto, R. Ferrando, *Rev. Mod. Phys* **2005**, *77*, 371

[128] W. G. Burgers, L. J. Groen, *Discuss. Faraday Soc.* **1957**, *23*, 183

[129] K. Joshi, D. G. Kanhere, S. A. Blundell, *Phys. Rev. B* **2002**, *66*, 155329

[130] A. A. Shvartsburg, M. F. Jarrold, *Phys. Rev. Lett.* **2000**, *85*, 2530

[131] P. Pawlow, *Z. Phys. Chem.* **1909**, *65*, 1

[132] Ph. Buffat, J. P. Borel, *Phys. Rev. A* **1976**, *13*, 2287

[133] M. Takagi, *J. Phys. Soc. Jpn* **1954**, *9*, 359

[134] S. L. Lai, J. Y. Guo, V. Petrova, G. Ramanath, L. H. Allen, *Phys. Rev. Lett.* **1996**, *77*, 99

[135] K. Joshi, D. G. Kanhere, S. A. Blundell, *Phys. Rev. B* **2003**, *67*, 235413

[136] F. Chuang, C. Z. Wang, S. Ögüt, J. R. Chelikowsky, K. M. Ho, *Phys. Rev. B*, *69*, 165408

[137] G. A. Breaux, C. M. Neal, B. Cao, M. F. Jarrold, *Phys. Rev. B* **2005**, *71*, 073410

[138] S. Krishnamurty, K. Joshi, D. G. Kanhere, S. A. Blundell, *Phys. Rev. B* **2006**, *73*, 045419

[139] O. Oña, V. E. Bazterra, M. C. Caputo, J. C. Facelli, P. Fuentealba, M. B. Ferraro, *Phys. Rev. A* **2006**, *73*, 053203

[140] S. Yoo, X. C. Zeng, *J. Chem. Phys.* **2006**, *124*, 054304

[141] V. E. Bazterra, O. Oña, M. C. Caputo, M. B. Ferraro, P. Fuentealba, J. C. Facelli, *Phys. Rev. A* **2004**, *69*, 053202

[142] X. Zhu, X. C. Zeng, *J. Chem. Phys.* **2003**, *118*, 3558

[143] V. Kumar, Y. Kawazoe, *Phys. Rev. Lett.* **2001**, *87*, 045503

[144] B. K. Panda, S. Mukherjee, S. B. Behera, *Phys. Rev. B* **2001**, *63*, 045404

[145] A. A. Shvartsburg, B. Liu, M. F. Jarrold, K. M. Ho, *J. Chem. Phys.* **2000**, *112*, 4517

[146] K. M. Ho, A. A. Shvartsburg, B. Pan, Z. Y. Lu, C. Z. Wang, J. G. Wacker, J. L. Fye, M. F. Jarrold, *Nature* **1998**, *392*, 582

[147] B. Hartke, *Theor. Chem. Acc.* **1998**, *99*, 241

[148] A. Sieck, D. Porezag, Th. Frauenheim, M. R. Pederson, K. Jackson, *Phys. Rev. A* **1997**, *56*, 4890

[149] K. Raghavachari, *J. Chem. Phys.* **1986**, *84*, 5672

[150] J. Bai, L. F. Cui, J. Wang, S. Yoo, X. Li, J. Jellinek, C. Koehler, T. Frauenheim, L. S. Wang, X. C. Zeng, *J. Phys. Chem.* **2006**, *110*, 908

[151] B. Liu, Z. Y. Lu, B. Pan, C. Z. Wang, K. M. Ho, A. A. Shvartsburg, M. F. Jarrold, *J. Chem. Phys.* **1998**, *109*, 9401

[152] X. Jing, N. Troullier, J. R. Chelikowsky, K. Wu, Y. Saad, *Solid State Communications* **1995**, *96*, 231

[153] I. Vasiliev, S.Ögüt, J. R. Chelikowsky, *Phys. Rev. B* **2002**, *65*, 115416

[154] K. A. Jackson, M. Yang, I. Chaudhuri, Th. Frauenheim, *Phys. Rev. A* **2005**, *71*, 033205

[155] G. Maroulis, D. Begué, C. Pouchan, *J. Chem. Phys.* **2003**, *119*, 794

[156] R. Schäfer, S. Schlecht, J. Woenckhaus, and J. A. Becker, *Phys. Rev. Lett.* **1996**, *76*, 471.

[157] J. Müller, B. Liu, A. A. Shvartsburg, S. Ögüt, J. R. Chelikowsky, K. W. M. Siu, K. M. Ho, G. Ganteför, *Phys. Rev. Lett.* **2000**, *85*, 1666

[158] S. Ma, G. Wang, *J. Mol. Struct. (Theochem)* **2006**, *767*, 75

[159] J. Wang, J. G. Han, *J. Chem. Phys.* **2005**, *123*, 244303

[160] B. X. Li, F. S. Liang, Y. H. Zhu, G. Q. Lai, *J. Mol. Struct. (Theochem)* **2005**, *756*, 19

[161] S. Bulusu, S. Yoo, X. C. Zeng, *J. Chem. Phys.* **2005**, *122*, 164305

[162] J. Wang, G. Wang, J. Zhao, *Phys. Rev. B* **2001**, *64*, 205411

[163] B. Z. Li, P. L. Cao, *Phys. Rev. B* **2000**, *62*, 15788

[164] A. A. Shvartsburg, B. Liu, Z. Y. Lu, C. Z. Wang, M. F. Jarrold, K. M. Ho, *Phys. Rev. Lett.* **1999**, *83*, 2167

[165] I. Vasiliev, S.Ögüt, J. R. Chelikowsky, *Phys. Rev. Lett.* **1997**, *78*, 4805

[166] J. M. Hunter, J. L. Fye, M. F. Jarrold, J. E. Bower, *Phys. Rev. Lett.* **1994**, *73*, 2063

[167] R. E. Honig, *J. Chem. Phys.* **1953**, *21*, 573

[168] K. A. Gingerich, A. Desideri, D. L. Cocke, *J. Chem. Phys.* **1975**, *62*, 731

[169] A. B. Anderson, *J. Chem. Phys.* **1975**, *63*, 4430

[170] K. Balasubramanian, K. S. Pitzer, *J. Chem. Phys.* **1982**, *78*, 321

[171] K. Balasubramanian, *J. Chem. Phys.* **1986**, *85*, 3401

[172] D. Dai, K. Balasubramanian, *J. Chem. Phys.* **1992**, *96*, 8345

[173] D. Dai, K. Balasubramanian, *J. Phys. Chem.* **1992**, *96*, 9236

[174] D. Dai, K. Balasubramanian, *J. Phys. Chem.* **1996**, *100*, 19321

[175] D. Dai, K. Balasubramanian, *J. Chem. Phys.* **1998**, *108*, 4379

[176] V. E. Bondybey, M. Heaven, T. A. Miller, *J. Chem. Phys.* **1983**, *78*, 3593

[177] K. Laihing, R. G. Wheeler, W. L. Wilson, M. A. Duncan, *J. Chem. Phys.* **1987**, *87*, 3401

[178] G. Ganteför, M. Gausa, K. H. Meiswes-Broer, H. O. Lutz, *Z. Phys. D* **1989**, *12*, 405

[179] S. Yoshida, K. Fuke, *J. Chem. Phys.* **1999**, *111*, 3880

[180] T. P. Martin, H. Schaber, *J. Chem. Phys.* **1985**, *83*, 855

[181] X. Ren, K. M. Ervin, *Chem. Phys. Lett.* **1992**, *198*, 229

[182] W. Plass, H. Stoll, H. Preuss, A. Savin, *J. Mol. Struct. (Theochem)* **1995**, *339*, 67

[183] A. A. Shvartsburg, M. F. Jarrold, *Phys. Rev. A* **1999**, *60*, 1235

[184] A. A. Shvartsburg, M. F. Jarrold, *Phys. Rev. Lett.* **2000**, *317*, 615

[185] C. Jo, K. Lee, *J. Chem. Phys.* **2000**, *113*, 7268

[186] C. Majumder, V. Kumar, H. Mizuseki, Y. Kawazoe, *Chem. Phys. Lett.* **2002**, *356*, 36

[187] Y. Tai, J. Murakami, C. Majumder, V. Kumar, H. Mizuseki, Y. Kawazoe, *J. Chem. Phys.* **2002**, *117*, 4317

[188] Y. Tai, J. Murakami, C. Majumder, V. Kumar, H. Mizuseki, Y. Kawazoe, *Eur. Phys. J. D* **2003**, *24*, 295

[189] R. Pushpa, S. Narasimhan, U. Waghmare, *J. Chem. Phys.* **2004**, *121*, 5211

[190] C. Majumder, V. Kumar, H. Mizuseki, Y. Kawazoe, *Phys. Rev. B* **2001**, *64*, 233405

[191] C. Majumder, V. Kumar, H. Mizuseki, Y. Kawazoe, *Phys. Rev. B* **2005**, *71*, 035401

[192] L. F. Cui, X. Huang, L. M. Wang, D. Y. Zubarev, A. I. Boldyrev, J. Li, L. S. Wang, *J. Am. Chem. Soc.* **2006**, *128*, 8390

[193] J. Wang, G. Wang, F. Ding, H. Lee, W. Shen, J. Zhao, *Chem. Phys. Lett.* **2001**, *341*, 529

[194] Vienna *ab initio* simulation package:
G. Kresse, J. Furthmüller, *Phys. Rev. B* **1996**, *54*, 11169

[195] ECP28MDF + (10s/10p/7d/5f/4g) for **Sn** (Basis A)
B. Metz, H. Stoll, M. Dolg, *J. Chem. Phys.* **2000**, *113*, 2563
K. A. Peterson, *J. Chem. Phys.* **2003**, *119*, 11099

ECP28MDF + (6s/7p/4d) for **Sn** (Basis B)
all-electron (33s/27p/18d/5f) for **Sn** (Basis C)
See Appendix for details on basis set.

[196] A. D. Becke, *J. Chem. Phys.* **1993**, *98*, 5648

[197] Z. Y. Lu, C. Z. Wang, K. M. Ho, *Phys. Rev. B* **2000**, *61*, 2329

[198] Sascha Schäfer, Technische Universität Darmstadt (Germany), *Private Communications*

[199] T. Fleig, *Phys. Rev. A* **2005**, *72*, 052506

[200] M. Schnell, C. Herwig, J. A. Becker, *Z. Phys. Chem.* **2003**, *217*, 1003

[201] C. E. Moore *Atomic Energy Levels, VOL III* (National Bureau of Standards, Washington, 1957)

[202] A. Aguado, *Phys. Rev. B* **2003**, *67*, 212104

[203] H. J. Hutchings, *Catalysis by Gold* (Imperial College Press, 2006)

[204] M. Haruta, T. Kobayashi, H. Sano, N. Yamada, *Chem. Lett.* **1987**, *2*, 405

[205] M. Haruta, K. Saika, T. Kobayashi, S. Tsubota, Y. Nakahara, *Chem. Express* **1988**, *3*, 159

[206] M. Haruta, *The Chemical Record* **2003**, *3*, 75

[207] P. Schwerdtfeger, *to be published*

[208] P. Schwerdtfeger, *Angew. Chem. Ind. Ed.* **2003**, *42*, 1892

[209] P. Pyykkö, *Angew. Chem. Ind. Ed.* **2004**, *43*, 4412

[210] P. Pyykkö, *Chem. Rev.* **1997**, *97*, 597

[211] P. Schwerdtfeger, M. Dolg, W. H. E. Schwarz, G. A. Bowmaker, P. D. W. Boyd, *J. Chem. Phys.* **1989**, *91*, 1762

[212] P. Pyykkö, *Angew. Chem. Int. Ed.* **2002**, *41*, 3573

[213] C. Jackschath, I. Rabin, W. Schulze, *Ber. Bunsenges. Phys. Chem.* **1992**, *96*, 1200

[214] I. Katakuse, T. Ichihara, Y. Fujita, T. Matsuo, T. Sakurai, H. Matsuda, *Int. J. Mass Spectrom. Ion Proc.* **1986**, *74*, 33

[215] I. Rabin, C. Jackschath, W. Schulze, *Z. Phys. D* **1990**, *19*, 153

[216] J. Ho, K. M. Ervin, W. C. Lineberger, *J. Chem. Phys.* **1990**, *93*, 6987

[217] P. Schwerdtfeger, *Chem. Phys. Lett.* **1991**, *183*, 457

[218] O. D. Häberlen, S-C. Chung, M. Stener, N. Rösch, *J. Chem. Phys.* **1997**, *12*, 5189

[219] H. Häkkinen, U. Landman, *Phys. Rev. B* **2000**, *62*, R2287

[220] J. Wang, G. Wang, J. Zhao, *Phys. Rev. B* **2002**, *66*, 035418

[221] F. Furche, R. Ahlrichs, P. Weis, C. Jacob, S. Gilb, T. Bierweiler, M. M. Kappes, *J. Chem. Phys.* **2002**, *117*, 6982

[222] V. Bonačić-Koutecký, J. Burda, R. Mitrić, M. Ge, G. Zampella, P. Fantucci, *J. Chem. Phys.* **2002**, *117*, 3120

[223] H. Häkkinen, M. Moseler, U. Landman, *Phys. Rev. Lett.* **2002**, *89*, 033401

[224] H. Grönbeck, P. Broqvist, *Phys. Rev. B* **2005**, *71*, 073408

[225] J. Li, X. Li, H-J. Zhai, L-S. Wang, *Science* **2003**, *299*, 864

[226] J. Wang, G. Wang, J. Zhao, *Chem. Phys. Lett.* **2003**, *380*, 716

[227] R. B. King, Z. Chen, P. v. R. Schleyer, *Inorg. Chem.* **2004**, *43*, 4564

[228] K. Wu, J. Li, C. Lin, *Chem. Phys. Lett.* **2004**, *388*, 353

[229] E. Aprá, R. Ferrando, A. Fortunelli, *Phys. Rev. B* **2006**, *73*, 205414

[230] J. Zhao, J. Yang, J. G. Hou, *Phys. Rev. B* **2003**, *67*, 085404

[231] E. M. Fernández, J. M. Soler, I. L. Garzón, L. C. Balbás, *Phys. Rev. B* **2004**, *70*, 165403

[232] E. M. Fernández, J. M. Soler, L. C. Balbás, *Phys. Rev. B* **2006**, *73*, 235433

[233] L. Xiao, L. Wang, *Chem. Phys. Lett.* **2004**, *392*, 452

[234] J. Rogan, R. Ramírez, A. H. Romero, M. Kiwi, *Eur. Phys. J. D* **2004**, *28*, 219

[235] R. M. Olson, S. Varganov, M. S. Gordon, H. Metiu, S. Chretien, P. Piecuch, K. Kowalksi, S. A. Kucharski, M. Musial *J. Am. Chem. Soc.* **2005**, *127*, 1049

[236] Y-K. Han, *J. Chem. Phys.* **2006**, *124*, 024316

[237] M. Diefenbach, K. S. Kim, *J. Phys. Chem. B* **2006**, *110*, 21639

[238] R. Remacle, E. S. Kryachko, *J. Chem. Phys.* **2005**, *122*, 044304

[239] A. V. Walker, *J. Chem. Phys.* **2005**, *122*, 094310

[240] L. Xiao, B. Tollberg, X. Hu, L. Wang, *J. Chem. Phys.* **2006**, *124*, 114309

[241] W. Fa, C. Luo, J. Dong, *Phys. Rev. B* **2005**, *72*, 205428

[242] W. Fa, J. Dong, *App. Phys. Lett.* **2006**, *89*, 013117

[243] S. Bulusu, X. C. Zeng, *J. Chem. Phys.* **2006**, *125*, 154303

[244] K. Hansen, A. Helert, L. Schweikhard, M. Vogel, *Phys. Rev. A* **2006**, *73*, 063202

[245] X-B. Li, H-Y. Wang, X-D. Yang, Z-H. Zhu, Y-J. Tang, *J. Chem. Phys.* **2007**, *126*, 084505

[246] J. C. Idrobo, W. Walkosz, S. Fan Yip, S. S.Ögüt, J. Wang, J. Jellinek, *Phys. Rev. B* **2007**, *76*, 205422

[247] G. A. Bishea, M. D. Morse, *J. Chem. Phys.* **1991**, *95*, 5646

[248] M. Seidl, K-H. Meiwes-Broer, M. Brack, *J. Chem. Phys.* **1991**, *95*, 1295

[249] M. A. Cheeseman, J. R. Eyler, *J. Phys. Chem.* **1992**, *96*, 1082

[250] K. J. Taylor, C. L. Pettiette-Hall, O. Cheshnovsky, R. E. Smalley, *J. Chem. Phys.* **1992**, *96*, 3319

[251] I. Rabin, W. Schulze, *Chem. Phys. Lett.* **1993**, *201*, 265

[252] H. Handschuh, G. Ganteför, P. S. Bechthold, W. Eberhardt, *J. Chem. Phys.* **1994**, *100*, 7093

[253] Y. S. Lee, W. C. Ermler, K. S. Pitzer, A. D. McLean, *J. Chem. Phys.* **1979**, *70*, 288

[254] W. C. Ermler, Y. S. Lee, K. S. Pitzer, *J. Chem. Phys.* **1979**, *70*, 293

[255] K. Balasubramanian, P. Y. Feng, *Chem. Phys. Lett.* **1989**, *159*, 452

[256] K. Balasubramanian, *J. Mol. Struct. (Theochem)* **1989**, *202*, 291

[257] C. W. Bauschlicher Jr., S. R. Langhoff, H. Partridge, *J. Chem. Phys.* **1989**, *91*, 2412

[258] K. Balasubramanian, K. K. Das, *Chem. Phys. Lett.* **1991**, *186*, 577

[259] E. Eliav, U. Kaldor, Y. Ishikawa, *Phys. Rev. A* **1994**, *49*, 1724

[260] U. Wahlgren, B. Schimmelpfennig, S. Jusuf, H. Strömsens, O. Gropen, L. Maron, *Chem. Phys. Lett.* **1998**, *287*, 525

[261] B. A. Hess, U. Kaldor, *J. Chem. Phys.* **2000**, *112*, 1809

[262] R. Wesentrup, T. Hunt, P. Schwerdtfeger, *J. Chem. Phys.* **2000**, *112*, 9356

[263] M. Mayer, S. Krüger, N. Rösch, *J. Chem. Phys.* **2001**, *115*, 4411

[264] X. Wang, X. Wan, H. Zhou, S. Takami, M. Kubo, A. Miyamoto, *J. Mol. Struct. (Theochem)* **2002**, *579*, 221

[265] R. Guo, K. Balasubramanian, X. Wang, L. Andrews, *J. Chem. Phys.* **2002**, *117*, 1614

[266] T. Saue, H. J. Aa. Jensen, *J. Chem. Phys.* **2003**, *118*, 522

[267] T. Fleig, L. Visscher, *Chem. Phys.* **2004**, *311*, 113

[268] K. Barakat, T. R. Cundari, *Chem. Phys.* **2004**, *311*, 3

[269] F. Wang, W. Liu, *Chem. Phys.* **2005**, *311*, 63

[270] A. A. Rusakov, E. Rykova, G. E. Scuseria, A. Zaitsevskii, *J. Chem. Phys.* **2007**, *127*, 164322

[271] Y-X. Qui, S-G. Wang, W. H. E. Schwarz, *Chem. Phys. Lett.* **2004**, *397*, 374

[272] L. Gagliardi, P. Pyykkö, *Phys. Chem. Chem. Phys.* **2004**, *6*, 2904

[273] K. Manninen, P. Pyykkö, H. Häkkinen, *Phys. Chem. Chem. Phys.* **2005**, *7*, 2208

[274] ECP60MDF+(5s/5p/3d/2f/1g) for **Au**
D. Figgen, G. Rauhut, M. Dolg, H. Stoll, *Chem. Phys.* **2005**, *311*, 227
The basis set listed in the above reference, (6s/6p/4d/3f/2g), was reduced to (5s/5p/3d/2f/1g). D. Figgen, *Private Communication*

[275] J. P. Perdew, in *Electronic Structure of Solids* '91, Ed. P. Ziesche, H.Eschrig (Akademie Verlag, Berlin, 1991)
J. P. Perdew, J. A. Chevary, S. H. Vosko, K. A. Jackson, M. R. Pederson, D. J. Singh, C. Fiolhais, *Phys. Rev. B.* **1992** *46* 6671
J. P. Perdew, J. A. Chevary, S. H. Vosko, K. A. Jackson, M. R. Pederson, D. J. Singh, C. Fiolhais, *Phys. Rev. B.* **1993** *48* 4978
J. P. Perdew, K. Burke, Y. Wang *Phys. Rev. B* **1996**, *54*, 16533

[276] P. Neogrady, V. Kellö, M. Urban, A. J. Sadlej, *Int. J. Quant. Chem.* **1997**, *63*, 557

[277] P. Schwerdtfeger, G. A. Bowmaker, *Chem. Phys. Lett.* **1994**, *100*, 4487

[278] C. Kittel, *Introduction to Solid State Physics (third ed.)* (John Wiley & Sons, Inc., New York, 1976)

[279] H. Heimel, L. Romaner, J-L. Brédas, E. Zojer, *Surf. Sci.* **2006**, *600*, 4548

[280] M. B. Knickelbein, *Chem. Phys. Lett.* **1992**, *192*, 129

[281] H. Akeby, I. Panas, L. G. M. Petterson, P. Siegbahn, U. Wahlgren, *J. Chem. Phys.* **1990**, *94*, 5471

[282] O. B. Christensen, K. W. Jacobsen, J. K. Norskov, *Phys. Rev. Lett.* **1991**, *66*, 2219

[283] K. A. Jackson, *Phys. Rev. B* **1993**, *47*, 9715

[284] U. Lammers, G. Borstel, *Phys. Rev. B* **1994**, *49*, 17360

[285] C. Massobrio, A. Pasquarello, R. Car, *Chem. Phys. Lett.* **1995**, *238*, 215

[286] P. Calaminici, A. M. Köster, N. Russo, D. R. Salahub, *J. Chem. Phys.* **1996**, *105*, 9546

[287] C. Massobrio, A. Pasquarello, A. D. Corso, *J. Chem. Phys.* **1998**, *109*, 6626

[288] P. Calaminici, A. M. Köster, A. Vela, K. Jug, *J. Chem. Phys.* **2000**, *113*, 2199

[289] K. Jug, B. Zimmermann, A. M. Köster, *Int. J. Quant. Chem.* **2002**, *90*, 594

[290] K. Jug, B. Zimmermann, P. Calaminici, A. M. Kösterm *J. Chem. Phys.* **2002**, *116*, 4497

[291] P. Jaque, A. Toro-Labbé, *J. Chem. Phys.* **2002**, *117*, 3208

[292] M. Kabir, A. Mookerjee, A. K. Bhattacharya, *Phys. Rev. A* **2004**, *69*, 043203

[293] M. Yang, K. A. Jackson, *J. Chem. Phys.* **2005**, *122*, 184317

[294] S. Li, M. M. G. Alemany, J. R. Chelikowsky, *J. Chem. Phys.* **2006**, *125*, 034311

[295] M. Yang, K. A. Jackson, C. Koehler, T. Frauenheim, J. Jellinek, *J. Chem. Phys.* **2006**, *124*, 024308

[296] P. Calaminici, A. M. Köster, Z. Gómez-Sandoval, *J. Chem. Theory Comput.* **2007**, *3*, 905

[297] M. B. Knickelbein, *J. Chem. Phys.* **2004**, *120*, 10450

[298] ECP10MDF + (10s10p8d3f2g) for **Cu**
D. Figgen, G. Rauhut, M. Dolg, H. Stoll, *Chem. Phys.* **2005**, *311*, 227

[299] J. P. Perdew, K. Burke, M. Ernzerhof, *Phys. Rev. Lett.* **1996**, *77*, 3865

[300] K. P. Huber, G. Herzberg, *Constants of Diatomic Molecules* (Van Nostrand Reinhold, New York, 1979)

[301] E. A. Rohlfing, J. J. Valentini, *J. Chem. Phys.* **1986**, *84*, 6560

[302] P. Schwerdtfeger, G. A. Bowmaker, *J. Chem. Phys.* **1994**, *100*, 4487

[303] P. Neogrady, V. Kellö, M. Urban, A. J. Sadlej, *Int. J. Quant. Chem.* **1997**, *63*, 557

[304] Z. Cao, Y. Wang, J. Zhu, W. Wu, Q. Zhang, *J. Phys. Chem. B* **2002**, *106*, 9649

[305] O. Ingólfsson, U. Busolt, K. Sugawara, *J. Chem. Phys.* **2000**, *112*, 4613

[306] G. Maroulis, *J. Phys. Chem. A* **2003**, *107*, 6495

[307] M. Melnik, R. V. Parish *Coord. Chem. Rev.* **1986**, *70*, 157

[308] J. B. Foley, A. E. Bruce, M. R. M. Bruce *J. Am. Chem. Soc.* **1995**, *117*, 9596

[309] A. A. Mohamed, A. E. Bruce, M. R. M. Bruce *The Chemistry of Organic Derivatives of Gold and Silver*; S. Patai, Z. Rappoport, Eds.; Wiley: New York, **1999**, p 313

[310] M. C. Gimeno, A. Laguna, *Chem. Rev.* **1997**, *97*, 511

[311] K. P. Hall, D. M. P. Mingos, *Prog. Inorg. Chem.* **1984**, *32*, 237

[312] F. Scherbaum, A. Grohmann, B. Huber, C. Krüger, H. Schmidtbaur, *Angew. Chem. Int. Ed. Engl.* **1988**, *27*, 1544

[313] (a) F. Scherbaum, A. Grohmann, G. Müller, H. Schmidbaur, *Angew. Chem. Int. Ed. Engl.* **1989**, *28*, 463
(b) O. Steigelmann, P. Bissinger, H. Schmidbaur *Angew. Chem. Int. Ed. Engl.* **1990**, *29*, 1399

[314] N. Rösch, A. Göring, D. E. Ellis, H. Schmidbaur, *Angew. Chem.* **1989**, *101*, 1410

[315] H. Schmidbaur, *Chem. Soc. Ref.* **1995**, *24*, 391

[316] P. Schwerdtfeger, P. D. W. Boyd, *Inorg. Chem.* **1992**, *31*, 327

[317] P. Schwerdtfeger, H. L. Hermann, H. Schmidbaur, *Inorg. Chem.* **2003**, *42*, 1334 (and references therein)

[318] (a) G. Schmid, R. Pfeil, R. Boese, F. Bandermann, S. Meyer, G. H. M. Calis, J. W. A. van der Velden, *Chem. Ber.* **1981**, *114*, 3634
(b) J. P. Fackler Jr., C. J. McNeal, R. E. P. Winpenny, L. H. Pignolet, *J. Am. Chem. Soc.* **1989**, *111*, 6434

[319] V. W. W. Yam, C.-L. Chan, S. W.-K. Choi, K. M.-C. Wong, E. C.-C. Cheng, S.-C. Yu, W.-K. Chan, K.-K. Cheung, *J. Chem. Soc., Chem. Commun.* **2000**, 53

[320] H. Z. Zhang, C.-M. Che, *Chem. Eur. J.* **2001**, *7*, 4887

[321] Y. Jiang. S. Alvarez, R. Hoffman, *Inorg. Chem.* **1985**, *24*, 749

[322] a) P. Pyykkö, Y. Zhao, *Angew. Chem. Int. Ed. Engl.* **1991**, *30*, 604
b) P. Pyykkö, J. Li, N. Runeberg, *Chem. Phys. Lett.* **1994**, *218*, 133

[323] N. Runeberg, M. Schütz, H-J. Werner, *J. Chem. Phys.* **1999**, *110*. 7210

[324] L. Magnko, M. Schweizer G. Rauhut, M. Schütz, H. Stoll, H.-J. Werner, *Phys. Chem. Chem. Phys.* **2002**, *4*, 1006

[325] E. O'Grady, N. Kaltsoyannis, *Phys. Chem. Chem. Phys.* **2004**, *6*, 680

[326] S. Riedel, P. Pyykkö, R. A. Mata, H.-J. Werner, *Chem. Phys. Lett* **2005**, *405*, 148

[327] S. F. Boys, F. Bernadi, *Mol. Phys.* **1985**, *19*, 553

[328] (a) G. A. Bowmaker, J. D. Cotton, P. C. Healy, J. D. Kildea, S. Bin Silong, B. W. Skelton, A. H. White, *Inorg. Chem.* **1989**, *28*, 1462
(b) L.-J. Baker, G. A. Bowmaker, R. D. Hart, P. J. Harvey, P. C. Healy, A. H. White, *Inorg. Chem.* **1994**, *33*, 3925

[329] L.-J. Baker, G. A. Bowmaker, D. Camp, P. C. Healy, H. Schmidbaur, O. Steigelmann, A. H. White, *Inorg. Chem.* **1992**, *31*, 3656

[330] L.-J. Baker, R. C. Bott, G. A. Bowmaker, P. C. Healy, B. W. Skelton, P. Schwerdtfeger, A. H. White, *J. Chem. Soc., Dalton Trans.* **1995**, *8*, 1341

[331] M. J. Frisch, G. W. Trucks, H. B. Schlegel et al., GAUSSIAN 03, Revision C.02, Gaussian, Inc., Wallingford CT, 2004.

[332] a) C. W. Bauschlicher, S. R. Langhoff, H. Partridge, L. A. Barnes, *J. Chem. Phys.* **1989**, *91*, 2399
b) L. A. Barnes, M. Rosi, C. W. Bauschlicher, *J. Chem. Phys.* **1990**, *93*, 609

[333] I. Antes, G. Frenking, *Organometallics* **1995**, *14*, 4263

[334] P. Pyykkö, N. Runeberg, F. Mendizabal, *Chem. Eur. J.* **1997**, *3*, 1451

[335] A. A. Bagatur'yants, A. A. Safonov, H. Stoll, H.-J. Werner, *Chem. Phys.*, *109*, 3096

[336] N. Runeberg, M. Schütz, H.-J. Werner, *J. Chem. Phys.* **1999**, *110*, 7210

[337] ECP10MDF + [6s6p4d3f2g] → (10s10p8d3f2g) for **Cu**;
ECP28MDF + [6s6p4d3f2g] → (10s10p8d3f2g) for **Ag**;
ECP60MDF + [6s6p4d3f2g] → (10s10p8d3f2g) for **Au**;
D. Figgen, G. Rauhut, M. Dolg, H. Stoll, *Chem. Phys.* **2005**, *311*, 227

[338] ECP10MDF + aug-cc-pVDZ (9s8p8d)/[5s4p3d] for **Br**;
ECP28oldMDF + aug-cc-pVDZ (9s7p7d)/[5s4p3d] for **I**;
K. A. Peterson, D. Figgen, E. Goll, H. Stoll, M. Dolg, *J. Chem. Phys* **2003**, *119*, 11113

[339] G. A. Bowmaker, H. Schmidbaur, S. Krüger, N. Rösch, *Inorg. Chem.* **1997**, *36*, 1754

[340] P. Schwerdtfeger, M. Dolg, W. H. E. Schwarz, G. A. Bowmaker, P. D. W. Boyd, *J. Chem. Phys* **1989**, *91*, 1762

[341] G. Kickelbein, U. Schubert, *Inorg. Chem. Acta* **1997**, *262*, 61

[342] N. C. Baenziger, W. E. Bennett, D. M. Soboroff, *Acta Cryst., Sec. B* **1976**, *32*, 962

[343] K. Angermaier, E. Zeller, H. Schmidbaur, *J. Organomet. Chem* **1994**, *472*, 371

[344] E. R. T. Tiekink, *Acta Cryst., Sec. C* **1989**, *45*, 1233

[345] M. Seth, P. Schwerdtfeger, M. Dolg, K. Faegri, B. A. Hess, U. Kaldor, *Chem. Phys. Lett.* **1996**, *250*, 461

[346] P. Pyykkö, J. P. Desclaux, *Acc. Chem. Res.* **1979**, *12*, 276

Behnam Assadollahzadeh
email:behnam@gmx.net

New Zealand; a country full of beauty and the natural habitat of the elusive kingfish.